Assessing past oxygen in the ocean using Cr isotopes as a palaeo-proxy

Serginio R.C. Remmelzwaal

MSci Hons (University College London), 2014
Fellow of the Geological Society

A dissertation submitted to the University of Bristol in accordance with the requirements for the award of the degree of Doctor of Philosophy in the Faculty of Science.

School of Earth Sciences
6th of April 2018

Supervisors: Dr I.J. Parkinson, Professor D.N. Schmidt, Dr F.M. Monteiro

Word Count:
49926

‘Omnium rerum principia parva sunt’
Marcus Tullius Cicero

Acknowledgements

First and foremost, I would like to thank my supervisors Ian Parkinson, Daniela Schmidt and Fanny Monteiro. Without their expertise, input, and life advice completing my Ph.D. research would not have been possible. I would also like to express my gratefulness to Aleksey Sadekov, for his help and advice have proven invaluable to large parts of my work and he has been like a mentor to me. I would also like to thank all my friends for pulling me through my Ph.D., which was testing at times. Please accept my apologies for complaining so much to you and I promise to make more time for you now! I would like to especially mention my lovely flatmates, Emily, Rose and Gael for providing so much emotional support during my write-up, and all-star Elwyn for providing comic relief (or in his own words: "a funny distraction thanks to his chaotic personality"). Coming back to home-cooked dinner and your loveliness after work has made this process just so much more bearable! A special mention should also go to my lab buddy Lucie. The many hours of column chemistry, vial cleaning and mass spectrometry adventures would not have been fun without you there (although breaking the Neptune was maybe a little too adventurous!). I also thank Taryn and Hojung for being wonderful people I can talk to about all my problems at any point of the day despite the physical distance between us. Lastly, but definitely not least, to Chulinya, mama and oma I would like to say how much I appreciate having you as my family and that without you I would not have been able to have started this Ph.D. in the first place. Thank you for always supporting my choices and being such a steadfast rock to hold onto at all times.

Dankwoord

Ten eerste wil ik mijn begeleiders Ian Parkinson, Daniela Schmidt en Fanny Monteiro bedanken voor hun hulp. Zonder hun expertise, inbreng en levensadvies zou het voltooien van mijn promotie-onderzoek niet mogelijk zijn geweest. I wil graag ook Aleksey Sadekov bedanken. Zijn hulp en advies waren onmisbaar voor grote gedeeltes van dit werk en hij was als een mentor voor mij. Ik wil ook al mijn vrienden bedanken voor hun steun en begrip tijdens soms lastige tijden. Ik beloof dat ik niet meer zoveel zal klagen over mijn werk! Een speciaal bedankje gaat ook uit naar mijn huisgenoten, Emily, Rose en Gael voor de emotionele steun tijdens het schrijven van mijn promotie-onderzoek en Elwyn voor de vrolijke noot die hij is. Dat ik na een dag hard werken thuis kon komen en een warme maaltijd en jullie stralende gezichten voorgeschoteld kreeg maakte het allemaal draaglijk! Mijn dank gaat ook uit naar mijn labmaatje Lucie. De vele uren in het laboratorium zouden veel minder plezierig zijn geweest zonder jouw aanwezigheid. Ik bedank ook Taryn en Hojung, omdat ze een geweldige steun zijn geweest en ik hen, ondanks de fysieke afstand tussen ons, op elk willekeurig tijdstip heb kunnen bellen om mijn problemen te bespreken. Ik wil graag ook tegen Chulinya, mama en oma zeggen hoeveel ik het waardeer om jullie als mijn familie te hebben en dat ik zonder jullie nooit maar zelfs ervan had kunnen dromen om dit onderzoek te kunnen uitvoeren. Vanuit de grond van mijn hart bedank ik jullie voor jullie onvoorwaardelijke steun en dat ik altijd op jullie kan bouwen.

Author's declaration

I declare that the work in this dissertation was carried out in accordance with the requirements of the University's Regulations and Code of Practice for Research Degree Programmes and that it has not been submitted for any other academic award. Except where indicated by specific reference in the text, the work is the candidate's own work. Work done in collaboration with, or with the assistance of, others, is indicated as such. Any views expressed in the dissertation are those of the author.

SIGNED: …… DATE: ……

Abstract

As greenhouse gas emissions into the atmosphere persist, both oceanic and atmospheric temperatures are projected to continue rising with major consequences for the marine environment. One of the major environmental hazards of this century is the spread of low-oxygen environments or ocean deoxygenation. While modern hypoxic environments are closely monitored, the mechanisms leading to these conditions are not fully understood in the context of an Earth system. Past ocean deoxygenation can be used as an analogue to shed light on oceanic dissolved oxygen responses to global warming. The aim of this study is to ground truth the palaeo-redox proxy of the Cr isotopic composition of foraminifera and bulk carbonates to elucidate the processes that led to and the eventual extent of hypoxic and anoxic environments during past climatic events.

The potential of foraminiferal Cr isotopes as a new redox proxy was assessed by determining element partitioning and isotopic fractionation of Cr by foraminifera using a variety of geochemical techniques (LA-MC-ICP-MS, (MC-)ICP-MS, nanoSIMS). To date, Cr isotopes in biogenic carbonates have been interpreted to record the seawater δ^{53}Cr composition at the site of test mineralisation in the surface ocean. While Cr is distributed throughout the foraminiferal test in both fossil and modern samples, sediment (fossil) core-top samples have up to two orders of magnitude more Cr than non-sedimentary and culture samples. Iron and Cr cross-plots suggest that although at least part of the Cr signal in foraminifera is primary, the Cr signal is overprinted by the uptake of Cr in bottom and pore waters. In sediment samples, there is no interspecies isotope fractionation ("vital effect") and the Cr isotopic composition of tests is related to the size of the test through surface area/volume ratio effects on secondary Cr incorporation. This study concludes that Cr in foraminifera is mostly post-depositional and records bottom/pore water signals.

Chromium isotopes in carbonates were applied to study how climate change influenced ocean deoxygenation during the Pleistocene, Palaeocene-Eocene Thermal Maximum, Eocene Thermal Maximum 2, Ocean Anoxic Event 2 and Ocean Anoxic Event 1a. Chromium isotopes in carbonates record local seawater deoxygenation during these events. Open ocean deoxygenation can mainly be pinned to rising temperatures in intermediate ocean waters. Deoxygenation through the direct effects of temperature on the solubility of dissolved oxygen do not account for the inferred expansion of low-oxygen conditions. Indirect effects of elevated temperatures (e.g. enhanced microbial metabolic rates and remineralisation) are needed in addition to fully account for the episodic deoxygenation during the Cenozoic. The Cr isotope excursions during the Cretaceous are not governed by thermal effects in the same manner as during the Cenozoic which may be attributed to fundamental climatic and palaeogeographical differences between the Cretaceous and Cenozoic.

Table of contents

List of Figures

Chapter 1: Introduction and Methods

Chapter 2: Foraminifera as seawater chromium recorders

Chapter 3: Foraminiferal Cr isotopes and ocean deoxygenation during the PETM

Chapter 4: A critical assessment of deoxygenation through deep time using chromium isotopes in carbonates

Chapter 5: Rare Earth Element – Yttrium composition of carbonates

Chapter 7: Future research perspectives

Supplementary Material A: Geochemical data

Supplementary Material C: Hydrological and associated biogeochemical consequences of rapid global warming during the Palaeocene-Eocene Thermal Maximum (Carmichael et al., 2017)

List of Tables

Supplementary Material B: cGENIE model-data fit scores and dataset

Supplementary Material C: Hydrological and associated biogeochemical consequences of rapid global warming during the Palaeocene-Eocene Thermal Maximum (Carmichael et al., 2017)

List of Acronyms

ACC	-	Amorphous Calcium Carbonate
AMZ	-	Anoxic Marine Zone
BIF	-	Banded Iron Formation
BSE	-	Bulk Silicate Earth
CC	-	Calcite Crust
CIE	-	Carbon Isotope Excursion
ETM-2	-	Eocene Thermal Maximum 2
F	-	Final chamber (in foraminifera)
F-1	-	Chamber prior to final chamber (in foraminifera)
Ga	-	billion years ago
Gyrs	-	billion years
GAM / GAMC	-	Gametogenic calcite
GOE	-	Great Oxidation Event
ICL	-	Inner Calcite Layer
ICP-MS	-	Inductively Coupled Plasma Mass Spectrometry
Kyrs	-	thousands of years
Ka	-	thousand years ago
LA-MC-ICP-MS	-	Laser Ablation Multi Collector Inductively Coupled Plasma Mass Spectrometry
Myrs	-	million years
Ma	-	million years ago
MC-ICP-MS	-	Multi Collector Inductively Coupled Plasma Mass Spectrometry
MIS-6	-	Marine Isotope Stage 6
NanoSIMS	-	Nanoscale Secondary Ionisation Mass Spectrometry
OAE	-	Ocean Anoxic Event
OCL	-	Outer Calcite Layer
OIE	-	Oxygen Isotope Excursion
Ol	-	Organic layer
OLZ	-	Oxygen Limited Zone
OMZ	-	Oxygen Minimum Zone
PAL	-	Present Atmospheric Level
PETM	-	Palaeocene-Eocene Thermal Maximum
POM	-	Primary Organic Membrane
POS	-	Primary Organic Sheet
PTB	-	Permo-Triassic Boundary
REE / REE-Y	-	Rare Earth Element (-Yttrium)
SEM	-	Scanning Electron Microscope

Chapter 1

Introduction and Methods

A serious side-effect of global warming is the decrease of oceanic oxygen levels, also known as ocean deoxygenation. Over the last decades an increase in the extent and number of areas affected by deoxygenation has risen rapidly (e.g. Stramma et al. 2008; Schmidtko et al. 2017; Breitburg et al., 2018). As oxygen is essential for marine life, a decrease in oxygen will likely have a significant impact on the local ecosystem, especially when paired with thermal stress and ocean acidification (Doney et al., 2012). Suboxic waters are also a major controlling factor in the nitrogen cycle and an expansion of these waters will likely be accompanied by the release of the greenhouse gas N_2O (Gruber, 2008). Therefore, it is important to understand what consequences deoxygenation has and what controls its extent and rate of spreading.

1.1. Modern Oxygen Minimum Zones

1.1.1. What are Oxygen Minimum Zones?

Oxygen concentration profiles in the ocean are not uniform (e.g. Karstensen et al., 2008). Concentrations in the upper euphotic zone are highest due to photosynthesis and air-sea gas exchange (Gruber and Sarmiento, 2002). The high primary productivity in this uppermost layer produces marine snow – organic detritus – raining down to the deep-sea underneath (Gruber and Sarmiento, 2002). The respiration of this marine snow consumes oxygen and with depth oxygen levels decline through a zone deficient in oxygen (the Oxygen Limited Zone - OLZ) to a minimum – the so-called Oxygen Minimum Zone (OMZ; Gilly et al., 2013). Below the OMZ oxygen levels increase again due to remineralisation of organic matter (Gilly et al., 2013). OMZs in the open ocean are permanent features, unlike the 'dead zones' in shallow waters caused by eutrophication (Diaz and Rosenberg, 2008), and typically occur at intermediate water depths ranging from 400 – 1200 m (Keeling et al., 2010).

Oceanic oxygen levels are usually divided into four different categories: oxia, hypoxia, suboxia, and anoxia. The oxic-hypoxic boundary is defined as 60 µM O_2 (e.g. Gray et al., 2002; Keeling et al., 2010). This level is a threshold below which organisms start experiencing severe stress due to hypoxia (e.g.

Seibel, 2011; Vaquer-Sunyer and Duarte, 2008). When oxygen concentrations start dropping below 5 µM, the water becomes suboxic and experiences major changes in biogeochemistry (Keeling et al., 2010) which will be further elaborated on in section 1.1.3. Any waters that are completely devoid of oxygen or that have concentrations below the detection limit are anoxic (Thamdrup et al., 2012). Anoxic conditions are not wide-spread in the modern ocean (Keeling et al., 2010). Anoxic zones within the OMZ are sometimes referred to as Anoxic Marine Zones (AMZ; Ulloa et al., 2012).

Large OMZs in the Atlantic and Pacific are located in cyclonic gyres around the equatorial upwelling zones at the eastern side of the basin where water is most stagnant (Keeling et al., 2010).

1.1.2. Modern OMZ expansion

Over the past decades oxygen concentrations within OMZs have gradually declined by 0.09 – 0.34 µM per year in tropical intermediate waters and has been paired with shoaling and deepening of the OMZs (Gilly et al., 2013; Keeling et al., 2010; Stramma et al., 2008; Breitburg et al., 2018). In total, 4.8 petamoles (~ 2%) of dissolved oxygen has been lost since the 1960s (Schmidtko et al., 2017). Dissolved oxygen trends show large regional differences with some sites near OMZs exceeding a 4% loss (Schmidtko et al., 2017) and other sites a small increase (Helm et al., 2011; Keeling et al., 2010). Model projections suggest a global average loss of dissolved oxygen of up to 7% by the year 2100 and reflects losses expected with anthropogenic climate change (Schmidtko et al., 2017; Breitburg et al., 2018).

1.1.3. Controlling factors on OMZs

The degree of oxygen deficiency and the volume of low oxygen waters is primarily controlled by three processes; air-sea gas exchange, circulation patterns, and biological activity in surface and intermediate layers (Keeling et al., 2010).

1.1.3.1 Air-sea gas exchange

In the surface mixed layer dissolved oxygen is in equilibrium with atmospheric oxygen, although seawater is usually slightly undersaturated compared to the atmosphere by 3 – 10% in winter (Gordon and Huber, 1990) and higher in the summer due to the lower solubility of oxygen in warmer water (Keeling et al., 2010). As most deep-water is formed during the winter at high latitudes (Keeling and Manning, 2014), these conditions control the oxygen level in surface water prior to deep-water formation (initial O_2; Keeling et al., 2010). Other factors such as wind and humidity also exert minor controls on air-sea gas exchange that can alter initial dissolved gas levels in surface water (Nightingale and Liss, 2003).

1.1.3.2 Ocean circulation

The time since a parcel of seawater was last in contact with the atmosphere is called the ventilation age (Talley et al., 2011). Oxygen concentrations start at near saturation levels and will decrease with time due to remineralisation of organic matter (Gruber and Sarmiento, 2002). Ventilation ages are controlled by global ocean circulation and hence in general the further away from the sites of deep-water formation the water is, the lower the oxygen concentrations will be. The tendency to form OMZs therefore differs between ocean basins and is dependent on how well-ventilated the basin is overall (Karstensen et al., 2008). The Atlantic is well-ventilated and oxygen concentrations in the OMZs do not drop below 20 µM in the South Atlantic and even 40 µM in the North Atlantic – near the site of deep-water formation (Karstensen et al., 2008). In the Pacific and Indian Ocean suboxic and even anoxic levels are attained in the OMZ due to the relatively poor ventilation in these basins compared to the Atlantic (Karstensen et al., 2008).

1.1.3.3 The biological pump

The largest biological use of oxygen is by bacterial oxidation of organic detritus raining down from the euphotic zone. Higher oxygen utilisation rates will be underneath highly productive areas with a large export production (Keeling et al., 2010). This process is driven by the biological pump. The biological pump is the ocean's biological sequestration of carbon from the atmosphere to deep seawater and the sediment. The strength of the biological pump is limited by nutrient availability. In shallow waters, however, the nutrient supply can be so great that the biological pump can cause severe deoxygenation (eutrophication; Diaz and Rosenberg, 2008).

1.1.3.4 Microbial biogeochemistry in an OMZ

In oxygenated conditions bacteria will use O_2 as electron acceptors for respiration, however when oxygen levels fall below 5 µM (suboxia) bacteria will switch to anaerobic respiration and use NO_3^- as an electron acceptor (Keeling et al., 2010). In this process NO_3^- is reduced to NO_2^- and eventually N_2 through denitrification and anaerobic oxidation of NH_4^+ (anammox) (Canfield et al., 2010). The microbial activity in suboxic waters accounts for over 33% of the loss of fixed nitrogen (Codispoti et al., 2001). Fixed nitrogen is a limiting nutrient and suboxia therefore acts as a negative feedback on surface productivity (Codispoti et al., 2001). If the seawater is depleted in NO_3^-, microbes will start reducing SO_4^{2-} to SO_3^{2-} (Keeling et al., 2010). Evidence for sulphur-cycling was found in the Chilean OMZ in the Southeast Pacific (Canfield et al., 2010). Suboxic waters are thought of as an intermediate stage between fully oxygenated waters and sulphidic environments (Canfield et al., 2010).

1.1.3.5 Thermal forcings of oxygen outgassing

As oceans warm the solubility of oxygen decreases resulting in a less effective transfer of oxygen from the atmosphere into the ocean (Keeling et al., 2010). Approximately 15% of the total observed oxygen

losses is thought to have been caused by decreased solubility and slower ventilation (Helm et al., 2011; Schmidtko et al., 2017). In intermediate waters, the outgassing is in the same range as could be expected from thermally induced outgassing (Schmidtko et al., 2017). In some regions additional forcings are needed to fully explain the observed oxygen losses (Schmidtko et al., 2017).

Ocean stratification and the slowing down of ocean circulation are large drivers of deoxygenation as well and these processes have started to strengthen (e.g. Keeling and Garcia, 2002). A decrease in subduction and sluggish ventilation impacts the transport of oxygen to deeper waters (e.g. Deutsch et al. 2005). Models suggest that a switch from inorganic to organic transport of nutrients to subsurface waters caused by a higher nutrient utilisation (a higher productivity) also contribute to the loss of oxygen under stratified surface waters through oxidation of organic matter (Keeling et al., 2010). Oxygen concentrations are inversely proportional to the transport of inorganic nutrients to subsurface waters (Keeling et al., 2010). Thermally induced oxygen loss in intermediate and deep waters is estimated at 703 teramoles every decade (Schmidtko et al., 2017).

1.1.3.6 Warming impact on biological mediation of dissolved oxygen

Physical drivers are thought to have the largest impact on ocean deoxygenation, but changes in ecology, primary productivity and biogeochemistry also contribute to the loss of oxygen (Gilly et al., 2013). Global warming is thought to cause an enhanced hydrological cycle which, apart from stratification, will consequently increase nutrient delivery to the oceans with an associated increase in primary productivity. As noted before, an increased biological pump will create a depletion of oxygen in mid-depth waters through consumption of organic matter by microbial communities (Gilly et al., 2013). Primary productivity responses vary greatly regionally with reports of decreased productivity in oligotrophic areas in the open ocean (Behrenfeld et al., 2006; Doney et al., 2012) as well as increases, notably, in surface waters above OMZs (Behrenfeld et al., 2006).

Rising temperatures also increase metabolic rates (Davidson and Janssens, 2006; Altieri and Gedan, 2015). This relationship is expressed as $Q_{10} = (\alpha_2/\alpha_1)^{10/(\theta 2-\theta 1)}$ (Eppley, 1972), where α_1 and α_2 are growth rates at two temperatures θ_1 and θ_2. Metabolic rates generally double with a 10-degree temperature increase in microbes ($Q_{10} = 2$; Doney et al., 2012), but rate changes can be significantly higher in, for example, Arctic microbial communities (Kritzberg et al., 2010). This physiological response in turn also strengthens the biological pump, although in the longer term these temperature effects may be offset by a reorganisation of the microbial community structure (Doney et al., 2012). Macro-organisms will respond much in the same way creating an increased demand for oxygen in a shrinking oxygenated environment above the OMZs (Doney et al., 2012; Altieri and Gedan, 2015).

1.2. Ocean deoxygenation and rapid climate change in the geological past

The Earth's climate has experienced dramatic changes throughout geological time (e.g. Jenkyns, 2003). From modern observations of global warming, it is evident that the oceans are experiencing environmental changes such as sea level rise, ocean acidification and ocean deoxygenation (IPCC AR5, 2013). Similar effects have been observed in the geological record as well (e.g. Jenkyns, 2003; Jenkyns et al., 2010). Past episodes of climate change varied in magnitude, location and the background climate during which they occurred and can therefore inform us on how the Earth's system reacts to extreme disturbances. Periods of rapid and catastrophic climate change in the past have been identified mainly through palaeontological evidence for mass extinctions and geochemical evidence such as oxygen and carbon isotopes (Jenkyns, 2003). Some of the most dramatic environmental changes during the Phanerozoic occurred at the Permo-Triassic boundary (PTB), the Triassic-Jurassic boundary, the Mesozoic Ocean Anoxic Events (OAEs), the Palaeogene hyperthermals and the Pleistocene glacial-interglacial cycles. The effects of severe deoxygenation have been especially well-documented for the PTB and the OAEs.

The PTB crisis is recognised as the most severe mass extinction in Earth's history with a loss of approximately 90% of species (e.g. Erwin, 1994). During the PTB there was wide-spread anoxia as indicated by geochemical, petrographic and biomarker proxies (e.g. Lau et al., 2016; Elrick et al., 2017; Zhang et al., 2018). The actual extent and timing of anoxia during the PTB has been unclear but recent studies suggest wide-spread deoxygenation at intermediate water depths of 200-1000 m before the mass extinction and transient chemocline shallowing from the mass extinction onwards (Algeo et al., 2008; Winguth and Winguth, 2012; Feng and Algeo, 2014). Uranium isotope records from shallow water carbonates confirm there was a strong correlation between the mass extinction and a global development of anoxia during the PTB (e.g. Lau et al., 2016; Elrick et al., 2017; Zhang et al., 2018).

Ocean anoxic events are periods of severe anoxia typically associated with global warmth caused by the Jurassic and Cretaceous greenhouse climates (e.g. Jenkyns et al., 2010). Several of these events of nearly global anoxia have occurred throughout the Mesozoic. It was hypothesised that the occurrence of OAEs may have mainly concentrated in the Mid to Late Cretaceous due to a transgression submerging continents and leading to extensive epicontinental and marginal shallow seas (Schlanger and Jenkyns, 1976). Shallow seas are associated with high productivity and could have facilitated in extensive carbon burial as well as deoxygenation. Schlanger and Jenkyns (1976) also proposed that ocean circulation during the Cretaceous would have been sluggish due to high water temperatures leading to the expansion of OMZs and anoxic bottom waters. Many OAEs occur during periods with enhanced volcanic activity and along with methane hydrate release in marginal seas could have caused

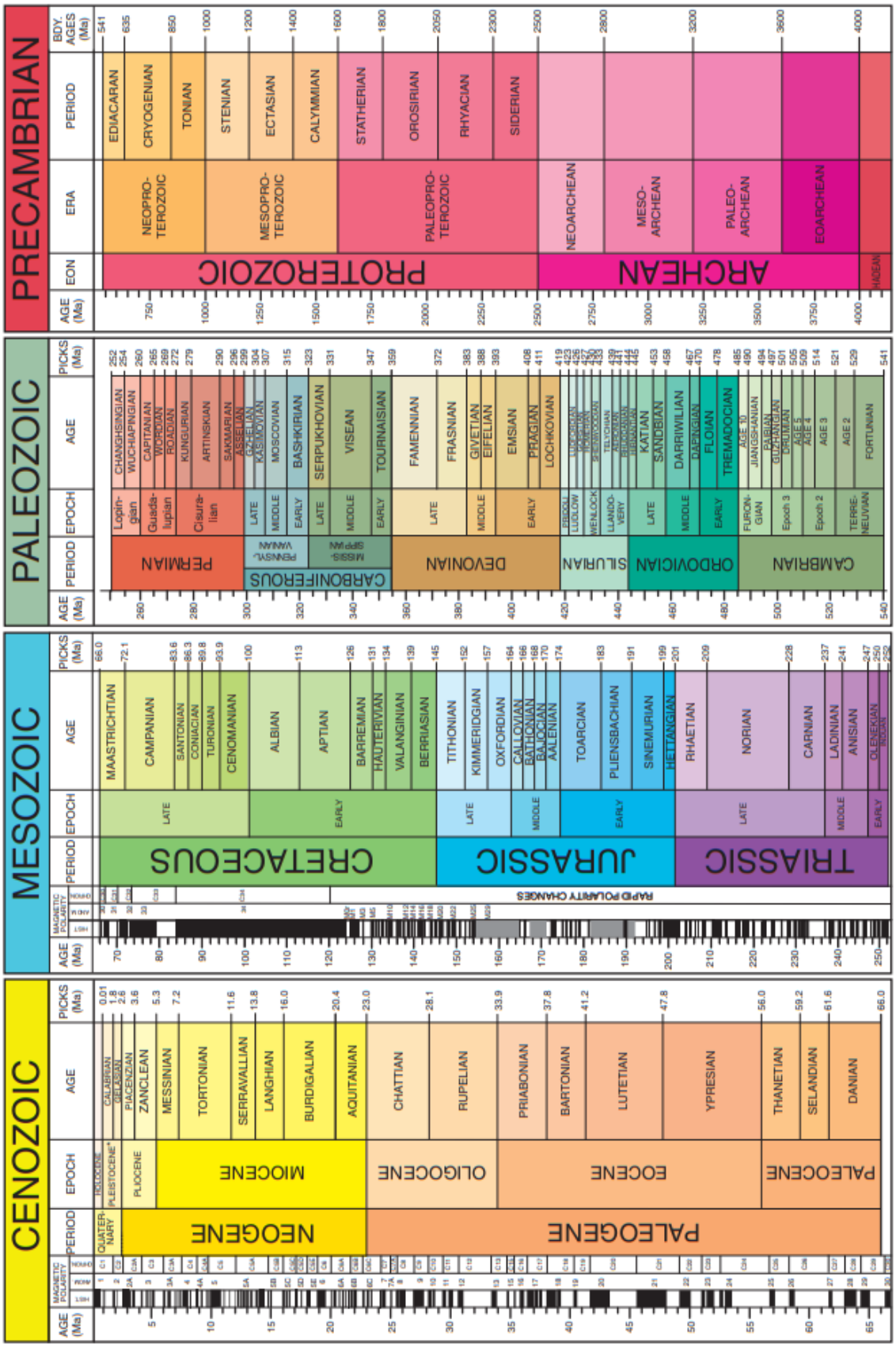

Figure 1.1 The geological timescale for the Mesozoic and the Cenozoic, Palaeozoic and Precambrian eras (after Walker et al., 2012).

rapid climatic shifts towards high temperatures and increased nutrient delivery to the ocean (e.g. Jenkyns et al., 2010). OAEs are marked by high organic carbon contents due to high primary productivity and intense ocean anoxia (e.g. Pedersen and Calvert, 1990; Bralower and Thierstein, 1984).

Similar scenarios to those that formed the OAEs have been proposed to explain the Palaeogene hyperthermal events (e.g. Gutjahr et al., 2017). Because the Palaeogene hyperthermals are less wide-spread and are of a shorter duration than OAEs it is believed that they may represent the onset stages of OAEs that 'failed' to develop further (Jenkyns et al., 2010).

1.3. Chromium Geochemistry

Chromium has multiple valence states, from 0 to +6, and is therefore redox-active. The two most common stable valence states in natural environments are Cr(III) and Cr(VI) with Cr(II) and Cr(0) as naturally occurring minor constituents. Cr(IV) and Cr(V) are meta-stable and therefore short-lived. Cr(III) is highly reactive and insoluble in water at a neutral pH range (Johnson and Bullen, 2004), whereas Cr(VI) is highly toxic (Kortenkamp et al., 1996) and soluble at neutral pH conditions in oxic waters. Chromium has four stable isotopes of which ^{52}Cr and ^{53}Cr are the most abundant with 83.785 atom% and 9.5059 atom%, respectively, and ^{50}Cr and ^{54}Cr being the minor isotopes (Johnson and Bullen, 2004). Recently, much attention has been given to Cr isotopes due to the potential they have for remediating carcinogenic Cr(VI) contaminants and for reconstructing the palaeoredox state of the oceans (Ellis et al., 2002).

1.3.1. Chromium speciation in seawater

Seawater Cr can be found as Cr(III) and Cr(VI) (Sirinawin et al., 2000). Elderfield (1970) predicted with thermodynamic calculations that oxidised Cr(VI) is the dominant valence state and can be found mainly in the forms of CrO_4^{2-} and $HCrO_4^-$ in seawater. Cr(III) usually constitutes <5% (Mugo and Orians, 1993) of the total Cr content, as would be expected from a thermodynamic perspective (Elderfield, 1970). The dominant valence state is strongly related to the Eh and thermodynamic dominance and will change from Cr(VI) to Cr(III) if the Eh drops below approximately 540 mV (Brookins, 1988). At a low pH, Cr(III) is dominant and with a higher pH the $Cr(OH)^{2+}$, $Cr(OH)_2^+$, $Cr(OH)_3$ and $Cr(OH)_4^-$ species become stable (Zink et al., 2010). However, the concentration of Cr(III) in seawater is not predicted by speciation calculations. In some cases Cr(III) has elevated concentrations up to 90 % of the total Cr concentration (Connelly et al., 2006; Sander et al., 2003). Reduction of hexavalent to trivalent Cr in oxic seawater can be induced by photochemical Fe(II) and organic matter (Schroeder and Lee, 1975).

Acid - neutral pH: $3Fe^{2+} + HCrO_4^- + 7H^+ \longrightarrow 3Fe^{3+} + Cr^{3+} + 4H_2O$

Alkaline pH: $3Fe^{2+} + CrO_4^{2-} + H_2O \longrightarrow 3Fe^{3+} + Cr^{3+} + 8OH^-$

$xCr^{3+} + (1-x)Fe^{3+} + 3OH^- \longrightarrow (Cr_xFe_{1-x})(OH)_3\ (s)$

Oxidation of Cr(III) to Cr(VI) is slower than the reduction to Cr(III) (Elderfield, 1970; Schroeder and Lee, 1975), causing Cr(III) concentrations to rise (Cutter, 1992). Alternatively, Cr(III) release from sinking particulate matter has been suggested to explain the high Cr(III) concentrations (Achterberg and Van Den Berg, 1997; Connelly et al., 2006). In a neutral to alkaline and anoxic environment the main reductant of Cr(VI) is Fe(II) while in a more acidic environment Fe(II) is less efficient (Pettine et al., 1998). Proposed reductants in acidic conditions include H_2O_2 and Cu(I) (Abu-Saba et al., 2000; Pettine et al., 2002).

1.3.2. Isotope Fractionation Systematics

There are two types of isotope fractionation: equilibrium fractionation and kinetic fractionation. Equilibrium fractionation is governed by a set of qualitative rules (Schauble, 2004) that govern which chemical species will be enriched in heavier isotopes. Firstly, equilibrium fractionation is inversely related to temperature. Equilibrium fractionation is also dependent on the difference in isotopic masses, where light elements and elements with a large mass difference experience the largest fractionation. The size of fractionation follows $(m_{heavy}) - (m_{light}) / (m_{light} * m_{heavy})$, where m stands for the different isotopic masses (Schauble, 2004). When an isotope system is at equilibrium, the reaction product with the stiffest bonds will be enriched in heavy isotopes. A great stiffness of chemical bonds corresponds with, amongst others, a high oxidation state of the element itself or of the atom to which it is bonded, a low coordination number, and covalent bonds between elements with a comparable electronegativity - fractionation is less likely to occur in ionic bonds. According to the above rules, Cr should be able to provide information on ancient and modern redox conditions (Schauble, 2004).

Kinetic isotope fractionation involves unidirectional reactions during an incomplete exchange of isotopes between different phases, where this exchange is limited due to an exchange activation energy. Kinetic fractionation is based on the fact that light isotopes are more reactive and therefore reaction products are depleted in heavy isotopes. In other words, heavier isotopes have a higher activation energy (lower molecular velocity) which inhibits its reactivity. This is related to the basic physical equations $E = 0.5hv$ (Planck's equation) and $KE = 0.5mv^2$. All molecules of the same species have the same kinetic energy at ground state, but the isotopologues have different masses and therefore different velocities with the lighter isotopologues being faster. Kinetic fractionation is less sensitive to temperature changes than equilibrium fractionation, but is more sensitive to other factors such as reaction rates (Schauble, 2004). In an open system, unlimited fractionation will occur. In a closed system, there will be Rayleigh fractionation, where there is an increasingly lighter reactant pool. If a reaction has several steps, the

slowest reaction is the so-called rate-limiting step. The overall isotopic shift is equal to that of the kinetic fractionation of the rate-limiting step and any equilibrium fractionation preceding it. All steps after the rate-limiting step have no influence on the overall fractionation. It is possible to have more than one rate-limiting step in a reaction chain (Canfield, 2001).

Fractionation can be expressed in terms of the fractionation factor, α. α is related to the difference in isotope ratios between species exchanging isotopes through:

$$\alpha_{A\text{-}B} = R_A^{i/j} / R_B^{i/j}$$

Where R is the isotopic ratio of the isotopes i and j for chemical species A and B. Equilibrium fractionation α can also be obtained through $\alpha = K^{1/n}$, where usually $n = 1$ and where K is the equilibrium constant. It is the fractionation factor that is inversely related to temperature through $1/T^2$ at temperatures below ~ 500 ˚C (Bigeleisen and Mayer, 1947).

1.3.3. The Chromium Isotope System

Chromium isotope data is presented in the so-called delta notation, where the permille (‰) deviation of a sample ratio from a standard ratio is displayed. The rationale behind the delta notation is a mathematical simplification of physical processes affecting the stable isotope system (Albarède and Beard, 2004).

$$\delta^{53}Cr = \left(\frac{R_{sample}^{53/52}}{R_{SRM979}^{53/52}} - 1 \right) * 10^3$$

The standard used is NIST SRM-979, which is a high purity $Cr(NO_3)_3.9H_2O$ crystalline solid. NIST SRM-979 has an absolute $^{53}Cr/^{52}Cr$ value of 0.1134561 (Bonnand et al., 2011).

The fractionation factor can also be expressed in terms of $\delta^{53}Cr$:

$$\alpha = \frac{1000 + \delta^{53}Cr_{Cr(III)}}{1000 + \delta^{53}Cr_{Cr(VI)}}$$

The fractionation factor is usually close to unity (approximately 1) and therefore the fractionation can be made clearer by making use of $1000\ln\alpha_{(Cr(III)\text{-}Cr(VI))} \approx (\alpha_{(Cr(III)\ -\ Cr(VI))} - 1)*10^3 = \varepsilon$, which leads to the relationship as defined in Johnson et al. (2004):

$$\varepsilon \approx 1000 ln\alpha_{(Cr(III)-Cr(VI))} \approx \delta^{53}Cr_{Cr(III)} - \delta^{53}Cr_{Cr(VI)} \equiv \Delta_{(Cr(III)-Cr(VI))}$$

The approximate isotopic fractionation can therefore be found by subtracting the different δ-values of a reagent and reaction product. Fractionation factors can also be determined by using multiple isotopic ratios for elements with more than two isotopes. If fractionation of both ratios is mass-dependent, the difference between two or more ratios will also be mass-dependent. Chromium has 4 naturally occuring isotopes, which can be used to determine the fractionation. Ratios $R^{Cr\text{-}53/Cr\text{-}52}$ and $R^{Cr\text{-}54/Cr\text{-}52}$ can be related through the function $\alpha^{Cr\text{-}54/Cr\text{-}52} = (\alpha^{Cr\text{-}53/Cr\text{-}52})^Z$ where $Z = (m_{Cr\text{-}54}/m_{Cr\text{-}52})[(m_{Cr\text{-}53}-m_{Cr\text{-}52})/(m_{Cr\text{-}53}-m_{Cr\text{-}52})]$, which leads to $\delta^{53}Cr \approx [(^{54}Cr - {}^{52}Cr)/(^{53}Cr-{}^{52}Cr)]\ \delta^{54}Cr$ (Johnson et al., 2004). More on the use of different Cr isotope ratios will follow in section 1.6.

1.3.4. Abiotic Reduction

The reduction of Cr(VI) to Cr(III) is accompanied by an isotopic fractionation (Ellis et al., 2002). During reduction of Cr(VI) the lighter ^{52}Cr isotope enriches reaction products containing Cr(III), as they preferentially react compared to ^{53}Cr. The reactants, therefore, get isotopically heavier (Ellis et al., 2002). This behaviour is typical of Rayleigh processes and experiments by Ellis et al. (2002) show that as Cr(VI) concentrations dropped, as expected during its reduction, the $\delta^{53}Cr$ of the reagent increases. The redox reactions involved most likely do not reach equilibrium at surface temperatures (Johnson and Bullen, 2004) and therefore equilibrium fractionation is unlikely to have a major effect in contrast to Rayleigh fractionation (Johnson and Bullen, 2004). Altman and King (1961) hypothesised that the slow equilibration was due to the multiple electron transfers involved in the reduction of Cr(VI), as well as a coordination change from tetrahedral to octahedral.

The magnitude of fractionation of Cr(VI) has been determined both theoretically for equilibrium effects (Schauble, 2004) (Table 1.1) and experimentally (Ellis et al., 2002; Johnson and Bullen, 2004; Zink et al., 2010) for kinetic effects (Table 1.2).

Table 1.1 Equilibrium fractionation between Cr species (Schauble et al., 2004)

Cr exchange	$1000ln\alpha_{A-B}\ (0^oC)$	$1000ln\alpha_{A-B}\ (25^oC)$
$CrO_4^{2-} - Cr(H_2O)_6^{3+}$	7.6	6.6
$Cr(H_2O)_6^{3+} - Cr\ (s)$	3.9	3.5
$Cr(H_2O)_6^{3+} - Cr(Cl)_6^{3-}$	4.0	3.5

The relatively strong fractionation between $Cr(H_2O)_6^{3+}$ and Cr(Cl) points towards complexing of Cr(III) in aqueous media as a result of a bond between Cr and elements that are not oxygen (Johnson and Bullen, 2004). Redox processes are dominant in fractionating Cr, but other effects, such as speciation

or precipitation, might also influence the total fractionation (Johnson and Bullen, 2004). However, the magnitude of these has not yet been fully assessed. As mentioned earlier, isotopic equilibrium is most likely not attained within the range of temperatures on Earth and therefore kinetic fractionation is more probable. Table 1.2 shows the kinetic fractionation factors found by several different studies:

Table 1.2 Experimentally derived kinetic isotope fractionation factors of Cr.

ε	α	pH	Reaction	Reference
<0.04	0.99996	4 - 6	Cr(VI) adsorption	Ellis et al. (2004)
-3.4	0.9966	7	Cr(VI) (aq) $\longrightarrow$ Cr(III) (s)	Ellis et al. (2002)
-5	0.995	7	Cr(VI) (aq) $\longrightarrow$ Cr(III) (aq)	Zink et al. (2010)
+0.6	1.0006	10.5	Cr(III) oxidation (Cr(III) fraction)	Zink et al. (2010)
+0.2	1.0002	10.5	Cr(III) oxidation (Cr(VI) fraction)	Zink et al. (2010)

Ellis et al. (2002) found that lighter Cr isotopes react preferentially during Cr(VI) reduction in sediments and magnetite. Autoclaved experiments have similar reduction rates to the unautoclaved samples and therefore reduction must be predominantly abiotic. The similarity of the fractionation factors shows that the reduction mechanisms in all experiments were the same and due to its abiotic nature likely caused by kinetic effects (Ellis et al., 2002). In the experiments of Ellis et al. (2002) and Johnson and Bullen (2004) Cr(III) was adsorbed to organic and inorganic matter. The experiments performed by Zink et al. (2010) kept trivalent and hexavalent Cr in solution. These experiments show that differences in the handling of reagents does not affect fractionation. However, at a neutral pH (Zink et al., 2010) found a much larger fractionation (ε = -5‰) than Ellis et al. (2002) who found ε = -3.4‰ (Table 1.2). At a pH of <1 Cr fractionates at -3.5‰, which is within the uncertainty of the findings by Ellis et al. (2002). The low pH prevented Cr(III) from forming hydroxides and precipitating. Additionally, a low pH increases the formal potential of the reduction, which in its turn increases the reduction rate leading the system to a quicker attainment of equilibrium (Zink et al., 2010). The resulting -3.54‰ seems to be constant and indicative of equilibrium fractionation in agreement with the calculations by Schauble et al. (2004). The pathway of Cr(VI) reduction is complex with multiple rate-limiting steps that affect the overall fractionation (Zink et al., 2010). The fractionation factors and reduction rates for the reduction steps are still debated, however (Pettine et al., 2002). Zink et al. (2010) also found that Cr reduction is not time dependent.

1.3.5. Biotic Reduction

Reduction of Cr(VI) also occurs microbially with associated isotopic fractionation. Sikora et al. (2008) found a variable ε in *Shewanella odeinensis* cells of 4.1‰ in an electron donor-poor environment and of 1.8‰ in a donor-rich environment (α = 0.9965 and 0.9975, respectively). Microbial fractionation therefore has the potential to be larger than the abiotic fractionation determined by Ellis et al. (2002).

Various workers have compared chromate reduction to sulphate reduction to explain this difference in fractionation (Myers et al., 2000; Johnson and Bullen, 2004; Sikora et al., 2008). Sulphur isotope research shows that the magnitude of fractionation is strongly dependent on nutrient availability to the micro-organisms, where an abundance of nutrients facilitates little fractionation and vice versa (Herbel et al., 2000; Johnson and Bullen 2004). Since microbial life is omnipresent in nature, hexavalent Cr reduction associated with its metabolism is likely a large contributor to the overall fractionation. Chromium isotopes could therefore potentially give an insight into terrestrial and oceanic microbial processes. However, these findings are hard to reconcile with the reported small contribution of biotic effects (Ellis et al., 2002).

1.3.6. Sorption & Speciation Effects

During transport of Cr(VI) in an aqueous environment (e.g. rivers) sorption occurs. Ellis et al. (2004) show that sorption has a negligible effect on Cr isotope fractionation with equilibrium fractionation being less than 0.04‰ (Table 1.2). Equilibrium curves show a nearly instantaneous isotope ratio shift with no further fractionation afterwards. However, a kinetic effect has also been observed by Ellis et al. (2004), which may be of importance in systems that have not reached full equilibrium. Furthermore, there is a possibility that small amounts of fractionation might occur at the fringes of plumes during transport (Ellis et al., 2004). Beforementioned findings are supported by a study on Cr isotopic data of the Paraná River which found that despite a substantial change in Cr concentration between the tributaries, the major Paraná River and the estuary in which it drains, there is no significant change in the $\delta^{53}Cr$ values (Frei et al., 2014). The same study by Ellis et al. (2004) found that there is no measurable effect associated with the speciation of chromate and bichromate. No significant isotopic exchange takes place between dissolved Cr(III) and Cr(VI) either (Zink et al., 2010).

1.3.7. Chromium Oxidation

The isotopic effect of oxidation of Cr(III) to Cr(VI) is considerably smaller than Cr reduction (Zink et al., 2010) and is even negligible according to (Izbicki et al., 2008). Chromium (III) oxidation takes place in seconds and roughly plots along a Rayleigh function with an ε of +0.6‰ for the Cr(III) fraction. The Cr(VI) fraction, however, does not plot along the expected Rayleigh function and instead has an ε of +0.2‰ (Zink et al., 2010), which may be due to a complex oxidation system with intermediary products that is not yet fully understood (Zink et al., 2010). Intermediary Cr(V) formation is postulated as being the rate-limiting step (Impert et al., 2008). The $\delta^{53}Cr_{Cr(III)}$ shows a decrease with reaction time during Cr(III) oxidation, whereas the $\delta^{53}Cr_{Cr(VI)}$ does not show this behaviour (Zink et al., 2010). This increased fractionation over time is thought to be caused by a slow and continuous oxidation with a possible small-scale back reduction (Zink et al., 2010).

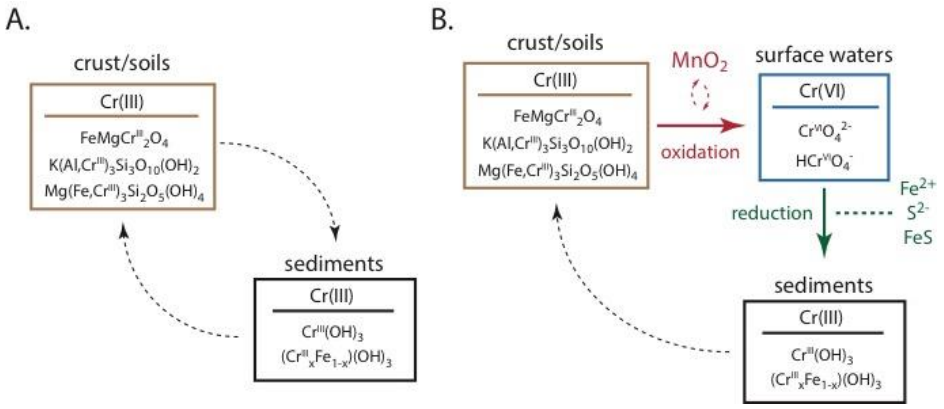

Figure 1.2: Overview of low temperature Cr cycling after Saad et al. (2017): A. Cr(III) cycling is thought to be characterized by limited isotope fractionations. However, this framework has not been tested. B. At high oxygen levels, dissolved Cr(III) will oxidise to Cr(VI) through a MnO_2 catalisation. This reaction is thought to be necessary for Cr isotopic variability in the geological record.

1.3.8. Redox-independent Cr isotope fractionation

In the presence of common microbial exudates (such as siderophore and small organic acids) Cr(III) is released from solid phases such as Cr(III)-Fe(III)-(oxy)hydroxides (Saad et al., 2017a). Microbial exudates promote the Cr(III) release via both ligand complexation and increased solid solubility (Saad et al., 2017a). Recent work has also shown that Cr solubilisation through ligands is paired with an isotopic fractionation of -0.27 to +1.23‰ in the solubilised Cr(III) (Saad et al., 2017b). It is important to consider the effects of the redox-independent isotopic fractionation of Cr through Cr(III)-ligand solubilisation on the seawater δ^{53}Cr.

1.3.9. Chromium Reservoirs and Fluxes

Chromium isotopic values vary across different reservoirs and the fluxes in between these reservoirs and is affected by various processes as Cr-bearing phases travel through space and time. Firstly, a main source of chromium is from the mantle. Chromium is a compatible trace metal and is therefore abundant in the mantle with concentrations of 0.41% to 0.55% (McDonough and Sun, 1995). Mafic rocks, due to the behaviour of Cr during partial melting, have higher Cr concentrations (often > 1,000 ppm or even 2,000 ppm) than felsic and sedimentary rocks, which usually contain less than 100 ppm of Cr (Faure and Mensing, 2009). The continental crust has an average Cr concentration of around 100 ppm (McLennan, 2001). Mantle-derived chromites ($FeMgCr_2O_4$) collected across the world point towards an isotopically uniform mantle chromite reservoir of -0.079 ± 0.129‰ that stayed within ± 0.100‰ over the last 3.5 billion years, and which Farkaš et al. (2013) call the 'canonical' mantle signature. This uniformity is to be expected considering the decreasing influence of equilibrium fractionation with higher temperatures through the relationship $1/T^2$ (Bigeleisen and Mayer, 1947). The canonical value is within the uncertainty of the bulk silicate earth data (-0.124 ± 0.101‰) that Schoenberg et al. (2008)

derived from igneous silicates from the mantle and indicates a heterogeneous distribution of Cr isotopes within the mantle (Farkaš et al., 2013).

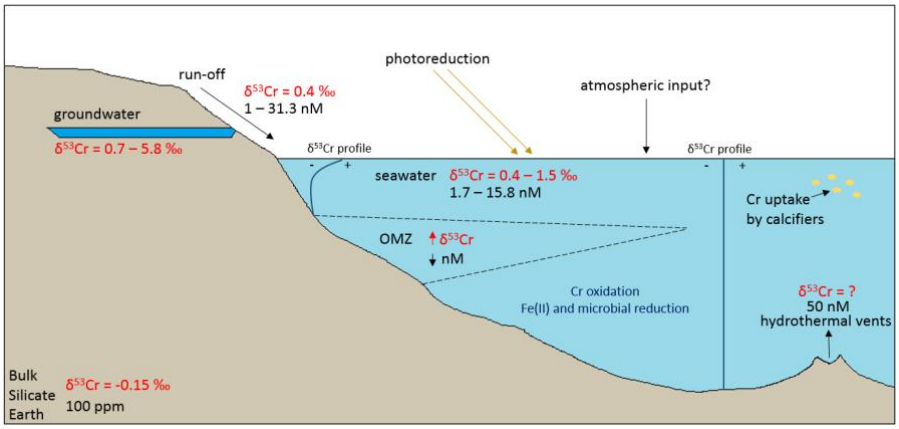

Figure 1.3: Overview of the Cr cycle and reservoirs after Bonnand (2011).

Farkaš et al. (2013) also found, in contrast to Schoenberg et al. (2008), that the $\delta^{53}Cr$ systematically becomes heavier with an increasing serpentinisation and alteration of ultramafic rocks. Frei and Polat (2013) found the system to be in balance with negatively fractionated Cr (-0.43‰) in Palaeoproterozoic weathered basaltic palaeosoils at Schreiber Beach (Canada) and positively fractionated Cr (+0.39‰) in the run-off inferred from overlying cherts. Similar results were found by Crowe et al. (2011) in Indonesian laterites, where the topsoil has a $\delta^{53}Cr$ composition of -1.19 ± 0.25‰ and the run-off a heavy $\delta^{53}Cr$ of +2.60 ± 0.08‰. A study on laterite profiles from subtropical Argentina by Frei et al. (2014) found that removal of Cr is associated with an isotopic shift of 0.6‰ within the soil profile and is caused by Cr(III) oxidation (with values of +0.15 and +0.23‰ in the topsoil thought to contain trapped run-off) similar to the findings of Frei and Polat (2013). The above-mentioned studies imply that Cr(VI), enriched in heavy ^{53}Cr, is preferentially mobilised into the run-off, leaving behind soils depleted in heavy Cr isotopes.

Data on riverine Cr concentrations and $\delta^{53}Cr$ is sparse and has only been determined for a handful of rivers in North America (Cranston and Murray, 1980; Campbell and Yeats, 1984; Taylor et al., 2012; Wu et al., 2017), Europe (Pettine et al., 1992; Comber and Gardner, 2003; Dragun et al., 2009; Farkaš et al., 2013; Novak et al., 2014; D'Arcy et al., 2016), South America (Frei et al., 2014; Mora et al. 2009), and the Indian subcontinent (Paulukat et al., 2015). Several studies have attempted to determine the $\delta^{53}Cr$ of river waters (Table 1.3), which they found to be on average +0.35 ± 0.14‰ in the Paraná river system (from the tributaries through the main river channel to the estuary; Frei et al., 2014), range within -0.17 to +0.92‰ in the Connecticut river (Wu et al., 2017), are on average +1.02 and +1.33‰ in the Damsal and Brahmani rivers on the Indian subcontinent (Paulukat et al., 2015), range between -0.17 to +1.68 in Ireland (D'Arcy et al., 2016), and fall between -0.1 to +3.96‰ in Central Europe

(Farkaš et al., 2013; Novak et al., 2014). These riverine values are consistent with the run-off values from Frei et al. (2014) and the weathered rocks in the Connecticut river catchment area (Wu et al., 2017). The Cr isotope signature in the Paraná remained similar from the tributaries to the estuary, indicative of conservative behaviour (Frei et al., 2014).

The major source of Cr in the ocean is through weathering of mafic rocks on land (Crowe et al., 2011; Frei et al., 2014). Rivers have relatively constant concentrations of dissolved Cr of an average of approximately 55 nM along their length with a drop of 50% in estuaries (Frei et al., 2014; table 1.3). Seawater from the open ocean (Argentine Basin) has Cr contents of 0.9 – 10.95 nM (Table 1.4). Seawater Cr concentrations, as expected, diminish the further away one gets from the river mouth due to dilution in the ocean (Frei et al., 2014). In early studies it was found that Cr concentrations were low in surface seawater and that it was therefore comparable to nutrients (Whitfield and Turner, 1987). Recent research has revealed, however, that there is only a modest depletion of Cr at the seawater surface and that there is no correlation between nutrients and Cr, nor a significant difference between the Pacific and Atlantic Oceans (Sirinawin et al., 2000; Bonnand et al., 2013). The lack of difference between the Pacific and Atlantic Oceans latter suggesting there is no substantial loss of Cr during global ocean circulation. Chromium has an estimated residence time of 3,000 - 9,000 years (Reinhard et al., 2014; Qin and Wang, 2017) which is in accordance with its classification between a nutrient and conservative element. The Cr isotopic signature of the Paraná River and its estuary (+0.35 ± 0.14‰) have been found to roughly match the local δ^{53}Cr of ocean water from the Argentine Basin (+0.41 to +0.56‰) into which the Paraná discharges its load (Bonnand et al., 2013; Frei et al., 2014) with a particularly striking match between measurements from the Paraná estuary and Argentine Basin surface water. Therefore, there is an indication that the Cr isotope signal transported by large rivers is preserved in the ocean surface water (Frei et al., 2014).

Table 1.3 Published fluvial Cr concentration and δ^{53}Cr data

Rivers	δ^{53}Cr(‰)	Cr(VI) (nM)	Total Cr (nM)	Reference
Po River			10 - 54	Pettine et al. (1992)
Sava River			4.8 - 6.5	Dragun et al. (2009)
Humber Estuary		1.5 - 6.2	1.2 - 17.1	Comber and Gardner (2003)
Glenariff River catchment	-0.17 - +1.68		2.3 - 28.9	D'Arcy et al. (2016)
Mohelno Stream	+2.48 - +3.96		150,012 - 448,111	Farkaš et al. (2013)
Central European waters	-0.1 - +3.9		13.5 - 73.1	Novak et al. (2014)
Orinoco River			1.4 - 11.3	Mora et al. (2009)
Paraná River & tributaries	+0.23 - +0.44		13.5 - 53.8	Frei et al. (2014)
Paraná Estuary	+0.44		21.2	Frei et al. (2014)
Damsal River	+1.33		577	Paulukat et al. (2015)
Brahmani Estuary	+1.02		5.8	Paulukat et al. (2015)
St Lawrence River			2.7 - 15.4	Campbell and Yeats (1984)
Sacramento River			1 - 7	Taylor et al. (2012)
Columbia River		1.7 - 3.5	1.8 - 3.8	Cranston and Murray (1980)
Connecticut River catchment	-0.17 - +0.92		1.2 - 10	Wu et al. (2017)

Next to riverine input, there is also a small flux of atmospherically transported Cr into the ocean (Connelly et al., 2006), which can be seen as negligible considering the residence time of Cr compared to this flux. Chromium export to the deep ocean is equally small as the atmospheric influx when there is low productivity, but during times characterised by high productivity at the ocean surface there is an increased removal of Cr that correlates with the increased organic carbon flux to the deep ocean (Connelly et al., 2006). Connelly et al. (2006) argued that the seasonal variability in Cr speciation might be linked to biological activity with most of the Cr in surface seawater being recycled between Cr(III) and Cr(VI). This seasonal variability extends to the $\delta^{53}Cr$ composition of seawater (Paulukat et al., 2016). Chromium isotope values in the Baltic Sea were heavier in October and April than in June by +0.21 to +0.45‰ which can potentially be attributed to seasonal redox changes and/or seasonal algal blooms which have the potential to reduce Cr(VI) to Cr(III) (Paulukat et al., 2016).

Table 1.4 Published seawater $\delta^{53}Cr$ values, and Cr(VI) and total Cr concentrations.

Ocean body	$\delta^{53}Cr$(‰)	Cr(VI) (nM)	Total Cr (nM)	Reference
NE Pacific Ocean		1.6 - 3.5		Cranston and Murray (1978)
NE Pacific Ocean			1.7 - 4.0	Cranston (1983)
NE Pacific Ocean	0.61 - 0.91		3.76 - 4.53	Scheiderich et al. (2015)
Oregon Coast	1.41		2.05	Scheiderich et al. (2015)
Eastern Pacific Ocean		1.1 - 6.0		Murray et al. (1983)
East Pacific Rise			1.9 - 15.8	Jeandel and Minster (1984)
South Pacific Ocean			2.4	Golimowski et al. (1985)
South Pacific (French Polynesia)	0.53 - 0.67		6.57 - 7.33	Paulukat et al. (2016)
South Pacific (Australia)	0.75		3.83	Paulukat et al. (2016)
South and North Pacific Ocean			2.3 - 6.5	Jeandel and Minster (1987)
Pacific Ocean		2.1 - 4.2	2.9 - 4.6	Isshiki et al. (1989)
Pacific Ocean		0.7 - 6.8	6.3 - 19.4	Sander et al. (2003)
North Pacific Ocean		2.3 - 4.3	2.3 - 4.3	Mugo and Orians (1993)
North Pacific (California)	0.77 - 0.96		3.30 - 7.66	Paulukat et al. (2016)
Indian Ocean		0.3 - 2.4	0.9 - 2.8	Ghaddaf (1990)
Baltic Sea	0.13 - 0.80		1.59 - 7.78	Paulukat et al. (2016)
Mediterranean and Alboran			2.5 - 5.9	Sherrell and Boyle (1988)
NW Mediterranean		4.5 -5.8		Boussemart et al. (1992)
Mediterranean	0.81 - 0.96		4.60 - 5.89	Paulukat et al. (2016)
Mediterranean (Greece)	1.13	10.95	10.95	Economou-Eliopoulos et al. (2016)
Mediterranean (Gibraltar)		1.7 - 3.5	1.7 - 4.7	Achterberg and Van Den Berg (1997)
Atlantic (Gibraltar)			2.9 - 3.5	Sherrell and Boyle (1988)
Sargasso Sea	0.96		3.13	Scheiderich et al. (2015)
Sargasso Sea			2.5 - 6.5	Connelly et al. (2006)
NW Atlantic Ocean			3.2 - 5.2	Campbell and Yeats (1984)
North Atlantic Ocean			2.0 - 4.6	Jeandel and Minster (1987)
North-South Atlantic Ocean		3.1 - 7.3		Sirinawin et al. (2000)
North Atlantic Ocean			2.5 - 4.5	Mugo and Orians (1993)
North Atlantic Ocean	0.70 - 0.81		4.30 - 5.07	Paulukat et al. (2016)
North Atlantic (Portugal)	0.98		3.36	Paulukat et al. (2016)
North Atlantic (North Sea)	0.31 - 1.05		2.29 - 9.79	Paulukat et al. (2016)
North Atlantic (Baffin Bay)	0.70 - 0.75		3.28 - 3.68	Paulukat et al. (2016)
North Atlantic (UK)	1.50 - 1.51		1.83 - 1.86	Bonnand et al. (2013)
SW Atlantic Ocean	0.41 - 0.66		5.8 - 6.5	Bonnand et al. (2013)
South Atlantic (Brazil)	0.84 - 1.05		4.18 - 6.97	Periera et al. (2015)
Atlantic Ocean	1.08 - 1.71		2.19 - 3.00	Goring-Harford et al. (2018)
Arctic Ocean		3.0 - 6.1		Sirinawin et al. (2000)
Arctic Ocean	0.99 - 1.55		1.45 - 3.24	Scheiderich et al. (2015)
Arctic Ocean	1.24		4.57	Paulukat et al. (2016)
Southern Ocean	0.54 - 0.58		4.62 - 7.44	Paulukat et al. (2016)
Caribbean Sea		1.5 - 2.5		Sander et al. (2003)
Caribbean Sea (Yucatan)	1.13		2.78	Holmden et al. (2016)
Caribbean Sea (Jamaica)	1.11 - 1.17		2.71 - 2.87	Holmden et al. (2016)

The analysis of the top 25 cm of sediment cores from around an oxygen minimum zone (OMZ) off the coast of Pakistan (Staubwasser and Sirocko, 2002; Schoenberg et al., 2008) resulted in $\delta^{53}Cr$ values between +0.009 to -0.078‰ with an average of -0.032 ± 0.065‰. Similar measurements of $\delta^{53}Cr$ values in sediments deposited in the hypoxic Cariaco basin and Peruvian upwelling zone resulted in a $\delta^{53}Cr$ composition of +0.38 ± 0.10‰ and +0.61 ± 0.06‰, respectively – comparable to modern deep-water values (Gueguen et al., 2016). Oxic sediments had $\delta^{53}Cr$ values of around -0.05 ± 0.10‰, which are within analytical error of BSE (Gueguen et al., 2016; Schoenberg et al., 2008). This difference with igneous rocks is most likely due to river transport of Cr with slightly heavier $\delta^{53}Cr$ values (+0.35‰) (Frei et al., 2014). The sediments analysed by Schoenberg et al. (2008) have Cr concentrations ranging from 80 - 130 ppm. Black shales have very high concentrations of Cr ranging from 20 to 3000 ppm with an average of 100 ppm (Quinby-Hunt et al., 1997). In modern inorganic carbonates (ooids), the Cr concentration is approximately 2 - 4 ppm, which is significantly greater than the concentration in seawater (Bonnand et al., 2013). These measurements are also consistent with measurements of Cr in other carbonates, which range in value from 1 - 7 ppm (Frei et al., 2011, Bonnand et al., 2013). The isotopic composition of these ooids is 0.65 - 0.76‰, which is within the range of seawater $\delta^{53}Cr$ measurements (Table 1.4). The apparently small $\Delta^{53}Cr$ between ooids and seawater implies that no significant fractionation may have occurred during the preferential incorporation of Cr(VI) into carbonate lattices (Tang et al., 2007).

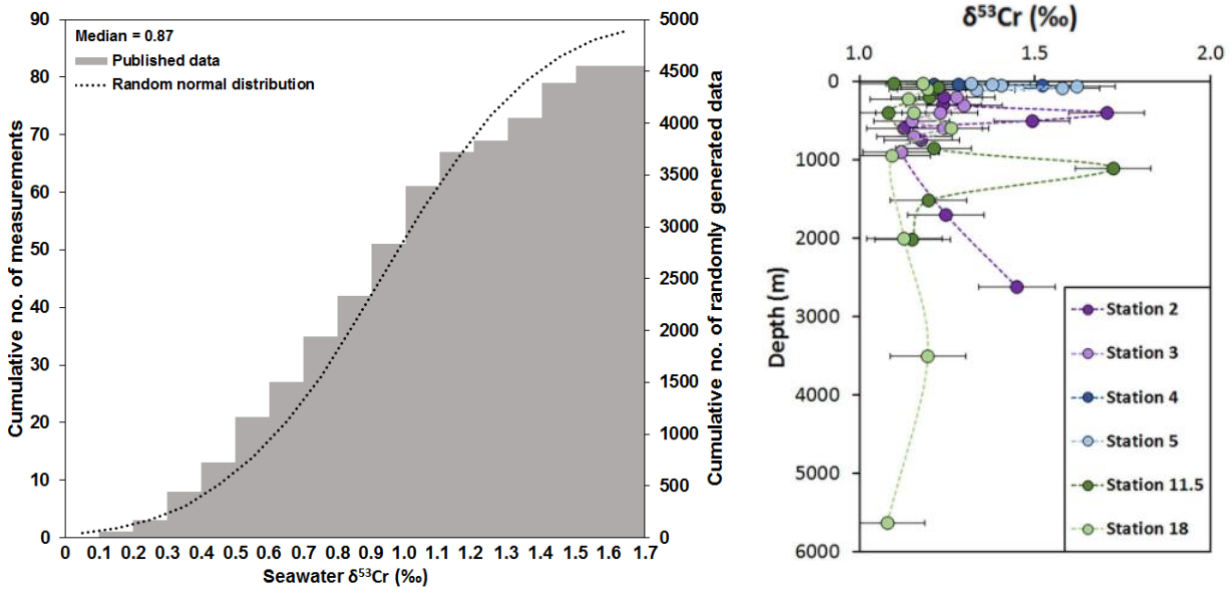

Figure 1.4: Left panel: A cumulative plot of published seawater $\delta^{53}Cr$ values show a normal distribution (Bonnand et al., 2013; Scheiderich et al., 2015; Paulukat et al., 2015; Economou-Eliopoulos et al., 2016; Paulukat et al., 2016; Pereira et al., 2016; Holmden et al., 2016; Goring-Harford et al., 2018). Right panel: Seawater $\delta^{53}Cr$ profiles in open seawater of the subtropical Atlantic Ocean (after Goring-Harford et al., 2018)

1.3.10. Published Cr Isotope Records

To date, only a handful of attempts have been made to construct a Cr isotope record (Figure 1.5). However, these have helped to understand the evolution of atmospheric oxygen by further constraining past atmospheric oxygen levels. Chromium isotopes from banded iron formations (BIFs) and palaeosols indicate that the formation of transient oxygen in the atmosphere goes back to about 2.6 - 2.9 billion years ago (Ga), and show evidence for Cr redox cycling at ~3 Ga, some 600 million years before the Great Oxidation Event (GOE) (Frei et al., 2009; Crowe et al., 2013; Planavsky et al., 2014). The δ^{53}Cr of up to 1.26‰ in the Mesoarchean, which is significantly outside the range for Cr with a high-temperature origin (Schoenberg et al., 2008; Crowe et al., 2013). During the Neoarchean BIFs show values of up to +0.29‰, which might point towards elevated levels of atmospheric oxygen and a slow build-up of transient oxygen over the 300 Myrs preceding the GOE (Frei et al., 2009). The BIFs deposited just before the GOE show almost no fractionation. No BIFS were deposited during the GOE and hence no Cr data has been retrieved yet. About 200 Myrs after the GOE, δ^{53}Cr values positively fractionated again, indicating a presence of minor amounts of free oxygen (Frei et al., 2009). Around 2 Ga there was no fractionation in δ^{53}Cr resulting in an inferred reducing environment again according to data by Frei et al. (2009). In contrast, Frei et al., (2013) found positive fractionation of up to +0.39‰ in 1.9-Gyr-old palaeosols from Schreiber Beach, Canada, which would support a slightly oxidising atmosphere. Subsequently, in the late Palaeoproterozoic, Cr isotope values started to rise again together with the oxygen levels (Frei et al., 2009). From the onset of the Statherian (1.8 Ga) throughout the Mesoproterozoic until the break-up of Rodinia at 750 Ma, the so-called Boring Billion, after which life rapidly evolved, oxygen concentrations were very low (< 0.1% PAL) as the δ^{53}Cr showed almost no difference to high-temperature igneous values (Planavsky et al., 2014). In the Cryogenian, approximately 750 Myrs ago δ^{53}Cr values increased significantly to values from +0.3 to +1.97‰ (Planavsky et al., 2014), after which the atmosphere has remained oxygenated to the modern day (Frei et al., 2009; Frei et al., 2011; Planavsky et al., 2014; Reinhard et al., 2014).

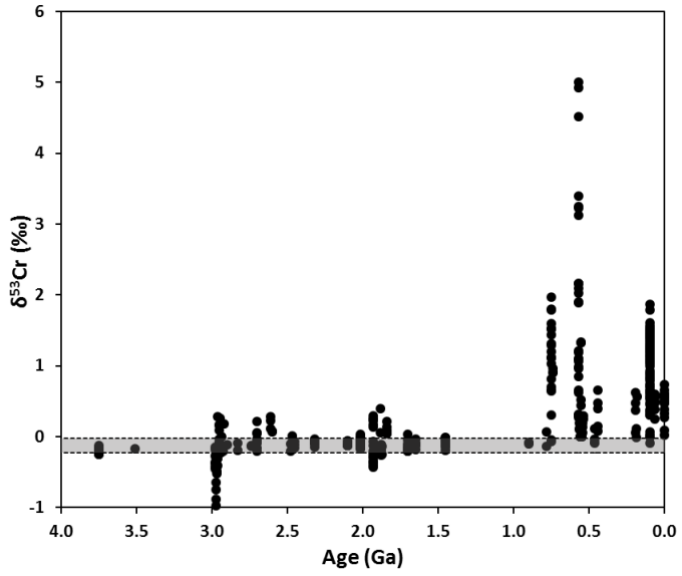

Figure 1.5: Chromium isotopic values throughout geological history (Frei et al., 2009,2011, 2013; Crowe et al., 2013; Planavsky et al., 2014; Reinhard et al., 2014; Wang et al., 2016; Holmden et al., 2016; Gueguen et al., 2016).

Chromium isotopic values during the Cenomanian-Turonian (~94 Ma) range from bulk silicate earth values up to +1.87‰ (Wang et al., 2016; Holmden et al., 2016). Changes in the Cr isotopic composition during OAE2 have been attributed to both volcanism (Holmden et al., 2016) and quantitative reduction (Wang et al., 2016) rather than presenting palaeoceanographic change. Quantitative reduction has also been proposed as an explanation of part of the $\delta^{53}Cr$ record during the last glacial maximum (Reinhard et al., 2014). During the last glacial maximum, a shift from oxic to anoxic waters occurred locally in the Cariaco Basin which has persisted since suggesting the Cr cycle has been at steady state for the entire Holocene (Reinhard et al., 2014). Similar shifts were observed during the Pleistocene glacial-interglacial cycles on the Peru margin (Gueguen et al., 2016).

1.4. Biomineralisation

In biogenic carbonates and other biominerals not only mineralogy and inorganic chemical processes but also the organism itself exerts control on the crystallography and chemical composition of the minerals it precipitates. When using biogenic carbonates, it is therefore imperative to understand the processes and controls at work resulting in the precipitation of biominerals before interpreting chemical data derived from these minerals.

1.4.1. General biomineralisation strategies

Both spatially and quantitatively, calcium carbonates are the most abundant minerals with a biological origin (Lowenstam and Weiner, 1989). Biominerals form in localised areas separated from the outer environment, usually physically delimited, where supersaturation can be attained (Erez, 2003). There are two different strategies organisms can adopt to form biominerals. Biomineralisation strategy end members are biologically induced mineralisation, and biologically controlled mineralisation (Weiner et al., 2004).

Biologically induced mineralisation is the process of secondary precipitation of biominerals as a result of environmental factors over which the organism can exert little to no control. The metabolism of the organism can slightly modify the surrounding environment, which could have an indirect impact on the nucleation and growth of a biomineral. Biominerals formed in this way are expected to be highly heterogeneous which will have a large effect on the trace element composition of the biomineral (Weiner et al., 2004).

However, some organisms are able to control the factors that govern the formation of biominerals. Biologically controlled mineralisation can be subdivided into three distinct strategies depending on the site of precipitation. Extracellular biomineralisation occurs on an organic matrix that is produced by the

cell. This matrix has the capacity to directly regulate the environment that is necessary for the precipitation of a specific biomineral (Weiner et al., 2004). The cell is able to transport elements necessary for biomineral formation to the matrix by actively pumping cations from outside of the cell membrane into the cell (Weiner et al., 2004). Transport outside of the cell is governed by diffusion processes or by actively pumping cations into a vesicle which is secreted from the cell and transported to the site of precipitation (Weiner et al., 2004). A second site of biomineralisation is in intercellular environments. This is a rarely followed strategy and can usually be encountered in single-celled organisms. Intercellular biomineralisation occurs on the epithelial surfaces of cells. Cations are transported through the cell membrane to the substrate both by active pumping and diffusion, so that the cell can exert control over the saturation state of the place of mineralisation (Weiner et al., 2004). The third and most common biomineralisation strategy occurs inside the cell. During intracellular biomineralisation, optimal conditions can be achieved and maintained in special vesicles and vacuoles. By physically completely isolating the nucleation and growth environment the cell can exert high levels of control on the concentrations of anions and cations necessary for the formation of the biomineral in question and the membrane is able to regulate environmental parameters such as pH and the trace element content (Weiner et al., 2004). There are, in general, two pathways intracellular mineralization can follow. After formation of a vesicle that has a high concentration of the biomineral building blocks through active pumping. Along the first pathway units of the biomineral are assembled either intracellularly to a larger structure and subsequently secreted, or individual units are secreted and assemblage occurs on an organic matrix. Along the second pathway the assembled biomineral will remain inside the cell (Weiner et al., 2004).

1.4.2. Vital Effects

During the process of mineralisation, organisms control the chemical and isotopic composition of their skeleton to varying degrees. Therefore, when using chemical tracers for oceanographic studies it is important to investigate the underlying processes in the organism, e.g. metabolism and mode of mineralisation, in order to better constrain the tracer system of interest. The combined effects an organism has on a tracer system are referred to as "vital effects" (Urey et al., 1951). Vital effects can be summarised as physiological effects that promote the precipitation of biominerals in isotopic disequilibrium with the surrounding environment.

There are two major groups into which vital effects can be categorised: kinetic vital effects and taxonomic vital effects. Kinetic vital effects might be caused by differing kinetics of uptake, transport and precipitation (Weiner et al., 2004). An example are the findings of McCrea (1950) that carbonates precipitate more readily at temperatures below 15 or above 60 °C. Taxonomic effects were discovered as workers started to see differences in strength of the vital effects between different phyla and species within a phylum with "good species" that precipitate their skeletons more or less in equilibrium with

the environment and "bad species" in which vital effects overprint the environmental signal (e.g. Birch et al., 2013).

There are several mechanisms organisms could use to control the precipitation of biominerals. One way of controlling biomineral formation is through the enzyme carbonic anhydrase, which is a catalyst for the hydration state of dissolved carbon dioxide. If present at the site of mineralisation, carbonic anhydrase will, besides catalysing the CO_2 (aq) hydration, eliminate any kinetic isotope effects for oxygen and other isotopes (McConnaughey, 1988). Secondly, the larvae of organisms from several phyla form the non-crystalline material amorphous calcium carbonate (ACC) before the final skeleton precipitates (Weiner et al., 2004). ACC precipitates from a supersaturated solution and needs the presence of elements such as Mg at high concentrations in order to proceed. In the absence of enough Mg certain proteins can also stabilise the ACC. Transient ACC is, in contrast to stable calcite, not hydrated and therefore possible isotope fractionation will be smaller than in hydrated calcite where equilibrium with the ambient environment is an important factor (Weiner et al., 2004).

The phase of the biomineral itself is also of importance when moving to a quantitative understanding of vital effects. The mineral phase, surface to bulk ratio of crystals, extent of crystalline order, and the presence of occluded macromolecules can all have substantial effects on the chemical composition of the biomineral. Other factors that potentially contribute towards the vital effects are the composition of the medium from which the biomineral precipitates, the crystal shape and maturation, and ontogenetic variations in mineralisation (Weiner et al., 2004).

1.4.3. Foraminiferal Biomineralisation

Foraminifera are single-celled amoebae that belong to the protists and precipitate the calcium carbonate polymorph calcite. There are, however, also two other groups of foraminifera can be defined based on test composition: foraminifera with organic test walls, and foraminifera with agglutinated tests. Foraminifera are generally associated with marine environments and are part of both the planktic and benthic communities in the ocean.

The calcitic radial (perforate) foraminifera first appeared in the Mesozoic and evolved throughout the Mesozoic and Cenozoic. Their tests are formed by radially oriented calcite crystals. Their alternative name, perforate, comes from the fact that the surface of the test is perforated with pores, which can be up to 10 µm in diatemeter (Erez, 2003). Another characteristic of perforate foraminifera is the lamination of their tests. Lamination forms over time as the pre-existing tests are covered with new layers of calcite. This happens every time the foraminifer builds a new chamber (Erez, 2003). Adult planktic foraminifera add a new chamber every 1-2 days (Hemleben et al., 1989). The perforate foraminifera form new chambers by firstly partially isolating itself from the environment through pseudopods. Secondly, an organic layer (Primary Organic Sheet/Membrane or POS/POM) in the shape

of the new chamber is formed over a cytoplasmic bulge that is the anlage. Onto the POS, crystals of $CaCO_3$ precipitate on both sides to create the chamber itself. Most of the calcite (about 90%) will precipitate onto the pre-existing chambers rather than forming part of the new chamber wall itself (Erez, 2003).

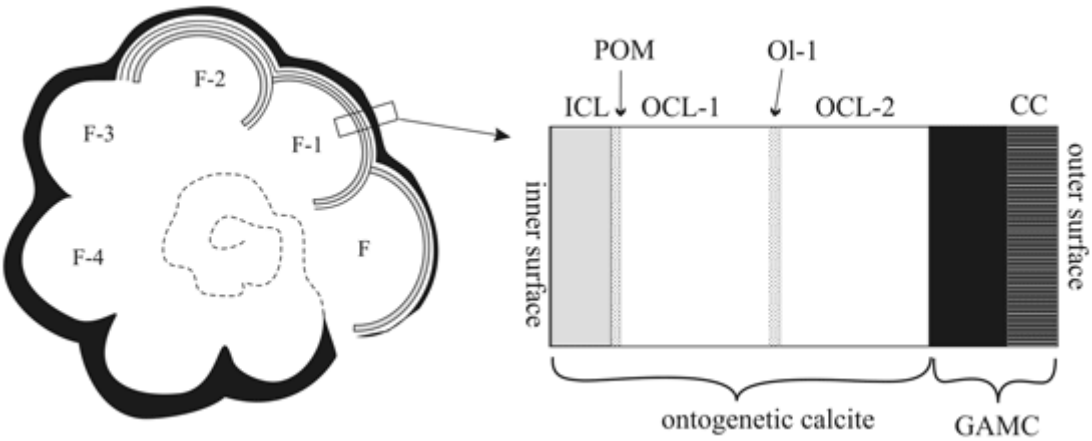

Figure 1.6: Schematic of planktic foraminiferal test and chamber wall construction by Sadekov et al. (2005). A new layer is precipitated over the test exterior during each new chamber construction. Calcite can also precipitate during and after gametogenesis (gametogenic calcite and calcite crust). The acronyms in the figure are: F (final chamber); F-1 (chamber before the final chamber); ICL (inner calcite layer); POM (primary organic membrane); OCL (outer calcite layer); Ol (organic layer); GAMC (gametogenic calcite); CC (calcite crust).

The chambers consist of ontogenetic calcite, which makes up most of the calcite in the foraminiferal test. However, at the end of a foraminifer's life cycle gametogenesis occurs, where the foraminifera eject gametes. During this process, the tests are covered by a final layer of calcite (gametogenic calcite or GAM) which is chemically and structurally distinct from ontogenetic calcite (Bé, 1980; Erez, 2003; Schmidt et al., 2008). This is most likely partly caused by deposition of GAM in deeper water (below the euphotic zone at a depth of several hundreds of meters) than ontogenetic calcite, where physical conditions, such as temperature and chemistry, are different to shallower waters (Erez, 2003; Bé, 1980). The thickness and the very presence is species dependent. For example, *Orbulina universa* have a large amount of GAM of up to 250% compared to its ontogenetic calcite, whereas *Globigerinoides ruber* does not have any GAM (Caron et al., 1990). The amount of GAM can also vary within one species (Bé, 1980; Caron et al., 1990). Schmidt et al. (2008) found that the proportion of gametogenic to ontogenetic calcite in *G.s truncatulinoides* does not vary with test size. However, this proportion does vary with the test weight per unit length, which means that smaller specimens will have a higher proportion of GAM than larger ones (Caron et al., 1990). Gametogenic calcite is found to have a higher concentration of trace elements than the ontogenetic calcite which creates an inhomogeneous trace element distribution in planktic foraminiferal tests.

Differences in element to calcium ratios have been recorded in foraminifera of different sizes from the same species (Schmidt et al., 2008). This suggests that specimens of a single species have undergone different growth rates during their life cycle and implies that foraminiferal growth rates can change the trace element uptake (Schmidt et al., 2008). However, it is unlikely that biologically induced changes in isotope and trace element ratios are caused by calcification rates, as foraminiferal calcification rates are significantly lower than inorganic precipitation rates (Schmidt et al., 2008). Against the expected trend, it was also shown that the distribution coefficient of Sr is inversely related to calcification rate which suggests foraminifera with higher growth rates behave more like open systems than foraminifera with lower growth rates (Erez, 2003). The environment has control over the optimal growth rate and thus the degree to which the system is open. In the optimal environment for a specific foraminiferal species, the growth rate will be higher resulting in larger (and more abundant) foraminifera of this species (Schmidt et al., 2008). It has been shown that perforate foraminifera have an internal calcium pool that provides for calcification solely (Erez, 2003). Foraminifera with large Ca pools have a low growth rate and are suspected to precipitate trace elements heterogeneously due to the restricted nature of the Ca pool. In contrast, foraminifera with a small Ca pools and high growth rates will use more seawater and their isotopic and chemical composition is expected to be closer to the inorganic values of the ambient environment (Erez, 2003). Ter Kuile et al. (1989) found the internal carbon pool to vary with both age and physiology and to be contaminated by metabolic carbon, which may affect the trace element content and isotopic composition in foraminiferal tests.

Another proposed mechanism through which foraminifera may precipitate their tests may be through solid-state transformation during dissolution and reprecipitation of metastable calcium carbonate phases such as ACC and vaterite to calcite (Jacob et al., 2017). This mechanism may also have a significant (although still unknown) impact on the trace element incorporation in foraminifera through introducing one or more extra fractionation steps during biomineralisation (Jacob et al., 2017).

1.5. Rationale and Dissertation Outline

A major effect of global warming is the decrease of oceanic dissolved oxygen levels, more commonly known as ocean deoxygenation. Over the last decades, a marked increase in the areal and bathymetric extent, as well as the number of areas affected by deoxygenation has risen rapidly (e.g. Stramma et al. 2008; Schmidtko et al. 2017). Oxygen is essential for the marine ecosystem and a decrease in oxygen will likely have a significant impact, especially when environmental pressure on organisms in amplified by thermal stress and ocean acidification (Doney et al., 2012). Suboxic waters are also a major source in the nitrogen cycle and an expansion of these waters will cause the release of the potent greenhouse

gas N_2O (Gruber, 2008). Therefore, it is important to understand what consequences deoxygenation has and what controls its extent and rate of spreading. This dissertation has as aim to disentangle the sequence of events and potential mechanisms leading to extreme deoxygenation in the past to provide a framework through which modern-day and future deoxygenation can be put into perspective. I use Cr isotopes as a proxy to infer past oceanic redox state variations and in this dissertation, I will assess the utility of Cr in biogenic carbonate as a palaeo-redox proxy. Following will be a short outline of each data chapter of this dissertation:

Chapter 2: Foraminifera as seawater chromium recorders

The conventional assumption has been that Cr isotopes in biogenic carbonates, which include foraminifera, record the seawater composition at the site of precipitation of the carbonate crystals. However, the uptake of Cr into foraminiferal tests and carbonates is still poorly understood. I assessed whether Cr associated with foraminiferal calcite is taken up during biomineralisation of the calcite crystal or is derived after sediment deposition. I used Laser Ablation-MC-ICP-MS and nanoSIMS imaging of individual tests to characterise the Cr distribution in both planktic and benthic foraminifera. Results imply that Cr is distributed throughout the foraminiferal test but that tests are enriched in Cr in prominent layers. Sedimentary foraminifera have up to two orders of magnitude more Cr than sediment trap, plankton net, and culture samples. In culture, Cr is incorporated in foraminiferal tests at low concentrations (0.04 – 0.13 ppm) with a distribution coefficient of ~250 ± 43 (2SE). Iron, Mn, and Cr cross-plots suggest part of the Cr signal in foraminifera is primary, but that this signal is overprinted by the exchange with Cr in bottom and pore waters. In sediment samples, there is no significant Cr isotopic offset between monospecific and bulk foraminiferal samples from the same size fraction. The >500 µm fraction is closer in isotopic composition to seawater than the smaller fraction 250 – 500 µm fraction with offsets of -0.3 to -0.5‰. This chapter concludes that Cr in foraminifera is mostly post-depositional and records bottom/pore water signals.

Chapter 3: Foraminiferal Cr isotopes and ocean deoxygenation during the PETM

The Palaeocene-Eocene Thermal Maximum (PETM) is a well-characterised time of geologically abrupt global warming approximately 56 million years ago. Changes in paleo-redox conditions caused by variations in dissolved oxygen availability have been assessed through the application of the palaeo-redox proxies of foraminiferal Cr isotopes ($\delta^{53}Cr$) and Ce anomalies (Ce/Ce*). Chromium isotopes and Cr concentrations show marked changes across the PETM in intermediate water to upper abyssal water depths, which is indicative of a widespread reduction in dissolved oxygen concentrations during the PETM. The strong correlation between the $\delta^{53}Cr$ and benthic $\delta^{18}O$ excursion sizes during the PETM points to temperature as one of the main controlling factors of open ocean deoxygenation. Atlantic Ocean samples suggest deoxygenation associated with warming and circulation changes and that less deoxygenation occurred in the Pacific Ocean. Geochemical data are supported by simulations from an

intermediate complexity climate model (cGENIE), which show that during the PETM anoxia was mostly restricted to the Tethys Sea, while hypoxia was more wide-spread in the Atlantic as a result of enhanced atmospheric CO_2 levels.

Chapter 4: An assessment of deoxygenation through deep time using Cr isotopes in carbonates

In this chapter, I used the past climate warming events of the Ocean Anoxic Event (OAE) 1a and OAE 2 in the Cretaceous, the Palaeocene-Eocene Thermal Maximum (PETM), the Eocene Thermal Maximum 2 (ETM-2) in the Palaeogene and Pleistocene glacial-interglacial cycles to quantify a potential link between warming and the spread of oxygen minimum zones throughout the geological past. Both $\delta^{53}Cr$ and chromium concentrations during the Eocene hyperthermals suggest a reduction in dissolved oxygen concentrations caused by warming and changes in ocean circulation. A significant correlation between the $\delta^{53}Cr$ and the benthic oxygen isotope excursion sizes during the Cenozoic imply temperature to be one of the key factors in past ocean deoxygenation. This correlation does not hold for the Mesozoic OAEs and may be due to a potential difference in the climate background state.

Chapter 5: Rare Earth Element – Yttrium composition of carbonates

All the carbonate samples used in this dissertation were also assessed for detrital contamination by monitoring Zr, Ti, and Th concentrations. None of the samples are likely to have been impacted by contamination and hence the REE-Y patterns and anomalies have been used to extract more palaeo-environmental information from the samples. This study finds that Er/Yb ratios in carbonates are not good depth range proxies but that Y/Ho in carbonates may have potential as a proxy for the distance of precipitation site to the coast (open sea versus coastal).

1.6. Analytical Methods

The following analytical methods are a detailed account of the preparation of foraminiferal and bulk carbonate samples and the analysis of these for trace element and Cr concentrations by a multi-collector inductively coupled plasma mass spectrometer (MC-ICP-MS) and inductively coupled mass spectrometer (ICP-MS). Details of the samples used in each chapter can be found in the relevant chapter. Methods specific to a chapter will also appear in the materials and methods section of the relevant chapter.

1.6.1. Sediment sample processing

Ocean sediment samples of 10-20 cm^3 were dried in glass conical flasks in an oven at 50 °C for at least 48 h but generally until no further mass loss from the evaporation of water in the sample (typically a week). The mass was checked twice daily. After the dry mass was recorded, 100 ml of de-ionised water

was added to the sediment and the flask was closed with parafilm. Instead of de-ionised water, Calgon was added to particularly lithified samples. Calgon was made by dissolving 4 g of sodium hexametaphosphate [$(NaPO_3)_6$] and 0.28 g of sodium carbonate ($NaCO_3$) in 1 L of de-ionised water. The resulting calgon should have a pH value between 7 and 8. Samples were then disaggregated on a shaking table for 24 h. After disaggregation, a further 100 ml de-ionised water was added. A clean 1-2 L glass beaker was lined with a plastic sample bag and a 63 µm sieve was placed on top. The disaggregated sediment suspension was gradually poured in while lightly spraying de-ionised water onto the sediment using a fill-spray-cylinder until the filtrate became clear. The coarse fraction (>63 µm) was then dried overnight in an oven at 50 °C and lastly its mass was recorded to determine what weight percentage of the sediment was the coarse fraction.

A mixture or single species of planktic foraminifera was picked from the coarse fraction in order to obtain about 0.11 g. Samples were then cleaned by following adapted methods by Barker et al. (2003). Firstly, the foraminiferal tests were gently cracked using two clean glass plates to open every test chamber. Foraminifera were placed onto the glass plate with some excess de-ionised water to prevent the loss of sample during crushing. The crushed test chambers were then positioned under a microscope to identify and remove any large silicate grains or other potential contamination. Samples were then moved into an acid-cleaned centrifuge tube. To remove small clay particles MilliQ was squirted onto the crushed foraminifera to create a clay suspension. After 30 s of letting the larger particles settle, the supernatant was removed using a pipette. A small volume of supernatant was left with the sample. The centrifuge tubes were then placed in an ultrasonic bath for approximately 1-2 min. Afterwards, MilliQ was squirted onto the sample and the larger carbonate particles were allowed to settle for a few seconds. The supernatant was subsequently removed leaving a small volume in the centrifuge tube. This series of steps was repeated until the supernatant was clear. The series of steps was then repeated one more time with Aristar methanol instead of adding MilliQ and a last time with MilliQ again to remove any remaining methanol. Organic matter was removed by adding alkali buffered 1% H_2O_2 to the sample. Alkali buffered 1% H_2O_2 was made by mixing 200 µl 30% Aristar grade H_2O_2 to 20 ml 0.1 M Aristar grade NaOH. The centrifuge tube containing the sample was then placed in boiling water for 10 min tapping the centrifuge every now and then to release gasses build up around the test fragments. The supernatant was then removed using a pipette and the series of steps to remove organic matter was then repeated. Remaining H_2O_2 was removed by filling the centrifuge tube with water and removing the supernatant. Baturin and Dubinchuk (2011) as well as laser ablation and sequential cleaning experiment data from this study (Chapter 2) suggest there is no significant contribution of Cr from ferromanganese coatings and therefore ferromanganese coatings were not removed to minimise sample loss.

The sample was then dissolved in 6 ml cold 0.5 M acetic acid. Acetic acid was added 1 ml at a time to minimise dissolution of any potential remaining non-carbonate phases in the sample. To speed up

dissolution samples were agitated in an ultrasonic bath. After the sample was completely dissolved, it was centrifuged at 4000 rpm for 5 min. The supernatant was then pipetted off into an acid-cleaned 15 ml Savillex Teflon beaker without disturbing the residue. Two millilitres of MilliQ were then added to the centrifuge tube and the sample was again centrifuged and the supernatant pipetted into the same Teflon beaker. This step was repeated twice.

1.6.2. Rock sample processing

Rock samples were split to access fresh surfaces with no signs of alteration by weathering processes. A fragment of fresh rock sample was then gently crushed into smaller pieces with a hammer. The sample was protected from metal contamination from the hammer by placing it in a sealed plastic bag wrapped in cloth. The small rock fragments were then powdered by hand in an agate mill. Approximately 0.11 g of sample was cleaned by adding alkali buffered 1% H_2O_2 into an acid-cleaned 15 ml Savillex Teflon beaker to oxidise any organic matter. The H_2O_2 was then removed by pipette. MilliQ water was added to the beaker and then removed by pipette to remove any remaining H_2O_2. The sample was subsequently dissolved following the dissolution procedures in section 1.6.1.

1.6.3. Trace element analysis

All vials and beakers used in trace element analysis (and Cr isotope analysis) were cleaned by rinsing three times with MilliQ water and boiling overnight at 110 °C in concentrated Analar HCl. Beakers were again rinsed three times with MilliQ water and boiled overnight at 110 °C in concentrated SpA HNO_3. Lastly, beakers were rinsed three times with MilliQ water and boiled overnight at 110 °C in MilliQ water.

Aliquots approximate to ~0.01g of dry mass were taken from the dissolution and was dried down to incipient dryness and re-dissolved in 2 ml of 2% HNO_3. This step was repeated twice. The solution was transferred to an acid-cleaned HDPE bottle and diluted by 4000 times with 2% HNO_3 to produce a 100 ppm Ca solution (~40 ml of solution). Synthetic standard solutions of 2 % HNO_3 with 100 ppm Ca and 0, 0.02, 0.05, 0.1, 0.2, 0.5, 1, 2, 4 ppb of 40 trace elements (including Cr and the REE-Y) were used as an external calibration. REE-Y and Cr concentrations were measured in He and O_2 mode respectively and in medium resolution on an Agilent 7500s ICP-QQQ-MS at the Open University. REEs in this study are normalised to PAAS concentrations (Taylor and McLennan, 1985).

1.6.4. Chromium isotope analysis

The rest of the sample (roughly equivalent to a dry mass of 0.1 g where available) was processed for Cr isotope analysis as described in Bonnand et al. (2011). The sample was dried down and an isotopically enriched ^{50}Cr-^{54}Cr double-spike was added (Bonnand et al., 2011). Adding the correct amount of spike

depends on the Cr concentration in the sample and therefore trace element analysis is mandatory prior to Cr isotope analysis (Figure 1.7). The target composition of the spike-sample mixture is $^{50}Cr/^{52}Cr$ = 0.40000574, $^{53}Cr/^{52}Cr$ = 0.11399965 and $^{54}Cr/^{52}Cr$ = 0.20242642. After isotope spiking the sample, 2 ml of 6 M HCl were added and the sample was subsequently dried down until completely dry. This step was repeated twice. Then 0.5 ml of 6 M HCl was added and the solution was boiled overnight at 110 °C to equilibrate the spike-sample mixture. Just prior to Cr extraction the sample was diluted with MilliQ water to a 0.5 M HCl solution.

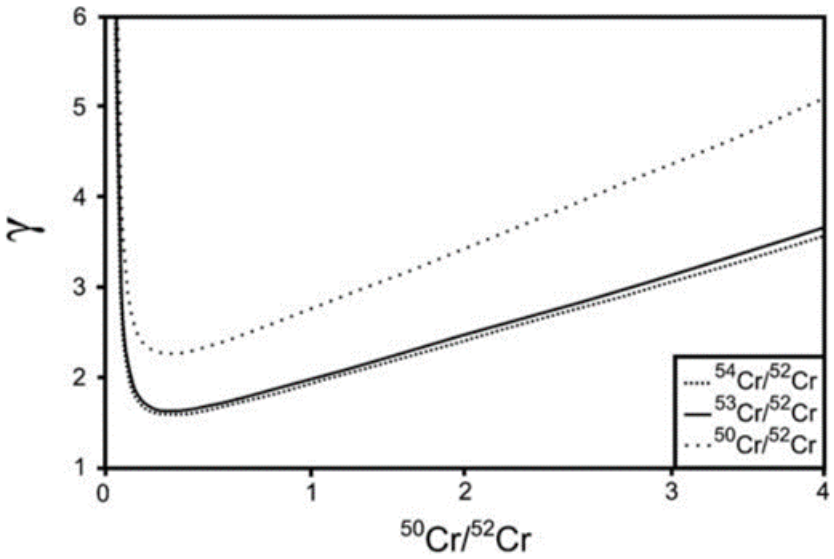

Figure 1.7: The error magnification term (γ) for the deconvolved $^{50}Cr/^{52}Cr$, $^{53}Cr/^{52}Cr$ and $^{54}Cr/^{52}Cr$ as a function of $^{50}Cr/^{52}Cr$ in the spike-sample mixture shows there is a spike-sample mixture where the error magnification is the lowest (Bonnand et al., 2011).

Chromium was separated from the matrix by a cation exchange resin. BioRad AG 50W-X8 (200-400 mesh) resin was placed in a 1 L acid-cleaned Savillex beaker and was cleaned with MilliQ water and 2% HNO_3 in alternate turns. The supernatant was removed after each clean. This was repeated until the supernatant was clear and no suspension was visible. A 30 ml Savillex column with an internal diameter of 6.4 mm was loaded with 2.9 ml of resin. Prior to Cr extraction, each column was cleaned with 40 ml of 6 M HCl and 40 ml of MilliQ water. The column was then pre-conditioned with 12 ml of 0.5 M HCl. The sample was loaded onto the column in a solution of 6 ml of 0.5 M HCl. Subsequently, another 1-3 ml of 0.5 M HCl was added to the column depending on the Fe concentration of the sample. Therefore, each cation exchange procedure produced 7-9 ml of Cr solution. The matrix cations remaining in the resin were then eluted with 10 ml of 6 M HCl. The resin was used for multiple Cr extractions. The Cr elution was evaporated to complete dryness and re-dissolved in 1 ml of 2% HNO_3 due to the low Cr concentration of the samples. There are two peaks of Cr in the Cr elution curve (Bonnand et al., 2011). The smaller second Cr peak at an elution of 20 ml elutes along with other elements. In this study, therefore, only Cr from the first elution peak was collected (Figure 1.8). The yield from the first elution

peak is approximately 70-80% and since a difference in the isotopic composition was reported (Trinquier et al., 2008), the Cr isotope analysis requires an isotope spike prior to the column chemistry. The total procedural blank using this cation exchange method is ~0.2 ng Cr which is negligible compared to the usual approximately 250 ng Cr in sample and standard solution loaded onto the resin.

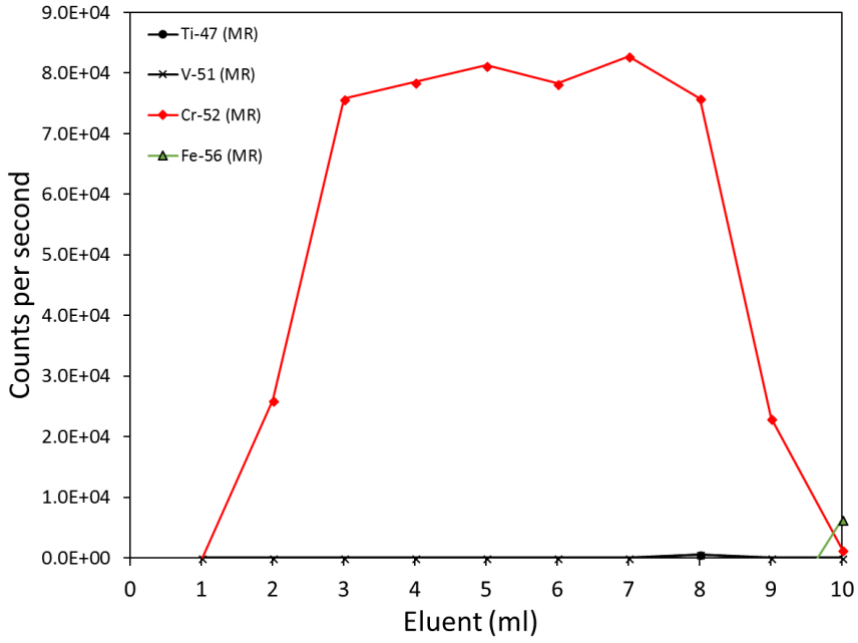

Figure 1.8: Elution curve for the separation of Cr from matrix and interfering elements showing the elution peak of Cr during the first 10 ml of elution (0.5 M HCl) coming through the resin following Bonnand et al. (2011).

The Cr isotopic composition of samples were measured by using a multi-collector inductively coupled plasma mass spectrometer (MC-ICP-MS; ThermoFisher Scientific Neptune) at the School of Earth Sciences, University of Bristol. The MC-ICP-MS was fitted with ThermoFisher X-cones. All four Cr isotopes and ^{56}Fe, ^{49}Ti and ^{51}V were measured on 7 faraday cups. Each faraday cup was connected to a 10^{11} Ω amplifier. Measuring ^{56}Fe, ^{49}Ti and ^{51}V was necessary for applying a correction for the isobaric interferences of ^{54}Fe on ^{54}Cr, as well as ^{50}V and ^{50}Ti on ^{50}Cr. The faraday cups used were L3 (^{49}Ti), L2 (^{50}Cr), L1 (^{51}V), C (^{52}Cr), H1 (^{53}Cr), H2 (^{54}Cr), and H3 (^{56}Fe). Polyatomic interferences on ^{53}Cr and ^{54}Cr are for example $^{40}Ar^{13}N$, $^{40}Ar^{14}N$, $^{40}Ar^{13}C$. All interferences were resolved by performing analyses in medium mass resolution in static mode ($5000<\Delta M/M<6500$; Figure 1.9). The sample was introduced into the MC-ICP-MS with an Aridus 2 desolvating sample introduction system. To produce a stable signal with a minimal interference from ArN, the Aridus was tuned with Ar and no N_2. The sensitivity of the MC-ICP-MS to ~50 ng ml^{-1} Cr using this set-up was ~4000 mA for ^{52}Cr (Figure 1.9).

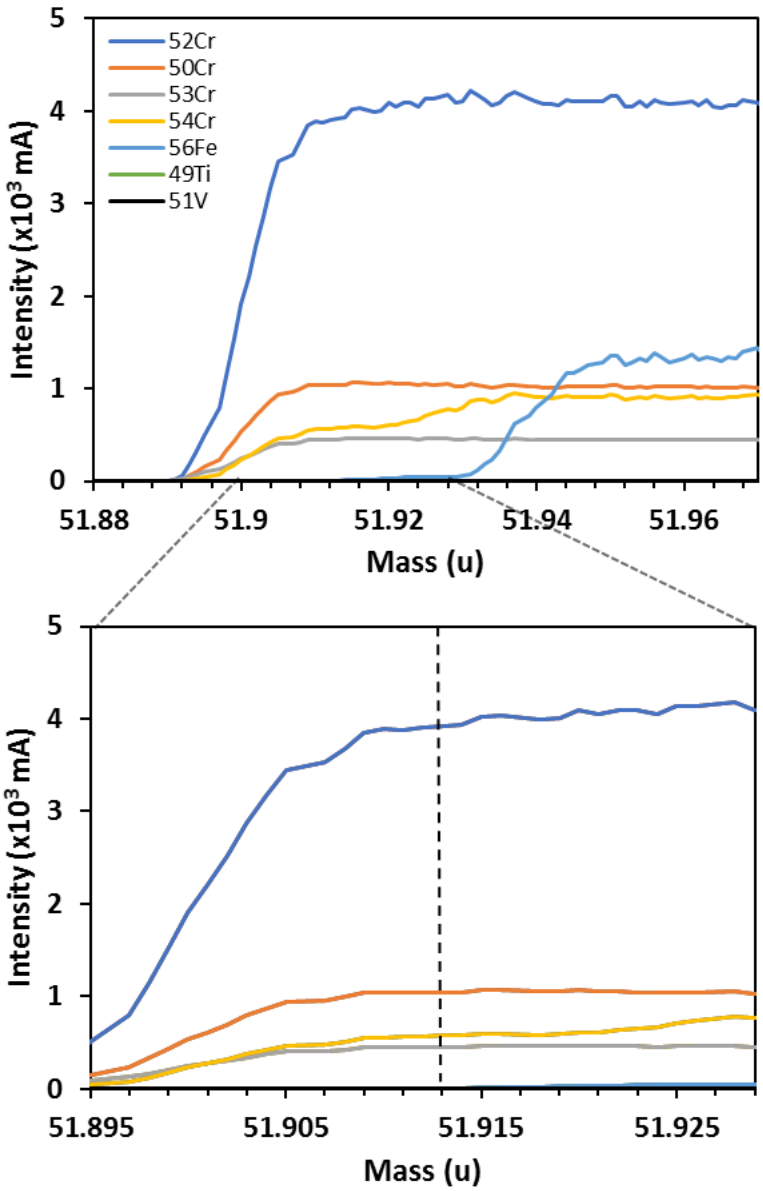

Figure 1.9: The peak shapes of NIST SRM979 spiked with a ^{50}Cr -^{54}Cr mixture in medium mass resolution on the Neptune MC-ICP-MS show the separation of ^{49}Ti, ^{50}Cr, ^{51}V, ^{52}Cr, ^{53}Cr, ^{54}Cr, ^{56}Fe. Measurements are made on the 'shoulder' of the peak at mass ~51.913 to avoid interference with Fe and Ar-oxides which is marked by the dashed line.

Prior to each analysis, the system is washed until the background ^{52}Cr signal drops to stable levels approximately 10 mV. Each Cr isotope analysis consisted of 100 measured ratios in 10 blocks of cycles of 10. Due to the very low Cr concentrations in some of the samples we increased the integration time of 8.4 s used by Bonnand et al. (2011) to 16 s. In combination with more concentrated samples, this significantly reduces the uncertainty on the measurement which is heavily dependent on the less abundant ^{53}Cr which is not enriched by a spike (Figure 1.10). An on-peak background was measured before and after each sample and standard analysis. Each analytical session started with the measurement of a Cr double-spiked NIST SRM 979 solution with Cr concentrations of 50 ng ml^{-1}. The

NIST SRM 979 solution was measured throughout the analytical session to monitor potential drift of the MC-ICP-MS.

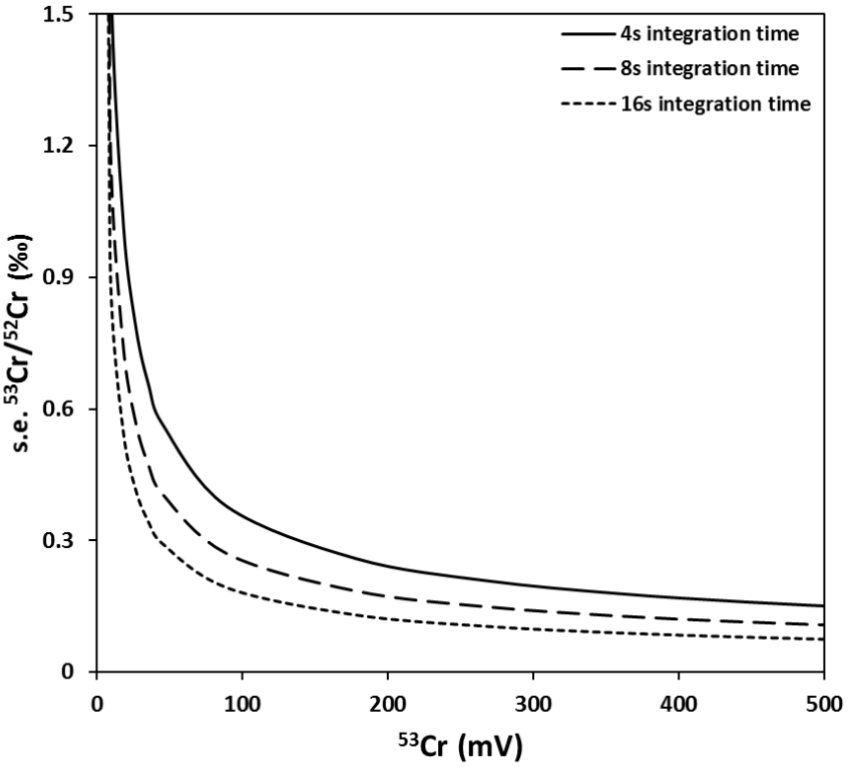

Figure 1.10: Uncertainty propagation calculations show that increasing the concentration of Cr in the sample solution in combination with a longer integration time of 16 s reduces the uncertainty on the measurement.

The external reproducibility of spiked NIST SRM 979 is $\delta^{53}Cr = +0.049 \pm 0.072‰$ (2σ, $n = 30$). The rock standard JDo-1 (Permian dolomite) was subjected to the same chemistry protocol as the samples. The value obtained for JDo-1 is $\delta^{53}Cr = +1.716 \pm 0.069‰$ (2σ, $n = 10$). These average $\delta^{53}Cr$ values were internally normalised to the daily average (Schoenberg et al., 2008; Bonnand et al., 2011). The values obtained in this study for NIST SRM 979 and JDo-1 are within error of that of published values for NIST SRM 979 ($\delta^{53}Cr = 0.000 \pm 0.031‰$) and JDo-1 ($\delta^{53}Cr = +1.719 \pm 0.057‰$) by e.g. Bonnand et al. (2011). The propagated measurement of accuracy in the Cr isotope measurements include added uncertainty due to the addition of a doubles-spike assuming natural samples were fractionated according to exponential mass bias (Bonnand et al., 2011).

Chromium isotopic compositions of samples and standards were baseline and gain corrected using ThermoFisher MC-ICP-MS software, whereas further data processing occurred offline following Albarede and Beard (2004) and Bonnand et al. (2011).

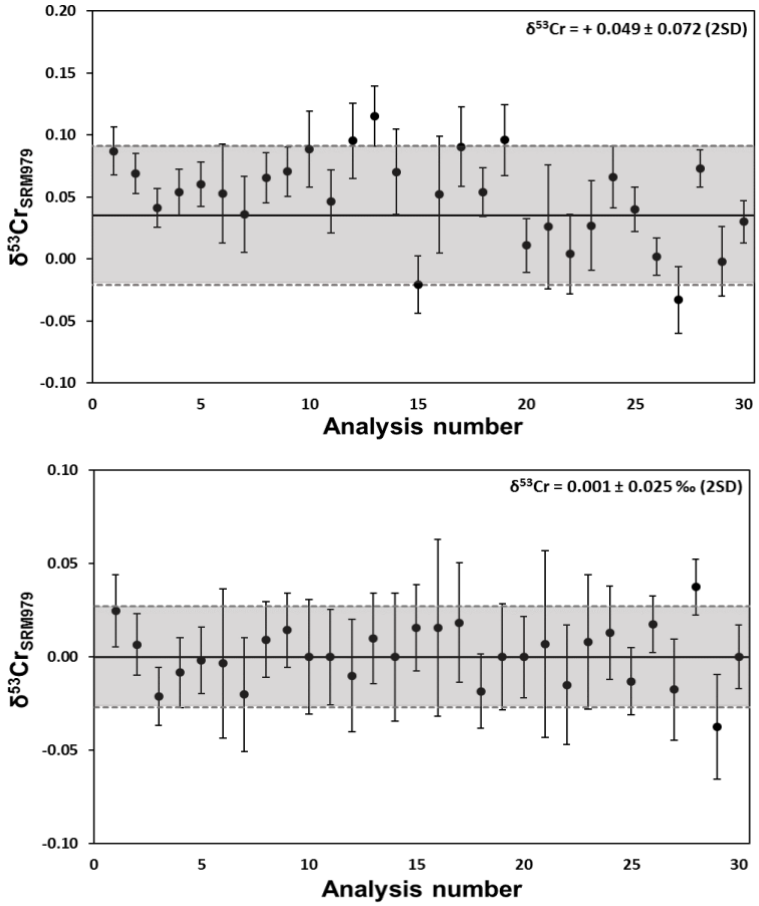

Figure 1.11: Standard reproducibility of NIST SRM979. The top panel shows uncorrected values for NIST SRM979, whereas the bottom panel is day-mean corrected.

1.6.5. Laser Ablation-MC-ICP-MS of foraminifera

Single species foraminiferal tests were picked from core-top, sediment trap, plankton net and cultured samples. The tests were cleaned by ultrasonication following Sadekov et al. (2008). The last three chambers of each test were removed using a surgical scalpel resulting in 8-21 test fragments per analysis. These chamber fragments were mounted concave-side (inner surface) up on black carbon tape. The cultured *Amphistegina* were mounted whole and were analysed 10-21 times per culture set. High-resolution LA-MC-ICP-MS analyses were performed at the Department of Earth Sciences at the University of Cambridge and the School of Earth Sciences at the University of Western Australia using a pulsed Analyte G2 Excimer Laser (Teledyne Photon Machines Inc.; λ = 193 nm) connected to a ThermoFisher Scientific Neptune Plus MC-ICP-MS following the methods of (Langer et al., 2016). Samples were ablated from the inner surface to the outer surface of the foraminiferal test along with the standards NIST SRM glasses 612 and 614, and a coral, JC7. The reproducibility of chromium concentrations for NIST SRM 612 was 36.45 ± 0.19 ppm (2SE), 0.91 ± 0.01 ppm (2SE) for NIST SRM 614, and 0.04 ± 0.004 ppm (2SE) for JC7. The species ^{48}Ca, ^{50}Cr, ^{51}V, ^{52}Cr, ^{53}Cr, ^{55}Mn and ^{56}Fe were measured in planktic foraminifera (core-top, sediment trap, plankton net, culture samples) as well as

cultured benthic foraminifera (Table 1). Data reduction of depth profiles removed the mean background intensity and standardised data to ^{48}Ca and NIST SRM 612 and 614 (Sadekov et al., 2008). Each depth profile took 10-24 s to measure depending on the thickness of the test and each single measurement within a depth profile was made over an average of 0.5 s. Laser spot sizes varied between 85 to 150 µm to best fit the test fragments (Table 1). Prior to analysis the test fragments were pre-ablated to remove the outer 1 µm of the surface for additional cleaning purposes (Sadekov et al., 2008).

1.6.6. NanoSIMS imaging of planktic foraminiferal test walls

Cleaned foraminifera tests were placed on parafilm, embedded in resin (Araldite 2020) discs of 1 cm diameter and 5 mm height, and cured at 20 ˚C for 48 hours. The discs were polished using silicon carbide wet grinding paper with decreasing coarseness (HERMES, WS Flex 18C, 230 mm, P 800 and ATM, SIC wet grinding paper, grain 4000) to expose cross sections perpendicular to the test walls of the embedded foraminifera. When the exposure was sufficient, as determined by light microscopy, final polishing was carried out using agglomerated alpha alumina powder (Struers AP-A powder, grain size 0.3 µm) and SiO2 powder (Logitech SF1 Polishing Suspension, grain size 0.035 µm). Polished samples were subsequently cleaned in ethanol in an ultrasonic bath for 5 seconds and coated with a 20 nm Au layer using a sputter coater (JEOL JFC-2300HR high resolution fine coater, JEOL FC-TM20 thickness controller). For orientation purposes the samples were imaged with a table-top SEM (JEOL JCM-6000PLUS NeoScope Benchtop SEM). Nanoscale secondary ion mass spectrometry was performed with a nanoSIMS 50L instrument (Cameca) operated at Utrecht University. Using an element standard (SPI Supplies, 02757-AB 59 Metals & Minerals Standard), magnetic field and exact positions of the electron multiplier detectors were adjusted to enable detection of secondary ions $^{24}Mg^+$, $^{44}Ca^+$, $^{52}Cr^+$, $^{55}Mn^+$ and $^{56}Fe^+$. The correct tuning for ^{52}Cr was verified by initially measuring also the isotope ^{50}Cr from both the SPI standard and the sample, which gave the correct $^{50}Cr/^{52}Cr$ ratio of 0.052. Before each measurement, the sample area of interest (rectangles of 40 × 70 µm in size) was presputtered with a primary O^- ion beam of 280 pA (using diaphragms D0-2 and D1-1) for 8-10 min until the secondary ion count rates stabilised. Subsequently, secondary ion images were acquired by rastering the primary O^- ion beam of about 50 pA over the sample surface (square of 30-45 µm in size) and detecting the ions with a dwelling time of 2-5 ms/pixel and with the diaphragm and slit settings of D0-2, D1-3, ES-3, AS-2 and EnS-1. For these settings, the nominal size of the primary O^- ion beam was 400-600 nm. Due to the very low count rates of the trace elements Cr, Mn and Fe, measurements took between 5-14 hr per sample area. Overall, five wall sections from a Holocene *T. sacculifer* from the Karibik core-top sample (Caromel et al., 2014; section 2.1.) were imaged. Processing and analysis of the nanoSIMS data was done using Look@nanoSIMS as previously described by Polerecky et al. (2012).

Chapter 2

Foraminifera as seawater chromium recorders

Parts of this chapter have been submitted to *Earth and Planetary Science Letters* for publication.

Author contributions and declaration: The study was designed, and data were interpreted by Serginio R.C. Remmelzwaal, Professor Daniela N. Schmidt, Dr Ian J. Parkinson and Dr Aleksey Yu. Sadekov. Laser ablation data were collected by Serginio R.C. Remmelzwaal and Dr Aleksey Yu. Sadekov. The culture studies were carried out by Serginio R.C. Remmelzwaal and Danna Titelboim. NanoSIMS analysis was carried out by Serginio R.C. Remmelzwaal, Anne Roepert, Dr Lubos Polerecky, and Michiel Kienhuis. Plankton net, North Atlantic core-top and planktic foraminiferal culture samples were provided by Dr Katsunori Kimoto, Dr Gerald Ganssen, Dr Barbara Donner, Dr Katherine Holland, and Dr Katherine A. Allen. Seawater Cr isotope measurements were made by Serginio R.C. Remmelzwaal with the assistance of Dr Heather Goring-Harford. ICP-MS data were acquired with the assistance of Dr S. Hammond (School of Environment, Earth & Ecosystems, The Open University) at the Open University and were processed and interpreted by Serginio R.C. Remmelzwaal.

Abstract

Present-day ocean deoxygenation has major implications for marine ecosystems and the biogeochemical cycling in the oceans. Chromium isotopes are used as a proxy to infer changes in past oceanic redox state. So far, it has been assumed that Cr isotopes in carbonates, including the prime proxy carrier foraminifera, record the seawater composition at the site of crystallisation. However, the uptake of Cr into foraminiferal tests and carbonates is still poorly understood. I assess whether Cr in foraminiferal calcite is taken up during biomineralisation or has a post-depositional origin. Laser Ablation-MC-ICP-MS and NanoSIMS imaging of individual tests were used to characterise the distribution of Cr in both planktic and benthic foraminifera. Results suggest that Cr is distributed throughout the foraminiferal test ranging from a homogeneous distribution to enrichment in Cr at the rims of the test. NanoSIMS measurements show prominent layers enriched in Cr which may also explain some of the variability seen by LA-MC-ICP-MS. Foraminifera in sediment core-top samples

have up to two orders of magnitude more Cr than sediment trap, plankton net, and culture samples. In culture, Cr is incorporated in foraminiferal tests at low concentrations (0.04 – 0.13 ppm) with a distribution coefficient of ~250 ± 43 (2SE). While Fe and Cr cross-plots suggest at least part of the Cr signal in foraminifera is primary, this signal is overprinted by the uptake of Cr in bottom and pore waters. In sediment samples, there is no significant offset between individual species and bulk foraminiferal calcite from the same size fraction. The >500 µm fraction is closer in isotopic composition to seawater than the smaller fraction 250 – 500 µm fraction with an offset of -0.3 to -0.5‰. I propose that Cr in foraminifera is mostly post-depositional and records bottom/pore water signals. This is contrary to current interpretations of the foraminiferal Cr isotope proxy as a surface seawater redox proxy.

2.1. Introduction

Anthropogenic global warming has caused dissolved oxygen levels in the oceans to drop globally by 2% over the past decades (Schmidtko et al., 2017). This loss of oxygen is projected to continue by up to -0.64 µM per year (Stramma et al., 2012). As ocean deoxygenation threatens marine ecosystems and fisheries (Keeling et al., 2010), a more robust understanding of the effects of deoxygenation on biogeochemical cycling, the carbon pump and marine life is important. One way of untangling the effects of deoxygenation is by looking at its response during past climate perturbations.

Chromium occurs in two valence states, Cr(III) and Cr(VI), in the marine environment and is therefore sensitive to redox changes (e.g. Elderfield, 1970; Cranston and Murray, 1978; Bonnand et al., 2013; Reinhard et al., 2014; Wang et al., 2016). In modern well-oxygenated seawater chromium is predominantly present as Cr(VI)-oxyanions, whereas Cr(III) is insoluble and will adhere to particles thus forming a sink to the seafloor and depleting low oxygen seawater in chromium (Cranston and Murray, 1978). Chromium speciation is redox coupled to Mn and Fe (e.g. Schroeder and Lee, 1975; Cranston and Murray, 1978) and is therefore thought to track hypoxia dynamics in the present and past.

Additional to the Cr concentrations, Cr isotopes have been suggested as a way to reconstruct past oxygenation. There are four stable Cr isotopes of which ^{52}Cr and ^{53}Cr are the most abundant, and so stable Cr isotope variations are assessed using the $^{53}Cr/^{52}Cr$ ratio expressed as $\delta^{53}Cr = [(^{53}Cr/^{52}Cr_{sample}) / (^{53}Cr/^{52}Cr_{NBS\ 979}) - 1] \times 1000$ (e.g. Bonnand et al., 2011). A partial reduction of Cr(VI) to Cr(III) is paired with a fractionation of up to 7‰ enriching the remaining Cr(VI) pool in ^{53}Cr (Ellis et al., 2002). The sensitivity of $\delta^{53}Cr$ to changes in dissolved O_2 content has not yet been directly assessed. Carbonate chromium isotope ratios are thought to reflect seawater values (Tang et al., 2007; Frei et al., 2011; Bonnand et al., 2013) through the substitution of the carbonate ion by CrO_4^{2-}. Fossilised remains of

marine calcifiers such as foraminifera are archives of past climate proxies. To use the foraminiferal chromium records in the past, it is imperative to piece together where chromium in the test originates from and what controls its uptake.

Previous studies into the fractionation of Cr isotopes in carbonates have yielded widely variable results. Scleractinian corals show a large disequilibrium with seawater resulting in a fractionation from -0.5 to +0.33‰ (Pereira et al., 2016). Bulk carbonate samples of mainly macroalgal origin from the Caribbean have Cr isotope values offset from seawater by -0.46‰ (Holmden et al., 2016). A recent study assessing the fractionation associated with Cr uptake by foraminifera (Wang et al., 2017) concluded that it is unclear whether the chromium isotopic composition of foraminifera reflects surface seawater $\delta^{53}Cr$ values, as different species from the same sample site and same depth habitats show significant variations in $\delta^{53}Cr$. As the study presented by Wang et al. (2017) analysed multiple species of foraminifera larger than 125 µm, mixing a wide range of sizes, it does not consider any potential effects growth rates or differences in ontogeny may have on $\delta^{53}Cr$ which could partially explain the variability they found in foraminiferal $\delta^{53}Cr$. Changes in surface area to volume ratios (A/V) due to size variations would facilitate different rates of post-depositional exchange with bottom and pore waters with smaller specimens more prone to this effect.

To fully assess the potential of Cr isotopes in foraminifera as a palaeoproxy, Cr uptake by foraminifera from their ambient environment needs to be determined. Previous estimates of distribution coefficients of Cr ($D_{Cr} = [Cr]_{foraminifer} / [Cr]_{seawater}$) in foraminiferal calcite range from 303 to 4,000 and are based on core-top planktic foraminifera and seawater Cr concentrations averaged over the Pacific and Atlantic Ocean basins (Wang et al., 2017). Distribution coefficients in other biogenic carbonates range from 7143 – 65,643 in macroalgal carbonates to 107 – 329 in scleractinian corals (Holmden et al., 2016; Pereira et al., 2016) and are higher than inorganic precipitation experiments (Tang et al., 2007; Rodler et al., 2015) in which $D_{Cr(VI)}$ values range from approximately 0.1 to 3.4. Cultures of foraminifera under controlled conditions allow for a more accurate determination of the distribution coefficient in foraminifera whilst ruling out any post-depositional enrichment in Cr and any effects caused by the high heterogeneity of Cr in seawater (Bonnand et al., 2013; Scheiderich et al., 2015; Paulukat et al., 2015; Economou-Eliopoulos et al., 2016; Paulukat et al., 2016; Pereira et al., 2016; Holmden et al., 2016).

Another critical factor in applying the Cr proxy to the fossil record is the lack of understanding of where in a foraminiferal test the Cr resides. Wang et al. (2017) concluded that <14% of Cr is adsorbed to clay particles and that the remaining Cr is foraminiferal in sedimentary foraminifera. That study, like Holmden et al. (2016), does not take into account any potential post-depositional effects, though

Holmden et al. (2016) do raise the issue that it is unclear whether uptake of Cr into carbonates takes place during precipitation or after deposition in the sediment.

In this study, I aimed to test how representative foraminiferal chromium is of seawater chromium. Using laser ablation multi-collector ICP-MS (LA-MC-ICP-MS) and nanoscale SIMS (NanoSIMS) I analysed Cr concentrations in planktic (core-top, plankton net, sediment trap, cultured samples) as well as benthic (cultured samples) foraminifera. First, I assess the distribution of Cr across foraminiferal test walls at high spatial resolution. Then I compared Cr concentrations between core-top, sediment trap, plankton net, and cultured samples. I present a benthic foraminiferal Cr culture data to better constrain the distribution coefficient for Cr into foraminiferal calcite. Finally, I assessed potential growth rate or surface area to volume ratio effects on the Cr isotopic composition in different size fractions of core-top foraminifera.

2.2. Material and Analytical Methods

2.2.1. Material

Foraminiferal specimens from four different sample types were used for this study: core-tops, plankton nets, sediment traps, and growth cultures (Table 1). The planktic foraminifera *Trilobatus sacculifer* and *Orbulina universa* were picked from core-tops SO456 and SO488 from the NW Australian margin. *T. sacculifer* and *Globigerinoides ruber* were picked from core-top GeoB3915 located off the North-Brazilian coast. The planktic foraminifera *O. universa*, *G. menardii*, *G. ruber*, *G. truncatulinoides* were picked from core-top samples from the Caribbean (Karibik; Caromel et al., 2014) and North Atlantic (T86-15S; Troelstra et al., 1987).

Sediment trap samples from off the coast of Cape Blanc in Mauretania (CB14) were picked for specimens of the planktic *G. truncatulinoides* and *T. sacculifer*. Specimens of *T. sacculifer* and *G. bulloides* were obtained from plankton net samples from the East China Sea (KT02-15B).

Cultures were performed on the benthic foraminifer *Amphistegina sp.* from Israel, and the planktic *O. universa* and *G. ruber* from the Caribbean (Allen et al., 2016; Holland et al., 2017). *Amphistegina lobifera* specimens were collected from several sites along the Mediterranean coast of Israel (Nahsholim and Tel Shikhmona) and *Amphistegina sp.* were collected from the Red Sea coast of Israel (Eilat). Seawater for the culture medium of these benthic foraminifera was collected in cubitainers from Tel Shikhmona.

Sample	Type	Species	Laser Spot Size	Location
SO456 0-1 cm	Core-top	*T. sacculifer*	150 x 150	NW Australian margin
		O. universa		
SO488 0-1 cm	Core-top	*T. sacculifer*	150 x 150	NW Australian margin
GeoB3915	Core-top	*T. sacculifer*	150 x 150	Off Northern Brazil
		G. ruber	85 x 85	
CB14	Sediment trap	*G. truncatulinoides*	85 x 85	Cape Blanc, Mauritania
		T. sacculifer		
KT02-15 B-2 10 m	Plankton net	*T. sacculifer*	130 x 130	East China Sea
KT02-15 B-2 50 m	Plankton net	*T. sacculifer*	130 x 130	
KT02-15 B-2 75 m	Plankton net	*T. sacculifer*	130 x 130	
KT02-15 B-2 100 m	Plankton net	*T. sacculifer*	130 x 130	
KT02-15 B-5	Plankton net	*G. bulloides*	130 x 130	
Amphistegina sp.	Culture	*Amphistegina.*	85 x 85	Israel
O. universa	Culture	*O. universa*	130 x 130	Puerto Rico
G. ruber	Culture	*G. ruber*	130 x 130	Puerto Rico

Table 2.1: Foraminiferal samples used for measuring Cr by LA-MC-ICP-MS. These include core-top samples, sediment trap samples, plankton net samples as well as cultured benthic foraminifera (this study) and planktic foraminifera (*O. universa* and *G. ruber*; Allen et al., 2016; Holland et al., 2017).

2.2.2. Culturing *Amphistegina sp.* in chromium-doped seawater

To create the culture medium, LiCl was added to 10 L of seawater to create a 500 µM Li solution. Li is used to distinguish newly formed foraminiferal chambers from chambers that formed prior to culturing following Titelboim et al. (2017). The Li-doped seawater was then divided into acid-cleaned 2 L HDPE bottles. Three 2 L aliquots were doped with 280 nmol, 560 nmol, and 840 nmol chromium from a chromate standard, respectively. Two litres of undoped seawater served as a control on the experiment. Live specimens of *Amphistegina sp.* from Israel were picked, cleaned with a brush, and checked for activity. Twenty specimens were transferred to a sealable glass beaker containing the culturing medium with appropriate Cr concentration. All culture incubations were replicated. The foraminifera from the Mediterranean and Red Sea were kept separated. The seawater was refreshed once every week, and all experiments were performed at a temperature of 26 ˚C. Oxygen levels were monitored by Winkler titrations and with a PreSens Pst3 Oxygen Dipping Probe throughout the one month of culturing. The oxygen concentrations in the 1x [Cr] seawater for Mediterranean foraminifera were 171.3 and 172 µM at the beginning of the experiment measured by Winkler titration and dipping probe, respectively. The initial oxygen concentration in the 1x [Cr] seawater for Red Sea foraminifera measured by dipping

probe was 155 µM. After the experiment, the specimens were cleaned and mounted whole onto carbon tape for LA-MC-ICP-MS analyses at the University of Cambridge, as described below (section 2.3.).

One litre of the Li-doped seawater and 100 mL aliquots of the Li and Cr-doped seawater were immediately acidified, and an additional 1 L of Li-doped seawater and 100 mL aliquots of Li and Cr-doped seawater were not acidified until the end of the experiment to track any changes in Cr content in the culture medium. The undoped seawater was analysed by ThermoFisher Scientific Neptune MC-ICP-MS at the National Oceanography Centre in Southampton following Scheiderich et al. (2015). Doped seawater was analysed by ThermoFinnigan Element ICP-MS at the University of Bristol due to its limited volume. Doped seawater was diluted in 2% HNO_3 by 4000 times. Synthetic standards containing Cr and other trace elements at a range of concentrations were used as calibration.

2.2.3. Laser Ablation-MC-ICP-MS of foraminifera

Single species foraminiferal tests were picked from core-top, sediment trap, plankton net and cultured samples. The tests were cleaned by ultrasonication following Sadekov et al. (2008). The last three chambers of each test were removed using a surgical scalpel resulting in 8-21 test fragments per analysis. These chamber fragments were mounted concave-side (inner surface) up on black carbon tape. The cultured *Amphistegina* were mounted whole and were analysed 10-21 times per culture set. High-resolution LA-MC-ICP-MS analyses were performed at the Department of Earth Sciences at the University of Cambridge and the School of Earth Sciences at the University of Western Australia using a pulsed Analyte G2 Excimer Laser (Teledyne Photon Machines Inc.; λ = 193 nm) connected to a ThermoFisher Scientific Neptune Plus MC-ICP-MS following the methods of (Langer et al., 2016). Samples were ablated from the inner surface to the outer surface of the foraminiferal test along with the standards NIST SRM glasses 612 and 614, and a coral, JC7. The reproducibility of chromium concentrations for NIST SRM 612 was 36.45 ± 0.19 ppm (2SE), 0.91 ± 0.01 ppm (2SE) for NIST SRM 614, and 0.04 ± 0.004 ppm (2SE) for JC7. The species ^{48}Ca, ^{50}Cr, ^{51}V, ^{52}Cr, ^{53}Cr, ^{55}Mn and ^{56}Fe were measured in planktic foraminifera (core-top, sediment trap, plankton net, culture samples) as well as cultured benthic foraminifera (Table 1). Data reduction of depth profiles removed the mean background intensity and standardised data to ^{48}Ca and NIST SRM 612 and 614 (Sadekov et al., 2008). Each depth profile took 10-24 s to measure depending on the thickness of the test and each single measurement within a depth profile was made over an average of 0.5 s. Laser spot sizes varied between 85 to 150 µm to best fit the test fragments (Table 1). Prior to analysis the test fragments were pre-ablated to remove the outer 1 µm of the surface for additional cleaning purposes (Sadekov et al., 2008).

2.2.4. NanoSIMS imaging of planktic foraminiferal test walls

Cleaned foraminifera tests were placed on parafilm, embedded in resin (Araldite 2020) discs of 1 cm diameter and 5 mm height, and cured at 20 ˚C for 48 hours. The discs were polished using silicon carbide wet grinding paper with decreasing coarseness (HERMES, WS Flex 18C, 230 mm, P 800 and ATM, SIC wet grinding paper, grain 4000) to expose cross sections perpendicular to the test walls of the embedded foraminifera. When the exposure was sufficient, as determined by light microscopy, final polishing was carried out using agglomerated alpha alumina powder (Struers AP-A powder, grain size 0.3 µm) and SiO2 powder (Logitech SF1 Polishing Suspension, grain size 0.035 µm). Polished samples were subsequently cleaned in ethanol in an ultrasonic bath for 5 seconds and coated with a 20 nm Au layer using a sputter coater (JEOL JFC-2300HR high resolution fine coater, JEOL FC-TM20 thickness controller). For orientation purposes the samples were imaged with a table-top SEM (JEOL JCM-6000PLUS NeoScope Benchtop SEM).

Nanoscale secondary ion mass spectrometry was performed with a nanoSIMS 50L instrument (Cameca) operated at Utrecht University. Using an element standard (SPI Supplies, 02757-AB 59 Metals & Minerals Standard), magnetic field and exact positions of the electron multiplier detectors were adjusted to enable detection of secondary ions $^{24}Mg^+$, $^{44}Ca^+$, $^{52}Cr^+$, $^{55}Mn^+$ and $^{56}Fe^+$. The correct tuning for ^{52}Cr was verified by initially measuring also the isotope ^{50}Cr from both the SPI standard and the sample, which gave the correct $^{50}Cr/^{52}Cr$ ratio of 0.052. Before each measurement, the sample area of interest (rectangles of 40 × 70 µm in size) was presputtered with a primary O^- ion beam of 280 pA (using diaphragms D0-2 and D1-1) for 8-10 min until the secondary ion count rates stabilised. Subsequently, secondary ion images were acquired by rastering the primary O^- ion beam of about 50 pA over the sample surface (square of 30-45 µm in size) and detecting the ions with a dwelling time of 2-5 ms/pixel and with the diaphragm and slit settings of D0-2, D1-3, ES-3, AS-2 and EnS-1. For these settings, the nominal size of the primary O^- ion beam was 400-600 nm. Due to the very low count rates of the trace elements Cr, Mn and Fe, measurements took between 5-14 hr per sample area. Overall, five wall sections from a Holocene *T. sacculifer* from the Karibik core-top sample (Caromel et al., 2014; section 2.1.) were imaged. Processing and analysis of the nanoSIMS data was done using Look@nanoSIMS as previously described by Polerecky et al. (2012).

2.2.5. Chromium analysis of planktic foraminifera by (MC-)ICP-MS

Approximately 0.1 g of multiple planktic foraminiferal species (*O. universa, G. menardii, G. ruber, G. truncatulinoides*) were picked from core-top samples from the Caribbean (Karibik; Caromel et al., 2014) and North Atlantic (T86-15S; Troelstra et al., 1987) in different size fractions (>500 µm and 250

- 500 µm). Samples were cleaned by gently cracking open the foraminiferal tests followed by rinsing with MilliQ water to remove clay particles and with alkali buffered H_2O_2 to remove organic matter (Barker et al., 2003). Baturin and Dubinchuk (2011) reported no significant contribution of authigenic Cr in ferromanganese coatings on the outside of the foraminiferal shell to the overall Cr content and therefore I decided not to remove these to preserve as much of the sample as possible for analysis. The samples were then dissolved in cold 0.5M acetic acid. An aliquot of 0.01 g of sample was dried down to incipient dryness and re-dissolved and diluted in 2% HNO_3 to produce a 100 ppm Ca solution. Matrix-matched synthetic standards doped with 100 ppm Ca and containing trace elements at a range of concentrations were used as calibration. Chromium was measured in O_2 collision mode on an Agilent 7500s ICP-QQQ-MS at the School of Environment, Earth and Ecosystem Sciences at the Open University. Chromium concentrations were reproducible within ~2%. Chromium isotopes were measured on a ThermoFisher Scientific Neptune MC-ICP-MS at the School of Earth Sciences at the University of Bristol by using a ^{50}Cr-^{54}Cr double-spike technique following Bonnand et al. (2011). The contribution of the blank is negligible with a total procedural blank for Cr of ~0.2 ng. The standard JDo-1 was subjected to the same cation exchange chromatography protocol as the samples and the average value of JDo-1 was $\delta^{53}Cr = 1.716 \pm 0.069‰$ (2σ, n = 10). The external reproducibility of 50 ng of NBS 979 was $\delta^{53}Cr = 0.049 \pm 0.072‰$ (2σ, n = 30). Our values for JDo-1 and NBS979 are within uncertainty of previously published values (Bonnand et al., 2011).

2.3. Results

2.3.1. Chromium uptake by benthic foraminifera

Amphistegina sp. and *A. lobifera* Cr concentrations increase with rising concentrations in the culture medium (Figure 2.1). While there are some outliers in the dataset, the data are clustered in bands preserving the overall trends. Chromium concentrations of bulk single foraminifera were obtained by averaging LA-ICP-MS profiles. Average Cr concentrations in *Amphistegina* strongly correlate with total Cr concentrations in the culture medium ($R^2 = 0.78$; $p = 0.002$; Figure 2.2), showing that availability of Cr exerts a direct control on uptake by foraminifera. The distribution coefficient was 250 ± 43, as determined from the slope of a linear regression between the Cr concentrations in the test walls and in the culture medium.

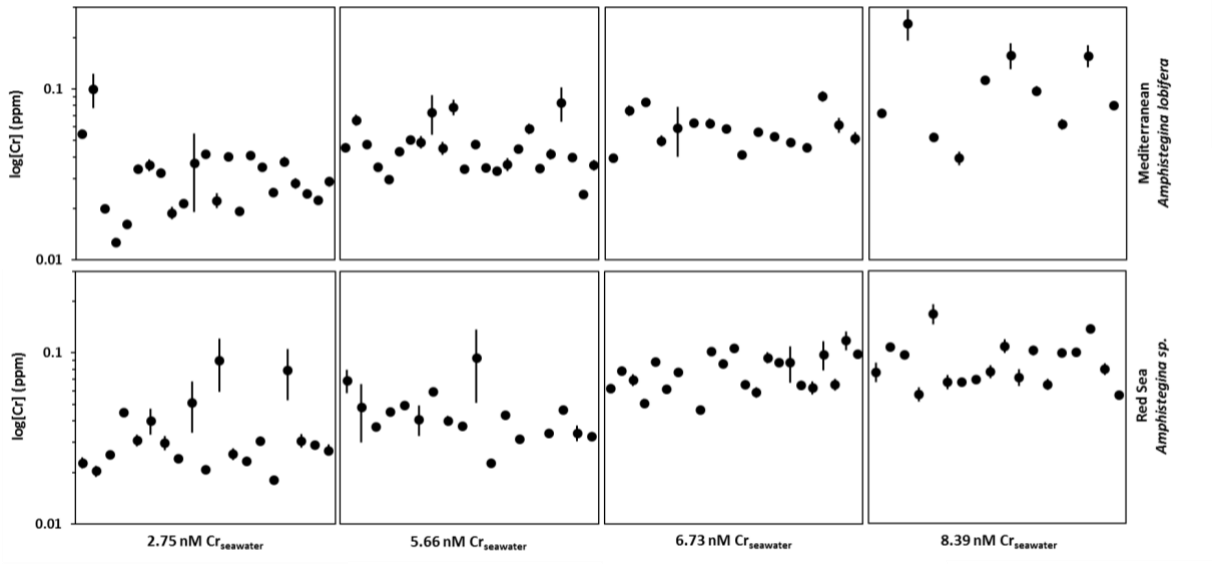

Figure 2.1: The Cr concentrations of single foraminifera in cultures of the larger benthic foraminifer *Amphistegina sp.* measured by LA-MC-ICP-MS. Culturing conditions were under natural seawater (2.75 nM Cr), and seawater spiked with Cr to reach final concentrations of 5.66 nM, 6.73 nM, and 8.39 nM. Chromium concentrations in the foraminifers increase with increasing dissolved Cr concentrations in the water. Where error bars are not visible, the analytical errors are smaller than the size of the data point.

With final Cr concentrations in the culture medium between 2.75 and 8.39 nM (Figure 2.2), our incubations fall within the range of natural seawater with concentrations of ~ 1.2 - 9.5 nM (e.g. Scheiderich et al., 2015; Paulukat et al., 2016). This is less than expected from the amount of chromate solution that was added to the seawater and implies that I was not able to create the stable Eh-pH levels required to prevent precipitation of Cr (Bonnand et al., 2013).

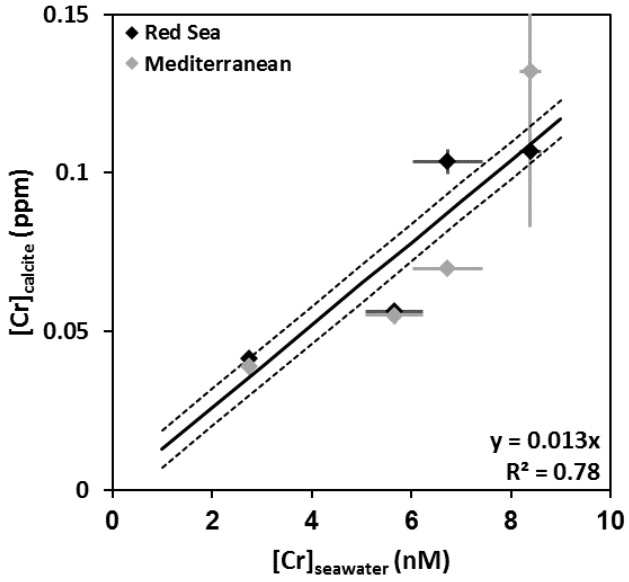

Figure 2.2: The specimens of *Amphistegina sp.* from the Red Sea and *A. lobiferai* from the Mediterranean were cultured in natural and chromate-spiked Mediterranean seawater with concentrations between 2.75 – 8.39 nM Cr. Black diamonds represent average Cr concentrations in the *Amphistegina sp.* cultures from the Red Sea, whereas grey diamonds are average Cr concentrations in the *A. lobifera* cultures from the Mediterranean. The solid black line is the linear regression of the data and has a slope of 0.013 ± 0.006 (2SE) with $p = 0.0015$ and $R^2 = 0.78$. The dashed lines outline the 2SE of the slope. The correlation between the average total Cr concentration in seawater and in the foraminiferal test results in a distribution coefficient of $D_{Cr} = 250 \pm 43$ (2SE). Where error bars are not visible, the analytical errors are smaller than the data point.

2.3.2. Spatial distribution and concentrations of chromium in planktic foraminifera

The distribution of Cr in core-top foraminifera determined by LA-MC-ICP-MS ranges from homogeneous to strong enrichments in Cr towards the rim of the test in core-top foraminifera (Figure 2.3; Supplementary Material). Average chromium concentrations in foraminifera reveal differences of up to two orders of magnitude. Core-top foraminifera have elevated Cr levels (~0.82 ppm) compared to ~0.09 ppm in foraminifera that come from sediment traps, plankton nets, and cultures (Figure 2.4).

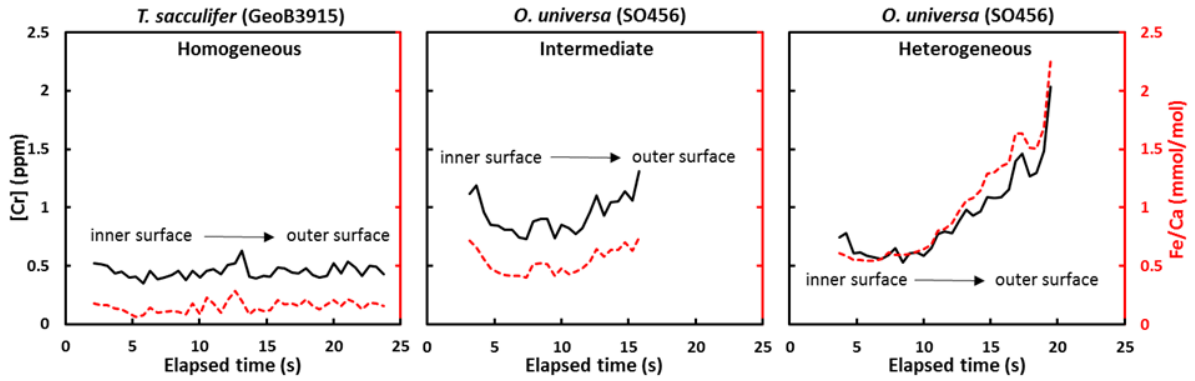

Figure 2.3: Three laser ablation (LA-MC-ICP-MS) profiles of Cr concentrations, and Fe/Ca through planktic foraminiferal calcite (*T. sacculifer* and *O. universa*) in two core-top samples (GeoB3915 and SO456). These are representative of the Cr profiles in foraminifera which display a distribution ranging from homogeneity throughout the test to strong enrichment at the rim of the test. An overview of all planktic foraminiferal Cr concentration profiles obtained through LA-MC-ICP-MS can be found in the Supplementary Material.

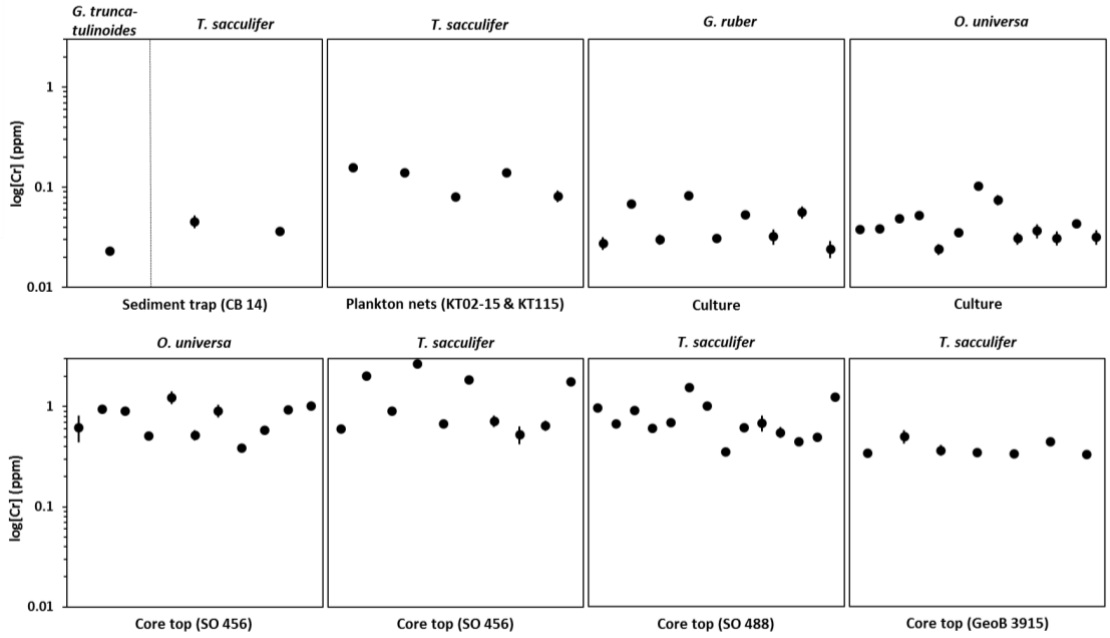

Figure 2.4: Chromium concentrations of individual planktic foraminifera measured by LA-MC-ICP-MS in core-top, sediment trap, plankton net, and culture samples. Chromium concentrations are higher in core-top samples than in non-sedimentary (sediment trap, plankton net, cultured) foraminifera. Where error bars are not visible, the analytical errors are smaller than the size of the data point.

NanoSIMS analysis of a Caribbean core-top *T. sacculifer* confirm the relatively homogeneous distribution of Cr through the test shown by laser ablation data. However, elevated Cr concentrations were observed in prominent Mg-rich bands that align with the primary organic sheet (POS), as identified by grooves in the calcite (Figure 2.5). While the Cr-rich bands were always co-localised with elevated Mg, Mn and Fe concentrations, only some of the Mg and Mn bands had elevated Cr concentrations (Figure 2.5).

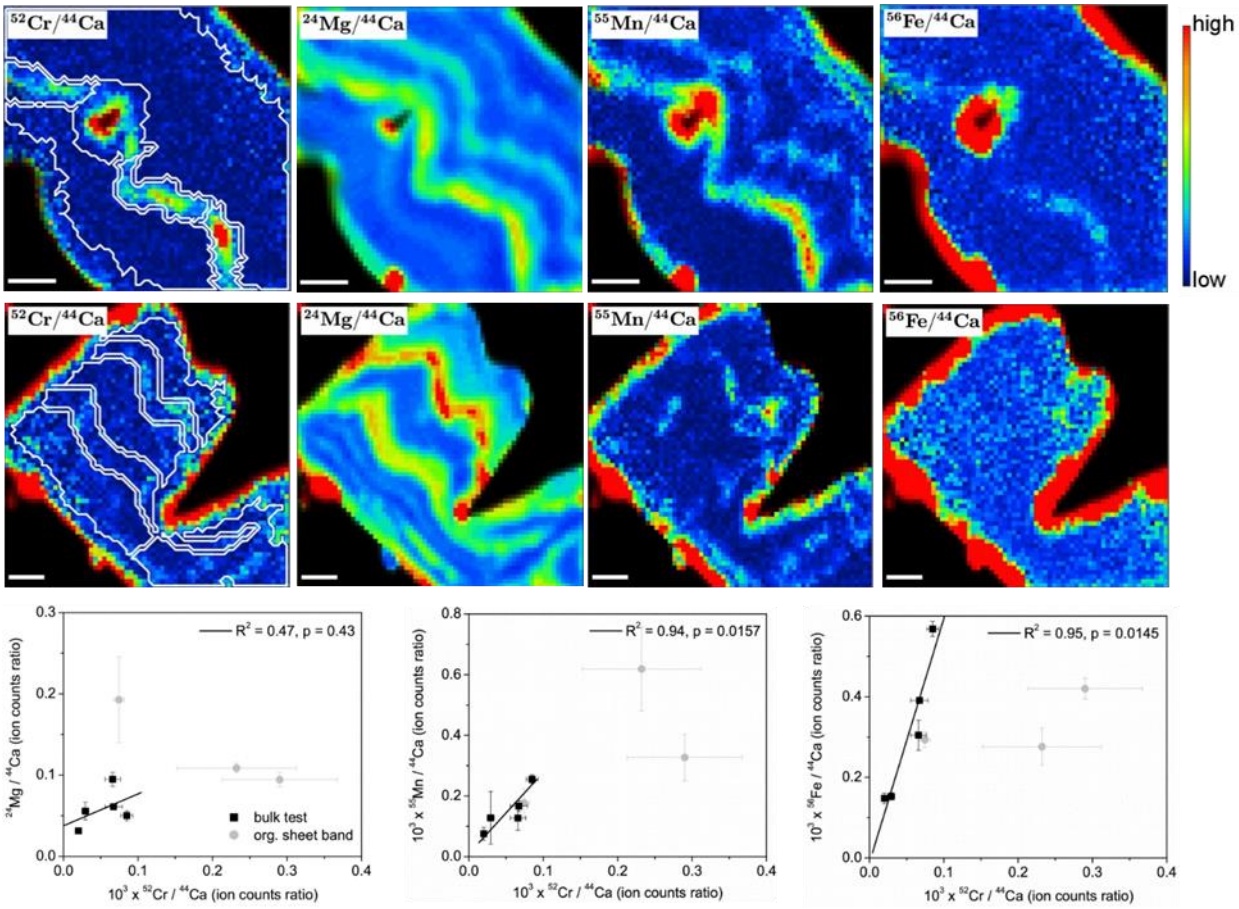

Figure 2.5: NanoSIMS images and analysis of core-top *T. sacculifer* specimens from the Caribbean (Caromel et al., 2014). NanoSIMS image panels show ^{52}Cr, ^{24}Mg, ^{55}Mn, and ^{56}Fe to ^{44}Ca ratios within the test walls. All trace elements were enriched in a layer associated with the POS. The apparent increase in Cr/Ca ratios at the rim of the foraminiferal tests is an analytical artefact of the transition from higher Cr and lower Ca counts in the resin to lower Cr and higher Ca counts in the test, caused by the limited spatial resolution of the nanoSIMS beam used in this study (1-2 µm). This artefact occurs for all element/Ca ratios. Regions of interest (ROIs), indicated by the white outlines in the left panels, were drawn to calculate average Cr/Ca, Mn/Ca and Fe/Ca ratios in the 'bulk' test and the Cr-rich bands. ROIs were divided into 3-4 approximately equal parts to estimate variability within an ROI. Within the bulk tests, the correlations between Cr/Ca, Mn/Ca and Fe/Ca are significant, whereas there is no apparent correlation with Mg/Ca. The Cr-rich bands associated with the POM do not follow the trends defined by the bulk test.

LA-MC-ICP-MS based Cr concentrations correlate strongly with Fe/Ca of the foraminifera (R^2 = 0.84) suggesting a common uptake pathway into the foraminiferal test. There are two distinct populations in

the Cr to Fe/Ca and Cr to Mn/Ca cross-plots with non-sedimentary foraminifera plotting in a separate population along a separate trend (Figure 2.6a and 2.6b). The foraminifera with high Cr concentrations have high Fe concentrations and low Mn concentrations (Figure .26c). These strong correlations are confirmed by the NanoSIMS analysis of core-top foraminifera (Figure 2.5) and shows that also Cr and Mn/Ca strongly correlate within a single *T. sacculifer* specimen.

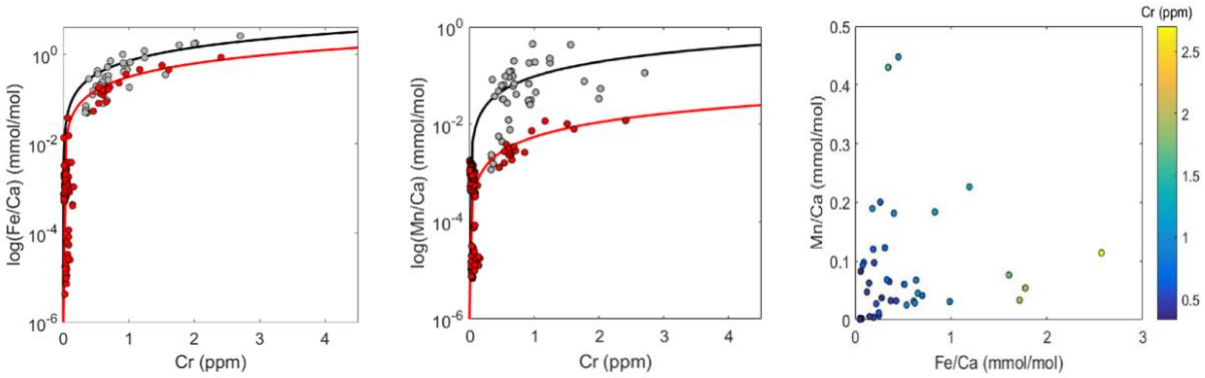

Figure 2.6: a. Cross-plot of average Cr concentrations and Fe/Ca obtained by LA-MC-ICP-MS in single foraminifera. Core-top samples are in grey and non-sedimentary foraminifera are in red. There are two populations with distinct trends in the core-top samples of which one overlaps with the non-sedimentary foraminifera. **b.** Cross-plot of average Cr concentrations and Mn/Ca obtained by LA-MC-ICP-MS of single foraminifera. Core-top samples are in grey and non-sedimentary foraminifera in red. There is no trend in the core-top samples. There is, however, a significant trend within non-sedimentary foraminifera. **c.** There is no correlation between Mn/Ca and Fe/Ca. Chromium is present in high concentrations in foraminifera with high Fe concentrations. Samples with a high Fe and Cr content have lower Mn concentrations.

2.3.3. Chromium isotopic composition of core-top planktic foraminifera

Chromium concentrations in core-top samples from the Caribbean are higher (0.15 – 0.38 ppm) compared to those from the North Atlantic (0.06 – 0.08 ppm) while δ^{53}Cr was ~ 0.4‰ lower. Specimens from the >500 µm fraction have 0.3 – 0.5‰ higher δ^{53}Cr values than those from the 250 – 500 µm size fractions in both the Caribbean and North Atlantic (Figure 2.7). Offsets in Cr concentrations associated with size fractions of foraminifera are less clear. While the smaller foraminifera, and particularly *G. ruber*, may have higher Cr concentrations in the Caribbean, this is not the case for foraminifera from the North Atlantic with a Cr concentration difference of 2 ppb which may fall within natural variability.

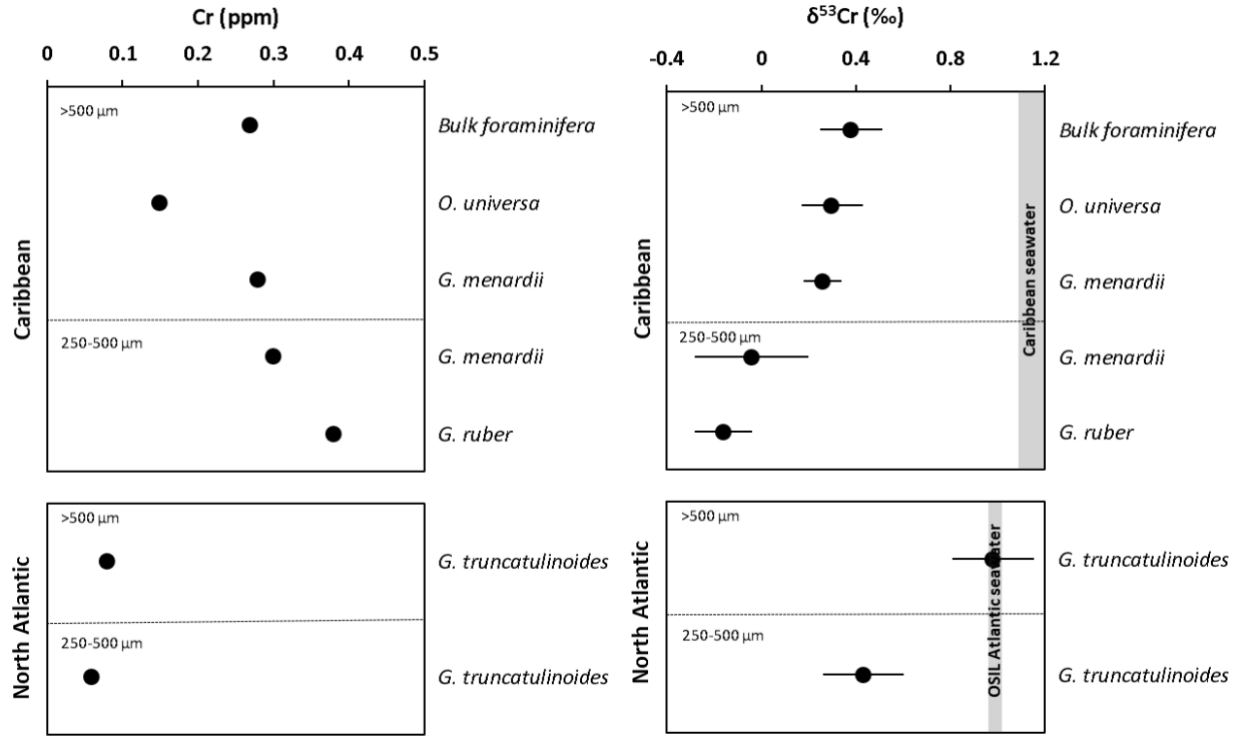

Figure 2.7: The $\delta^{53}Cr$ composition (left panels) and Cr content (right panels) of foraminifera of different sizes from the Caribbean and North Atlantic (T86-15S). There are no vital effects between different species of foraminifera of the same size fraction. There is, however, an isotopic offset between size fractions. Seawater $\delta^{53}Cr$ values are from Scheiderich et al. (2015) and Holmden et al. (2016). Where error bars are not visible, the analytical errors are smaller than the size of the data point.

2.3.4. Sequential Leaching Experiments on Core-top Foraminifera

The samples used were bulk planktic foraminifera from the Caribbean consisting mainly of *T. sacculifer*, *G. ruber*, *O. universa* and *G. menardii* (Caromel et al., 2014). All cleaning steps reduced the concentration of measured Cr in the sample (Figure 2.8). However, most Cr (~ 47%) was removed by thoroughly rinsing the sample with MilliQ and methanol until the supernatant had no visible suspended particles. Oxidative cleaning with alkali-buffered H_2O_2 removed approximately 3% of total measured Cr, whereas a weak acid leach removed about 5% of total Cr. To be certain the Fe-Mn coating was removed, the REEs were measured after each of the leaching steps as well (Figure 2.8), as REEs reside mostly in the coating (Palmer, 1985). REE-Y in the foraminifera were low (likely below detection limit) after leaching with weak nitric acid, in contrast to Cr concentrations, suggesting Fe-Mn coatings contributed little to the overall Cr concentrations in core-top foraminifera. This is in agreement with concentrations of Cr in the range of 8 – 40 ppm in Fe-Mn nodules (Baturin and Dubinchuk, 2011).

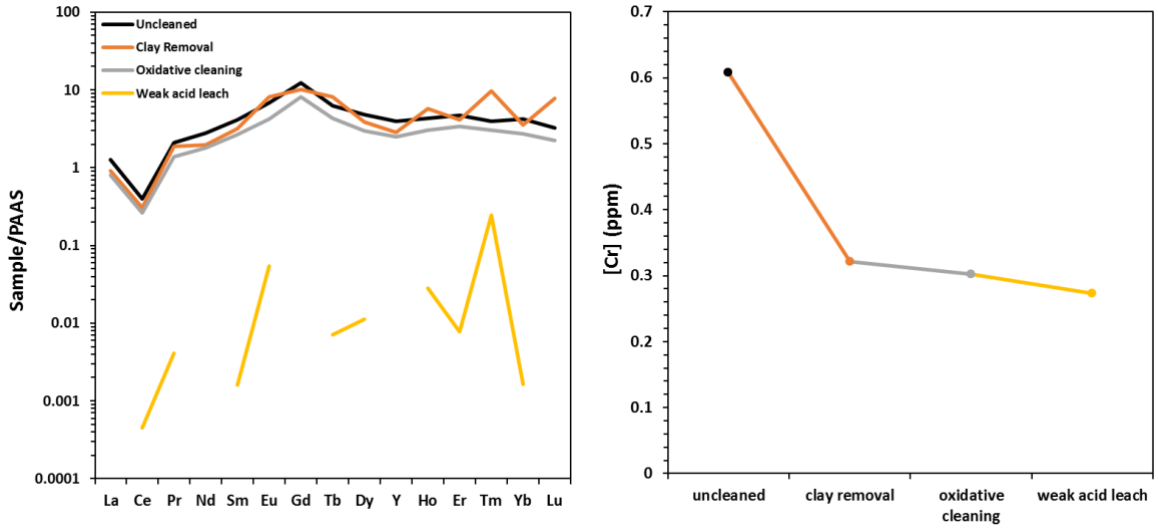

Figure 2.8: Sequential leaching study modified from Barker et al. (2004) showing the effective removal of REE-Y in the ferromanganese coating after a weak acid leach. Chromium concentrations are mostly affected by removing detrital material. Oxidation of organic matter and removal of the ferromanganese coating have little impact on overall Cr concentrations relative to Ca.

2.4. Discussion

Before foraminiferal Cr can be confidently applied as a palaeoproxy for past oxygen concentrations, an assessment of the uptake mechanism of Cr, in what foraminiferal phase Cr can be found, and the fractionation of Cr isotopes by foraminifera is mandatory.

2.4.1. Chromium uptake by benthic and planktic foraminifera

The distribution coefficient of the larger benthic foraminifera *Amphistegina sp.* (D_{Cr} = 250 ± 43) are comparable to the D_{Cr} = 107 – 329 of scleractinian corals (Pereira et al., 2016) and agrees with the low endmember of previous estimates by Wang et al. (2017) for planktic foraminifera despite the difference in atomic structures between aragonite and calcite (Soldati et al., 2016).

On average, core-top specimens have two orders of magnitude higher concentrations (0.82 ppm) than non-sedimentary foraminifera, which have 0.09 ppm Cr (Figure 2.4). Therefore, our laser ablation measurements imply that most Cr (~89%) in foraminifera is derived through post-depositional processes. Concentrations similar to those of non-sedimentary foraminifera were found in non-sedimentary scleractinian corals (0.04 – 0.07 ppm; Pereira et al., 2016). Combining these low concentrations with our culture derived understanding of distribution coefficients, suggests that at natural seawater Cr concentrations (e.g. Scheiderich et al., 2015; Paulukat et al., 2016) carbonates have

a limited Cr uptake. Chromium concentrations in the benthic *Amphistegina sp.* (0.04 – 0.13 ppm; Figure 2.1) have a strong positive correlation with total dissolved Cr in the seawater at the natural range of Cr concentrations in seawater ($R^2 = 0.79$; Figure 2.2). Any unlikely remnants of clay in pores of the core-top foraminifers would not have caused a two orders of magnitude increase in Cr implying that the largest amount of Cr in foraminifera is derived through post-depositional incorporation into the lattice as suggested earlier by Holmden et al. (2016).

2.4.2. Spatial distribution of chromium in planktic foraminifera

Chromium is present across the whole test (Figure 2.3). The enrichment in chromium near the rims of some of the tests (Figure 2.3) indicates a potential penetration into the test from the bottom and pore water in which they reside and supports post-depositional processes as a main source of Cr into the test (Figure 4). The considerable spatial variability in some laser ablation depth profiles warranted increased spatial resolution analyses by NanoSIMS. NanoSIMS imagery showed increased Cr counts in the most prominent cyclical Mg-rich bands (Figure 2.5). The fact that not all Mg-rich bands were accompanied by increased Cr counts was potentially due to the relatively low Cr concentrations (<1 ppm; Figure 2.7) combined with the sensitivity of the NanoSIMS. There are two possible interpretations for these higher Cr concentrations. Firstly, the higher concentration could be post-depositional Cr overprints. Interestingly, the Cr-rich bands aligned with discontinuities in the calcite which are remnants of the position of the primary organic sheets (POS) (Figure 2.5). This suggests Cr in core-top foraminifera may have penetrated the tests through cracks which acted as access points for pore waters and thus provides Cr (and likely other elements) an alternative pathway to diffuse through the test. Alternatively, the alignment of Cr-rich bands with regions associated with the primary organic sheet suggests that Cr may be concentrated in the initial inner calcite layer.

The initial inner calcite layer makes up a small fraction of the total foraminiferal shell compared to the rest of the ontogenetic calcite and potential gametogenic calcite and is thought to be enriched in trace elements (Eggins et al., 2003; Erez, 2003). Erez (2003) hypothesised that a potential initial calcification mechanism may be through endoplasmatic granules or organic matrix which would lead to higher trace element concentrations. Jacob et al. (2017) suggest the initial stages of foraminiferal biomineralisation occur via metastable carbonate phases such as vaterite, and potentially also amorphous calcium carbonate. Vaterite is fibrous and has nanopores which likely contain organic material (Li et al., 2011; Jacob et al., 2017) which increases the potential of high Cr concentrations.

It is important to note that the NanoSIMS is extremely sensitive to surface topography and could artificially produce enriched layers caused by cracks in the surface. The enrichment of Cr in Mg-rich bands was not detected by laser ablation techniques likely a result of the lower spatial resolution of the

laser (85-140 µm) compared to the NanoSIMS (1-2 µm), which average the distinct Cr-rich layers with the bulk calcite.

2.4.3. Source of Cr in the geological archive

When plotting Fe/Ca, Mn/Ca and Cr in core-top foraminifera obtained by laser ablation methods, foraminifera fall within two separate populations; one with high Fe/Ca and Mn/Ca ratios and one that overlaps with non-sedimentary foraminifera (Figure 2.6). Foraminifera with a high Cr content have high Fe and low Mn concentrations, which reinforces the observation that foraminiferal Cr is independent of Mn and may be predominantly influenced by oxyhydroxides low in Mn. There is a correlation between Cr and Mn/Ca within non-sedimentary specimens, but this does not extend to a clear correlation between core-top samples (Figure 2.6). The highest Cr and Fe contents in non-sedimentary foraminifera are found in the upwelling zone off the coast of Mauritania (Table 2.1) which receives large amounts of Fe and other metals from Saharan dust (e.g. Hatta et al., 2015). The strong correlation between Fe and Cr within foraminiferal tests suggests that they have a similar pathway into foraminiferal calcite controlled by the same process (Figure 2.6). The two distinct populations following separate trend lines seen in the Cr to Fe/Ca and Mn/Ca cross-plots (Figure 2.6) suggest two modes of Cr uptake. The strong correlation between Cr and Fe/Ca as well as Mn/Ca within a single core-top planktic foraminifer is also visible in the NanoSIMS analysis (Figure 5). Minerals common in the environment containing both Fe, Mn and Cr include Fe-Mn and Cr(III)-Fe(III) oxyhydroxides (Tang et al., 2010). Chromium(III)-Fe(III) oxyhydroxides are a reaction product of Cr(VI) reduction by Fe(II) (Ellis et al., 2002). Iron and Mn bearing oxyhydroxides could influence foraminiferal $\delta^{53}Cr$ by the reduction of Cr(VI) to Cr(III) by Fe(II) and the oxidation of Cr(III) to Cr(VI) by Mn in pore and bottom waters (e.g. Schroeder and Lee, 1975; Døssing et al., 2011). A potential pathway for elevating Cr and Fe concentrations in pore and bottom waters is through solubilisation of Cr(III) and Fe(III) bound to Cr(III)-Fe(III) oxyhydroxides by ligand complexation (Saad et al., 2017).

Taken together, our data indicate that Cr is initially taken up by foraminifera upon precipitation of their carbonate shell. This signature is preserved in core-top foraminifera, but heavily overprinted by exchange with bottom and pore waters after deposition in the sediment. Since Cr concentrations associated with post-depositional enrichment in core-top foraminifera are substantially greater than the Cr uptake associated with the live phase, core-top and down-core foraminifera most likely carry a bottom and pore water Cr isotopic signature rather than a sea surface Cr isotopic value. The overlap between some core-top foraminifera low in Mn and Fe and non-sedimentary specimens may provide a useful criterion for distinguishing foraminifera affected by post-depositional diffusion of Cr into their tests.

2.4.4. Chromium isotopic composition of core-top planktic foraminifera

To corroborate our interpretation of the potential post-depositional origin of Cr is assessing the impacts this would have on the Cr isotopic composition of foraminifera. The absence of species-specific fractionation (Figure 2.7) between foraminifera of the same size class indicates that the Cr isotopic composition in core-top foraminifera is not determined by biological processes, including growth rates, as I assessed specimens from different water depth and ecologies. While *G. ruber* and *O. universa* live in the upper mixed layer and have symbionts which add to the foraminifer's control on changing the oxygen concentration around the test, *G. menardii* and *G. truncatulinoides* dwell below the thermocline for a large amount of time during calcification without symbionts.

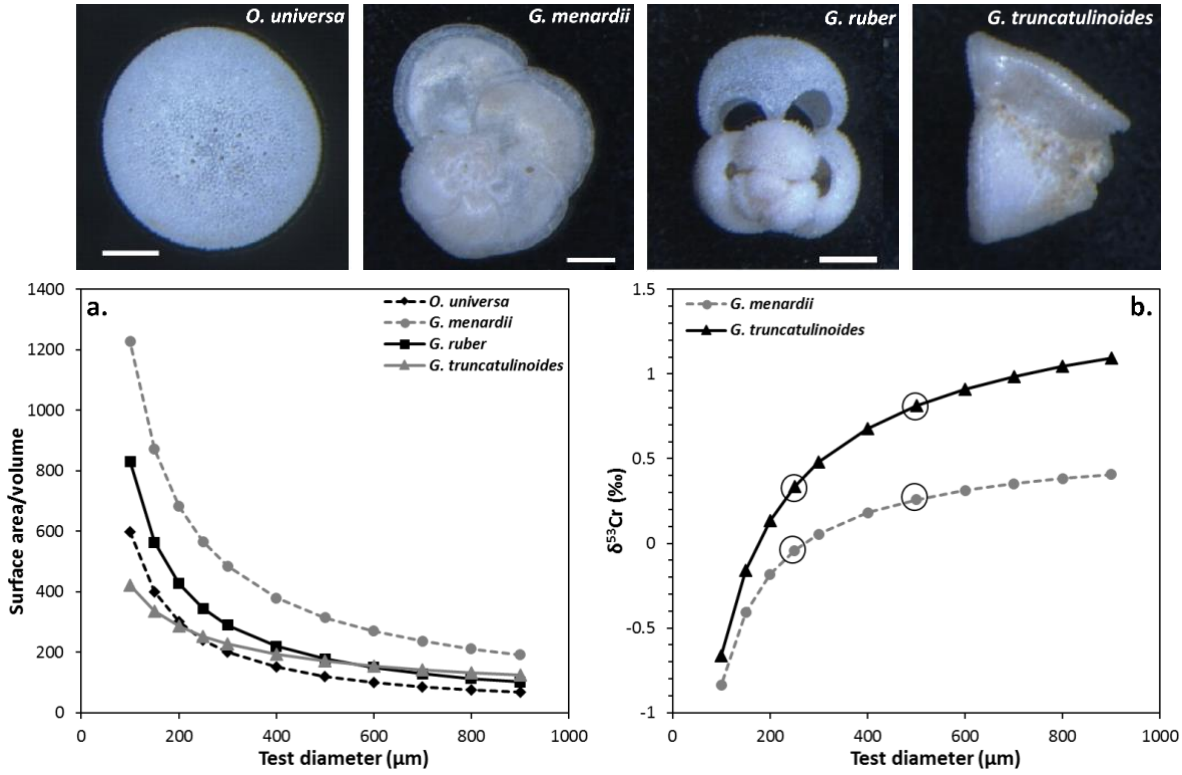

Figure 2.9: a. This study simulated surface area to volume (A/V) ratios based on volume – test diameter measurements by Caromel et al. (2014) show that A/V ratios in planktic foraminifera increase markedly in smaller size fractions (< 500 µm). Smaller foraminifera are therefore more susceptible to diagenetic processes. **b.** A model of linear dependence of foraminiferal Cr isotopes on the A/V ratio shows that the largest changes in isotopic composition would occur at smaller test diameters. The original Cr isotope data on which the linear model is based is encircled. Microscope images of planktic foraminifera to illustrate the shapes of the foraminiferal used for modelling A/V ratios are from Caromel et al. (2014).

A potential abiotic control on the relationship between size and chromium is the change in surface area to volume ratio. The inverse relationship between test diameter and $\delta^{53}Cr$ is associated with a higher surface area to volume ratios (A/V) in smaller specimens. As such, their calcite volume is more exposed

to post-depositional Cr enrichment via exchange with Cr in bottom and pore waters (e.g. Hönisch and Hemming, 2004; Ni et al., 2007). I expect pore waters to be closer in $\delta^{53}Cr$ to bulk silicate earth values (-0.124‰; Schoenberg et al., 2008) due to the large quantities of Cr available for remobilisation in the sediment. However, it is peculiar that foraminifera with widely differing shell shapes, pore volumes and thicknesses record a similar isotopic offset. Due to their shape, the discoidal *G. menardii* are more prone to changes in A/V than the spherical *O. universa*, globular *G. ruber*, and conical *G. truncatulinoides* (Figure 2.9). Despite these differences in shape, all planktic foraminifera show a sharp change in slope in the A/V ratio between 250 – 300 µm. Foraminifera smaller than 250 µm are likely to record even larger isotopic offsets due to the increase of the A/V ratio with decreasing test size (Figure 2.9). A/V calculations are based on the test volume determined from the same samples by Caromel et al. (2014). Surface areas were calculated assuming a spherical shape for *O. universa* and *G. ruber* ($A = 4\pi r^2$); a discoidal shape ($A = \pi*d*(d/2 + h)$) for *G. menardii*; and a conical test ($A = \pi r*(r + \sqrt{(h^2 + r^2)})$) for *G. truncatulinoides*. Assuming a linear dependence of the Cr isotopic composition of *G. menardii* and *G. truncatulinoides* on the A/V ratio (taken as the A/V ratio for the lowest end-member of the size fractions, i.e. 250 and 500 µm), the variability in foraminiferal Cr isotopes reported by Wang et al. (2017) can be explained by potential differences in the sizes of the foraminifera analysed (Figure 2.9). These surface area approximations are a minimum estimate for *G. ruber*, which is highly porous and has an open test structure and as such is more prone to overprinting.

2.5. Conclusions

This chapter explored the uptake and distribution of Cr in foraminiferal tests and the findings have furthered the understanding of Cr in carbonates. Firstly, *Amphistegina* cultures indicate a distribution coefficient (D_{Cr}) of 250 ± 43, which is comparable with scleractinian corals. Cultured *Amphistegina* have Cr concentrations ranging between 0.04 to 0.13 ppm under natural seawater Cr concentrations. Secondly, Cr is distributed across the whole foraminiferal shell and is mostly associated with the calcite phase of the foraminifer. Foraminiferal Cr concentrations are higher in Mg-rich bands closely linked to the previous location of the primary organic sheet. These regions likely form a pathway for secondary Cr to enter the test. Sedimentary foraminifera have on average an order of magnitude more Cr than foraminifera collected before deposition. As such, I suggest post-depositional addition of Cr to be the main uptake mechanism of Cr. This is corroborated by two distinct populations in Cr to Fe/Ca and Mn/Ca cross-plots which also suggest a post-depositional overprint in core-top foraminifera. The overlap between some core-top and non-sedimentary specimens may provide a tool for assessing the impact of post-depositional incorporation of Cr into foraminiferal tests.

In agreement with the small biological uptake of Cr, there is no significant interspecies isotope fractionation observed in the analysed foraminifera from the Caribbean and North Atlantic. There are, however, isotopic compositional changes related to size of the test potentially caused by surface area/volume ratio effects on the exchange with Cr in pore and bottom waters. A direct Cr isotope and O_2 calibration in the form of a foraminiferal culture would help to quantify the Cr response to oxygenation, but will be challenging given the low distribution coefficients of live foraminifera and pristine biogenic calcite.

Chapter 3

Foraminiferal Cr isotopes and ocean deoxygenation during the Palaeocene-Eocene Thermal Maximum

---

This chapter has been submitted to *Paleoceanography and Paleoclimatology* for publication.

Author contributions and declaration: Dr I.J. Parkinson and Professor D.N. Schmidt (School of Earth Sciences, University of Bristol) provided supervision and advice on the design and execution of the study. Dr F.M. Monteiro (School of Geography, University of Bristol) provided supervision and assistance in earth system modelling. Professor P. Sexton (School of Environment, Earth & Ecosystems, The Open University), and Professor Richard Norris (Scripps Institution of Oceanography, University of California at San Diego) provided samples from DSDP Site 401. The International Ocean Discovery Program provided foraminiferal PETM samples from ODP Sites 1210 and 1263. S. Dixon (School of Environment, Earth & Ecosystems, The Open University) analysed some of the foraminiferal samples from site 401 for trace metal content and Cr isotopes. All other ICP-MS data were acquired with the assistance of Dr S. Hammond (School of Environment, Earth & Ecosystems, The Open University) at the Open University and were processed and interpreted by S.R.C. Remmelzwaal. And all other MC-ICP-MS data were acquired, processed, and interpreted by S.R.C. Remmelzwaal. Feedback on the manuscript was given by Dr I.J. Parkinson, Professor D.N. Schmidt, Dr F.M. Monteiro, Professor P. Sexton, Professor R.H. James (National Oceanography Centre Southampton, University of Southampton) and Dr M. Fehr (Institute of Geochemistry and Petrology, ETH Zürich).

Abstract

Over the past several decades, oxygen minimum zones have rapidly expanded due to rising temperatures raising concerns about the impacts of future climate change. One way to better understand the drivers behind the expansion is to evaluate the links between climate and seawater deoxygenation in the past especially in times of geologically abrupt climate change such as the Palaeocene-Eocene Thermal Maximum (PETM), a well characterised period of rapid warming ~56 million years ago. We have developed and applied the novel redox proxies of foraminiferal Cr isotopes ($\delta^{53}Cr$) and Ce anomalies (Ce/Ce*) to assess changes in paleo-redox conditions arising from changes in oxygen

availability. Both $\delta^{53}Cr$ and Cr concentrations decrease notably over the PETM at intermediate to upper abyssal water depths, indicative of widespread reductions in dissolved oxygen concentrations. The strong correlation between the sizes of $\delta^{53}Cr$ and benthic $\delta^{18}O$ excursions during the PETM suggests temperature is one of the main controlling factors of deoxygenation in the open ocean. ODP Sites 1210 in the Pacific and 1263 in the Southeast Atlantic suggest that deoxygenation is associated with warming and circulation changes, as supported by Ce/Ce* data. Our geochemical data are supported by simulations from an intermediate complexity climate model (cGENIE), which show that during the PETM anoxia was mostly restricted to the Tethys Sea, while hypoxia was more wide-spread as a result of increasing atmospheric CO_2 (from 1 to 6 times pre-industrial values).

3.1. Introduction

As emitted greenhouse gasses accumulate in the atmosphere, temperatures are rising in both the atmosphere and the oceans with unclear consequences for marine ecosystems (Pörtner et al., 2014). One of the hazards associated with global warming is a decrease in oceanic dissolved oxygen content. Over the past 50 years O_2 levels have been steadily declining, leading to the expansion of so-called oxygen minimum zones – areas of hypoxic to suboxic levels of O_2 at intermediate water depths due to the decreased solubility of O_2 and increased metabolic rates of heterotrophic microbes as temperatures rise (Keeling et al., 2010). Understanding the effect of ocean warming on the expansion and intensification of oxygen minimum zones and deep ocean hypoxia is particularly needed (Pörtner et al., 2014). In this study, we assess the development of ocean hypoxia under high temperatures by using extreme warming in the geological past as an analogue for modern anthropogenic warming.

The climate of the Palaeocene and Eocene greenhouse periods experienced several extreme transient warming events of which the largest, the Palaeocene-Eocene Thermal Maximum (PETM; e.g. Cramer et al., 2003) occurred about 56 Ma (Westerhold et al., 2009). The PETM is a particularly pertinent time interval because of its parallels to present-day anthropogenic global warming (Pörtner et al., 2014). Global climate warmed rapidly by ~ 5 degrees Celsius (Dunkley-Jones et al., 2013) within 4,000 – 20,000 years (Zeebe et al., 2016; Gutjahr et al., 2017), with warming lasting for ~200 kyr (Röhl et al., 2007). The cause of the carbon isotope excursion (CIE) towards lighter $\delta^{13}C$ is still heavily debated (Gutjahr et al., 2017) with much of the literature pointing toward an injection of biogenic methane into the ocean-atmosphere system (e.g. Svensen et al., 2004). The injection of large amounts of carbon resulted in a decrease in alkalinity and intense dissolution of $CaCO_3$. The estimated change in pH was about -0.3 units in the surface ocean (Penman et al., 2014; Gutjahr et al., 2017) with an accompanying rise in the calcite compensation depth (CCD) of up to 2 km in the Atlantic Ocean (Zachos et al., 2005) though significantly less in the Pacific (>500 m; Colosimo et al., 2006).

The warming of the ocean, increased nutrient run-off, enhanced stratification, and the oxidation of a large body of reduced carbon are all suggested to have reduced oxygen levels in the oceans during the PETM (Nicolo et al., 2010; Dickson et al., 2012; Pälike et al., 2014). Deoxygenated bottom waters are thought to have been commonplace in marginal settings (e.g. Dickson et al., 2014) and oxygen minimum zones have been suggested to have expanded (Chun et al., 2010; Pälike et al., 2014; Zhou et al., 2016). The presence of geochemical indicators for deoxygenation (U, Mn) in the Atlantic and an absence of these in the Pacific Ocean strongly suggest the carbon source was situated in the Atlantic Ocean (Chun et al., 2010; Pälike et al., 2014; Zhou et al., 2016) as does the difference in change in the CCD. We propose here to further investigate the presence and development of hypoxia during the PETM in the Atlantic and Pacific using Cr isotopes in foraminifera.

Chromium isotopes have received attention in the past few years owing to their potential for reconstructing the palaeoredox state of the oceans (e.g. Bonnand et al., 2013; Reinhard et al., 2014). Chromium has multiple valence states and is therefore redox-active. In the marine environment, Cr can occur as either Cr(III) or Cr(VI) species, with Cr(VI)-oxyanions the dominant species in oxic seawater (Cranston and Murray, 1978). Chromium has four stable isotopes of which the difference in the $^{53}Cr/^{52}Cr$ ratio compared to NIST SRM979 is reported in the delta notation as $\delta^{53}Cr_{SRM979}$, where $\delta^{53}Cr_{SRM979} = 1000*[(^{53}Cr/^{52}Cr)_{sample} - (^{53}Cr/^{52}Cr)_{SRM979}] / (^{53}Cr/^{52}Cr)_{SRM979}$. As seawater becomes less oxic, Cr(VI) will be reduced to Cr(III) which is removed into oceanic sediments, resulting in lower dissolved Cr concentrations. The reduction of Cr is accompanied by a substantial isotope fractionation of up to 7‰ (Ellis et al., 2002). Recent studies have shown that the $\delta^{53}Cr$ of modern seawater is heterogeneous varying between 0.1 – 1.8 ‰, which can partly be explained by a short residence time of ~3,000 years (Qin and Wang, 2017; Goring-Harford et al., 2018) relative to the average ocean overturning time of ~1500 years. There appears to be a negative correlation between [Cr] and $\delta^{53}Cr$ in seawater samples measured to date (Scheiderich et al., 2015; Paulukat et al., 2016) that has been attributed to partial reduction of Cr(VI) in surface waters and oxygen minimum zones (with a $\Delta_{Cr(III)-Cr(VI)}$ of -0.79‰), coupled with Cr(III) re-oxidation in deep waters (Scheiderich et al., 2015; Paulukat et al., 2016).

Experimental data and studies on carbonates show that Cr is incorporated into the calcite lattice of carbonates (Tang et al., 2007; Bonnand et al., 2013) as a chromate ion and therefore marine carbonate records can be used as a potential archive for seawater Cr. A recent investigation into seawater controls on the Cr isotopic composition of core-top foraminifera (Wang et al., 2017) left open questions as to what might drive incorporation of Cr into foraminifera. No direct calibrations of this proxy in foraminiferal calcite have been performed. However, recent work has shown that while some Cr is incorporated during calcification most Cr in sedimentary foraminifera has a post-depositional origin

and therefore will record bottom and pore water Cr compositions (Chapter 2). Foraminiferal $\delta^{53}Cr$ values are not species dependent, but rather dependent on foraminiferal test size meaning that the surface area/volume ratio controls Cr exchange between the test and bottom water and/or sediment pore waters (see Chapter 2 for more detail). Questions around the empirical relationship between $\delta^{53}Cr$ and $[O_2]$ as well as potential dissolution effects remain unanswered. We thus interpret $\delta^{53}Cr$ data here in a qualitative sense, in terms of the sign of change, as an indicator of bottom and pore water ocean deoxygenation.

To better constrain bottom water ocean deoxygenation during the PETM, we combine Cr isotope data with observations of cerium (Ce), a potentially useful rare earth element (REE) to reconstruct oxidation states (e.g. Zhou et al., 2016). Unlike most REEs, Ce has two oxidation states, Ce(III) and Ce(IV), and like Cr is redox sensitive. Modern seawater has a characteristic negative Ce anomaly. This anomaly has been suggested to have been caused by the oxidation of Ce(III) to the insoluble and particle-reactive Ce(IV) in surface waters and estuaries where seawater is consequently depleted in Ce with respect to La, Pr and Nd (De Baar et al., 1988). In anoxic waters Ce concentrations are high and the Ce anomaly vanishes or even becomes slightly positive (De Baar et al., 1988). Ce/Ce* values (defined in Section 2.3.2) are approximately 1.0 in anoxic seawater, 0.5-1.0 in hypoxic pore waters and lower than 0.5 for oxic seawater (Zhou et al., 2016). Cerium mostly resides in authigenic ferromanganese coatings that form after sediment deposition (Palmer et al., 1985).

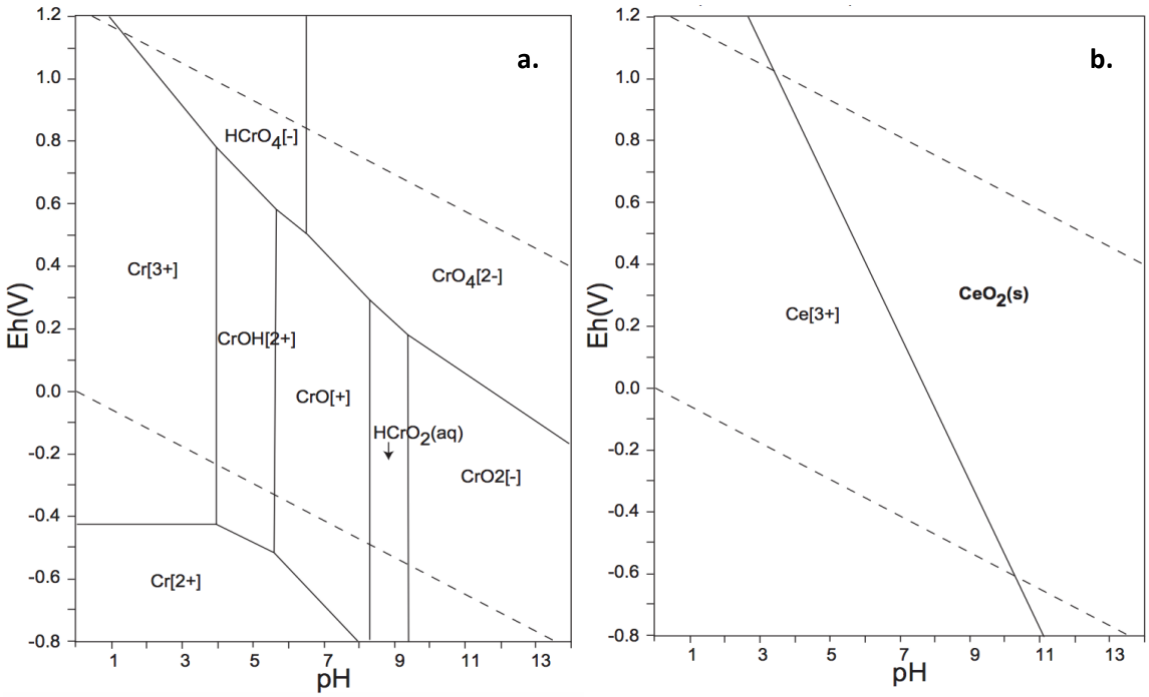

Figure 3.1: Eh-pH diagrams of Cr and Ce showing the sensitivity of both proxy systems to changes in redox conditions. Dashed lines mark the stability field of water and solid lines of the Cr and Ce species (Takeno, 2005).

The Cr and Ce systems show different sensitivities to changes in redox state (Figure 3.1). The transition of CrO_4^{2-} to Cr(III) in seawater conditions (pH = 8.2) occurs at an Eh between approximately 0.3-0.4 (Takeno, 2005; Bonnand et al., 2013) and the transition between Ce(III) and CeO_2 under similar conditions occurs at Eh ~ 0 (Takeno, 2005). Chromium and Ce both change speciation in the 'transition' area between an oxidising and a fully reducing environment (Brookins, 1988). The difference in the sensitivity of the proxies allows for assessing what degree of hypoxia the deoxygenation of seawater caused when Cr and Ce are applied at the same time.

In this study, we investigate the development of open ocean deoxygenation during the PETM using the foraminiferal redox proxies $\delta^{53}Cr$ and Ce/Ce*. We compare our data with published geochemical, sedimentological and micropalaeontological studies that inform on redox conditions during the PETM. We also perform some ocean biogeochemical model simulations; this model-data comparison allows us to assess the evolution of ocean deoxygenation in intermediate and upper abyssal waters, and the extent to which the oceans experienced hypoxia and anoxia.

3.2. Materials and Methods

3.2.1. Sample site selection

Our geochemical data are derived from three sites drilled by the Deep-Sea Drilling Program (DSDP) and Ocean Drilling Program (ODP): DSDP Site 401is located in the Bay of Biscay (north-eastern Atlantic) with a palaeodepth of 1900 m, ODP Site 1263 is on Walvis Ridge (south-eastern Atlantic) with a palaeodepth of 1500 m, and ODP Site 1210 is on Shatsky Rise (North Pacific) with a palaeodepth of 2400 m (Figure 3.1; Pälike et al., 2014, and references therein). Site 1210 is located in the North Pacific where more vigorous deep-water formation has been suggested to have occurred during the PETM (Tripati and Elderfield, 2005, Lunt et al., 2010), whereas a slowdown purportedly occurred in the South Atlantic (Site 1263) (Tripati and Elderfield, 2005). It must be noted, however, that there is no consensus on the site of deep-water formation during the PETM with the North Atlantic as location of downwelling (Bice and Marotzke, 2002; Nunes and Norris, 2006; Alexander et al., 2015). Site 1263 was located near a major oxygen minimum zone (Chun et al., 2010). Site 401 was in the comparatively narrow North Atlantic that was gradually widening in association with major volcanic activity during the Palaeocene-Eocene (Svensen et al., 2004).

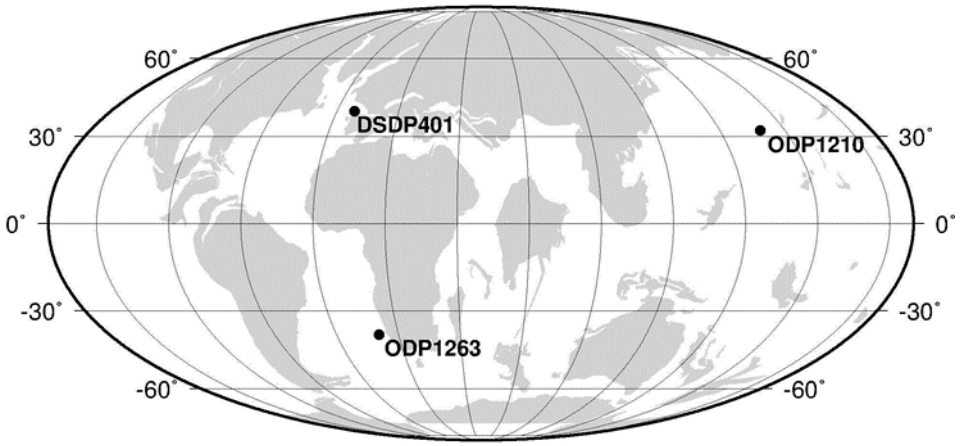

Figure 3.2: Palaeogeographic reconstruction for 56 Ma (www.odsn.de) with sample sites marked.

3.2.2. Age models

Age models were derived from the cyclostratigraphic analyses by Gutjahr et al. (2017) for Site 401, Westerhold et al. (2008) for Site 1210, and Röhl et al. (2007) for Site 1263. These were anchored to a timescale following the age constraint of the PETM by Westerhold et al. (2009). Linear sedimentation rates were used to calculate the ages for all the data plotted.

3.2.3. Analytical methods

3.2.3.1 Sample processing

Sediment samples of 10-20 cm^3 were wet sieved with a 63 µm sieve to obtain enough material for analysis. Coarse fractions are the dry mass of the particles larger than 63 µm as the weight percentage of the dry mass of the total sample prior to sieving. A mixture of planktic foraminiferal species was picked from these samples to obtain about 0.11 g. Samples were cleaned by gently cracking open the foraminiferal tests, with subsequent removal of clay particles and organic matter by ultrasonication in Milli-Q (MQ) grade water and by leaching in alkali buffered H_2O_2, respectively (Barker et al., 2003). Analysis of the chemical composition of Fe-Mn-rich crusts show that these have relatively low Cr concentrations [8 - 40 ppm Cr; Baturin and Dubinchuk (2011)]. Similar observations for Fe-Mn coatings were made in Chapter 2 and therefore the Fe-Mn coatings were not removed to preserve as much of the calcite as possible for analysis.

3.2.3.2 Trace element analysis

Cleaned samples of ~0.01 g were dissolved in cold 0.5M acetic acid, dried down to incipient dryness and subsequently were dissolved and diluted with 2% HNO_3 acid by ~4000 times to produce a 100 ppm Ca solution. A suite of synthetic standards containing 40 trace elements at a variety of concentrations and doped with 100 ppm Ca were used to produce a calibration curve. Rare earth elements and Cr concentrations were measured in He and O_2 collision mode respectively on an Agilent 7500s ICP-QQQ-

MS (Triple Quadrupole ICP-MS) at the Open University. Rare earth element concentrations are normalised to Post Archaean Australian Shale (PAAS) concentrations (Taylor and McLennan, 1985). Anomalies in Ce are expressed as $Ce/Ce^* = (Ce/Ce_{PAAS})/[Pr/Pr_{PAAS}*(Pr/Pr_{PAAS})/(Nd/Nd_{PAAS})]$ (Tostevin et al., 2016). Measurements are reproducible within ~ ±2% for Cr and ~ ±9% for Ce/Ce* based on replicate analysis of the carbonate standard reference material JDo-1.

3.2.3.3 Cr isotope analysis

Approximately 0.1 g of sample (down to 0.03 g during the height of the dissolution event at ODP Site 1263) was dissolved by ultrasonication in 0.5M acetic acid to prevent any potential leaching of any remaining detrital material left after cleaning. Chromium was subsequently extracted following the cation exchange chromatographic separation procedures described in Bonnand et al. (2011) with procedural blank Cr contributions of ~0.2 ng. JDo-1 was subjected to the same chemistry protocol as the samples. Chromium isotopes were measured on a ThermoFisher Scientific Neptune MC-ICP-MS by using a ^{50}Cr-^{54}Cr double-spike technique following Bonnand et al. (2011). The average value obtained for JDo-1 is $\delta^{53}Cr = 1.715 \pm 0.059$ (2σ, $n = 8$), which is within error of previously published values of $\delta^{53}Cr = 1.719 \pm 0.059$ (Bonnand et al., 2011). The external reproducibility of NIST SRM 979 is $\delta^{53}Cr = 0.002 \pm 0.026$ (2σ, $n = 20$).

3.2.4. cGENIE modelling set-up

To estimate the global extent of deoxygenation during the PETM, proxy observations of ocean redox state are compared with model simulations of the Paleogene ocean following the approach described in Monteiro et al. (2012). The model employed was the Earth system model of intermediate complexity cGENIE, a 3D ocean biogeochemical model coupled to a 2D zonally averaged energy-moisture balance atmospheric model (Ridgwell et al., 2007). The ocean model horizontal grid is uniform in longitude (10º resolution) and varies from ~3º at the equator to ~19º at the poles representing a 36x36 equal-area grid. The ocean model vertical grid accounts for 16 vertical levels varying from ~80m at the surface to 750m at depth. (Ridgwell et al., 2007). cGENIE is configured for the Eocene using bathymetry and continental configuration derived from the higher resolution model Fast Ocean Atmosphere Model (FOAM) simulations. The annual average wind field transformed to the cGENIE grid comes from the Eocene FOAM experiment run with 4x CO_2 (relative to the preindustrial atmospheric value). cGENIE biogeochemistry accounts for carbon, phosphorus, nitrogen, oxygen and sulphur cycling as described by Monteiro et al. (2012), including equations and parameter values for ocean productivity, which is limited by temperature, light and nutrients. In particular, oxygen regulation depends in the model on air-sea gas exchange at the surface of the ocean, the removal via remineralisation of organic matter, nitrification (represented as 1 step process of ammonium oxidation into nitrate), and oxidation of hydrogen sulphide (the end product of sulphate reduction). Organic matter is in the model represented by both dissolved organic matter, which is carried around by ocean currents, and particulate organic

matter, which follows a fixed vertical profile of remineralisation. Here the model uses a double exponential equation to account for a labile and a refractory fraction of POM (Hulse et al., 2017)

The parameter values for ocean productivity and nutrient cycling have been tuned to match modern observations of export production, nitrogen fixation, and concentrations of phosphate, nitrate and oxygen. While productivity and nutrient cycling are both dynamic entities of the model (calculated as a function of ocean currents, temperature and biogeochemical interactions), applying the model to the Eocene makes the assumption that biology (as inherent in the model parameterisation) behaves more or less the same as today towards productivity and recycling. Because the iron cycle is not well-enough constrained at the Eocene, it was assumed there was no iron limitation of ocean productivity.

Marine productivity of phytoplankton is modelled through the net depletion of non-fixing phytoplankton and diazotrophs. In the model, the phytoplankton biomass is related to the concentration of the limiting nutrient (based on the Michaelis-Menten form assuming a minimum limitation law between phosphate and fixed nitrogen for non-fixing phytoplankton, and N_2 for diazotrophs), temperature (based on the Eppley curve), and light limitation (Monteiro et al., 2012). cGENIE has dynamical nitrogen fixation and oligotrophy thresholds based on competition to account for climatic change. The nitrogen cycle also includes the nitrification process of the oxidation of ammonium into nitrate (Monteiro et al., 2012). In the model, denitrification occurs when oxygen concentrations drop below 30 μmol O_2 l^{-1}, which is higher than modern values due to the low model resolution and the omission of sediment denitrification in cGENIE (Monteiro et al., 2012).

In cGENIE, the remineralisation of particulate organic carbon instantaneously occurs throughout the water column. Remineralisation of both dissolved organic and inorganic carbon is coupled to the total availability of electron acceptors. When dissolved oxygen is depleted, denitrification will occur, and if nitrate becomes depleted, sulphate reduction will occur (Ridgwell et al., 2007). If there are not enough electron acceptors, remineralisation will be limited (Ridgwell et al., 2007). Sediments are not modelled in cGENIE. Therefore, organic matter burial and phosphorus regenerations in anoxic environments are not modelled, and instead are represented by a fixed global phosphate inventory which assumes all organic phosphorus that reaches the seafloor returns to phosphate at the bottom of the ocean (Monteiro et al., 2012). cGENIE is limited by not modelling the feedback between bottom-water hypoxia/anoxia and sedimentary processes.

The model is run under different environmental forcings to steady state (which is reached in 10-20 kyrs depending on CO_2 concentrations), varying the oceanic phosphate inventory and atmospheric CO_2 to investigate the impact of changes in nutrient supply and temperature on oceanic oxygen levels during the PETM. As found in Monteiro et al. (2012), the model shows that ocean oxygen levels at the Eocene

are more sensitive to changes in phosphate inventory than changes in atmospheric CO_2 (see supplementary material). Varying atmospheric CO_2 experiments highlights the impact of increased temperatures on oxygen supply and marine productivity, whereas the oceanic phosphate experiments highlight the impact of marine productivity with increasing nutrient inventory. The model results are compared with published data for seawater deoxygenation and photic zone euxinia across the PETM (Carmichael et al., 2017) (Tables A5 and A6).

A score of agreement is calculated between the model results and data for before and during the PETM (0-1, where 0 indicates no agreement and 1 indicates perfect agreement, Monteiro et al., 2012). Here, the distinction between anoxia/suboxia (< 10 µM O_2; Diaz and Rosenberg, 2008) and hypoxia (10-60 µM O_2; Diaz and Rosenberg, 2008; Vaquer-Sunyer and Duarte, 2008) has been added to better capture the subtler deoxygenation that is believed to have taken place during the PETM in comparison to Mesozoic Ocean Anoxic Events (OAEs). The geographical extent of photic zone euxinia has been assessed with a threshold of > 0 µM H_2S (Monteiro et al., 2012). The score for the model-data agreement is modified from Monteiro et al. (2012), and is a combination of bottom water anoxia and hypoxia, and photic-zone euxinia (Table A4) and is calculated as follows:

$$\Phi = \frac{\left(\frac{\sum_{i=N_{obs}} A_i W_i}{\sum_{i=N_{obs}} W_i} + 1\right)}{2}$$

Where N_{obs} is the number of sample sites, A_i is the model agreement with data *i* at a specific site, set to 1 for when model and data agree, and to -1 for when they disagree. In addition to oxic and anoxic/suboxic conditions (similar to Monteiro et al., 2012), we add here the comparison of the model results with observations of hypoxic conditions (10 – 60 µM O_2). The score is subsequently rescaled between 0-1, so that 0 indicates no agreement and 1 indicates perfect agreement. W_i is the certainty (weight) of the data. Where there is conflicting or questionable evidence W_i is set to 0.5, and where the data is unequivocal it is set to 1. There is no need to correct for the volume of the grid cell because the score is calculated only for horizontal surfaces (seafloor and photic zone) and because cGENIE has an equal-area horizontal grid. Φ is the eventual score of the agreement between the model and the data. There were 12 sites with published datasets for the Late Palaeogene and 15 sites for during the PETM for bottom water oxygenation. There were 3 sites with evidence for euxinia.

3.3. Results

3.3.1. Chromium and cerium anomalies

Site 401, located in the North Atlantic, shows a rapid increase in foraminiferal $\delta^{53}Cr$ of about 1.4‰ paired with a decrease in [Cr] of about 1.5 ppm just prior to the CIE (Figure 3.3). No Cr isotope data

are available for the onset of the PETM itself as this was an interval of intense dissolution. The highest $\delta^{53}Cr$ values are prior to the onset of the CIE and they recovered to background values 68 kyrs after the CIE onset. Chromium concentrations reach their lowest values of 0.27 ppm prior to the CIE minimum and do not recover within our 400 kyr-record. The severe carbonate dissolution at Site 1263, as indicated by a steep drop of ~4.8% in the coarse fraction (CF), a monitor of $CaCO_3$ dissolution through this interval, meant that our foraminiferal analysis was unable to capture the onset of the event. $\delta^{53}Cr$ values show a difference of approximately +3.5‰ between peak-CIE and non-peak CIE conditions, and suggest severe deoxygenation during the main body of the event. While Cr concentrations are highly variable prior to the PETM and after peak-CIE conditions, [Cr] attains its lowest values during the peak of the CIE. The timing of the crash and recovery in [Cr] corresponds with that of the CF record.

In the Pacific basin, at Site 1210 the Cr concentrations are extremely low (down to 0.01 ppm) during the PETM and decrease prior to the CIE. Chromium concentrations are variable prior to the PETM and during the carbon isotope recovery at this site. The maximum $\delta^{53}Cr$ value at Site 1210 is 0.71‰ with the highest $\delta^{53}Cr$ values occurring approximately 20 kyrs after the onset of the PETM in the middle of the $\delta^{18}O$ excursion. This pattern is unlike the observations at Site 401, where $\delta^{53}Cr$ values shift at the onset of the PETM.

Foraminiferal cerium anomalies of 0.10 – 0.28 (Figure 3.3 confirm previous findings that the North Pacific Ocean is more oxygenated than the Atlantic Ocean with values at Site 1263 of 0.72 – 1.14 falling within the range found by Zhou et al. (2016). Cerium anomalies of 0.60 – 1.31 at Site 401 suggest that North Atlantic bottom and pore waters were severely hypoxic and potentially anoxic.

Multiple 100-kyr eccentricity and 19-23-kyr precession cycles have been recorded throughout the PETM and late Palaeogene to Early Eocene (e.g. Röhl et al., 2007; Westerhold et al., 2017). Chromium concentrations during the PETM show variations at orbital timescales in both Atlantic and Pacific open ocean sites and move in tandem with Fe and Ba except during extreme climatic change (Figure 3.3; Röhl et al., 2007). Elevated Cr concentrations coincide with precession cycles both before and after the main body of the PETM at cycles -1, 4, 6, and 7 identified by Röhl et al. (2007). The amplitude of Cr concentration changes descends with time from the onset of the PETM starting with ~1.5 ppm in the Pacific (ODP Site 1210) and ~0.75 ppm in the South Atlantic (ODP Site 1263) for precession cycle 4 and ending with ~0.22 ppm in the South Atlantic and ~0.35 ppm in the Pacific for precession cycles 6 and 7, respectively (Figure 3.4). However, the observation of possible astronomical cyclicity must be approached with caution due to the low temporal resolution of the Cr record.

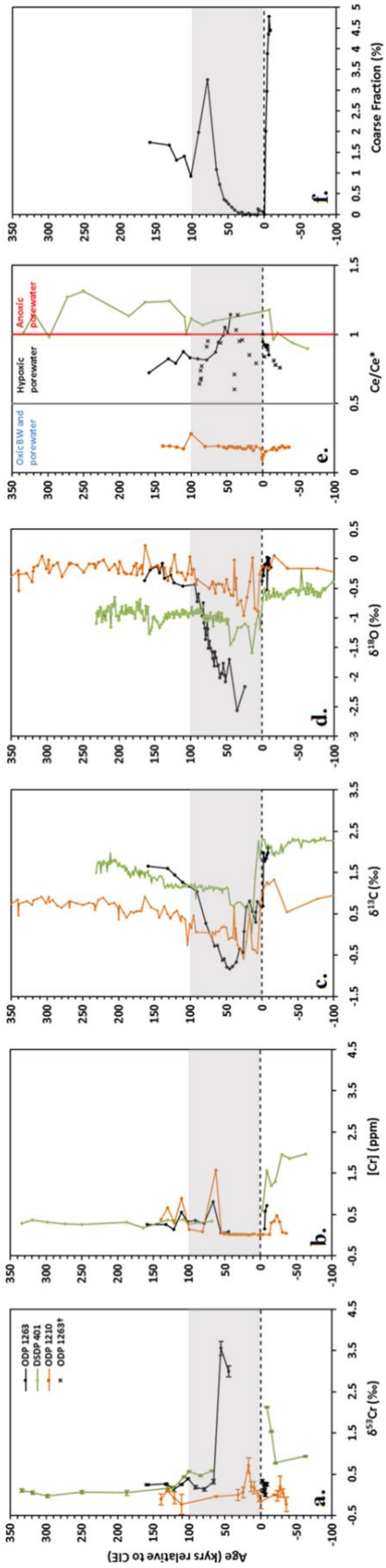

Figure 3.3: Records for Sites 401, 1210 and 1263 across the PETM of **a.** $\delta^{53}Cr$ (‰) **b.** chromium concentrations (ppm) **c.** benthic $\delta^{13}C$ (‰) for Sites 401 and 1210 (Nunes and Norris, 2006; Westerhold et al., 2011), bulk $\delta^{13}C$ (‰) for Site 1263 (Zachos et al., 2005) **d.** benthic $\delta^{18}O$ (‰) from *N. truempyi* (Nunes and Norris, 2006; McCarren et al., 2008; Westerhold et al., 2011) show large differences in timing and size between the $\delta^{53}Cr$ excursions **e.** Cerium anomalies show that Northwest Pacific bottom waters were oxic and Atlantic bottom waters were hypoxic. Ce/Ce* above 1 indicates anoxic conditions and below 0.5 bottom waters are oxic (Haley et al., 2004). †Fish tooth Ce/Ce* data for ODP 1263 by Zhou et al. (2016) **f.** Coarse fraction (> 63 µm) at Site 1263; a measure of $CaCO_3$ dissolution, measured for this study and in agreement with high resolution records by Kelly et al. (2010). The dotted line corresponds to the onset of the CIE associated with the PETM. The grey bar represents the onset, main body and recovery from the PETM based on carbon isotopes.

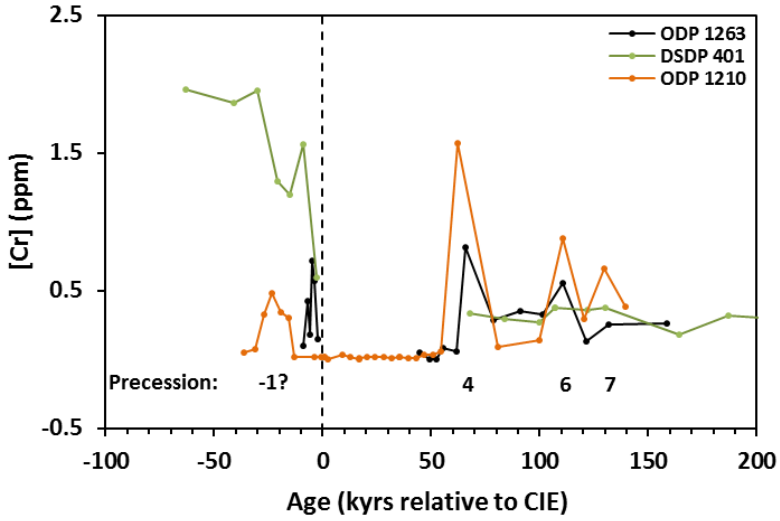

Figure 3.4: Chromium concentrations records from ODP Sites 1210 and 1263 (Pacific Ocean and South Atlantic Ocean) show elevated Cr concentrations during precession maxima at roughly 23.3 kyrs prior to the CIE and ~64.0, ~110.8 and ~129.8 kyrs after the CIE. These dates correlate with precession cycles -1, 4, 6, and 7 (Röhl et al., 2007). DSDP Site 401 does not display any orbitally paced variations in Cr concentrations. The dashed line represents the onset of the CIE.

3.3.2. 3D Model - data comparison

We reconstructed the change in deoxygenation across the PETM by comparing the data as compiled by Carmichael et al. (2017) (Tables A5 and A6) with the cGENIE model results. The best model fit to the data for pre-PETM conditions is achieved with the modern oceanic phosphate inventory (1 x PO_4) and 1-2 times preindustrial atmospheric CO_2 (1-2 x CO_2) (Table A1). The best model fit for the PETM is achieved under 1 x PO_4 and 6 x CO_2 conditions (Supplementary Material B; Figure 3.5) and falls within the estimated *p*CO2 for the PETM (e.g. Schubert and Hope Jahren, 2013; Gutjahr et al., 2017). In our model, the Tethys Sea and North Atlantic experience hypoxic to suboxic conditions (Figure 4) even with pre-industrial forcings while significantly less deoxygenation occurs in the Eastern Pacific and Southern Ocean.

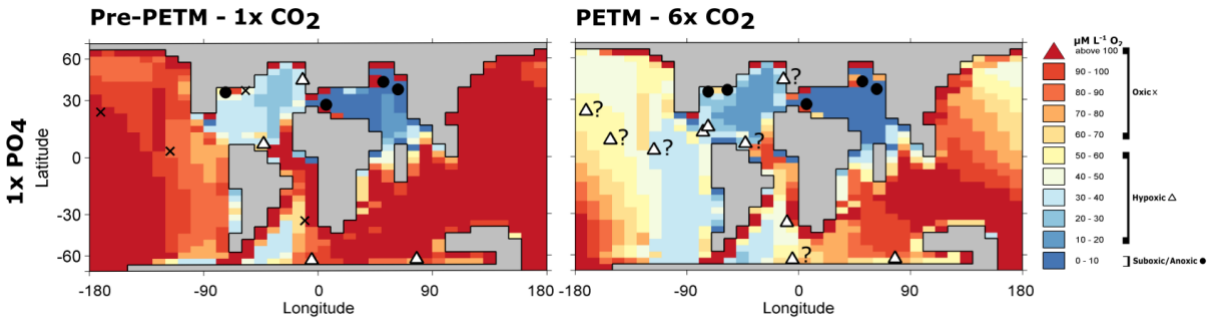

Figure 3.5: cGENIE model result for the best fit conditions for both before and during the PETM plotted with evidence for oxia (cross), hypoxia (triangle) and anoxia (circle). The best model-data fits were achieved under 1x pre-industrial CO_2 values (1x CO_2) and 6x pre-industrial CO_2 values (6x CO_2) in the model.

3.4. Discussion

Our model-data comparison indicates that the Tethys Sea and North Atlantic Ocean both experience hypoxia to suboxia (Figure 3.5), even during pre-PETM conditions. While anoxia/suboxia seems to be restricted to the Tethys Sea before and during the PETM, hypoxia spread from the North Atlantic Ocean and some part of the South Atlantic Ocean to the Eastern Pacific Ocean. According to our reconstruction across the PETM, hypoxia rose by 15% to reach 27% of the global ocean volume and anoxia/suboxia rose by 2% to reach 4% of the global ocean volume (from 1 to 6 x CO_2 forcings in the model). Our Cr isotope and concentration records are different both stratigraphically and in absolute values at the three sites and suggest a local redox control. Therefore, variations in $\delta^{53}Cr$ values do not necessarily represent a global signal. We suggest that a range of mechanisms were responsible for the differences in the $\delta^{53}Cr$ records between the sites, which we will explore in further detail in the following sections.

Published seawater data shows that modern seawater $\delta^{53}Cr$ measurements are distributed within the range of 0.1-1.8‰ with a median value of 1.2‰ (Bonnand et al., 2013; Scheiderich et al., 2015; Economou-Eliopoulos et al., 2015; Pereira et al., 2016; Paulukat et al., 2016; Holmden et al., 2016; Goring-Harford et al., 2018). Less oxygenated waters are expected to have a heavier $\delta^{53}Cr$ due to partial isotopic fractionation under more reducing conditions (Ellis et al., 2002). The $\delta^{53}Cr$ values for the PETM at Site 1210 fall within the oxic and hypoxic range (Goring-Harford et al., 2018). Peak Cr isotope values at Sites 401 and 1263 are higher than the modern range for oxic and hypoxic seawater. We assume this implies that Sites 1263 and 401 might yield Cr isotope values that can be interpreted as reflecting hypoxic-anoxic conditions during the PETM, whereas the Pacific recorded minor deoxygenation within the upper bounds of modern oxic seawater. These findings are consistent with Ce anomalies which suggest the North Pacific remained oxic in contrast to the North and South Atlantic (Figure 3.3).

3.4.1. Deoxygenation through ocean circulation changes

A switch to warmer, more corrosive and less oxygenated intermediate waters at Walvis Ridge in the South Atlantic as postulated by Lunt et al. (2010) can explain the correlation between $\delta^{53}Cr$, [Cr], the CF record (generated for this study and in agreement with the higher-resolution CF record by Kelly et al. (2010)), and the intensified carbonate dissolution this represents (Figure 3.3). While there is no agreement about the circulation switch (e.g. Nunes and Norris, 2006; Alexander et al., 2015), it is thought that during the latest Palaeocene, deep ocean formation in the Southern Ocean decreased while a new circulation cell developed in the North Pacific (Tripati and Elderfield, 2005). During the PETM an abrupt switch to North Pacific convection and a salinity-stratified ocean occurred leading to substantial warming of intermediate and deep waters (Tripati and Elderfield, 2005; Lunt et al., 2010). Additional evidence for fundamental changes in intermediate and deep-water circulation during the

latest Palaeocene and PETM comes from Nd isotopes that suggest changes in deep-water circulation started prior to PETM warmth (Abbott et al., 2016). Model simulations of bottom water circulation during the PETM show that corrosive bottom waters built up in the North Atlantic and flowed to the South Atlantic during the PETM (Alexander et al., 2015). This is, however, in disagreement with the Nd isotope data, which suggests a more limited exchange of waters between ocean basins (Abbott et al., 2016). The warming of South Atlantic intermediate and deep waters would trigger a reduction in oxygen concentrations and could provide an explanation for the response in Cr isotopes. The extraordinarily high $\delta^{53}Cr$ at Site 1263 (~ +3.5‰) can be partly attributed to partial reduction associated with the expansion of a major oxygen minimum zone off the West-African coast into intermediate waters as suggested by Mn and U enrichment factors (EF; Chun et al., 2010). Unlike the Mn_{EF} and U_{EF} at Site 1263 (Chun et al., 2010) and our Ce/Ce* results (Figure 3.2), the $\delta^{53}Cr$ record at Site 1263 does not provide any evidence for hypoxia prior to or after the CIE (Figure 3.3) leaving open questions and disagreement with previous studies (Chun et al., 2010; Pälike et al., 2014; Zhou et al., 2016).

The Ce/Ce* at Site 1263 peaks when $\delta^{53}Cr$ values are highest, around 40 kyrs after the onset of the PETM, and subsequently recovers to values indicative of near oxic conditions. The Ce/Ce* record at Site 1263 by Zhou et al. (2016) also peaks approximately 35 kyrs after the CIE at anoxic values. However, our foraminiferal cerium anomalies seem more coherent over the course of the PETM than the Ce/Ce* from fish teeth (Zhou et al., 2016). Geochemical evidence exists for oxic conditions at the nearby deeper Site 1262 (Chun et al., 2010; Zhou et al., 2016), although it is thought transient hypoxia did occur in the carbonate-free interval at Site 1262 (Post et al., 2016). This suggests that deoxygenation mainly occurred at intermediate depths in the South Atlantic, and less so deeper in the water column.

Our model-data comparison and Cr isotope data support oxic bottom water conditions before the PETM at Site 1263 in the South Atlantic (Figure 3.4) in line with a more intense deep convection in the Southern Ocean prior to and after the PETM (Tripati and Elderfield, 2005; Nunes and Norris, 2006; Lunt et al., 2010). Hosing experiments in two climate models (CCSM3 and GENIE) show that stratification can lead to a severe loss of oxygen in the South Atlantic and Indian Oceans (Zhou et al., 2016). Oxic conditions before the PETM are consistent with our Cr isotope data but are in disagreement with trace metal geochemical data (Chun et al., 2010; Pälike et al., 2014; and Zhou et al., 2016). A difference in standard reduction potentials between CrO_4^{2-}, MnO_2, Ce^{4+} and $UO_2(CO_3)_3^{4-}$ may cause this apparent discrepancy.

The smaller magnitude of the $\delta^{53}Cr$ excursion at Site 1210 compared to the other sites (Figure 3.3) indicates less intense deoxygenation in the subtropical Pacific gyre than in the Atlantic Ocean (Figure 3.3). The oligotrophic environment, which would have been increased due to higher stratification during the PETM compared to background, in combination with the position of the $\delta^{53}Cr$ peak within the acme

of warming indicated by benthic $\delta^{18}O$ (Zachos et al., 2003; Tripati and Elderfield, 2005) suggests the $\delta^{53}Cr$ anomaly can be attributed mainly to ocean warming driving decreased oxygen solubility. Our model-data reconstruction also suggests that deoxygenation across the PETM was due to warming resulting from a 3 to 6-fold increase in atmospheric CO_2. It must be noted that alternatively the model is very sensitive to nutrient fluxes and therefore only a small increase in nutrient run-off would create a similar effect. This interpretation would support studies showing increases in weathering (e.g. Ravizza et al., 2001; Gavrilov et al., 2003; John et al., 2008; Dickson et al., 2015) although it is not clear whether the increased run-off, increasing productivity in coastal sites, made it out into the open ocean (e.g. Gibbs et al., 2006; Carmichael et al., 2017). The switch to North Pacific deep-water formation as discussed earlier can explain the more pronounced change in [Cr] than in $\delta^{53}Cr$ during the CIE due to a decreased transport of Cr to the open ocean. Mn_{EF} and U_{EF} support the observation from $\delta^{53}Cr$ and Ce/Ce* that Pacific intermediate waters remained oxic (Pälike et al., 2014). The recovery in $\delta^{53}Cr$ at Site 1210 is rapid as intermediate waters cool.

3.4.2. Evolution of deoxygenation

To pinpoint a source for the introduction of reduced carbon during the PETM it is imperative to assess the timing of deoxygenation occurring at each of the sites. In the Bay of Biscay (DSDP 401), near the proposed site of biogenic methane injection and volcanism, $\delta^{53}Cr$ values become more positive prior to the CIE and peak 9,000 years before the onset of the PETM (Figure 3.3a) and are corroborated by a drop in Cr concentrations. Ce/Ce* attain anoxic values (Ce/Ce* > 1) at the same time approximately 9,000 years before the onset of the PETM (Figure 3.2e). Chromium isotope values in the Pacific (ODP Site 1210) peak 20 kyrs after the CIE onset, during maximum warmth (McCarren et al., 2008; Figure 3.3a). The timing of deoxygenation and response of $\delta^{53}Cr$ at Walvis Ridge cannot be determined due to the severe carbonate dissolution during the onset and main body of the PETM at this site. However, fish teeth Ce/Ce* data from Zhou et al. (2016) along with foraminiferal Ce/Ce* from this study suggest peak anoxia in the South Atlantic occurred approximately 35 - 45 kyrs after the onset of the PETM. Importantly, deoxygenation in the Pacific occurred before that in the South Atlantic as shown by $\delta^{53}Cr$ at Shatsky Rise in the North Pacific and Ce/Ce* at Walvis Ridge in the South Atlantic (Chun et al., 2010; Zhou et al., 2016) making the interpretation of a dissipation of the signal due to circulation impossible. Our model-data comparison reinforces previous suggestions that anoxia developed more easily in the Tethys Sea and Atlantic Ocean than in the Pacific Ocean during the PETM (Chun et al., 2010; Pälike et al., 2014; Zhou et al., 2016) with conditions of anoxia and hypoxia present in these basins even under pre-PETM conditions. However, our model-data comparison (Figure 3.5) shows that during the PETM the Pacific Ocean experienced some deoxygenation reaching oxic-hypoxic conditions in the North Pacific Ocean and hypoxia in the eastern Pacific Ocean.

However, one must approach the relative timings between the C, Cr, and Ce excursions with some caution. In DSDP Site 401, Cr isotopes and concentrations, as well as Ce/Ce* show changes prior to the carbon excursion. Chromium concentrations at ODP Site 1210 and ODP Site 1263 also drop prior to the CIE which defines the PETM. This may be due to environmental changes in the lead up to the PETM but can also have been caused by the burndown of carbonate associated with the CIE. Due to this carbonate burndown it is also difficult to establish when exactly Cr isotopes reached peak values at DSDP Site 401 and ODP Site 1263. The highest Cr isotope and Ce/Ce* values at ODP Site 1263 occur around 50 kyrs after the onset of the CIE which is concurrent with the maximum extent of the CIE (Figure 3.3). At ODP Site 1210, the Cr isotope excursion and Ce/Ce* values peak approximately concurrently with the CIE at 20 kyrs after the onset of the CIE. Extrapolating this to DSDP Site 401 would place the maximum Cr isotope excursion at around 20 kyrs after the onset of the CIE.

Location	Method	Pre-PETM	PETM	Post PETM
DSDP Site 401 Bay of Biscay (North Atlantic)	**Ce/Ce***	Hypoxic	Anoxic	Anoxic
	δ^{53}Cr	Oxic	Hypoxic Anoxic	Oxic?
	cGENIE	Oxic	Hypoxic	-
	$^{\dagger}Mn_{EF}$ and U_{EF}	Less oxic	Less oxic	Less oxic
ODP Site 1210 Shatsky Rise (Pacific)	**Ce/Ce***	Oxic	Oxic	Oxic
	δ^{53}Cr	Oxic	Oxic	Oxic
	cGENIE	Oxic	Oxic	-
	$^{\dagger}Mn_{EF}$ and U_{EF}	Oxic	Oxic	Oxic
ODP Site 1263 Walvis Ridge (South Atlantic)	**Ce/Ce***	Hypoxic	Anoxic	Hypoxic
	δ^{53}Cr	Oxic	Hypoxic Anoxic	Oxic
	cGENIE	Oxic	Hypoxic	-
	$^{\dagger}Mn_{EF}$ and U_{EF}	Less oxic	Less oxic	Less oxic

Table 3.1 Summary of findings for the palaeo-redox state of the bottom waters at intermediate water depths during the PETM at DSDP Site 401, ODP Sites 1210 and 1263. Interpretations of the redox state are based on Ce/Ce* and δ^{53}Cr results from this study, cGENIE model-data comparison results from this study. $^{\dagger}Mn_{EF}$ and U_{EF} results are from Pälike et al. (2014). Since oxygenation regimes (oxic, hypoxic, suboxic, anoxic) are not defined in Pälike et al. (2014), 'suboxia' is reinterpreted here as 'less oxic'.

Comparing the published evidence for bottom water palaeo-redox conditions during the PETM with the findings from this chapter for proxy systems with different sensitivities to changes in redox state (Table 3.1). allows for a more detailed view on the development of deoxygenation through assessing the degree of hypoxia of seawater. As previously mentioned in section 3.1, Ce and Cr are sensitive to speciation changes in the transition between fully oxidising and reducing conditions at Eh values of 0 and 0.3-0.4,

respectively. Speciation changes occur in the transition area (Eh ~ 0.3-0.4) for Mn and in fully reducing conditions (Eh ~ -0.1) for U. Overall, the different redox proxies and cGENIE agree that deoxygenation occurred to a higher degree in the Atlantic than the Pacific Ocean (Table 3.1). However, in detail these proxies display complex behaviour in the Atlantic. In contrast to Cr isotopes, Mn and U EF, and Ce/Ce* show degrees of deoxygenation prior to and after the main warming event of the PETM. This likely signifies that under environmental conditions Cr is less sensitive to redox changes than other redox proxies. In addition, dissolved oxygen levels before and after the PETM were therefore closer to oxic conditions in the transitional environment between fully oxidising and reducing conditions (Brookins, 1988) classified as 'hypoxic' in this thesis, whereas hypoxic-anoxic conditions occurred during the PETM itself. The full extent of deoxygenation during the PETM is difficult to gauge using Eh-pH diagrams as these only indicate boundaries between oxic, hypoxic, and anoxic conditions.

3.4.3. Temperature control on open ocean deoxygenation

Comparing the maximum excursion size in $\delta^{53}Cr$ at the onset of the PETM against the maximum carbon and benthic oxygen isotope excursions (CIE and OIE, respectively) illustrates that the size of the carbon cycle perturbation does not appear to have an impact on the size of the $\delta^{53}Cr$ signal (Figure 3.6). In contrast, a positive correlation is found with the magnitude of the benthic OIE, implying that warming exerts significant control on the size of the $\delta^{53}Cr$ perturbation and by extrapolation over the expansion of open ocean low-oxygen environments during the Late Palaeocene – Early Eocene. Converting the benthic OIE into temperature-associated dissolved oxygen loss (Broeker and Peng, 1982) shows that thermal effects account for a loss of -13.0 to -32.7 µmol/kg O_2 at the study sites which by itself is not enough to produce hypoxia. These are likely upper estimates, since the maximum test size of planktic foraminifera may have increased by up to 150 µm during the PETM depending on the foraminiferal species although overall decreases in test size have also been reported (Kaiho et al., 2006; Petrizzo, 2007; Alegret et al., 2010). Based on Chapter 2, the change in $\delta^{53}Cr$ composition associated with the increase in foraminiferal test size and assemblage could account for a maximum of +0.1‰ to +0.3‰ of the Cr isotope signal during the PETM depending on the test shape if a test increase is assumed. However, size changes in the foraminiferal assemblage have not yet been quantified and likely the response of test size to warming is species-dependent. Warming will have additionally increased microbial metabolic rates (Pörtner et al., 2014). It has been suggested that the open ocean experienced increasing oligotrophy during the PETM (Gibbs et al., 2006).

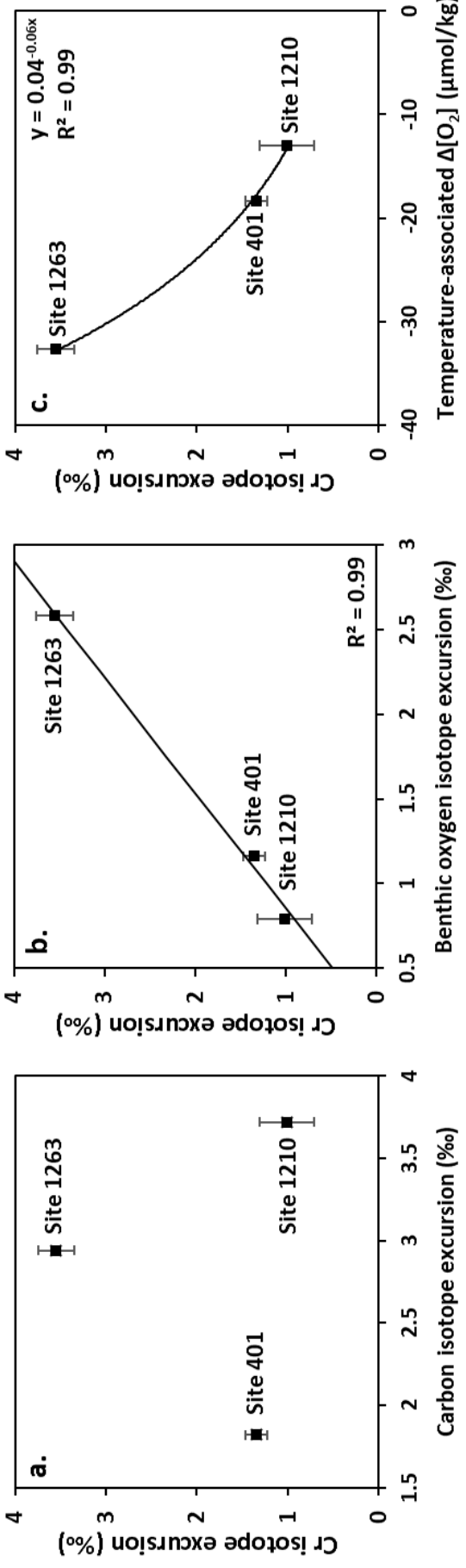

Figure 3.6: The Cr isotope excursion size does not correlate with CIE of organic carbon (Zachos et al., 2003; Zachos et al., 2005; Nunes and Norris, 2006) (a), but strongly correlates with the benthic oxygen isotope excursion (Nunes and Norris, 2006; McCarren et al., 2008; Westerhold et al., 2011) (b). The oxygen isotope excursion is translated into temperature-associated dissolved oxygen loss by following Broecker and Peng (1982) (c).

This, however, would not necessarily imply less biological and biogeochemical activity (Ma et al., 2014). In combination with increased metabolic rates and more extensive remineralisation, a constant or even decreasing primary productivity in the open ocean could have resulted in amplifying deoxygenation associated with warming of the ocean through increased export productivity. We suggest that warming of intermediate waters was one of the principal drivers of deoxygenation during the PETM with the scale of warming (~5 degrees Celsius; Dunkley-Jones et al., 2013) producing wide-spread hypoxia throughout the North and South Atlantic. Our findings align with modern observations that warming is a major controlling factor on open ocean deoxygenation. The extent of deoxygenation during the PETM shows that rapid temperature increases have caused wide-spread open ocean hypoxia in the past and that future oceans may also experience wide-spread deoxygenation due to anthropogenic global warming.

3.4.4. Orbital cyclicity recorded by Cr concentrations

Precession of the Earth's axis causes variations in seasonality and therefore may have driven differences in run-off due to a seasonally accelerated hydrological cycle. The lack of change in the Cr isotopic record can only be explained if there is no change in the isotopic composition of the source material and if the enhanced Cr input induced by precession cycles does not promote ocean deoxygenation. Precession cycles 1, 2, and 3 occurred during the main body of the PETM and we expect environmental change associated with the carbon perturbation to have masked the orbital signal in the record. Precession cycle 5 at the end of the $\delta^{13}C$ recovery from the PETM is missing in the Cr record as well and may be due to a 100-kyr eccentricity minimum occurring around this time (Röhl et al., 2007; Laskar et al., 2011). An eccentricity minimum would diminish an increase in seasonality caused by a precession maximum. This is corroborated by the small variation in Fe and Ba intensities across cycle 5 (Röhl et al., 2007).

A lack of orbitally controlled Cr concentrations at DSDP Site 401 in the Bay of Biscay can be attributed to its more restricted location compared to ODP Sites 1210 and 1263. It is likely that low-oxygen environments may have persisted after the PETM (Table 3.1) and that this site experienced a return to more eutrophic conditions (Tremolada and Bralower, 2004). Chromium concentrations would therefore have been affected by a strong redox-controlled removal flux suppressing any orbital variations. The indication by Ce/Ce*, Mn_{EF} and U_{EF} that very low oxygen concentrations persisted and may have intensified after the PETM is contradicted by the $\delta^{53}Cr$ record for DSDP Site 401. These light and apparently 'oxic' values may have been caused by the effective removal of Cr through quantitative reduction which has been proposed for past negative Cr isotope excursions (Reinhard et al., 2014; Wang et al., 2016) and has been invoked as an explanation for relatively light $\delta^{53}Cr$ values in anoxic waters of the modern-day Black Sea (Goring-Harford et al., 2017).

3.5. Conclusions

This study shows that foraminiferal $\delta^{53}Cr$ across the PETM is controlled by local factors contributing to seawater deoxygenation, which is in line with the heterogeneity of Cr in modern oceans and its comparatively short residence time. Our model output indicates that deoxygenation was widespread throughout the global oceans during the PETM, while our Cr datasets add valuable information on local variation in bottom water deoxygenation. We attribute the deoxygenation mainly to rising temperatures in intermediate ocean waters due to higher atmospheric CO_2, based on the strong correlation between the magnitude of the benthic oxygen isotope and the chromium isotope excursions. Warmer intermediate waters, an increased microbial loop and remineralisation, and declines in oxygen solubility jointly are suggested to have caused the lower oxygen concentrations. If any geographical spreading of deoxygenation occurred, it appears to have originated in the North Atlantic (Site 401), in line with evidence for this basin having been proximal to the location of injection of reduced carbon (Svensen et al., 2004). Chromium isotope values and Ce anomalies at Site 1210 indicate this site may have been less impacted by deoxygenation than the two Atlantic sites.

Chapter 4

A critical assessment of deoxygenation through deep time using chromium isotopes in carbonates

Author contributions and declaration: Dr I.J. Parkinson and Professor D.N. Schmidt provided supervision and advice on the design and execution of the study. Dr B.D.A. Naafs (School of Chemistry, University of Bristol), and L. O'Connor, Dr S. Batenburg, Dr S.A. Robinson and Professor H.C. Jenkyns (Department of Earth Sciences, University of Oxford) provided samples from OAE1a and the Plenus Marls (OAE2), respectively. The International Ocean Discovery Program provided foraminiferal samples from ETM2. Professor G.-J. Reichart (Department of Earth Sciences, Utrecht University) provided foraminiferal samples from MIS6. ICP-MS data was acquired and processed with assistance of Dr S. Hammond (School of Environment, Earth & Ecosystems, The Open University) at the Open University. All MC-ICP-MS data has been acquired and processed by S.R.C. Remmelzwaal.

Abstract

The recent expansion of oxygen minimum zones caused by anthropogenic global warming raises questions about the scale of this expansion with different emission scenarios. In this chapter, past climate warming events were used to quantify a potential link between warming and the spread of oxygen minimum zones during four main climatic events: Ocean Anoxic Event (OAE) 1a and OAE 2 in the Cretaceous, the Palaeocene-Eocene Thermal Maximum (PETM), the Eocene Thermal Maximum 2 (ETM-2) in the Palaeogene and the Pleistocene glacial-interglacial cycles. The proxy of chromium isotopes ($\delta^{53}Cr$) were applied to planktic foraminifera from the Cenozoic and bulk carbonate from the Mesozoic to assess redox changes during these periods. Both $\delta^{53}Cr$ and chromium concentrations respond markedly during the Eocene hyperthermals suggesting a reduction in dissolved oxygen concentrations caused by warming and changes in ocean ventilation. A strong correlation between the excursion size of $\delta^{53}Cr$ and the benthic oxygen isotope excursion during the Cenozoic suggest temperature changes to be one of the main drivers of ocean deoxygenation in the past. This correlation does not hold for the Cretaceous OAEs. This finding suggests a potential difference in the climate background state of the Cretaceous lead to different deoxygenation mechanisms and Cr behaviour.

4.1. Introduction

Anthropogenically emitted greenhouse gasses have been accumulating in the atmosphere since the Industrial Revolution and have caused warming of the atmosphere and oceans (Stocker et al., 2013). In response, oceanic dissolved oxygen concentrations have been on a steady decline over the past half century and oxygen minimum zones (OMZs) have expanded both in geographic and bathymetric extent (Stramma et al., 2008). The current deoxygenation of the oceans is directly coupled to a rise in temperature through a decreased solubility of oxygen in water under higher temperatures (e.g. Schmidtko et al., 2017). This process is further accelerated by an increase in remineralisation of organic matter and in the metabolic rates of heterotrophic microbes which consume oxygen (Keeling et al., 2010). Additionally, increased nutrient delivery, circulation changes, stratification, as well as oxidation of reduced carbon such as methane hydrates can also impact the extent and local intensity of deoxygenation (Keeling et al., 2010). The links between these processes and which of these are the key to understanding deoxygenation on longer geological time-scales are still unclear. To better assess the relationships between deoxygenation and environmental change, I propose here to assess long-term hypoxia during extreme climate events over the course of the geological past.

A multitude of natural climatic events have taken place over the course of Earth's history. These events span a wide range of magnitudes and time-scales from global perturbations during the Cretaceous, the so-called ocean anoxic events, through transient Palaeogene hyperthermals to glacial-interglacial cycles.

Ocean Anoxic Events (OAEs) are often associated with sediments rich in organic matter ("black shales") typified by globally increased carbon burial (Schlanger and Jenkyns, 1976; Jenkyns, 1980). Numerous of these events have been identified of which most occur in the Cretaceous (Jenkyns, 2010) and one during the Jurassic (Early Toarcian OAE [T-OAE] or Posidonienschiefer (Jenkyns, 2010)). Schlanger and Jenkyns (1976) originally explained the formation of OAEs by the Mid-Late Cretaceous transgression leading to an increase in the areal extent of highly productive epicontinental and marginal seas and an increase in carbon burial (Schlanger and Jenkyns, 1976). Schlanger and Jenkyns (1976) also proposed that the greenhouse climate of the Cretaceous slowed down deep-water formation and led to less-oxygenated bottom waters and expanded OMZs. As these OAEs are often associated with large-scale volcanic activity (e.g. Weissert and Erba, 2004; Jenkyns, 2010; Holmden et al., 2016) today's interpretation links Large Igneous Province (LIP) volcanism and/or methane hydrates to abrupt temperature rises through rapid CO_2 emissions into the atmosphere (Jenkyns, 2010). In turn, higher temperatures induced an enhanced hydrological cycle and increased nutrient delivery into the oceans boosting primary productivity leading to increased carbon burial (e.g. Pedersen and Calvert, 1990). An

alternative hypothesis to explain the deposition of high C_{org}-sediments is an increased preservation due to the inhibiting effect of intensified oceanic anoxia on degradation of organic matter (e.g. Bralower and Thierstein, 1984; Tyson, 2001).

Palaeogene hyperthermals have been termed 'failed OAEs' and are thought to have been initiated by volcanic or methane injection processes similar to those at the onset of OAEs (e.g. Jenkyns, 2010; Gutjahr et al., 2017), while others suggest these hyperthermals were a series of events potentially linked through orbital cyclicity and therefore different to OAEs in their initiation mechanisms (e.g. Deconto et al., 2012; Zeebe, 2013). The Palaeogene hyperthermals occurred during a greenhouse climate, much like the Mesozoic OAEs (e.g. Littler et al., 2014; Lauretano et al., 2015). These hyperthermals were superimposed on a long-term warming trend leading to the Early Eocene Climatic Optimum (EECO) and are primarily recognised by major negative shifts in the $\delta^{18}O$ and $\delta^{13}C$ stable isotope records associated with elevated temperatures and an injection of light carbon, respectively. The hyperthermals are smaller perturbations compared to the OAEs (e.g. Jenkyns, 2010). The well-researched hyperthermals of the PETM and ETM2 are thought to be similar in climate response to the OAEs, but the trigger of these environmental changes remains contested (e.g. Lourens et al., 2005; Deconto et al., 2012; Gutjahr et al., 2017).

A main difference between the Cretaceous and the Cenozoic climates are the higher sea levels which flooded the continental margins and led to epicontinental seas in the Cretaceous. The wide-spread shallow seas of the Cretaceous facilitated low-oxygen environments since shallow seas are generally warmer and experience high primary productivity (Schlanger and Jenkyns, 1976). A second key difference between the Cretaceous and the Cenozoic is the effectiveness of ocean circulation. Due to a different continental configuration and warmer overall temperatures ocean circulation was likely less vigorous during the Cretaceous which would also have aided in the establishment of large anoxic and hypoxic areas in the ocean (Schlanger and Jenkyns, 1976). Where this may not have triggered OAEs per se, it may have created an environment more prone to anoxia during periods of climatic instability than seen in the Cenozoic. This suggestion is not supported by ocean models, however, which suggest ocean circulation recovers rapidly after an initial slowing down of circulation due to surface ocean stratification (Monteiro et al., 2012).

While studies comparing climatic events have focussed on the size of the carbon perturbation and direct effects of a large carbon injection such as ocean acidification (Ridgwell and Schmidt, 2010; Hönisch et al., 2012; Penman et al., 2014), comparatively few studies have compared local deoxygenation responses to look for common mechanisms between thermal events and have tended to investigate these events in isolation (e.g. Pancost et al., 2004; Meyer and Kump, 2008; Jenkyns, 2010; Monteiro et al., 2012; Dickson et al., 2012; Dickson et al., 2014).

Past redox conditions have been reconstructed using a plethora of proxies including the composition of the sediment (e.g. organic carbon content; Schlanger and Jenkyns, 1976), inorganic geochemical techniques (rare earth element patterns, trace metal concentrations, and redox-sensitive isotope systems such as V, Cr, Mo, U), organic geochemical compounds (e.g. isorenieratane; Sinninghe Damsté and Köster, 1998), and micropalaeontological parameters (e.g. benthic foraminiferal accumulation rates, ostracod abundance; Herguera, 2000; Yamaguchi and Norris, 2012). All these proxies have different sensitivities to changes in redox state and have their own specific drawbacks which often lead to local environmental settings overwhelming a global signal (e.g. Dickson et al., 2014). The search for a truly global redox proxy is still ongoing with uranium isotopes currrently one of the most promising contenders (Romaniello et al., 2013; Zhang et al., 2018) . A direct comparison between different climate events is thus complicated by the wide range in proxies and environmental settings used in studies of past deoxygenation episodes. One might expect marked differences in drivers of ocean deoxygenation between climate events in the Mesozoic and the Cenozoic due to dissimilarities in the background climate state, continental configuration, and strength of ocean ventilation. For a more meaningful comparison, samples from similar settings should be analysed with the same proxy method. In this chapter, I use Cr isotopes from carbonate successions deposited in intermediate water depths in both marginal seas and the open ocean during several time intervals characterised by severe climatic perturbations.

4.1.1. Chromium isotopes as a redox proxy

Chromium isotopes have been in the spotlight of the geochemical community over the past years due to the potential of the proxy to elucidate the redox state of the palaeo-oceans (e.g. Bonnand, et al., 2013; Reinhard et al., 2014). Chromium (Cr) exists in multiple valence states in the natural environment and is therefore sensitive to changing redox conditions. In seawater, Cr occurs predominantly as the Cr(III) or Cr(VI) species, with Cr(VI)-oxyanions the more dominant species under well-oxygenated conditions (Cranston and Murray, 1978). Under less oxygenated conditions Cr(VI) is reduced to insoluble Cr(III) which acts as a sink of dissolved Cr and results in lower dissolved Cr concentrations. There are four stable Cr isotopes of which the deviation in the $^{53}Cr/^{52}Cr$ ratio is compared to NIST SRM979 and is expressed as $\delta^{53}Cr_{SRM979}$, where $\delta^{53}Cr_{SRM979} = 1000*[(^{53}Cr/^{52}Cr)_{sample} - (^{53}Cr/^{52}Cr)_{SRM979}] / (^{53}Cr/^{52}Cr)_{SRM979}$. During the reduction of Cr, a substantial isotope fractionation of up to 7‰ occurs (Ellis et al., 2002). The isotopic composition of chromium in modern seawater is heterogeneous and varies between 0.1 – 1.6 ‰, which is partly caused by a relatively short residence time of approximately 3,000 years (Paulukat et al. 2016; Qin and Wang, 2017). There is a negative correlation between [Cr] and $\delta^{53}Cr$ in seawater (Scheiderich et al., 2015; Paulukat et al., 2016) which is likely due to partial reduction of Cr(VI) in surficial seawater and oxygen minimum zones and Cr(III) re-oxidation in bottom waters (Scheiderich et al., 2015).

Experimental data show Cr(VI) is incorporated into carbonate lattices (Tang et al., 2007; Bonnand et al., 2013) as a chromate ion which enables us to use marine carbonates as an archive of seawater Cr. Recent work into the Cr isotopic composition of foraminifera revealed that Cr in planktic foraminifera is primarily acquired after deposition on the seafloor (Chapter 2). However, some Cr is still incorporated during calcification. Therefore, foraminiferal Cr will predominantly record bottom and/or pore water conditions (Chapter 2). Questions around the empirical relationship between $\delta^{53}Cr$ and $[O_2]$ as well as potential dissolution effects remain unanswered, although measurements of oxygen concentrations and Cr isotopes from the same seawater samples have recently been made (Goring-Harford et al., 2018). We therefore interpret $\delta^{53}Cr$ data merely as a qualitative indicator of bottom and pore water ocean deoxygenation.

Previous work on Cr isotope anomalies during the PETM shows a correlation between the benthic water temperature and the magnitude of the observed chromium isotope anomaly (Chapter 3). Additional processes, such as increased biological activity and remineralisation, are needed to reach the levels of hypoxia seen during the PETM. In this chapter, the response of local deoxygenation during of a variety of past climate perturbations is compared using the redox proxy of $\delta^{53}Cr$ derived from carbonates. While carbonate $\delta^{53}Cr$ has been applied to several climatic events before (e.g. the last glacial maximum and Ocean Anoxic Event 2; Reinhard et al., 2014; Wang et al., 2016; Holmden et al., 2016), the responses of Cr during these events have not been compared to each other. The aim is to shed light on the contribution of different potential controls on ocean deoxygenation during periods of drastic climate change in both the greenhouse worlds of the Palaeogene and Cretaceous as well as the icehouse world of the Pleistocene. I assess the magnitude of the chromium isotope excursion and compare this to the temperature anomaly as well as the carbon perturbation associated with the climate event.

4.2. Descriptions of studied climatic events

The multifarious time intervals discussed in this chapter occupy a wide range of magnitudes, background climate states and potential triggers. Therefore, a brief introduction to each event is given below to highlight the differences and similarities in climatic perturbation and the reaction of oceanic dissolved oxygen concentrations between the Mesozoic OAEs, the Palaeogene hyperthermals, and the Pleistocene glacial-interglacial cycles. The following events are discussed in chronological order in this chapter: OAE1a (120 Ma), OAE2 (94 Ma), the PETM (56 Ma), the ETM-2 (54 Ma), and MIS6 (0.15 Ma) during the glacial-interglacial cycles.

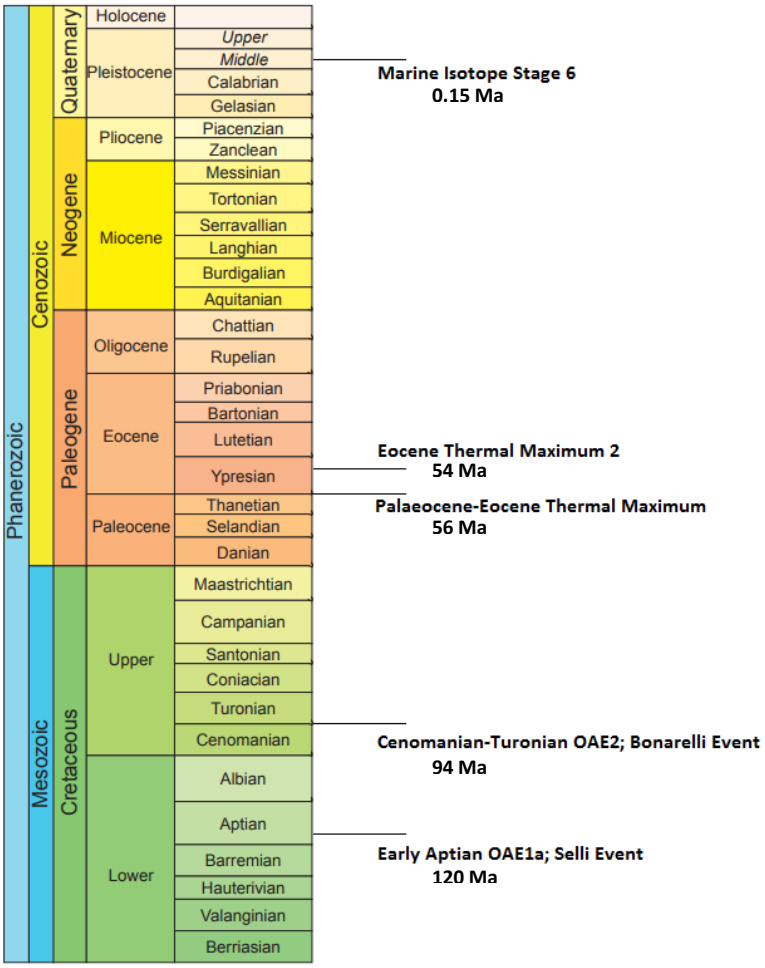

Figure 4.1: The climatic events studied in this chapter marked on the chronostratigraphic chart after Gradstein et al. (2012).

4.2.1. The Selli Event (Ocean Anoxic Event 1a)

Ocean Anoxic Event 1a, also known as the Selli Event from its first identification in Italy (Coccioni et al., 1987; Arthur et al., 1990), occurred during the Early Aptian about 120.21 –to 119.11 Ma and lasted for approximately 1 to 1.3 Myrs (Jenkyns, 2010). Ocean anoxic Event 1a is characterised by a widespread occurrence of sediments rich in organic matter (Jenkyns, 2010), rapid biotic turnovers (e.g. Erba, 1994, 2004), as well as a distinct carbon isotope excursion (CIE; e.g. Ando et al., 2002; Ando and Kakegawa, 2007). Together with the OAE2 around 94 Ma, the Selli Event is thought to be one of the most intense OAEs ever recorded and probably one of the most dramatic climatic events of the last 250 Myrs (Jenkyns, 2010). The exact mechanism that triggered the Selli Event is not fully understood. The current accepted mechanism is that LIP volcanism tied to the emplacement of the Ontong-Java Plateau introduced large quantities of light carbon into the ocean and atmosphere leading to the observed negative CIE at the onset of the event (e.g. Arthur et al., 1985; Tejada et al., 2009; Bottini et al., 2012; Gomes et al., 2016; Méhay et al., 2009; Naafs et al., 2016), although the destabilisation of methane hydrates may also have played a role (Jahren et al., 2001; Beerling, 2002). Carbon dioxide levels doubled from background Early Cretaceous values of roughly 800-1200 ppmv to 1400-2800 ppmv

during the event itself (Naafs et al., 2016). Observations of sea surface temperatures suggest an accompanying rise of 4-8°C during the Selli Event (Ando et al., 2008; Mutterlose et al., 2014).

After the rapid initial negative CIE (27-44 kyrs; Li et al., 2008), a pronounced positive CIE during the main body of and recovery from the event which has been attributed to enhanced carbon burial (e.g. Weissert, 1981; Gomes et al., 2016). Increased carbon burial is thought to have been caused by higher primary productivity through increased nutrient cycling (e.g. Tejada et al., 2009; Föllmi, 2012), as well as increased preservation of deposited organic matter due to hypoxic-anoxic conditions on the seafloor (Jenkyns, 2010).

4.2.2. The Bonarelli Event (OAE2)

The Bonarelli Event (OAE2) at the Cenomanian-Turonian boundary (~94 Ma) lasted approximately 440 kyrs. Tropical sea-surface temperatures reached 33-42°C (e.g. Jenkyns et al., 1994; Norris et al., 2002; Bice et al., 2006; Forster et al., 2007; Jenkyns, 2010; Ogg and Hinnov, 2012). Ocean Anoxic Event 2 is characterised by a positive CIE caused by enhanced organic matter burial (Kolonic et al., 2005; Sageman et al., 2006; Kuroda et al., 2007; Jarvis et al., 2011; Pogge von Strandmann et al., 2013). Atmospheric CO_2 levels were potentially extremely high prior to OAE2 (500-3300 ppmv) and probably increased due to extensive volcanism associated with the large igneous provinces developing in the Caribbean, Arctic and Madagascar (e.g. Sinninghe Damsté et al., 2010; Hay, 2011; Jarvis et al., 2011; Jenkyns et al., 2017; Dickson et al., 2017). Warming temperatures are thought to have increased weathering and hence the nutrient supply from the land to the ocean enhanced marine primary productivity which would have sustained bottom-water hypoxia/anoxia (e.g. Monteiro et al., 2012; Clarkson et al., 2018). Hypoxic and anoxic conditions were already present prior to OAE2 on the seafloor of many ocean basins (e.g. Schlanger et al., 1987; Sinninghe Damsté and Köster, 1998; Tsikos et al., 2004; Forster et al., 2007; Takashima et al., 2011) and have been attributed to limited deep-water formation in the proto-North-Atlantic Ocean and an enclosed basin (Monteiro et al., 2012). During the event, seafloor anoxia spreaded to most ocean basins (Monteiro et al., 2012). Climate model-data reconstructions and U-isotope studies of OAE2 estimate low-oxygen conditions expanded to approximately 50% and 8 – 15% of the ocean's volume during the peak of OAE2, respectively (Monteiro et al., 2012; Clarkson et al., 2018).

High organic carbon burial rates have been proposed as a mechanism to draw down significant amounts of CO_2 from the atmosphere causing transient cooling events (also known as 'hypothermals') during OAE2 (Arthur et al., 1988; Freeman and Hayes, 1992; Kuypers et al., 1999; Jarvis et al., 2011; Jenkyns et al., 2017). The Plenus Cold Event (PCE) is one of such hypothermals during OAE2 (Jefferies, 1961, 1963; Gale and Christensen, 1996). The PCE occurs in two cool pulses as can be observed in both temperature (e.g. Van Helmond et al., 2014) and $\delta^{13}C$ records (Erbacher et al., 2005; Voigt et al., 2008;

Jarvis et al., 2011). An incursion of boreal fauna is supported by a drop in SSTs around 4°C with amplification in the north Atlantic to up to 11°C (Forster et al., 2007; Sinninghe Damsté et al., 2010; Van Helmond et al., 2013, 2015). Jenkyns et al. (2017) suggest colder and more oxygenated water spread from the proto-North Atlantic towards the South.

4.2.3. The Palaeocene-Eocene Thermal Maximum

The PETM is the largest of a series of extreme ephemeral warming events during the Palaeogene (e.g. Cramer et al., 2003) about 56 million years ago (Westerhold et al., 2009). During the PETM the climate warmed in a minimum of 4,000 years (Zeebe et al., 2016) by approximately 5-6°C (Dunkley Jones et al., 2013). The elevated temperatures lasted for about 200 kyr into the Eocene (Röhl et al., 2007). The cause of the carbon isotope excursion (CIE) towards light carbon isotope values is subject to heavy debate including the injection of biogenic methane into the ocean-atmosphere system (e.g. Svensen et al., 2004) and the resulting warming leading to the disassociation of methane hydrates (e.g. Lunt et al., 2010). Recent work also suggested a large injection of relatively heavy carbon by massive volcanism in the North Atlantic may have been the main driver and was subsequently amplified by organic carbon feedbacks (Gutjahr et al., 2017).

Ocean deoxygenation during the PETM has been attributed to a number of phenomena including warming of the oceans, increased continental run-off, sluggish ocean ventilation, and the oxidation of a large body of methane injected at the onset of the PETM (e.g. Lunt et al., 2010; Nicolo et al., 2010; Dickson et al., 2012; Pälike et al., 2014; Jennions et al., 2015). Oxygen-deficient bottom waters were widespread in marginal seas (e.g. Dickson et al., 2014) and oxygen minimum zones expanded in more open ocean settings (Chun et al., 2010; Pälike et al., 2014; Zhou et al., 2016; Carmichael et al., 2017; Chapter 3).

4.2.4. The Eocene Thermal Maximum 2

The second-largest Palaeogene hyperthermal is the Eocene Thermal Maximum 2 (ETM2) which occurred ~54 Ma (Littler et al., 2014; Lauretano et al., 2015). Like the PETM, the ETM2 has been globally recognised in both marine and terrestrial sections (e.g. Lourens et al., 2005; Abels et al., 2012; D'haenens et al., 2012; Dedert et al., 2012; Slotnick et al., 2012; Jennions et al., 2015). The carbon perturbation was about half the size of that of the PETM (McCarren et al., 2008; Stap et al., 2009; Jennions et al., 2015) and lasted approximately 100 kyrs (Stap et al., 2009). The carbon perturbation caused bottom water temperatures globally to rise by 3-4°C (Stap et al., 2010). The response of the ocean's oxygen concentrations to the temperature and carbon perturbations during the ETM2 was likely limited in comparison to the PETM because of the absence of wide-spread benthic foraminiferal extinctions (Jennions et al., 2015). However, Jennions et al. (2015) suggested that the benthic

foraminiferal assemblages in the South Atlantic indicate increasingly oligotrophic conditions in bottom waters. Due to the warming and associated change in ocean circulation (D'Haenens et al., 2014; Jennions et al., 2015), enhanced biological reaction rates in combination with potential increased remineralisation of organic matter (e.g. Jenkyns, 2010; Ma et al., 2014; Pörtner et al., 2014; Jennions et al., 2015; Arreguín-Rodríguez et al., 2016) may have led to bottom water oligotrophy and deoxygenation in the South Atlantic. Evidence for oligotrophy has also been found for sites in the NE Atlantic (D'Haenens et al., 2012; Arreguín-Rodríguez et al., 2016). So far, there is no geochemical or sedimentological evidence for hypoxia during the ETM2.

4.2.5. The Pleistocene of the Arabian Sea

At present, the Arabian Sea is the location of one of the most intense OMZs in the world with dissolved oxygen concentrations reaching values lower than 2 μM (Van Bennekom and Hiehle, 1994). Strong seasonal monsoon winds cause upwelling promoting plankton blooms with annual productivity of between 200 to 400 g C m^{-2} (Qasim, 1982; Codispoti, 1991). This high primary productivity, in combination with a relatively weak ventilation, creates an OMZ at depths between 150-1250 m (e.g. Olson et al., 1993). The strength of the primary productivity, and hence of the OMZ, is strongly linked to the intensity of summer monsoonal winds (Reichart et al., 1997, 1998, 2002). Orbitally controlled climate cycles have dramatically impacted Indian Ocean monsoon strengths and resulted in great variability in the intensity and extent of the OMZ in the Arabian Sea (Reichart et al., 1997, 1998; Sinninghe Damsté et al., 2002). Generally, the Arabian Sea OMZ eroded during glacial periods due to a weaker summer monsoon and deep convective winter mixing and expanded to greater depths during interglacials (Reichart et al., 1997, 1998; Sinninghe Damsté et al., 2002). Superimposed are suborbital climatic changes leading to both weakened summer monsoons in interglacials and stronger monsoons during glacial periods (Reichart et al., 1997).

4.3. Material and Methods

4.3.1. Material and Sample Locations

Chromium isotope and concentration data have been derived from bulk planktic foraminiferal samples for the PETM (DSDP Site 401, ODP Site 1210, ODP Site 1263), ETM2 and Pleistocene records, and from bulk carbonate for the PETM (Contessa Road section), OAE1a and OAE2 records.

OAE1a samples come from the Cau drill core in the Baetic Cordillera in SE Spain (38.70 N, 0.00 E). The Cau core was drilled through an expanded section composed of hemipelagic marls and marlstones with abundant planktic foraminifera and calcareous nannofossils deposited on a distal shallow carbonate

ramp (Ruiz-Ortiz et al., 2016). OAE1a is marked by a black marl horizon (Ruiz-Ortiz et al., 2016). The samples are comprised of 35-73% carbonate (this study).

OAE2 samples come from the Plenus Marls in the English Chalk at Shakespeare Cliff in Dover, SE England. Carbonate content is between 74-97% (Lauren O'Connor, unpublished data). The Dover Plenus Marls were deposited in the epicontinental Anglo-Paris Basin. The Plenus Marls are a 2-3 m thick set of 8 marly chalks in between chalk facies rich in calcareous nannofossils and calcispheres (Jeans et al., 1991). This marl-chalk succession is superimposed on a general trend of upward coarsening of the sediment associated with long-term shallowing water (Jeans et al., 1991). Each marly chalk was deposited atop an erosional surface. The position of the Plenus Marls on top erosional surfaces suggests deposition in higher energy environments and shallower water depths than the chalk (Jeans et al., 1991). It has been suggested this section may have undergone oxidative weathering (Jenkyns et al., 2017).

Samples covering the PETM derived from ODP Site 1210 in the North Pacific, ODP Site 1263 in the South Atlantic and DSDP site 401in the North Atlantic. These samples are composed of planktic foraminifera. More information on the ODP and DSDP samples from the PETM can be found in chapter 2. For the PETM, samples have been taken from the Contessa Road section near Gubbio, Central Italy. These samples are a part of the Scaglia Rossa Formation which is characterised by its red pelagic limestones. These limestones were deposited in the Umbria-Marche Basin in the Tethys Ocean. The Palaeocene-Eocene transition in this section is comprised of a succession of micrite limestones and marly limestones with a carbonate content between 30-90% (Galeotti et al., 2000; Galeotti et al., 2010). The PETM itself is marked by two ~10cm thick clay layers and a marl layer. The limestone just prior to the clay associated with the onset of the PETM shows some remineralised sparry calcite which might have been subjected to diagenesis. Numerous studies indicate the possibility of diagenetic alteration in the Scaglia Rossa Formation (Corfield et al., 1991) and potential remobilisation of metals by pressure-solution and dissolution (Arthur, 1976; Geiser and Sonsone, 1981; Alvarez, 2009).

The ETM2 samples are comprised of planktic foraminifera and were taken from ODP Site 1263 (Walvis Ridge; 32.74 S, 2.69 E). At a palaeodepth of 1500 m these foraminifera were deposited in intermediate Atlantic waters located below a major OMZ (Pälike et al., 2014).

Bulk planktic foraminiferal samples from the Pleistocene come from NIOP Site 464 in the Arabian Sea (22.15 N, 63.35 E). NIOP Site 464 is located in intermediate water depths (1470 m water depth; Reichart et al., 1997) below the OMZ associated with the upwelling zone in the Arabian Sea.

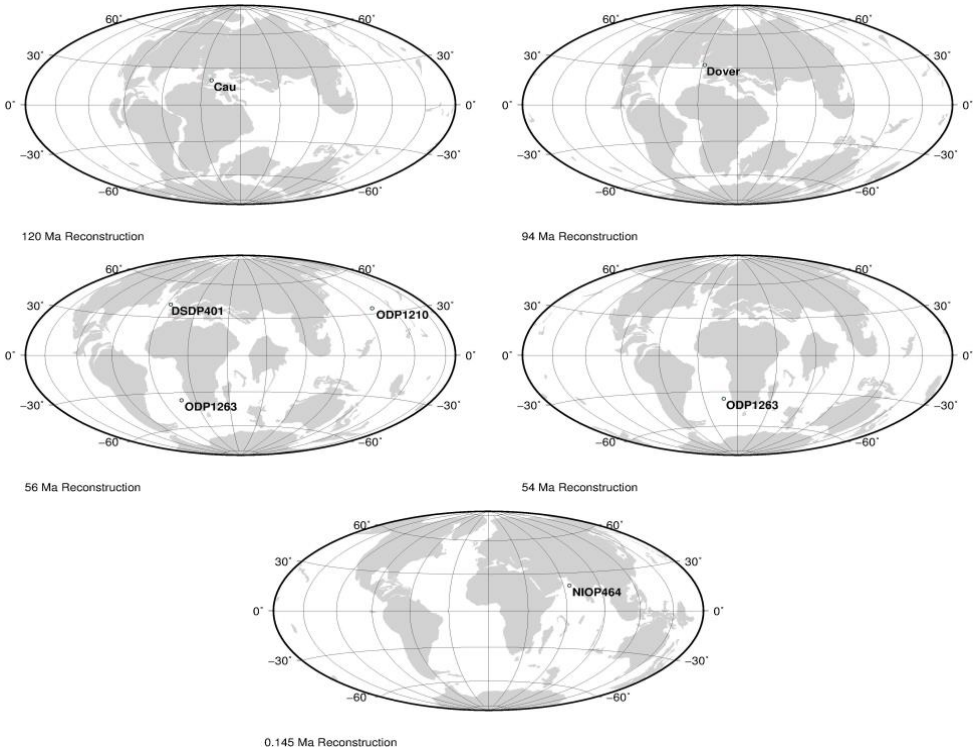

Figure 4.2: Palaeogeographic reconstructions (www.odsn.de) with samples sites marked.

4.3.2. Age models

The age model for the Pleistocene record from NIOP Site 464 is based on correlations of Mediterranean and Arabian Sea $\delta^{18}O$ records and were corrected by AMS ^{14}C, U/Th and dendrochronological ages, as well as the last occurrence level of planktonic foraminifer *Globigerinoides ruber* (pink) (Reichart et al., 1998; and references therein). Details of age models used for the PETM records from DSDP Site 401, ODP Site 1210 and ODP Site 1263 can be found in chapter 2. No age model has been applied to the ETM2, Contessa Road (PETM), OAE1a and OAE2 records and hence they are displayed against stratigraphic height.

4.3.3. Analytical methods

4.3.3.1. Sample processing

Samples of 10-20 cm^3 were wet sieved > 63 µm. Coarse fractions are the dry mass of the particles larger than 63 µm as the weight percentage of the dry mass of the total sample prior to sieving. A mixture of planktic foraminiferal species was picked from these samples to obtain about 0.11 g. Samples were cleaned by gently cracking open the foraminiferal tests, with subsequent removal of clay particles and organic matter by ultrasonication in Milli-Q (MQ) grade water and by leaching in alkali buffered H_2O_2, respectively (Barker et al., 2003). Bulk carbonate samples were ground by hand to a powder with a ceramic pestle and mortar to avoid contamination with any metals.

4.3.3.2. Trace element analysis

Cleaned samples of ~0.01 g were dissolved in cold 0.5M acetic acid, dried down to incipient dryness and subsequently were dissolved and diluted with 2% HNO_3 acid by ~4000 times to produce a 100 ppm Ca solution. A suite of synthetic standards containing 40 trace elements at a variety of concentrations and doped with 100 ppm Ca were used to produce a calibration curve. Rare earth elements and Cr concentrations were measured in He and O_2 collision mode respectively on an Agilent 7500s ICP-QQQ-MS (Triple Quadrupole ICP-MS) at the Open University. Measurements are reproducible within ~ 2% for Cr and ~ 9% for Ce/Ce* for JDo-1.

4.3.3.3. Chromium isotope analysis

Approximately 0.1 g of sample (where available; down to 0.03 g at the height of the carbonate burndown during the PETM at ODP Site 1263) was dissolved by ultrasonication in 0.5M acetic acid to prevent any potential leaching of any remaining detrital material left after cleaning. Chromium was subsequently extracted following the cation exchange chromatographic separation procedures as described in Bonnand et al. (2011) with procedural blank Cr contributions of ~0.2 ng. JDo-1 was subjected to the same chemistry protocol as the samples. Chromium isotopes were measured on a ThermoFisher Scientific Neptune MC-ICP-MS by using a ^{50}Cr-^{54}Cr double-spike technique following Bonnand et al. (2011). The average value obtained for JDo-1 is $\delta^{53}Cr = +1.715 \pm 0.059$ (2σ, $n = 8$), which is within error of previously published values of $\delta^{53}Cr = +1.719 \pm 0.059$ (Bonnand et al., 2011). The external reproducibility of NIST SRM 979 is $\delta^{53}Cr = +0.002 \pm 0.026$ (2σ, $n = 20$).

4.4. Results and Discussion

In the following section the behaviour of Cr concentrations and $\delta^{53}Cr$ values during OAE1a, OAE2, the PETM, the ETM-2, and the Pleistocene glacial-interglacials will first be described to highlight the evolution of deoxygenation during each time interval and to assess the reliability of the Cr signatures of redox changes at each section. Subsequently, the characteristics of these time intervals will be compared along with the magnitudes of the perturbations in the carbon, oxygen, and chromium isotope systems will be compared to assess whether chromium isotope fractionation, and thus ocean deoxygenation, is governed by processes related to carbon system dynamics (e.g. primary productivity, carbon injection) and/or changes in temperature.

4.4.1. The Selli Event (OAE1a)

Concentrations of Cr increased prior to the Selli Event at Cau from 1.03 to 2.24 ppm at a stratigraphic height of 58.70 m (Figure 4.3). Immediately preceding the event (62.70 m) the record presents a drop in Cr concentrations from 2.24 to 0.73 ppm. Across the onset (62.70 – 65.40 m), Cr concentrations

increased to 2.71 ppm and reached highest values within the main body of the OAE (70 m) at 3.69 ppm. After this peak, Cr concentrations steadily decreased back to a value of 0.54 ppm at 111.70 m. The evolution of the Cr isotopic composition during OAE1a shows similar patterns (Figure 4.3). Chromium isotope compositions became progressively lighter prior to the OAE and reaching a minimum of +0.11‰ at 64.50 m which is within the period of the onset of the event (62.70 – 65.40 m). Subsequently, $\delta^{53}Cr$ rapidly became heavier and reached a maximum value of +0.90‰ at 65.40 m. This increase in the chromium isotopic value coincides with the latter part of the first step of the CIE but seems to lag the carbon perturbation. It is, however, difficult to quantify the potential lag due to the low resolution of the $\delta^{53}Cr$ record across the onset of the OAE. After the peak at 64.50 m, Cr isotope are variable, but overall became increasingly lighter with values back to +0.47‰ at 111.70 m. The trend in Cr isotopic values during OAE1a shows a striking similarity to the bulk carbonate $\delta^{13}C$ record with the main isotopic shift in Cr (~ +0.79‰) occurring during the latter part of the onset of the carbon perturbation and slowly recovering to pre-event values towards the end of the CIE. Chromium isotopic values of the carbonate fraction positively correlate with $\delta^{13}C_{CARB}$ ($R^2 = 0.37$; $p = 0.01$). Assuming that high $\delta^{13}C$ corresponds to oxygen-reduced conditions at the seafloor, the heavy $\delta^{53}Cr$ values during the event could be interpreted as evidence for hypoxia (Ellis et al., 2002). This result is consistent with other data supportive of deoxygenation during OAE1a (e.g. Jenkyns et al., 2010). Observed $\delta^{53}Cr$ values became lighter (-0.32‰) during the first part of the onset. Unless in the unlikely event a pulse of oxygenation across the onset took place, only an increased input of light Cr can explain this drop. Potential sources of lighter Cr include increased weathering rates of silicates and enhanced volcanic activity. Both of which would have Cr isotopic values close to Bulk Silicate Earth (BSE; Schoenberg et al., 2008). OAE1a is associated with the Ontong-Jave Plateau LIP, which likely caused the global climate to change potentially resulting in increased silicate weathering rates through the emission of vast quantities of CO_2 into the atmosphere (e.g. Keller et al., 2011; Naafs et al., 2016). Enhanced weathering rates would have then caused oceanic deoxygenation through a higher nutrient supply from rivers and subsequent enhanced primary productivity which is confirmed by Ca, Li and Sr isotope data (Jenkyns et al., 1995; Blättler et al., 2011; Lechler et al., 2015; Figure 4.4). Thus, the observed Cr isotopic signal could represent relative changes in the input of light Cr from the Ontong-Java Plateau volcanism and a potential increase in weathering rates of a source with a light $\delta^{53}Cr$, and the removal of light Cr due to enhanced anoxia. Reducing conditions became more dominant in the Cr cycle during the second half of the onset of the CIE between 64.50 and 65.40 m, which is also when CO_2 attained its highest level of 2187 ppmv (Naafs et al., 2016). As volcanic outgassing decreased, weathering rates became lower resulting in a lower nutrient supply, diminished primary productivity and eventually better oxygenated ocean (e.g. Naafs et al., 2016).

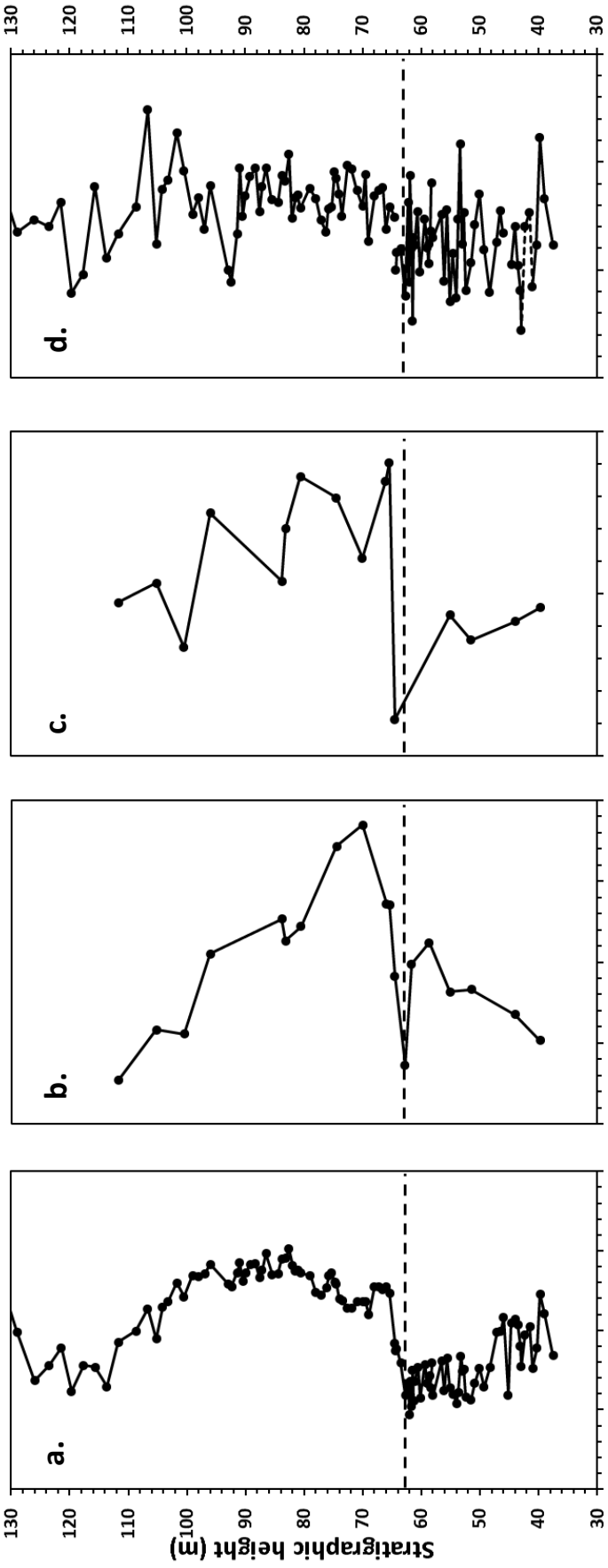

Figure 4.3: Bulk records for OAE1a from the Cau drill core (SE Spain) of **a.** $\delta^{13}C$ (‰) by Naafs et al. (2016) **b.** Cr concentrations (ppm) **c.** $\delta^{53}Cr$ (‰) **d.** $\delta^{18}O$ (‰) by Naafs et al. (2016). The dotted line represents the onset of the carbon isotope excursion.

Although oligotrophic waters became more fertile during OAE1a, there is no evidence for eutrophication at the surface of the ocean or anoxia in the whole water column (Menegatti et al., 1998; Premoli Silva and Sliter, 1999; Jenkyns, 2003; Erba, 2004; Luciani et al., 2004). The presence of benthic foraminifera suggests bottom waters were not anoxic (Luciani et al., 2004). A more plausible explanation for bottom-water deoxygenation and increased preservation of organic matter in marginal seas is enhanced water column stratification (Weissert, 1981; Luciani et al., 2004; Gomes et al., 2016). Due to the proximity of the Cau section to land during the Cretaceous (Figure 4.3), enhanced stratification could have been caused by freshwater run-off locally forming a freshwater lens. Contrary to the $\delta^{53}Cr$ record, the trend in Cr concentrations implies an increased oxygenation, due to the increased solubility of Cr at high oxygen levels (Cranston and Murray, 1978), at the start of OAE1a with marginal seas experiencing more reducing conditions over time as the OAE wanes. An alternative explanation is that weathering rates or volcanic input of Cr increased during the main stage of OAE1a. This is supported by the close resemblance of the patterns observed in both Cr concentrations and the reconstructed CO_2 record by Naafs et al. (2016). Both Cr concentrations and CO_2 dip at 62.70 m after which they peak and slowly recover (Figure 4.3).

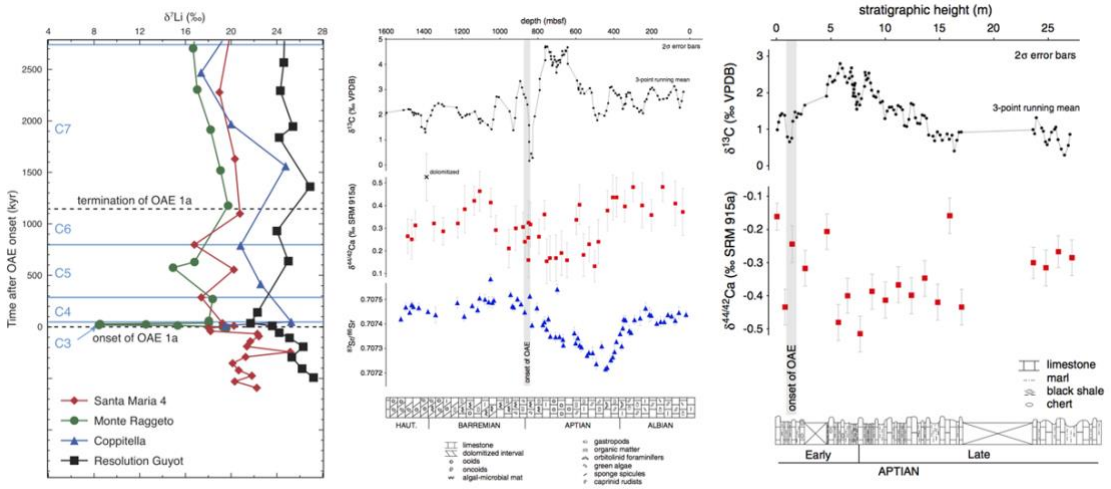

Figure 4.4: After Lechler et al. (2015) and Blättler et al. (2011). $\delta^{13}C$ (‰) by Jenkyns et al. (2017), $\delta^{7}Li$ (‰) by Lechler et al. (2015); Sr isotope data by McArthur et al. (1993); Ca isotope data by Blättler et al. (2011). Zinc, Li, Sr, Ca and U isotopes all change in composition during OAE2 and indicate an increase in weathering and increased oxygenation.

4.4.2. The Bonarelli Event (OAE2)

Chromium concentrations range between 0.3 – 2 ppm prior to the event (Figure 4.5). The lowest concentrations are at 160 m after which concentrations increase in the lead-up to the PCE. During the PCE, Cr concentrations rise to 5.5 ppm in two pulses with a dip to 2.7 ppm at 280 m resembling $\delta^{18}O_{carb}$. The peaks in Cr concentrations lag the $\delta^{18}O_{carb}$ peaks by 10 m. The $\delta^{53}Cr$ becomes increasingly lighter over time from a maximum of +1.2‰ down to -0.75‰ (Figure 4.5). During the PCE, $\delta^{53}Cr$ also display two peaks which are contemporaneous with the Cr concentrations. $\delta^{53}Cr$ values during the PCE are very light between -0.3 to -1.2‰.

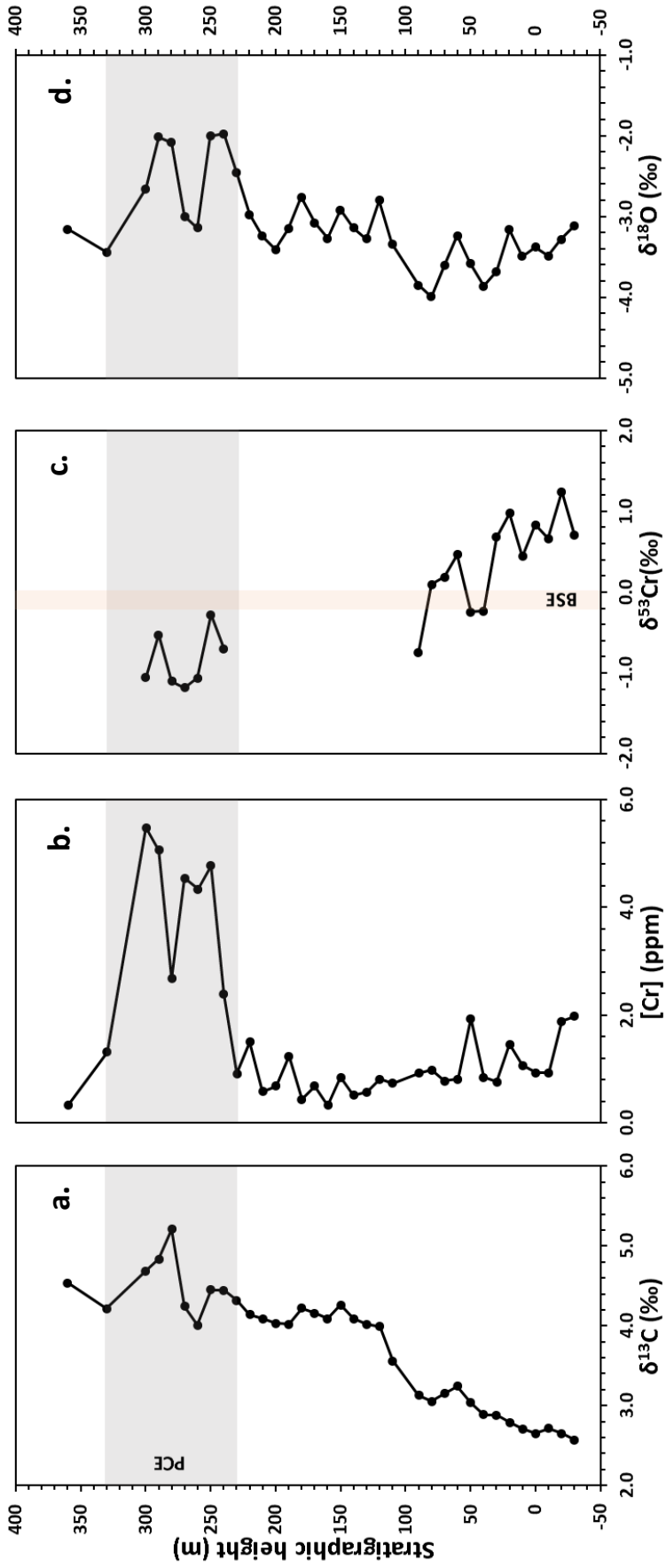

Figure 4.5: Bulk records for OAE2 from the Dover Plenus Marl section (SE England) of **a.** $\delta^{13}C$ (‰) by Lauren O'Connor (unpublished) **b.** Cr concentrations (ppm) **c.** $\delta^{53}Cr$ (‰) **d.** $\delta^{18}O$ (‰) by Lauren O'Connor (unpublished). The grey bar represents the Plenus Cold Event. The orange bar represents bulk silicate earth Cr isotope values (Schoenberg et al., 2008).

The PCE is clearly visible in the rock record as a set of marls and is also readily identifiable by negative $\delta^{18}O$ shifts which represent two cold periods (Figure 4.5). This study finds peak Cr levels of up to ~4.5 ppm in two pulses associated with the two PCE cold periods and is in agreement with previous works by Jenkyns et al. (2017) and Pearce et al. (2009) who also find Cr enrichments during the PCE. The enrichment of redox-sensitive trace metals such as Cr and Mn have also been found in Culver Cliff (Isle of Wight), sites in the Western Interior Seaway (WIS), Europe, the Atlantic Ocean, the Pacific Ocean, the Indian Ocean, and South America (Jarvis et al., 2001; and Orth et al., 1993). Orth et al. (1993) found that in northern sectors of the WIS only a single peak in Cr is present, whereas sections to the South in the WIS and in Colombia show two peaks. Orth et al. (1993) attributed this to the potential source of the Cr being located in the South, potentially from the present-day Gulf of Mexico/Caribbean region. Orth et al. (1993) postulated that the second pulse in trace metal enrichments did not reach the northern WIS. The Dover section provides the first evidence for two Cr enrichment peaks outside the WIS and Colombia. These enrichments have traditionally been interpreted as a volcanic signature - a hypothesis recently supported by Cr isotope data (Orth et al., 1993; Holmden et al., 2016). A neodymium isotope study identified the Arctic LIP as the main source of basalt-derived metals in the English Chalk during the PCE (Zheng et al., 2013).

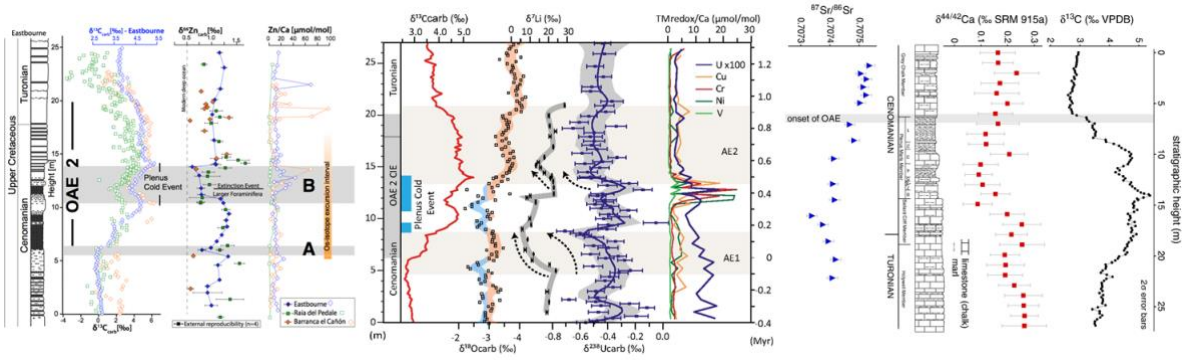

Figure 4.6: After Sweere et al. (2018), Clarkson et al. (2018) and Blättler et al. (2011). $\delta^{13}C$ (‰) and $\delta^{18}O$ (‰) by Jenkyns et al. (2017), $\delta^{66}Zn$ (‰) by Sweere et al. (2018), $\delta^{7}Li$ (‰) by Pogge von Strandmann et al. (2013); $\delta^{238}U$ (‰) and trace metal concentrations by Clarkson et al. (2018); Sr isotope data by McArthur et al. (1993) and Ca isotope data by Blättler et al. (2011). Zinc, Li, Sr, Ca and U isotopes all change in composition during OAE2 and indicate an increase in weathering and increased oxygenation.

Recently, Jenkyns et al. (2017) interpreted the PCE trace metal enrichments as a signal of increased oxygenation instead. Jenkyns et al. (2017) reasoned that the shift in osmium isotopes to less radiogenic values was not concurrent with trace metal enrichments. They proposed less effective sinks of trace metals like Cr and the oxidation of black shales must have taken place in addition to basalt-seawater interactions. Increased oxygenation during the PCE is supported by Ce/Ca ratios and sulphur isotopes (Jenkyns et al., 2017), as well as uranium and selenium isotopes (Clarkson et al., 2018; Sweere et al., 2018; Figure 4.6). The two PCE peaks are also recorded by $\delta^{53}Cr$ (Figure 4.5). The $\delta^{53}Cr$ values follow

a long-term downward trend from the onset of OAE2 and are extremely negative during the PCE. This long-term trend during OAE2 was also found by Wang et al. (2016) and Holmden et al. (2016). Wang et al. (2016) and Holmden et al. (2016) both attribute the negative trends in Cr isotopes to different processes. Holmden et al. (2016) pointed to an increased input of basaltic Cr from the Caribbean LIP, whereas Wang et al. (2016) suggested a decrease in seawater $\delta^{53}Cr$ values through quantitative reduction in euxinic environments (Reinhard et al., 2014; Wang et al., 2016). The data presented here cannot further elucidate which process was the likely cause of this negative trend. Lithium and Ca isotope data, however, points to increased silicate weathering which can have similar effects on seawater $\delta^{53}Cr$ values (Pogge von Strandmann et al., 2013; Blättler et al., 2011; Figure 4.6). The $\delta^{53}Cr$ peaks during the PCE are positive, which is associated with deoxygenation and warming (e.g. Bonnand et al., 2013; Reinhard et al., 2014) and is in stark contrast to both the $\delta^{18}O$ and $\delta^{238}U$ records which clearly show cooling and reoxygenation (Jenkyns et al., 2017; Clarkson et al., 2018). It is likely that climatic details have been overprinted by heavy oxidative weathering processes. Further recent research into redox conditions during the PCE using Zn isotopes at Eastbourne also shows clear re-oxygenation through lighter isotopic compositions (Sweere et al., 2018). Sweere et al. (2018) suggest that a decrease in organic-rich sinks on the continental margins and as well as oxidation of organic matter released light Zn into the ocean, and that, in addition to cooling, a perturbation to the micro-nutrient cycle (nutrification) also occurred as indicated by Zn concentrations. This reinforces previous observations in the literature and Cr behaviour.

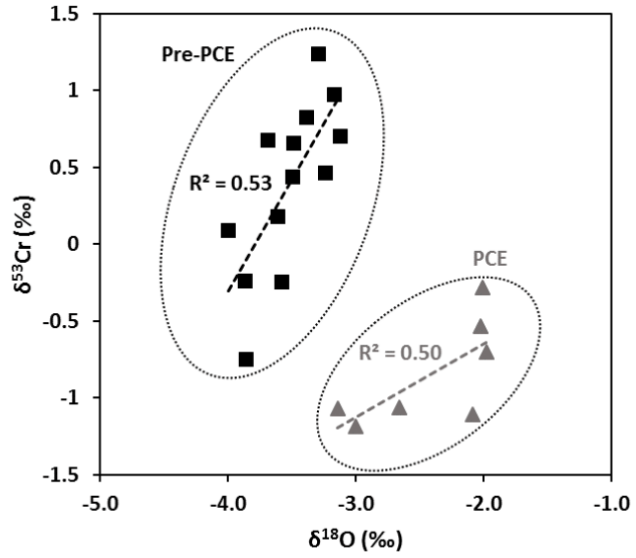

Figure 4.7: Cross-plot of $\delta^{18}O$ (‰) and $\delta^{53}Cr$ (‰) showing two distinct populations. There is a positive correlation between the two isotope systems prior to the PCE (during OAE2), but there is no significant correlation during the event itself.

$\delta^{53}Cr$ and $\delta^{18}O$ values are compared to highlight any correspondence between the isotope systems. In a cross-plot, $\delta^{53}Cr$ and $\delta^{18}O$ values fall into two distinct population with a significant positive correlation

for the pre-PCE (R^2 = 0.53; p = 0.005) and no significant correlation during the PCE (R^2 = 0.50; p = 0.07; Figure 4.7). Oxidative weathering has the potential to generate such negative Cr isotope values (e.g. Bonnand, 2011; Frei et al., 2014; Paulukat et al., 2015) through the oxidation of Cr(III) by manganese oxides (Frei et al., 2014). Highly weathered soil and carbonate samples have δ^{53}Cr values of down to -1.29 and -0.529‰, respectively (Bonnand, 2011; Paulukat et al., 2015). My new observation of extremely light δ^{53}Cr values at Dover support the increased oxidation during the PCE proposed by Jenkyns et al. (2017) because of the preferential removal of heavy Cr during oxidation (Berger and Frei, 2014).

4.4.3. The Palaeocene-Eocene Thermal Maximum

The Cr isotope and concentration records across the PETM from ODP Sites 1210, 1263, and DSDP Site 401 show that the Cr response is mainly influenced by local factors and does not record a global deoxygenation signal. All sites show signs of deoxygenation to varying degrees of severity and are suspected to be influenced by temperature and temperature-controlled effects. Detailed results of the foraminiferal PETM records can be found in chapter 3. At the Contessa Road section, chromium concentrations prior to and after the PETM vary between 0.12 and 1.12 ppm (Figure 4.8). During the PETM, in between the two clay layers, Cr concentrations peak at 2.88 ppm. The peak in Cr concentrations occurs at the onset of the CIE (at 31.29 and 31.28 m, respectively). Chromium isotope values are negative throughout the event with a minimum of -1.05‰ at 31.29 m during the peak CIE. After the event, δ^{53}Cr values return to positive values of +1.43 to +1.79‰.

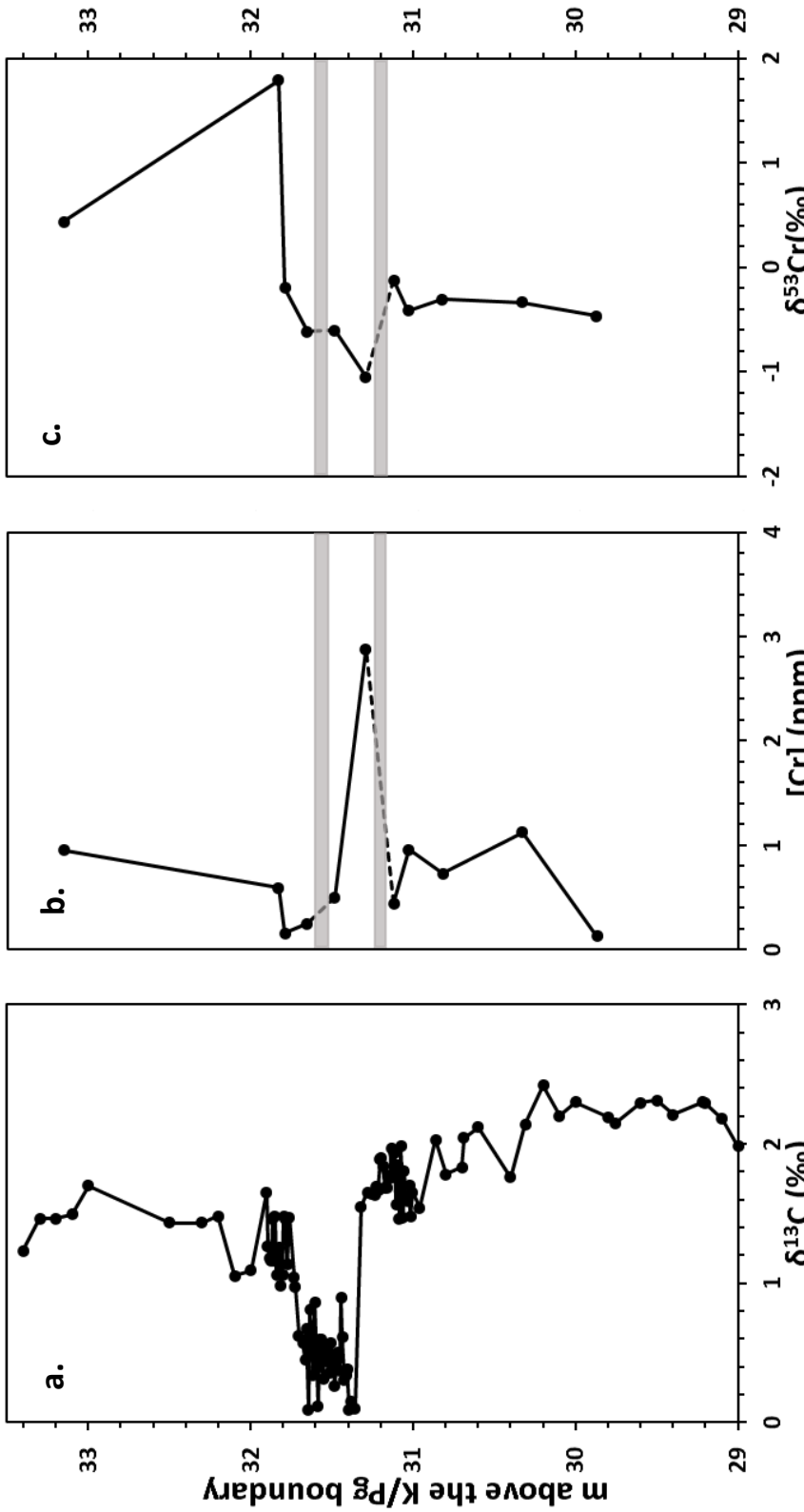

Figure 4.8: Bulk records for the PETM from the Contessa Road section (Central Italy) of **a.** $\delta^{13}C$ (‰) by Galeotti et al. (2000) **b.** Cr concentrations (ppm) **c.** $\delta^{53}Cr$ (‰). The grey bars represent marls during the PETM (Galeotti et al., 2000).

The Contessa Road section shows a different trend in Cr values than the foraminiferal records which show decreases in Cr concentrations and progressively heavier Cr isotope values characteristic of deoxygenation throughout the event. Palaeo-environmental implications of the geochemical composition of foraminiferal samples from the PETM are discussed in chapter 2. The Cr concentration record at Contessa Road differs from the foraminiferal 'open ocean' records in that Cr concentrations were low prior to and after the CIE and peaked during the CIE. For foraminiferal records, a marked drop in concentrations was observed. Apart from environmental setting, a major difference between the foraminiferal records and the Contessa Road record is that the latter was derived from bulk limestone samples. The pelagic limestones at Contessa are mainly comprised of calcareous nanofossils in addition to planktonic foraminifera. Currently, there is little understanding on the Cr composition of nanofossils. Additionally, the Scaglia Rossa formation at Contessa has a pronounced haematite component as opposed to the foraminiferal records (Lowrie et al., 1982). As Cr and Fe are intimately linked, the presence of relatively large quantities of Fe is likely to have impacted the Cr composition of the Contessa samples. This The concurrence of high Cr concentrations and a negative Cr isotope excursion during the onset of the CIE at the Contessa Road section could be interpreted as re-oxygenation which corroborates findings based on Ni/Co ratios that during the PETM there was a well-oxygenated Tethys Ocean (Giusberti et al., 2009). This is not consistent with most proxy evidence pointing to severe deoxygenation in this area (Carmichael et al., 2017). Chromium isotope values in the Contessa Road section are lighter than BSE values. These low values make fractionation through reductive reactions unlikely, as the lighter Cr isotopes preferentially participate in these (e.g. Schoenberg et al., 2008; Ellis et al., 2002). One process capable of generating values more negative than BSE is oxidative weathering (e.g. Bonnand, 2011; Frei et al., 2014; Paulukat et al., 2015) through the oxidation of Cr(III) by manganese oxides (Frei et al., 2014). Highly weathered sediments have δ^{53}Cr values of down to -1.29‰ (Paulukat et al., 2015) similar to the values obtained during the PETM at Contessa. Remobilisation of metals through dissolution of shales and limestones, pressure solution features, and flow along microcracks related to active tectonics on the Italian peninsula have been reported for the Scaglia Rossa formation (Arthur, 1976; Geiser and Sansone, 1981; Alvarez, 2009). Heavy diagenetic overprinting in δ^{18}O values have also been reported for the Scaglia Rossa Formation (Corfield et al., 1991). After the event, δ^{53}Cr values recover to high positive values of +1.43 to +1.79‰ and as such may be unaffected by oxidative weathering. The correlation between oxygen and chromium isotopes between sites during the same event (chapter 3) and within sites that have likely experienced oxidative weathering suggest there is a close link. At the Contessa Road section both oxygen and chromium isotopes have been affected by extensive diagenesis. Diagenetic overprints in the δ^{18}O of samples can potentially serve as a harbinger of diagenetically altered Cr isotope values.

4.4.4. The Eocene Thermal Maximum 2

Prior to ETM-2, Cr concentrations are highly variable (Figure 4.9). Cr concentrations increase towards the beginning of the ETM-2. Just prior to the onset of the ETM-2, there is a sharp increase in Cr concentrations from 0.06 to 0.7 ppm. These observed shifts in Cr concentration are accompanied by contemporaneous shifts in the abundance of planktonic foraminifera (number of planktonic foraminifera per gram of sediment) (Figure 4.9). During ETM-2, Cr concentrations drop to levels between 0.04 – 0.2 ppm during times of significant reduction in abundance of planktic foraminifera (D'Onofrio et al., 2014; Luciani et al., 2017). While the planktic foraminiferal abundance in the sediments recover at a depth of 294.87 m (revised composite depth, rmcd), Cr concentrations remain low until 294.79 m. Chromium isotope ratios prior to ETM-2 are within error of bulk silicate earth values (Figure 4.9; Schoenberg et al., 2008) but reach heavy values of approximately +1.9‰ at the onset of ETM-2. Unlike Cr concentrations, δ^{53}Cr recovers to +0.6‰ at an rmcd of 294.88 m.

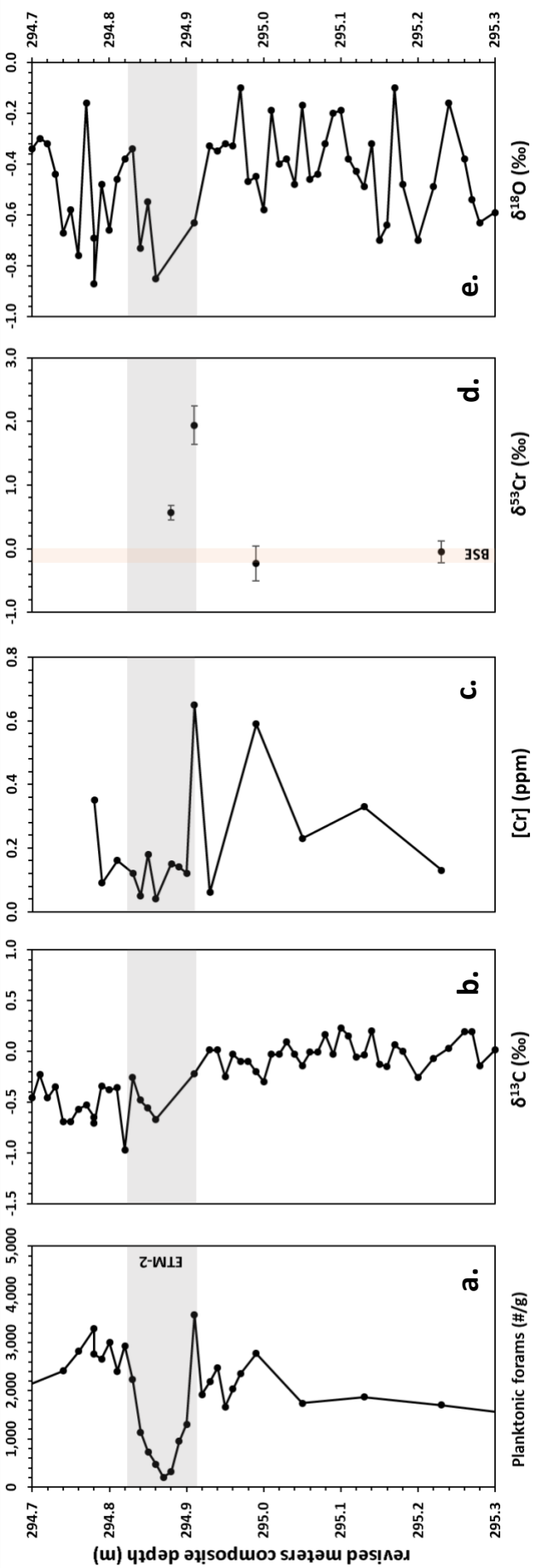

Figure 4.9: Planktic foraminiferal records for the ETM-2 from ODP Site 1263 (SE Atlantic) of **a.** planktic foraminiferal counts (#/g) by Jennions et al. (2015) **b.** $\delta^{13}C$ (‰) by Lauretano et al. (2015) **c.** Cr concentrations (ppm) **d.** $\delta^{53}Cr$ (‰) **e.** $\delta^{18}O$ (‰) by Lauretano et al. (2015). The grey bar represents the CIE associated with ETM-2. The orange bar represents bulk silicate earth Cr isotope values (Schoenberg et al., 2008).

The Cr concentrations follow shifts in the abundance of planktic foraminifera which suggests that there may be a common mechanism affecting both or that shifts in Cr concentrations are could be an artefact caused by differences in preservation state (dissolution) of the sample. Several studies suggest that Walvis Ridge became increasingly oligotrophic during the ETM-2 despite enhanced respiration and remineralisation of organic matter (e.g. O'Connor et al, 2009; Dedert et al., 2012; Ma et al., 2014; Jennions et al., 2015). Increased remineralisation of organic matter can cause an enhanced production of organic acids such as carbonic acid as well as deoxygenation through the consumption of oxygen during the oxidation process. While the increased acidity of bottom waters would cause increased dissolution of planktic foraminiferal tests resulting in lower counts observed in the sediment, the accompanying expansion of the OMZ on Walvis Ridge due to increased metabolic rates would have driven down Cr concentrations. The idea of an expanded OMZ has also been proposed to have occurred during the PETM (Chun et al., 2010; Pälike et al., 2014). Chromium isotope data peak at the onset of the ETM-2 which would suggest a downward expansion of low-oxygen waters (Figure 4.9). Chromium isotopes recover quickly, during the main event still, while Cr concentrations recover only after the event and after the planktic foraminiferal community has recovered (Figure 4.9). A potential explanation for the different timings of recovery between Cr isotopes and concentrations would be caused by the increasing oligotrophy thought to have occurred. As the environment became increasingly oligotrophic, productivity and remineralisation of organic matter started to become impeded which would have led to a contraction in the OMZ, as evidenced by $\delta^{53}Cr$ values. A decrease in remineralisation would also have led to less acidic waters prompting a recovery in the preservation of the planktic foraminiferal tests. Increased oligotrophy requires less nutrient inputs and therefore one would expect Cr concentrations to remain low after having been drawn down when the OMZ was expanded.

4.4.5. The Pleistocene of the Arabian Sea

The C_{org} content of the sediment of the OMZ show a clear cyclicity on a ~20 kyr timescale (Reichart et al., 1997). The high C_{org} values of 2.7 – 3.8% at 147 and 145 ka are associated with high Cr concentrations of 2.34-2.89 ppm and $\delta^{53}Cr$ values of +0.52 and +0.46‰, respectively (Figure 4.10). The isotopes drop to values within error of BSE (-0.12 ± 0.10‰; Schoenberg et al. 2008) at the same time as C_{org} values drop to 0.4 – 1.4% between ~118 – 85 ka. At approximately 82, 67 and 66 ka $\delta^{53}Cr$ values rise to +0.16‰, +0.08‰ and +0.09‰, whereas C_{org} values average at ~0.65%. Concentrations of Cr decline over time to 0.77 ppm at 66 ka (Figure 4.10).

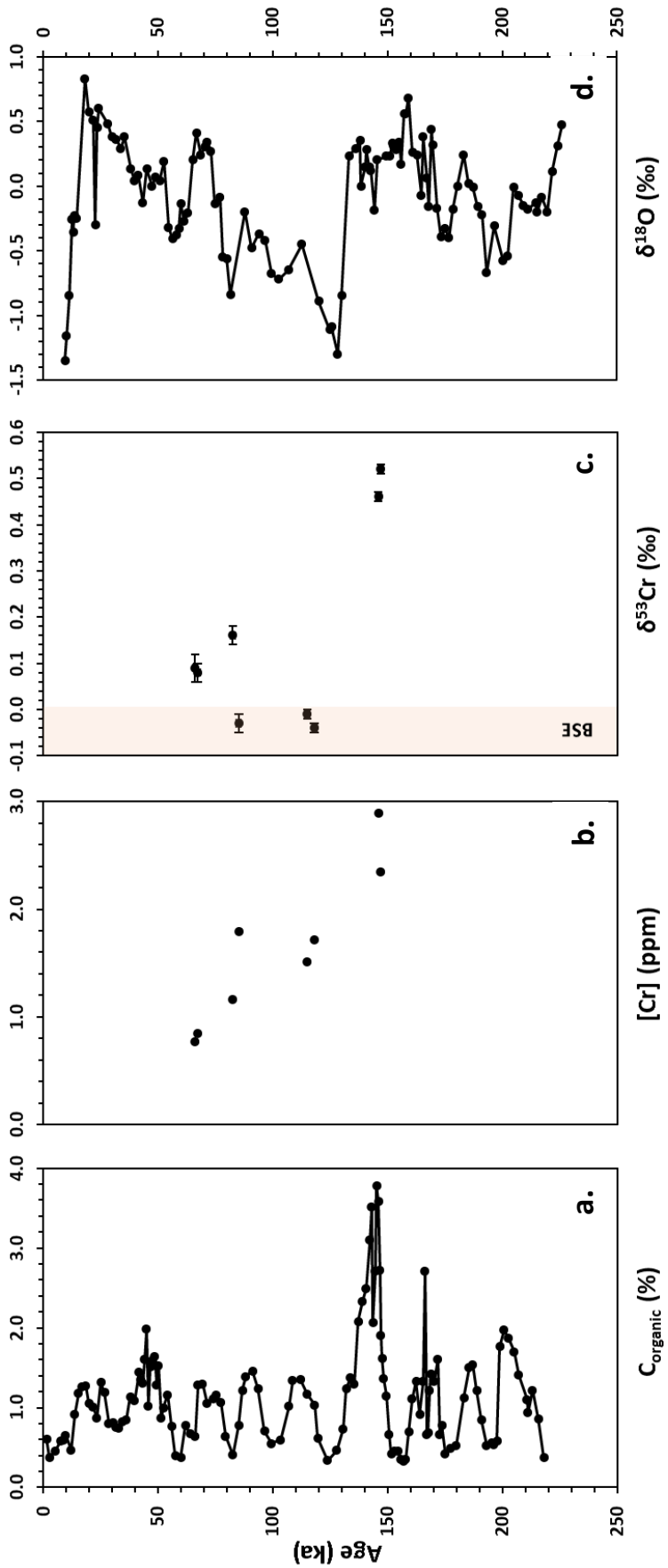

Figure 4.10: Planktic foraminiferal records for the Pleistocene from NIOP Site 464 (Arabian Sea) of **a.** organic carbon content (%) by Reichart et al. (1997) **b.** Cr concentrations (ppm) **c.** $\delta^{53}Cr$ (‰) **d.** $\delta^{18}O$ (‰) by Reichart et al. (1998). The orange bar represents bulk silicate earth Cr isotope values (Schoenberg et al., 2008).

Over the course of the Pleistocene, Cr concentrations steadily declined over time with the highest during the C_{org} peak at the end of MIS6 (Figure 4.10). The high C_{org} during MIS6 is traditionally interpreted as representative of an expanded OMZ. As such, one would expect lower Cr concentrations due to the removal of particle-reactive reduced Cr(III) into the sediment which leaves less dissolved chromate available for incorporation into carbonates. However, Cr concentrations peaked during the time of an expanded Arabian OMZ. Chromium concentrations correlate with the organic carbon content (R^2 = 0.76, p = 0.005; Figure 4.10). This correlation implies that the composition of the sediment has an influence on the Cr content of foraminiferal calcite beyond the removal of Cr in reducing environments. Considering the conclusion of Chapter 2 that foraminiferal Cr is mostly (89%) derived post-deposition, it is likely the high concentrations of Cr in foraminifera are directly influenced by the high Cr concentrations found in organic matter. Chromium enrichments in these foraminifera are therefore unlikely to be directly representative of redox conditions as they are not in line with partial reduction when taking into account the isotopic behaviour of Cr (Reinhard et al., 2014). Chromium enrichment in a carbonate is normally thought to signify more oxygenated conditions (e.g. Bonnand et al., 2013) but in this case may be a proxy for the organic matter content of the sediment and the preservation potential of organic carbon. However, the preservation potential of organic carbon is linked to the local redox conditions (e.g. Jenkyns et al., 2010).

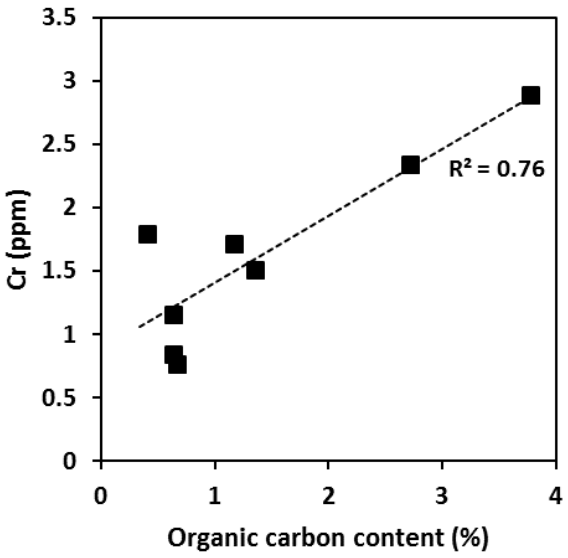

Figure 4.11: Cross-plot of organic carbon content (%) and Cr concentrations (ppm) displaying a significant positive correlation (R^2 = 0.76) between the two parameters in the Pleistocene Arabian Sea.

The foraminiferal δ^{53}Cr values from NIOP464 show a signal which is opposite to what one would expect from the Cr concentrations. When Cr concentrations were high (during MIS6), δ^{53}Cr values are also high (Figure 4.11). This means that under the reducing conditions of an expanded OMZ at 145 ka during

MIS6 (Reichart et al., 1997; Sinninghe Damsté et al., 2002), Cr isotopes directly recorded the redox conditions unlike Cr concentrations. An explanation for this paradox may be that organic matter could be enriched in the soluble Cr(VI). If the ratio of Cr(VI) to Cr(III) does not change within the organic matter, the Cr isotopic composition may not change substantially with increased deposition of organic matter during less oxygenated conditions. This suggestion requires further investigation into the incorporation of Cr into organic matter. In conclusion, foraminiferal $\delta^{53}Cr$ at NIOP464 faithfully records the expanded OMZ approximately 145 ka as suggested by Reichart et al. (1997). Since our foraminiferal $\delta^{53}Cr$ record records benthic oxygenation conditions (Chapter 2), the heavier $\delta^{53}Cr$ during MIS6 confirms that the OMZ extended to a depth of at least 1470 m (Reichart et al., 1997; Den Dulk et al., 2000; Sinninghe Damsté et al., 2002).

Previous higher-resolution studies into redox changes during the Pleistocene which use Cr isotopes (e.g. Reinhard et al., 2014; Gueguen et al., 2016). These studies focussed on authigenic Cr in marine sediments from the hypoxic-anoxic Cariaco Basin in the Atlantic Ocean during the termination of the Last Glacial Maximum (Reinhard et al., 2014) and the over several glacial-interglacial cycles including MIS6 (Gueguen et al., 2016). Both these studies indicate that $\delta^{53}Cr$ excursions were on the same order as found in the Arabian Sea (0.4 – 0.5%) and confirm the scale of change observed in Cr isotopes is similar in hypoxic-anoxic environments across glacial-interglacial cycles. Interestingly, although the scale of change is similar, Cr isotopes from the Cariaco record for MIS6 behave in an opposite manner to those of the Arabian Sea (Gueguen et al., 2016). Where $\delta^{53}Cr$ values are high during the glacials in the Arabian Sea, $\delta^{53}Cr$ values are low in the Cariaco Basin (and high during interglacials). This juxtaposition can be explained by the fact that the relatively restricted Cariaco Basin is less controlled by the strength of monsoonal winds which directly strengthen the OMZ by increasing upwelling during glacials in the Arabian Sea (Reichart et al., 1997. 1998; Sinninghe Damsté et al., 2002).

4.4.6. Synthesis

To assess the effects of temperature on deoxygenation, the maximum benthic oxygen isotope excursion was scaled to the maximum Cr isotope excursion relative to background values for the PETM, the ETM2 and the penultimate glacial cycle. This is the same approach I took in comparing PETM sections (Chapter 3), but here it has been extended to multiple climate events. Firstly, I converted the $\delta^{18}O$ signal into temperature difference to obtain temperature-associated dissolved oxygen loss (Broecker and Peng, 1982). I corrected the Pleistocene samples for ice-related $\delta^{18}O$ changes (Chappell and Shackleton, 1986). The resulting data show a significant positive correlation between Cr isotope excursion sizes and the benthic oxygen isotope excursions for the Cenozoic ($R^2 = 0.86$; $p = 0.024$; Figure 4.10a), but no significant correlation for the Mesozoic. Chromium isotopic values therefore record temperature-driven changes in the dissolved oxygen in bottom and pore waters. To investigate the potential effect the large Cr isotopic excursion at Site 1263 during the PETM might have as an outlier on the correlation between

Cr isotope excursions and benthic oxygen isotope excursions, a Pearson correlation coefficient and a Spearman Rank correlation coefficient were calculated and compared for data with and without the data from the PETM record at Site 1263. The Pearson's coefficient reduces from 0.94 to 0.73, whereas Spearman's rho reduces from 0.9 to 0.8. This highlights that the PETM record at Site 1263 does slightly enhance the correlation but that it does not differ substantially without it. For the Cenozoic, the correlation is slightly weaker but still significant after oxygen isotope excursions are converted into oxygen solubility loss ($R^2 = 0.81$; $p = 0.039$; Figure 4.12b). Dissolved oxygen losses due to temperature changes range from -13.0 to -32.7 µmol/kg (Figure 4.12b). This decrease in oxygen solubility is unlikely to have been sufficient on its own to have led to the low-oxygen conditions observed in the PETM (Sluijs et al., 2014; Carmichael et al., 2017; Chapter 3). Changes in temperature have indirect effects on dissolved oxygen levels as well: an enhanced hydrological cycle would cause increased nutrient supply and primary productivity (e.g. Schlanger and Jenkyns, 1976; Jenkyns et al., 2010). Temperature also governs metabolic rates, which would enhance both primary productivity and remineralisation at depth (e.g. Pörtner et al., 2014; Chapter 3). The correlation during the Cenozoic indicates temperature is a major control on deoxygenation, directly through the solubility of oxygen and indirectly through increased microbial metabolic rates. Similarly, changes of -13.3 µmol/kg O_2 during the ETM-2 and +8.9 µmol/kg O_2 after MIS-6 are not enough on their own to account for the severe declines of local oxygen concentrations associated with expanding OMZs (Stramma et al., 2008). There is no correlation between Cr isotope excursion sizes and the size of the CIE (Figure 4.12c).

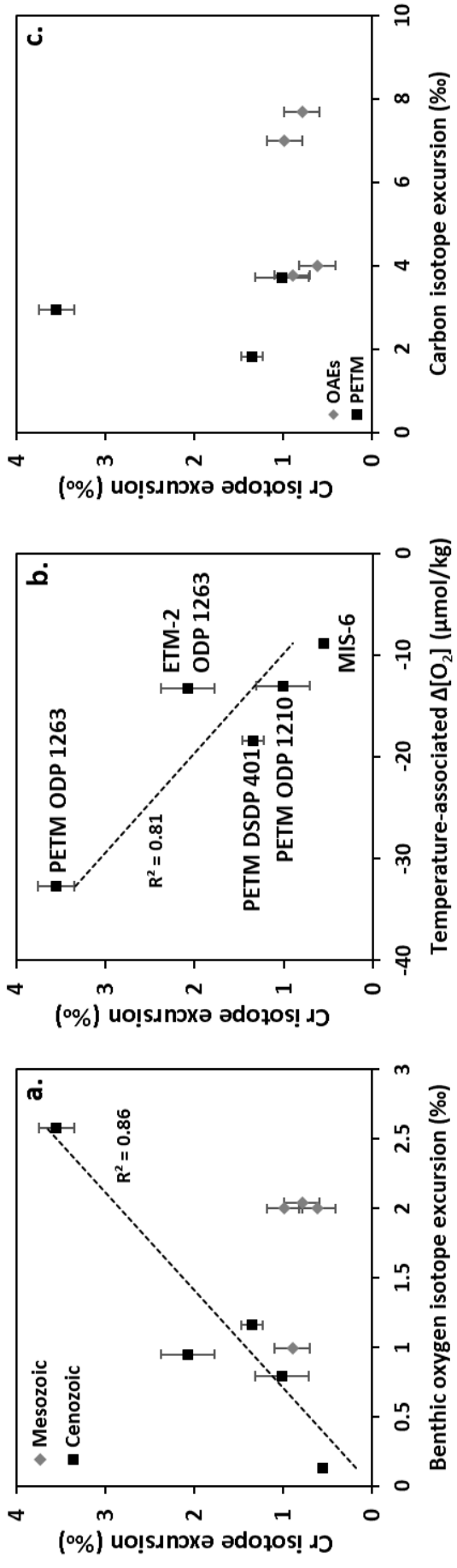

Figure 4.12: The Cr isotope excursion size strongly correlates with the benthic oxygen isotope excursion for the Cenozoic but not for the Mesozoic (Nunes and Norris, 2006; McCarren et al., 2008; Westerhold et al., 2011) **(a)**. Changes in dissolved oxygen are calculated by translating the oxygen isotope excursion into temperature-associated dissolved oxygen loss by following Broecker and Peng (1982) **(b)**. Chromium isotope excursions do not correlate with CIE of organic carbon both during OAEs and the PETM (Zachos et al., 2003; Zachos et al., 2005; Nunes and Norris, 2006) **(c)**.

During the Cretaceous, Cr isotope excursions vary between -1.10 to +0.79‰. The positive correlation between the $\delta^{18}O$ and $\delta^{53}Cr$ excursions breaks down if these events are added to the overall comparison of climate excursions (Figure 4.12a). Chromium isotope excursions also do not correlate with the magnitude of the CIE during OAEs. A reason for this could be that these samples were measured in bulk carbonates which have a variable composition and are usually dominated by calcareous nannofossils and therefore bulk oxygen and carbon isotopes will record sea surface values. All Cenozoic samples have been measured on planktic foraminifera, which record mostly benthic Cr signatures (Chapter 2) and have been compared to benthic foraminiferal oxygen isotopes. Furthermore, there is a difference in climate state and continental configuration between the Mesozoic and the Cenozoic with the Mesozoic climate sometimes referred to as a 'super greenhouse climate'. The implication of this suggestion is that OAEs may have been fundamentally different to the PETM, the ETM-2 and MIS-6 due to the background climate state. During the Mesozoic, sea levels were generally higher than during the Cenozoic leading to wide-spread shallow epicontinental and marginal seas (Schlanger and Jenkyns, 1976). Following this thought, one is lead to conclude that either the PETM is not a 'failed OAE' *in sensu stricto* (Jenkyns et al., 2010) or it has failed precisely because of differences in background climate, hydrological cycle, and tectonic configuration. Shallow and epicontinental seas experience high nutrient input and productivity creating an environment primed for low-oxygen conditions (Schlanger and Jenkyns, 1976). The comparatively large area covered by shallow seas during the Mesozoic compared to the Cenozoic may have facilitated the development of 'successful' OAEs which were much larger deoxygenation events than the Cenozoic hyperthermals. Similarly, the duration and scale of volcanism may have impacted the difference in the duration and intensity between the OAEs and the Cenozoic hyperthermals by determining the amount of volcanic CO_2 emitted into the atmosphere leading to warmer temperatures. The Mesozoic was a time of exceptional volcanic activity during the Phanerozoic (Jenkyns et al., 2010).

Open ocean deoxygenation during the climate events studied in this chapter is governed by local OMZs. The PETM, ETM-2 and MIS-6 have positive Cr isotopic excursions of up to +3.55‰, +2.08‰, and +0.56‰, respectively, which are partly due to the expansion of large OMZs above the sample locations and, in the case of the PETM and ETM-2, potentially due to changes in ocean circulation warming intermediate waters which would decrease dissolved oxygen concentrations (Chapter 3; Jennions et al., 2015). Chromium isotopic behaviour during the OAEs shows a clearer pattern with a positive excursion during OAE1a, but negative excursions during OAE2 (this chapter, Wang et al., 2016; Holmden et al., 2016). These negative excursions have been attributed to quantitative reduction causing an increase in removal of Cr due to an expansion of euxinic conditions (Wang et al., 2016) or volcanic activity masking redox-related fractionation (Holmden et al., 2016). None of the Cr isotope records from OAE2 generated so far therefore fit the simple hypothesis of isotopic fractionation due to partial reduction in contrast to OAE1a (Reinhard et al., 2014).

In Chapter 3 it is shown that the maximum excursion size in $\delta^{53}Cr$ at the onset of the PETM does not correlate with the CIE recorded by organic carbon. This illustrates that the magnitude of the carbon cycle perturbation itself does not have an impact on $\delta^{53}Cr$ values. Extending this observation, chromium isotope values across multiple events during the Cenozoic as well as the Cretaceous do not correlate with the size of the perturbation to the carbon cycle (Figure 4.12c). This chapter explored the past climatic events of the ETM-2, PETM, OAE1a, OAE2 and the Pleistocene glacial-interglacial cycles using a common framework of $\delta^{53}Cr$ values derived from carbonates. All the studied climate events show varying degrees of deoxygenation with the starkest shifts in $\delta^{53}Cr$ values recorded during the Eocene hyperthermals of the PETM and ETM-2 at Walvis Ridge (ODP Site 1263). The deoxygenation during the PETM and ETM-2 can be attributed to warming directly as well as increased microbial metabolic rates and increased remineralisation of organic matter (Jennions et al., 2015; Chapter 3). Chromium concentrations during the PETM and ETM-2 are closely correlated with the coarse fraction and the planktic foraminiferal abundance which points to a link between deoxygenation and acidification through remineralisation of organic matter into weak acids.

Event	Location	Pre-event	Event	Post event
MIS-6	**NIOP Site 464 (Arabian Sea)**	-	Oxic-Hypoxic?	Oxic
ETM-2	**ODP Site 1263 Walvis Ridge (South Atlantic)**	Oxic	Hypoxic	-
PETM	**Contessa Road (Tethys Sea)**	Altered?	Altered?	Hypoxic
	DSDP Site 401 Bay of Biscay (North Atlantic)	Oxic	Hypoxic-Anoxic	Oxic?
	ODP Site 1210 Shatsky Rise (Pacific)	Oxic	Oxic	Oxic
	ODP Site 1263 Walvis Ridge (South Atlantic)	Oxic	Hypoxic-Anoxic	Oxic
OAE2 (Plenus Cold Event)	**Dover Plenus Marls (proto-North Atlantic)**	Oxic	Oxidative weathering?	-
OAE1a	**Cau (proto-North Atlantic)**	Oxic	Hypoxic	Oxic

Table 4.1 Summary of findings for the palaeo-redox state of bottom waters during OAE1a and OAE2, during the PETM at DSDP Site 401, ODP Sites 1210 and 1263, and the Contessa Road section, during the ETM-2, and during MIS-6. Interpretations of the redox state are based on $\delta^{53}Cr$ results from this study.

In contrast, the OMZ in the Arabian Sea is sensitive to the strength of monsoonal winds and expands during interglacials due to stronger monsoonal winds and less deep convective mixing during winter (Reichart et al., 1997). Chromium isotopes record deoxygenation during MIS6 approximately 145,000 years ago which confirms the downward expansion of the OMZ as evidenced by the C_{org} content of the sediment. Chromium concentrations, however, behave contrary to the expected trend and attain their highest levels during the maximum expansion of the OMZ. Chromium concentrations instead correlate with the C_{org} content. Foraminiferal chromium concentrations in this case are likely to be more related to the preservation potential of organic matter rather than being a direct redox proxy.

The two studied OAEs, OAE1a (Selli Event) and OAE2 (Bonarelli Event), also show different types of behaviour in Cr isotope space. OAE1a is characterised by a clear positive shift in $\delta^{53}Cr$ towards heavier values, whereas OAE2 is marked by a negative shift in Cr isotopes at multiple locations (Wang et al., 2016; Holmden et al., 2016). While the $\delta^{53}Cr$ record of OAE1a displays the expected signature associated with deoxygenation during an event with extreme losses of oxygen, the potential explanation for the $\delta^{53}Cr$ shifts observed during OAE2 is less clear. Two explanations offered include an increase in quantitative reduction due to expanding euxinic environments (Wang et al., 2016) and increased volcanic activity masking the deoxygenation signal (Holmden et al., 2016). It is difficult to explain how $\delta^{53}Cr$ values lighter than Bulk Silicate Earth (BSE) could have been caused by a quantitative reduction of Cr and equally problematic with the volcanic explanation is the long lag between the osmium and chromium isotope excursions (Holmden et al., 2016).

Chromium isotope values during the Plenus Cold Event (OAE2) are very light and are characteristic of heavily oxidised carbonate samples (Bonnand, 2011; Frei et al., 2014; Paulukat et al., 2015). These values suggest oxidation of Cr, potentially through manganese oxides, during the PCE which is in agreement with the observations by Jenkyns et al. (2017). The double Cr enrichment also refutes the suggestion by Orth et al. (1993) that the Caribbean LIP was responsible for all trace metal enrichments during the PCE based on the absence of only single enrichment peaks further away from the LIP. It is more likely that the Cr enrichments in the English Chalk can be attributed to the nearby Arctic LIP (Jenkyns et al., 2017).

Chromium isotopes have initially been used to investigate the Earth's first oxygenation in the Proterozoic (e.g. Frei et al., 2009). Terrestrial Cr(III) oxidises through a reaction with manganese oxides which is thought to require a threshold level of atmospheric O_2 levels of 0.1% - 1% present atmospheric level (PAL; Planavsky et al., 2014) which was reached 1.1 Gyrs ago (Gilleaudeau et al., 2016). Fractionation of Cr during this time has been interpreted as indicating some level of oxygenation of the atmosphere (e.g. Frei et al., 2009; Planavsky et al., 2014). Given the highly reducing state of the Proterozoic, one would therefore also expect high $\delta^{53}Cr$ values compared to modern-day environments.

The $\delta^{53}Cr$ values of the Proterozoic (up to +2‰; Gilleaudeau et al., 2016) extend only slightly beyond the modern range of values in seawater (+1.71‰; Goring-Harford et al., 2018) and are comparable to values during the Mesozoic OAEs (this chapter and references therein). However, the Proterozoic values are considerably lower compared to the Palaeogene hyperthermals suggesting that the hyperthermals were extraordinary events which may relate to the relatively short timescales involved compared to the Mesozoic and Proterozoic events.

4.5. Conclusions

This chapter has provided the first comparison of Cr isotope data and a redox state interpretation for multiple global climate events ranging from the Cretaceous to the Pleistocene. Potential differences in the mechanism for (de)oxygenation were investigated as well as what may have caused the wide range in scale of these events, notably the OAEs in comparison to the Cenozoic hyperthermals. This difference between the OAEs and Cenozoic hyperthermals is still a matter of much debate. This chapter found that the PETM may not have been a so-called 'failed' OAE which may lead to understanding what set the OAEs apart from other climate events in their scale and intensity.

The correlation between chromium isotope excursions and benthic oxygen isotope excursions during the Cenozoic indicates temperature acted as a major control on deoxygenation. Direct temperature-driven solubility effects leading to a loss of dissolved oxygen cannot account for the inferred hypoxic and anoxic conditions during the PETM on Walvis Ridge and the Pleistocene on Murray Ridge and therefore indirect temperature effects, such as enhanced microbial metabolic rates and remineralisation are needed to fully explain severe oxygen losses during the Cenozoic (Chapter 3). During the Cretaceous, this correlation breaks down, which may be due to measurements having been obtained from bulk carbonate. However, a fundamental difference in climate state and continental configuration between the Cretaceous and the Cenozoic priming the Cretaceous for full-scale OAEs experiencing quantitative reduction may provide an alternative explanation. The implication of this would be that climate events may have been fundamentally different between the Mesozoic and the Cenozoic due to background climate and tectonic conditions. Further research into potential differences in the tectonic configuration, volcanic activity, and hydrological cycling (and their effects on climate) is needed. However, a potential reason for this breakdown in correlation could be that the Mesozoic samples are bulk carbonates with a variable composition usually dominated by calcareous nannofossils and therefore recording mixed sea surface and bottom water values. All Cenozoic samples have been measured on planktic foraminifera, which record mostly benthic Cr signatures (Chapter 2).

While Cr isotopes and concentrations in carbonates can contribute valuable information about past dissolved oxygen concentrations, some level of caution is recommended. As both the records from Dover and the Contessa Road Section show, Cr isotopes can be heavily affected by oxidative weathering. Oxidative weathering enriches the carbonate in light Cr isotopes leading to $\delta^{53}Cr$ values lighter than BSE. These light BSE values are the hallmark of heavily altered samples.

Elucidating the potential mechanisms for ocean deoxygenation during periods of past climatic change in both the greenhouse and icehouse worlds has provided evidence for multiple factors driving the different events depending on background climate state and regional setting. Deoxygenation due to current anthropogenic greenhouse gas emissions is thus likely to occur to different extents and a thorough understanding of local climate, oceanography and warming rates is key to deciphering the future behaviour of dissolved oxygen in the oceans.

Chapter 5

Rare Earth Element - Yttrium composition of carbonates

Author contributions and declaration: Dr I.J. Parkinson and Professor D.N. Schmidt provided supervision and advice on the design and execution of the study. Dr B.D.A. Naafs (School of Chemistry, University of Bristol), and Dr L. O'Connor, Dr S. Batenburg, Dr S.A. Robinson and Professor H.C. Jenkyns (Department of Earth Sciences, University of Oxford) provided samples from OAE1a and OAE2, respectively. The International Ocean Discovery Program provided foraminiferal samples from the ETM-2 and the PETM. Professor G.-J. Reichart (Department of Earth Sciences, Utrecht University) provided foraminiferal samples from MIS6. Professor G. Ganssen provided foraminiferal specimens from the North Atlantic. ICP-MS data were acquired with the assistance of Dr S. Hammond (School of Environment, Earth & Ecosystems, The Open University) at the Open University and were processed and interpreted by S.R.C. Remmelzwaal.

Abstract

In this chapter the carbonate samples used in this dissertation were assessed for detrital contamination by monitoring Zr, Ti, and Th concentrations and compared to a mixing line between sample and detrital material. None of the samples are likely to have been impacted by contamination and hence the REE-Y patterns and anomalies have been used to assess palaeo-environmental information of the samples. This study finds that Er/Yb ratios in carbonates are not good depth range proxies but that Y/Ho in carbonates has potential as a proxy for delineating open marine versus near shore environments. Prior to the Plenus Cold Event (OAE2) Y/Ho ratios became very low, which may indicate extensive weathering of the sediment or mixing with volcanically derived trace metals. A negative correlation between Y/Ho and Ce/Ce* during OAE1a and OAE2 indicates that a strenghtened halocline due to increased run-off may have led to a reduction in dissolved oxygen in shallow seas during these events. PETM MREE/MREE* values at Walvis Ridge peak during the main episode of hypoxia as determined by Cr isotopes. This was potentially caused through elevated nutrient input from river run-off which would have created a reduction in dissolved oxygen through enhanced biological activity.

5.1. Introduction

The rare earth elements (REE) or lanthanides are a group of metals with similar electrochemical properties and therefore display similar chemical behaviour. This group consists of fourteen elements from lanthanum (La) to lutetium (Lu). Most REEs have a single oxidation state (3+) apart from cerium (Ce) which can also exist as 4+ and europium (Eu) which can also exist as 2+. Yttrium (Y) is not a lanthanide but is often included in this group as it forms 3+ ions and has an almost identical ionic radius to holmium (Ho). The REE-Y elements can be divided into light REEs (LREE) from La to neodymium (Nd), middle REEs (MREE) from (samarium) Sm to dysprosium (Dy), and heavy REEs (HREE) from Ho to Lu. An electron is added to the 4f electron shell each time the atomic number of the REEs increases. Outermost orbitals shield these electrons and have the effect of preventing large variations in chemical activity normally caused by the changing electron configuration of an element.

Due to their behavioural coherency, the REE-Y elements produce smooth patterns when they are normalised to the Post-Archaean Australian Shale (PAAS; Taylor and McLennan, 1985). A recent study updated the PAAS values using a more accurate analytical technique and measured thulium (Tm) and ytterbium (Yb) concentrations in the shale rather than deriving abundances through interpolation (Pourmand et al., 2012). In this dissertation, the traditional Taylor and McLennan (1985) REE-Y abundances are used to remain consistent with the abundant published literature. Differences in chemical behaviour of the REE-Y elements can be quantified from the PAAS-normalised data by either calculating REE anomalies (REE/REE*) or by assessing the slope of the PAAS-normalised patterns (normalisation is denoted by the subscript *SN*; e.g. (Webb and Kamber 2000; Lawrence et al., 2006; Qu et al., 2009; Bonnand, 2011; Tostevin et al., 2016; Osborne et al., 2017):

Equation 5.1: $$\frac{Eu}{Eu^*} = \frac{Eu_{SN}}{({Sm_{SN}}^2 * Tb_{SN})^{1/3}}$$

Equation 5.2: $$\frac{Gd}{Gd^*} = \frac{Gd_{SN}}{({Tb_{SN}}^2 * Sm_{SN})^{1/3}}$$

Equation 5.3: $$\frac{Ce}{Ce^*} = \frac{Ce_{SN}}{[Pr_{SN} * (Pr_{SN}/Nd_{SN})]}$$

Equation 5.4: $\left(\frac{Er}{Yb}\right)_{SN} = \frac{Er_{SN}}{Yb_{SN}}$

Equation 5.5: $\frac{Y}{Ho} = \left[\left(\frac{Y_{SN}}{Ho_{SN}}\right) * 26.2\right] / K$

Equation 5.6: $\frac{HREE}{LREE} = \frac{Yb_{SN}}{Nd_{SN}}$

Equation 5.7: $\frac{MREE}{MREE^*} = \left(\frac{Gd_{SN} + Dy_{SN}}{2}\right) / \left(\frac{Nd_{SN} + Yb_{SN}}{2}\right)$

Cerium, europium and gadolinium anomalies as well as the MREE/MREE* and HREE/LREE ratios are negative when smaller than 1, positive when larger than 1 and there is no anomaly when equal to 1. Cerium anomalies have been calculated in different ways throughout the literature: either relative to La and Pr (e.g. (Zhou et al., 2016; Osborne et al., 2017) or to Pr and Nd (e.g. Lawrence et al., 2006; Tostevin et al., 2016). In this dissertation Ce anomalies are calculated relative to Pr and Nd due to the anomalous behaviour of La, which potentially results in artificially large Ce anomalies (e.g. Webb and Kamber, 2000).

Seawater ratios of Y/Ho are calculated following Qu et al. (2009) who found that Y/Ho ratios in carbonates are enriched in Ho relative to Y and therefore are fractionated with respect to seawater. The number 26.2 is representative of the continental crust ratio (Kamber et al., 2005). *K* = 0.695 and is the ratio of the distribution coefficients of Y and Ho, which can be taken as the average partition coefficient of Y/Ho between seawater and carbonates (Qu et al., 2009). This division by *K* recasts all the measured carbonate Y/Ho values into seawater values.

5.1.1. Chemical behaviour of REE-Y in the environment

The shape of the REE-Y pattern can be used to assess what the likely origin is of the REE-Y in sediment samples and therefore how representative samples are of seawater conditions or whether these are affected by post-depositional processes. The REE-Y elements are primarily delivered to the ocean through fluvial, aeolian and hydrothermal inputs (e.g. (Elderfield et al., 1990; Douville et al., 1999). Rivers are the primary source of REEs to the ocean (Dubinin, 2004). River water contains REEs in both suspension and dissolved state and carry a so-called 'flat' REE-Y pattern reflecting the pattern of the continental crust (Figure 5.1) but can be highly influenced by the local lithology of the drainage basin

(e.g. Dupré et al., 1996; Rachold et al., 1996). The REE-Y pattern of rivers is also heavily impacted by properties such as pH of the river water itself (Goldstein and Jacobsen, 1988; Elderfield et al., 1990; Sholkovitz, 1993). However, the REE-Y distribution pattern rapidly changes to a seawater-like pattern with characteristic anomalies as soon as riverine waters mix with seawater (Figure 5.1; Elderfield et al., 1990). While REE-Y particles in suspension settle on continental shelves away from the river, dissolved REE-Y is further transported to the open ocean resulting in concentrations of 2-50 pM in well-oxygenated seawater (Bertram and Elderfield, 1993; Sholkovitz, 1993). A secondary input of REE-Y elements into the ocean is through hydrothermal activity. Hydrothermal fluids in marine settings have high concentrations of MREEs relative to LREEs and HREEs (Figure 5.1) and are enriched in europium (Eu) due to high temperatures and a low pH leading to positive Eu anomalies with values of >1 (e.g. Bau, 1991; James et al., 1995; Bau and Dulski 1996).

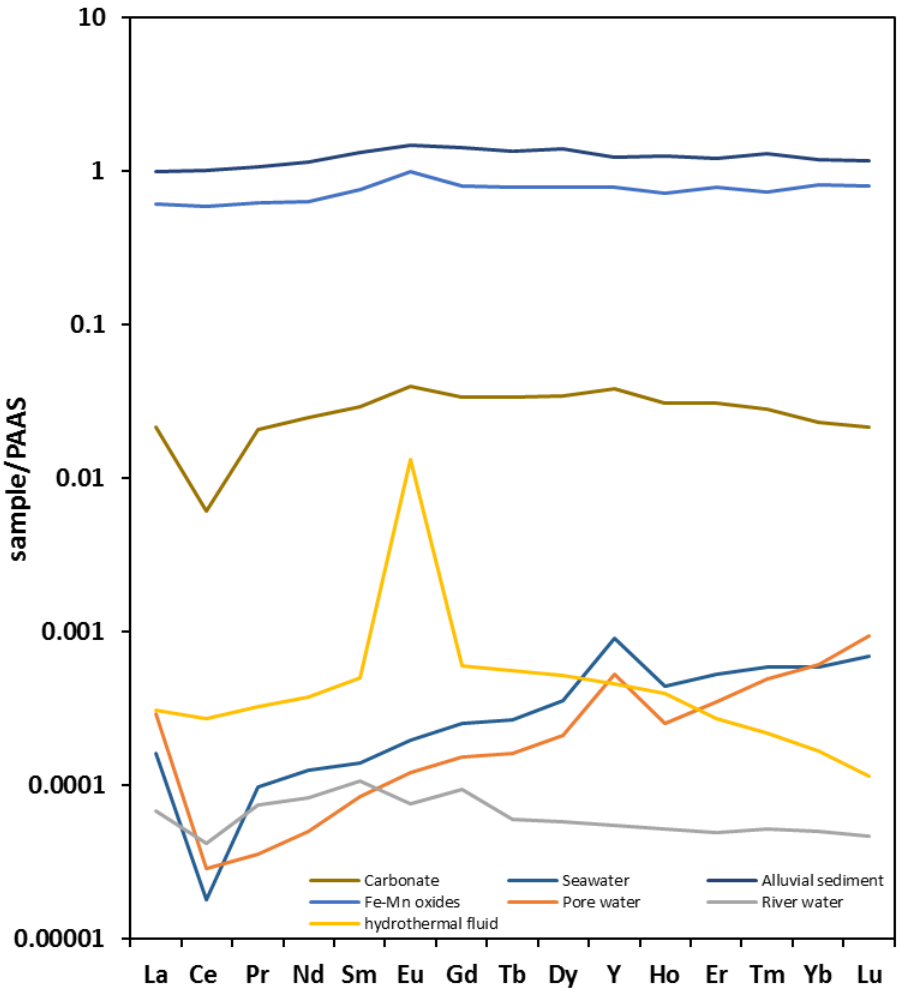

Figure 5.1: REE-Y patterns for carbonate (this study), seawater (Zhang and Nozaki, 1998), Fe-Mn oxides (Bau and Dulski, 1996), pore water (Soyol-Erdene and Huh, 2013), hydrothermal fluid (James et al., 1995), river water (Soyol-Erdene and Huh, 2013), alluvial sediment (Kamber et al., 2005).

The REE-Y elements are fractionated in seawater relative to crustal values (e.g. Taylor and McLennan, 1985), which is largely caused by differences in partition coefficients between seawater and suspended sediments (predominantly Fe-Mn oxyhydroxides and clays) (e.g. Palmer, 1985; Bau et al., 1996; Schijf et al., 2015; Osborne et al., 2017). These partition coefficients illustrate that the solubility and surface complexation as the atomic mass of REEs increases. Light REEs are preferentially scavenged from seawater by adsorption processes during sedimentation (Byrne and Kim, 1990; Schijf et al., 2015). The combination of this chemical behaviour results in seawater enriched in HREE and depleted in LREE (Sholkovitz, 1995; Zhang and Nozaki, 1998). Seawater from different water masses in the global ocean have been found to have distinct REE patterns as REE concentrations covary with salinity (German et al., 1995). Other studies also found that Pacific seawater is depleted in MREE and enriched in HREE, whereas the North Atlantic Ocean has high MREE concentrations and is relatively depleted in HREE (Osborne et al., 2017 and references therein). High MREE concentrations and low HREE concentrations relative to LREE are indicative of fluvial and aeolian inputs and the North Atlantic Ocean is therefore linked to young water with a REE-Y composition close to continental inputs (e.g. Elderfield et al., 1990; Greaves et al., 1994). As waters age and LREEs are scavenged and HREEs enriched in seawater, the REE-Y pattern changes and high HREE enrichments in combination with relatively low MREE concentrations are indicative of older water masses (Osborne et al., 2017). Seawater is also characterised by large negative Ce and positive Y and La anomalies (Figure 5.1). Europium anomalies in seawater range from 1.05 - 1.17 and Gd/Gd* in modern seawater falls within 1.05 - 1.23 (Zhang and Nozaki, 1998).

Positive Y anomalies develop in seawater due to a difference in speciation between Y and Ho (the neighbouring REE in the REE-Y pattern), such that Ho (and the REE in general) is preferential adsorbed on to suspended particles (Bau et al., 1997). This process produces $Y/Ho_{seawater}$ ratios in open seawater that range between 60-90 (Bau et al., 1997; Lawrence et al., 2006). $Y/Ho_{seawater}$ ratios are also elevated in the shallow marine environment with ratios of 30-60 (Bonnand, 2011). The $Y/Ho_{seawater}$ ratio can covary with salinity (Figure 5.2), which may reflect mixing with riverine inputs that have PAAS like Y/Ho ratios. $Y/Ho_{seawater}$ ratios can therefore potentially serve as a proxy for salinity and/or determine whether a sample is from the open ocean or a shallow marine setting.

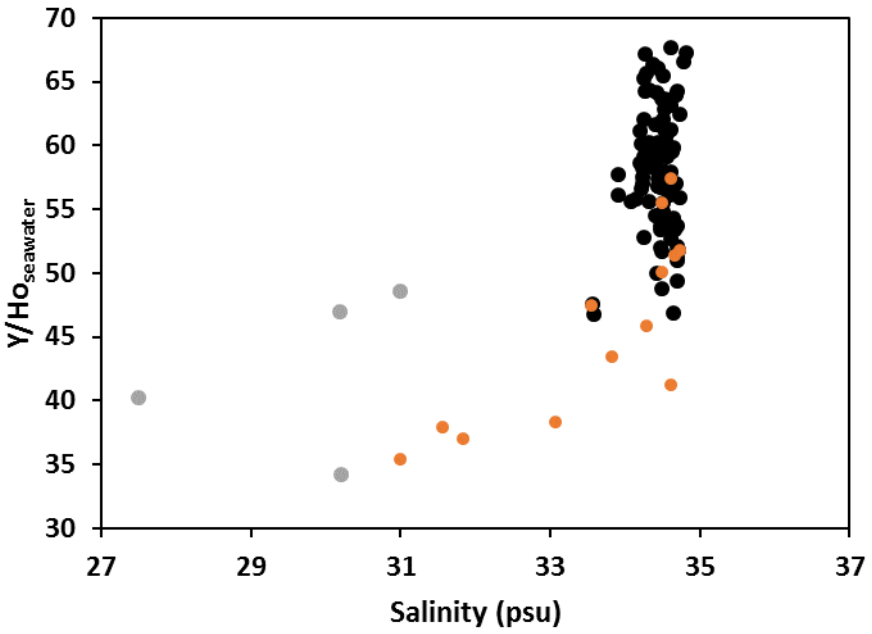

Figure 5.2: Y/Ho for seawater (black; Zhang and Nozaki, 1998), river and estuarine waters (grey; Nozaki et al., 1997), and coastal/offshore waters (Nozaki and Zhang, 1995). Low salinity waters have lower Y/Ho ratios.

The negative Ce anomaly characteristic of seawater REE-Y patterns forms in well-oxygenated seawater, where Ce(III) is oxidised to Ce(IV) on the surface of Mn oxyhydroxides and Mn oxides (German et al., 1991). Ce(IV) is insoluble and particle reactive, which depletes the seawater in Ce relative to trivalent REEs (De Baar et al., 1988; German and Elderfield, 1990). Because of the high reduction potentials of Mn and Ce the oxidation of Ce by Mn can only occur in seawater with high oxygen concentrations. Cerium anomalies vary widely in size in the modern ocean and respond to redox changes in the water column (e.g. De Baar et al., 1991; De Carlo and Green, 2002). The negative Ce anomaly which develops in oxic surface waters will diminish in less well-oxygenated intermediate water and is absent in deep anoxic waters in modern stratified settings such as the Black Sea due to the release of Ce from Mn-rich particles (German et al., 1991). In manganous seawater positive Ce anomalies form underneath the Mn redoxcline (e.g. De Carlo and Green, 2002).

In seawater Er/Yb ratios vary with depth (Figure 5.3) and are extremely variable at shallower depths (1.0-1.4) where values decrease with depth. Deep waters generally have a Er/Yb ratio of less than 1.1 but follow different trends with profiles either constant below a depth of approximately 2 km (Zhang and Nozaki, 1996, 1998) or with slightly increasing Er/Yb ratios with depth of up to 1.2 in water deeper than 4 km (German et al., 1991; Figure 5.3). Er/Yb ratios have been proposed to be a rough indicator of depth but this may be complicated by the Er enrichment in deep waters (German et al., 1991; Bonnand, 2011).

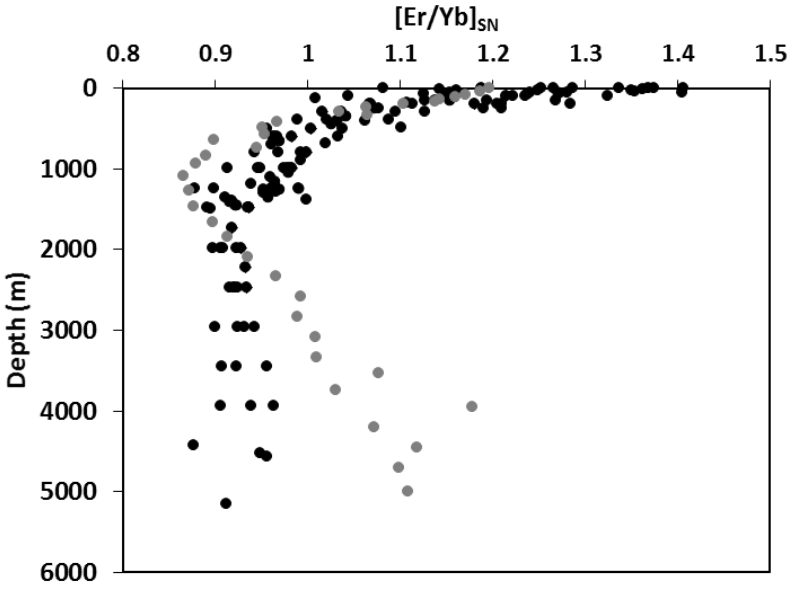

Figure 5.3: $(Er/Yb)_{SN}$ for modern seawater. Black circles are from Zhang and Nozaki (1996), whereas grey circles are from German et al., 1991).

5.1.2. REE-Y elements in carbonates

The carbonate record is thought to reflect seawater REE-Y patterns although this is heavily dependent on the type of carbonate (e.g. Tostevin et al., 2016). Sedimentary foraminifera, for example, record a global curved array of REE patterns in MREE/MREE* to HREE/LREE space which is similar to the curved array observed in seawater measurements across the global oceans (Osborne et al., 2017). REE-Y is present in three distinct phases in carbonates: lattice-bound, Fe-Mn coating-bound, and in detrital material with approximately 90% of REEs bound to the coating and typically low concentrations in the lattice (Palmer, 1985). REE-Y patterns in the coating are likely controlled by the relative concentrations of dissolved REE-Y in seawater, whereas REE-Y in the lattice phase is dominated by the solubility of REEs and the difference in size of the ionic radius to that of Ca^{2+} (Palmer, 1985). REEs in the lattice are taken up during precipitation of the carbonate, whereas coatings develop post-depositionally (Palmer, 1985; Palmer and Elderfield, 1986). Laser ablation studies indicate that in sedimentary foraminifera a large proportion of REE-Y is adsorbed between the inner calcite layers (Roberts et al., 2012). Lattice-bound REE-Y elements have high distribution coefficients (D_{REE} = 100-500) and have been proposed to reflect several palaeo-environmental conditions (Haley et al., 2005). Other studies conclude that uncleaned foraminifera (those including a coating phase) reflect bottom and pore water conditions and can be useful as proxies for large-scale oceanographic changes as well (e.g. Roberts et al., 2012; Osborne et al., 2017). Although skeletal carbonates are pure and often minimally contaminated by other phases, they form through complex biomineralisation and may therefore superimpose a species-specific fractionation onto the REE-Y pattern, which is at present poorly constrained (e.g. Tostevin et al., 2016; Osborne et al., 2017).

5.2. Materials and Methods

The REE-Y composition was determined for samples at the same time as the measurement of Cr concentrations by ICP-MS. Samples included in the study of REE-Y compositions are Holocene planktic foraminifera from the North Atlantic and Caribbean (T86-15S and Karibik; Chapter 2), Pleistocene planktic foraminifera from the Arabian Sea (NIOP 464; Chapter 4), the Palaeogene planktic foraminifera from the South Atlantic and North Pacific the Palaeocene-Eocene Thermal Maximum (PETM) and the Eocene Thermal Maximum 2 (ETM-2) (ODP Sites 1263 and 1210; Chapters 3 and 4). Besides foraminifera, bulk carbonate REE-Y compositions were measured for the Cretaceous Ocean Anoxic Events 1a and 2 from Cau (Spain) and Dover (UK), respectively (Chapter 4).

Approximately 0.01 g of each sample was dissolved in cold 0.5M acetic acid, dried to incipient dryness and re-dissolved and diluted in 2% HNO_3 by 4000 times to produce a 100 ppm Ca solution. Matrix-matched synthetic standards doped with 100 ppm Ca and containing trace elements at a range of concentrations were used as calibration. Chromium was measured in O_2 collision mode on an Agilent 7500s ICP-QQQ-MS at the School of Environment, Earth and Ecosystem Sciences at the Open University. Replicates of the dolomite standard reference JDo-1 were measured to determine an external reproducibility of REE-Y concentrations within ~9% and up to ~16% for REE anomalies. The REE-Y concentrations of samples are normalised against the Post-Archaean Australian Shale (PAAS) REE-Y values (Taylor and McLennan, 1985).

5.3. Results

Rare earth element - yttrium concentrations vary by roughly two orders of magnitude in the carbonates measured. Holocene and Pleistocene foraminifera have lower REE-Y concentrations than Palaeogene foraminifera and Cretaceous bulk carbonate samples (Figures 5.4-5.9). The REE-Y concentrations in this study are comparable to published values (e.g. Palmer, 1985; Palmer and Elderfield, 1986; Webb and Kamber, 2000; Nothdurft et al., 2004; Haley et al., 2005; Frimmel, 2009; Bonnand, 2011; Roberts et al., 2012; Tostevin et al., 2016; Osborne et al., 2017).

5.3.1. Palaeogene planktic foraminifera from Walvis Ridge (ODP Site 1263)

The REE-Y patterns for both PETM and ETM-2 samples from Walvis Ridge are similar (Figure 5.4). Planktic foraminifera from the PETM have well-defined negative Ce, and positive Gd and Y anomalies. By contrast, in the ETM-2 samples the Y anomaly is not well-defined, and the negative Ce anomaly is prominent. Both the PETM and ETM-2 foraminifera have REE-Y patterns that show an enrichment in

HREE (average HREE/LREE = 2.08 for the PETM and 1.75 for the ETM-2). MREE enrichments are small for both the PETM (average MREE/MREE* = 1.05) and the ETM-2 (average MREE/MREE* = 1.10). One sample from the PETM (ODP 1263 14H-1 101-103 cm) has a completely different REE-Y pattern, which shows the lower levels of HREE enrichment than the other PETM samples (HREE/LREE = 1.07) but is extremely enriched in MREE (MREE/MREE* = 1.76) compared to the average MREE value. The Y/Ho ratio (Y/Ho = 47.6) is of the same size as the other samples (average Y/Ho = 47.2) despite the high MREE levels. The Ce anomaly for this PETM sample (Ce/Ce* = 0.71) is much higher than average (average Ce/Ce* = 0.58), however. All samples from the PETM also have small positive Gd and Eu anomalies (average Gd/Gd* = 1.24, average Eu/Eu* = 1.26). Average Ce anomalies and Y/Ho ratios for the ETM-2 are Ce/Ce* = 0.38 and Y/Ho = 43.93.

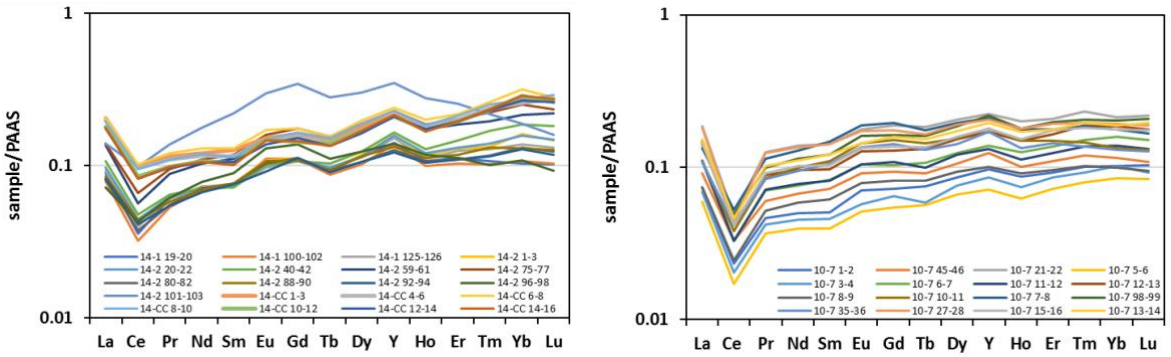

Figure 5.4: REE-Y patterns for bulk planktic foraminifera from across the PETM (left panel) and the ETM-2 (right panel) at Walvis Ridge (ODP Site 1263).

5.3.2. Palaeogene planktic foraminifera from Shatsky Rise (ODP Site 1210)

Planktic foraminiferal samples from the PETM at Shatsky Rise have extremely pronounced negative Ce/Ce* anomalies (average Ce/Ce* = 0.11; Figure 5.5). The REE-Y patterns also shows these samples on average have gadolinium (Gd/Gd* = 1.12), europium (Eu/Eu* = 1.23) and yttrium (Y/Ho = 45.97) anomalies. There is a small enrichment in HREE or MREE compared to LREE (average HREE/LREE = 1.54; average MREE/MREE* = 1.30). While most samples have similar REE-Y concentrations and patterns, two samples have higher and lower concentrations (ODP 1210 20H-6 67-68 cm, ODP 1210 20H-6 76-77 cm, respectively). These two outliers show the same general REE-Y pattern as the other samples.

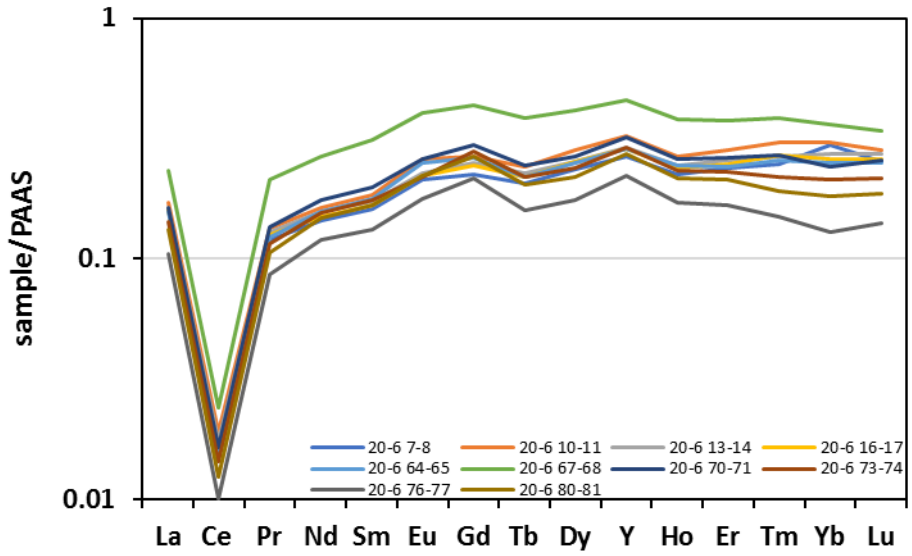

Figure 5.5: REE-Y patterns for bulk planktic foraminifera from across the PETM at Shatsky Rise (ODP Site 1210).

5.3.3. Pleistocene planktic foraminifera from the Arabian Sea (NIOP Site 464)

Both the bulk planktic foraminiferal and single-species *O. universa* samples show the similar REE-Y patterns with small Ce and Eu anomalies and a well-defined Y anomaly (average Ce/Ce* = 0.80; average Eu/Eu* = 1.19; average Y/Ho = 51; Figure 5.6). There is a slight enrichment in HREE and MREE compared to LREE. One sample (NIOP 464 152 *O. universa*) has much lower REE-Y concentrations, a near-absent Ce anomaly (Ce/Ce* = 0.97) and a smaller Y anomaly (Y/Ho = 48.01). Bulk foraminifera consistently have higher REE-Y concentrations than *O. universa* picked from the same sample.

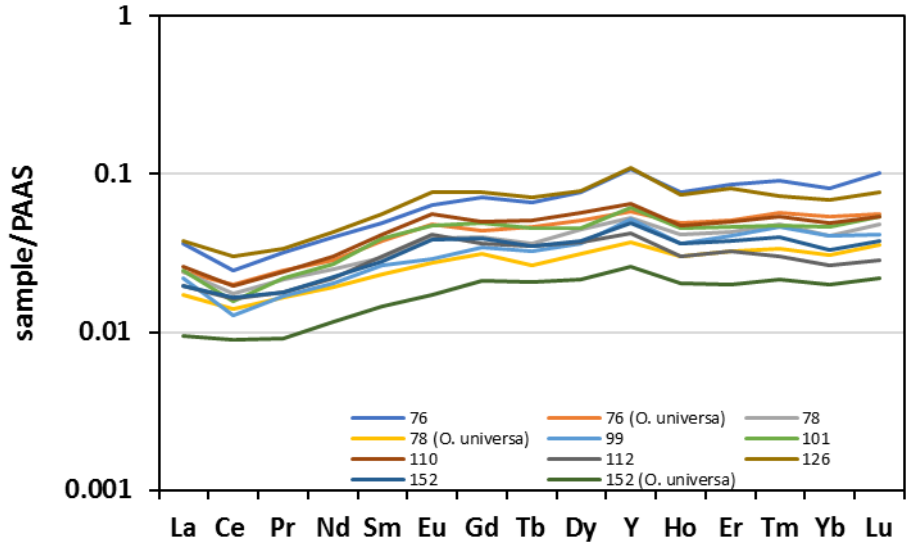

Figure 5.6: REE-Y patterns for bulk planktic foraminifera from across the Pleistocene at Murray Ridge in the Arabian Sea (NIOP Site 464).

5.3.4. Holocene core-top planktic foraminifera

Holocene single-species planktic foraminifera from the Caribbean and North Atlantic have similar REE-Y patterns and concentrations (Figure 5.7). Both have pronounced Ce anomalies (Ce/Ce* = 0.37 for the Caribbean and Ce/Ce* = 0.31 for the North Atlantic) and are relatively enriched in the MREE compared to HREE and LREE with MREE/MREE* = 1.61 and HREE/LREE = 0.92 for the Caribbean, and MREE/MREE* = 1.49 and HREE/LREE = 0.92 for the North Atlantic. Foraminifera from the North Atlantic have similar Y/Ho ratios (Y/Ho = 48.78) to foraminifera from the Caribbean (Y/Ho = 47.44). Differences in size fraction (>500 µm and 250-500 µm) have no effect on the REE-Y pattern or concentrations. In the Caribbean, *G. ruber* (pink) has slightly elevated REE-Y concentrations compared to other planktic foraminifera.

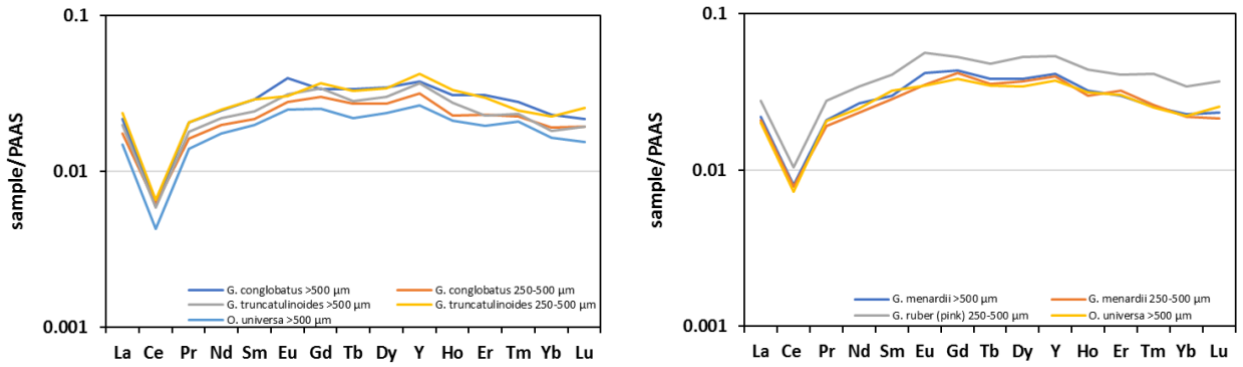

Figure 5.7: REE-Y patterns for single species planktic foraminifera (*G. conglobatus, G. truncatulinoides, O. universa, G. menardii, G. ruber* (pink)) from different size fractions (250 – 500 µm and >500 µm) from Holocene core tops in the North Atlantic Ocean (T86-15S; left panel) and Caribbean Sea (right panel).

5.3.5. Cau limestone (Aptian/Albian)

The bulk limestone samples from Cau (Figure 5.8) have REE-Y patterns which show a distinct Ce anomaly (Ce/Ce* = 0.71), Gd anomaly (Gd/Gd* = 1.20), and Eu anomaly (Eu/Eu* = 1.16). Most samples also have a small Y anomaly, although it is absent in some samples (Y/Ho = 39.4 to 50.9). Limestones are enriched in MREE compared to LREE and HREE (MREE/MREE* = 1.39; HREE/LREE = 0.84). Two samples (3 and 88) have lower REE-Y concentrations than the other carbonate samples. Sample 77 has similar LREE and MREE concentrations as all the other carbonate samples (sample 3 and 88 excluded) but has much lower HREE concentrations (HREE/LREE = 0.61).

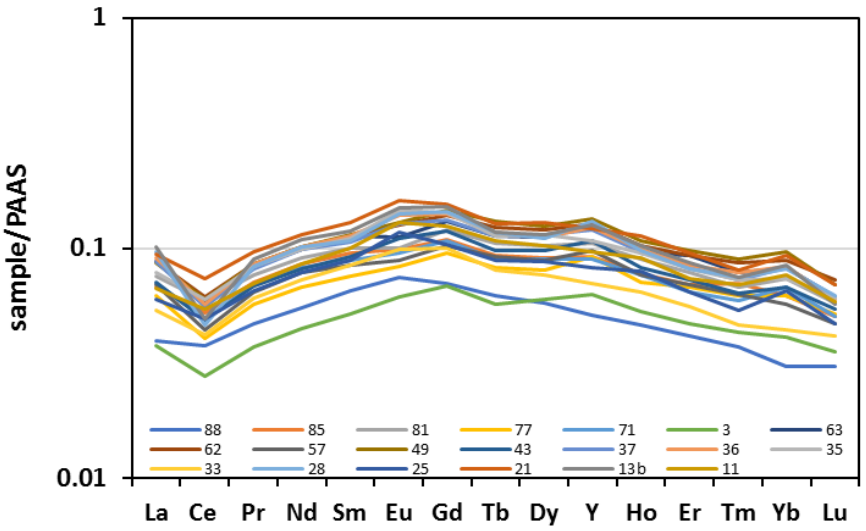

Figure 5.8: REE-Y patterns for bulk limestone across OAE 1a from the Cau drill core in SE Spain.

5.3.6. Plenus Marls from the English Chalk at Dover (Cenomanian/Turonian)

The bulk carbonate samples from the Plenus Marls at Dover (Figure 5.9) have REE-Y patterns with a prominent Ce anomaly and Y/Ho ratio (Ce/Ce* = 0.51; Y/Ho = 42.8) as well as small Gd and Eu anomalies (Gd/Gd* = 1.22; Eu/Eu* = 1.13). The Plenus Marl samples are enriched in MREE compared to LREE and HREE (MREE/MREE* = 1.31, HREE/LREE = 1.06).

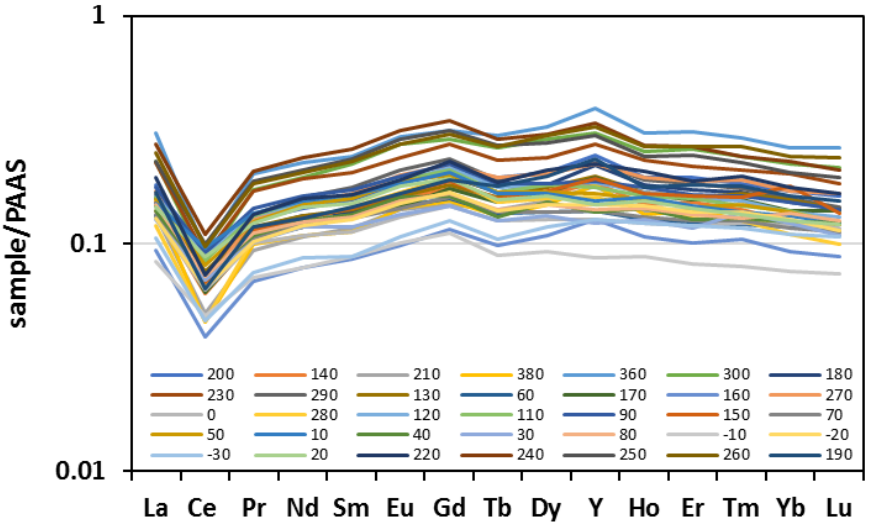

Figure 5.9: REE-Y patterns for bulk limestone across Ocean Anoxic Event 2 from the Dover Plenus Marl section in the English Chalk.

5.4. Discussion

Carbonate REE-Y patterns are thought to reflect the chemical composition of the seawater from which they precipitated (e.g. Palmer and Elderfield, 1986; Roberts et al., 2010, 2012). While REE-Y patterns

between seawater and carbonates are similar overall with a negative Ce anomaly and general enrichment in MREE and HREE relative to LREE, there are notable differences (e.g. Frimmel et al., 2009). Firstly, REE-Y is highly concentrated in carbonates compared to seawater by an order of up to 3 magnitudes (Figures 5.2-5.9; e.g. Zhang and Nozaki, 1998). Secondly, seawater has a pronounced positive Y anomaly which is not always well-defined, or even present at all, in carbonates.

5.4.1. Detrital contamination

To determine whether the carbonate samples analysed in this study were contaminated by detrital phases like PAAS, the concentrations of Zr, Ti, and Th were compared to the total REE-Y concentrations of the samples. Zirconium, Ti and Th are highly concentrated in detrital material such as clays and shales. REE-Y elements and Zr, Ti and Th would positively correlate if the carbonates are contaminated. However, there is no correlation between the REE-Y elements and elements indicative of contamination (Figure 5.10). There seem to be two groups in Th-REE space, a set with a positive correlation with low total REE but an increase in Th, and a set with no correlation and high REE and low Th. The high REE and low Th group are the PETM foraminiferal samples, whereas the low REE and high Th group is comprised of bulk limestone samples and foraminiferal samples from ETM-2 and the Pleistocene. Modern core-top foraminifera have both low total REE and Th concentrations. The highest REE-Y concentrations (of up to 188.9 ppm) have low detrital values.

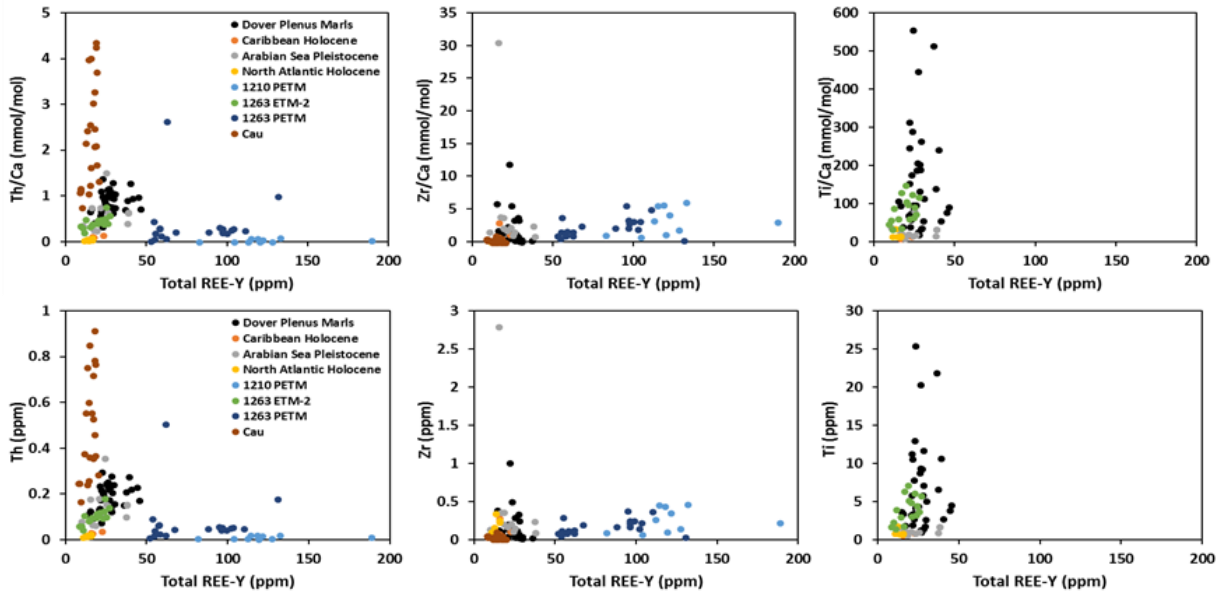

Figure 5.10: Assessment of potential contamination by looking at correlations between total REE-Y concentrations and Th (left panel), Zr (middle panel) and Ti (right panel). The cut-off concentration of Zr for likely contaminated samples is 1 ppm.

The bulk carbonates from Cau have the highest Th concentrations of up to 0.91 ppm (Figure 5.10) but have a low Zr content (< 0.05 ppm; Figure 5.10). A cut-off of 1 ppm Zr is used to exclude carbonates

which may have been compromised by detrital material (Gilleaudeau et al., 2016). Only one sample within this study has Zr concentrations above the 1 ppm cut-off with 2.79 ppm (Pleistocene *O. universa* from NIOP 464 78). These *O. universa* have a lighter isotopic composition ($\delta^{53}Cr$ = +0.22‰) than bulk planktic foraminifera from the same sample ($\delta^{53}Cr$ = +0.52‰) which is not observed in other samples (Supplementary Material A) and may be due to contamination with detrital material with bulk silicate earth values ($\delta^{53}Cr$ = -0.12‰) as suggested by Zr concentrations.

5.4.2 Environmental setting

Despite differences between seawater and carbonate REE-Y patterns, parameters such as Er/Yb and Y/Ho can nonetheless constrain the environmental setting in which the analysed carbonates were formed. The Er/Yb ratio allows for the separation of shallow and deep-water carbonates (German et al., 1991; Zhang and Nozaki, 1996, 1998; Bonnand, 2011), whereas Y/Ho ratio is used to determine whether a carbonate was precipitated in open marine conditions or in near-shore environments (Bau and Dulski, 1996; Nothdurft et al., 2004).

5.4.2.1. Depositional environment of planktic foraminifera (Palaeogene, Pleistocene, Holocene)

Values for Er/Yb of bulk Palaeogene planktic foraminifera range between 0.68 and 1.34 (Figure 5.11). The Er/Yb range is much smaller for the Pleistocene and Holocene: 0.95-1.23 and 1.18-1.47, respectively. The large range in Er/Yb implies that the depth of deposition at Walvis Ridge and Shatsky Rise varied between >5 km and <500 m during the PETM and ETM-2. While there were large climatic and oceanographic disturbances during the Palaeogene hyperthermals, it is not possible for open ocean sites like Shatsky Rise and Walvis Ridge, which are located in the Pacific and Atlantic Oceans, to have been impacted by such dramatic sealevel changes. ODP Site 1210 on Shatsky Rise has an estimated palaeodepth of ~2400 m and ODP Site 1263 on Walvis Ridge has an estimated palaeodepth of ~1500 m (Pälike et al., 2014). The expected range in the Er/Yb ratio at these two sites would therefore be 0.9-1.0, which is considerably narrower a range than those observed.

In contrast, the Er/Yb ratios of bulk and single-species Pleistocene and Holocene planktic foraminifera have a much narrower range of 0.95-1.23 for the Pleistocene in the Arabian Sea and 1.18-1.47 for the Holocene core-top samples. The implied depth ranges are anywhere between 0-5 km for the Pleistocene and >500 m for the Holocene samples. The core-top foraminifera from the North Atlantic (T86-15S) were collected from a depth of 3271 m (Troelstra et al., 1987) and the Caribbean foraminifera were collected from a depth of 2900 m (Caromel et al., 2014), which again does not confirm the depth range estimated by Er/Yb ratios. In short, despite the similarity of Er/Yb ratios in core-top and down-core planktic foraminifera, and seawater values, the Er/Yb ratios of foraminifera are not good indicators for the depth range at which REE-rich minerals precipitated. Very high Er/Yb ratios (>1.2) could be a

useful indicator for shallow seawater environments (Figure 5.11) although these are still recorded by foraminiferal ferromanganese coatings in intermediate water depths.

The Y/Ho ratios during the PETM varied between 44.40-52.35 on Walvis Ridge and 44.29-48.58 on Shatsky Rise. During the ETM-2 Y/Ho ratios ranged between 41.26-48.14 on Walvis Ridge. In the modern marine environment Y/Ho ratios are between values of ~45 to 90 (corresponding to a salinity of >34‰) (Zhang and Nozaki, 1996, 1998; Bau et al., 1997; Lawrence et al., 2006). This means that the planktic foraminfera that were analysed were deposited in a marine environment with values similar to that of the modern ocean with potential influence from fresher waters at times indicated by the lowest values.

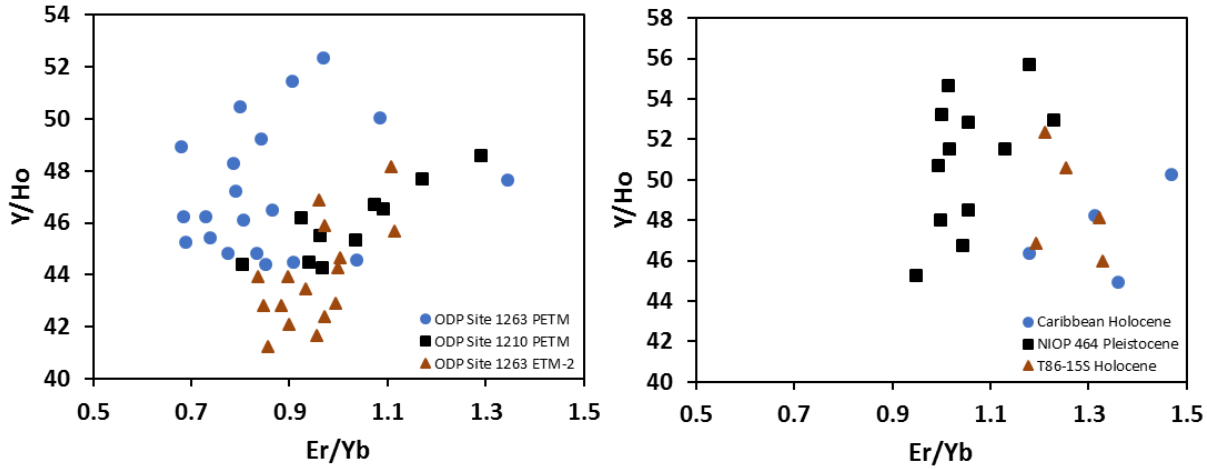

Figure 5.11: Carbonate Y/Ho ratios converted into seawater values (Qu et al., 2009) and $[Er/Yb]_{SN}$ cross-plots for the Palaeogene (left panel) and Pleistocene/Holocene (right panel) foraminiferal samples.

5.4.2.2. Depositional environment of Cretaceous carbonates

During the Cretaceous OAE1a and OAE2, Er/Yb ratios in bulk carbonates varied between 0.92-1.36 and 0.91-1.22, respectively (Figure 5.12). Much like the foraminiferal Er/Yb ratios (Figure 5.12), this variation implies large depth changes between ~1400 m and ~50 m (Figure 5.12), which is a possibility as the bulk carbonate samples were collected on land sections and were deposited in shallow seas (Naafs et al., 2016; Jenkyns et al., 2017). The Y/Ho ratios for these two events range between 40.2 - 50.9 for OAE1a and 36.1 - 50.9 for OAE2 (Figure 5.12). These values indicate more open marine settings but that potentially occasional freshwater inputs were present during at Cau OAE1a (an outer continental shelf location) and that the English Chalk was deposited in environments even nearer to the shore during OAE2. Typically, a cut-off of Y/Ho of 36 is used to distinguish whether authigenic REE-Y from the carbonate samples has been contaminated by non-carbonate phases (e.g. Tostevin et al., 2016). A couple of the samples from the Plenus Marls (DPM +10 to +40) are close to this cut-off with Y/Ho ratios between 36.1 - 36.6, and so the data may be compromised by other processes. This could mean that the

Plenus Marls mixed with phases with non-seawater-like REE-Y patterns (e.g. hydrothermal patterns associated with the High Arctic LIP), although this is unlikely because they have a low average Eu/Eu* of 1.13. Detrital contamination can be excluded due to the low Zr, Th and Ti levels (section 5.4.1.) and the data fall off detrital mixing lines (section 5.4.3.2) and the low Y/Ho ratios are therefore likely of an environmental origin.

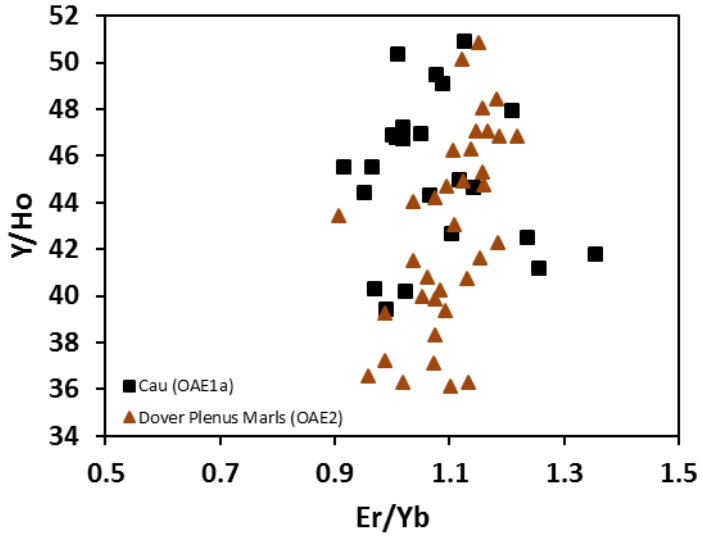

Figure 5.12: Carbonate Y/Ho ratios converted into seawater values (Qu et al., 2009) and $[Er/Yb]_{SN}$ cross-plots for the bulk limestone samples from OAE1a and OAE2.

5.4.3. Bottom water redox conditions

5.4.3.1. Cerium anomalies in planktic foraminifera

See chapter 3 for details on environmental changes during the on PETM determined by planktic foraminiferal Ce/Ce*. Cerium anomalies in planktic foraminifera analysed in this dissertation are remarkably constant compared to other REE-Y indicators but vary widely between sample sites and time periods. The Holocene samples from the Caribbean and North Atlantic and the PETM samples from Shatsky Rise in the Pacific concentrate around Ce/Ce* = 0.5 and 0.2, respectively, and are less variable than the Palaeogene samples from Walvis Ridge (Ce/Ce* = 0.4 - 0.7 and 0.7 – 0.9) and the Pleistocene Arabian Sea samples from Murray Ridge (Ce/Ce* = 1.0 - 1.4; Figure 5.13). A primary difference between these two sets of samples is the fact that over Walvis and Murray Ridge large OMZs are located in the modern ocean which have been thought to have been there in the past as well (e.g. Chun et al., 2010; Reichart et al., 1997). These OMZs have varied in areal and volumetric extent over time and have caused dramatic changes in dissolved oxygen concentrations (Chapters 3 and 4). Cerium anomalies of lower than 0.5 indicate that the Holocene North Atlantic and Caribbean, as well as the PETM Pacific and the ETM-2 Walvis Ridge were well-oxygenated, whereas during the PETM Walvis Ridge and during the Pleistocene Murray Ridge experienced hypoxic to anoxic conditions (Ce/Ce* = 0.5 – 1.0 and Ce/Ce* > 1; Zhou et al., 2016).

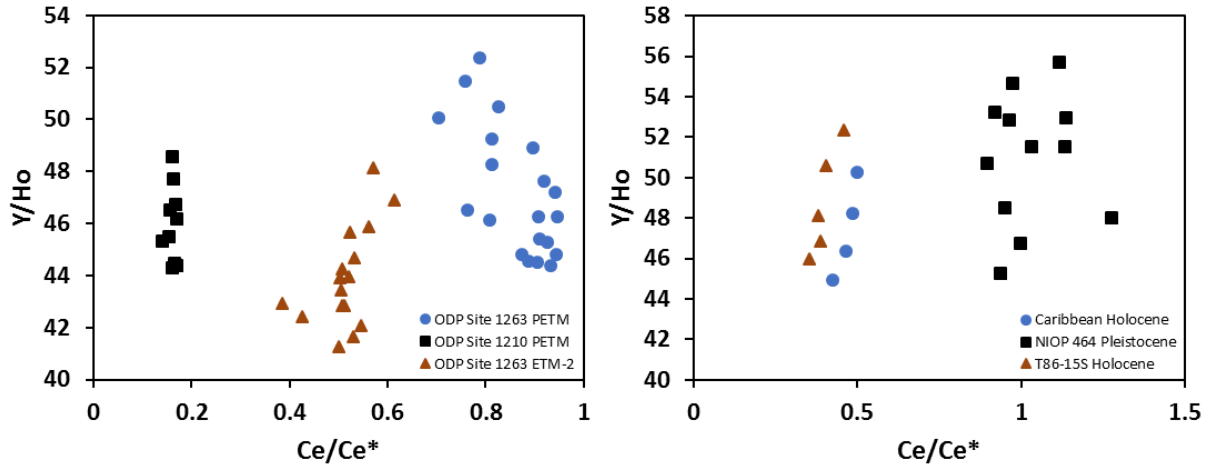

Figure 5.13: Carbonate Y/Ho ratios converted into seawater values (Qu et al., 2009) and Ce/Ce* cross-plots for the Palaeogene (left panel) and Pleistocene/Holocene (right panel) foraminiferal samples.

5.4.3.2. Cretaceous limestones

Cerium anomalies at Cau (OAE1a) indicate a fully hypoxic environment with values between 0.5-1.0. The Dover Plenus Marls (OAE2) are slightly more oxygenated than the Cau limestones and have Ce/Ce* values around the oxic-hypoxic boundary of 0.5. Interestingly, there is a negative correlation between Y/Ho and Ce/Ce* for both Cau ($R^2 = 0.32$; $p = 0.003$) and the DPM ($R^2 = 0.71$, $p << 0.00001$). Similar correlations may be present in NIOP 464 (Figure 5.14) and the PETM Walvis Ridge (Figure 5.14) too, but are statistically not significant. The implications of this would be that at lower salinities (lower Y/Ho ratios) there would be increased hypoxia (higher Ce/Ce* values). Since both sites are located on the shelf it is possible that a lower salinity was caused by an increased freshwater run-off creating a freshwater lens and intensified stratification through a strengthened halocline. Intense water column stratification would in turn lead to lower dissolved oxygen levels. It must be taken into account that the lowest Y/Ho values of the DPM might be contaminated by e.g. volcanic signals (Section 5.4.2.2.).

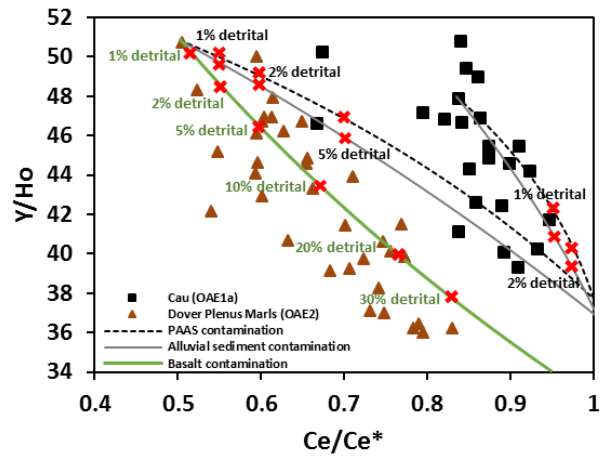

Figure 5.14: Carbonate Y/Ho ratios converted into seawater values (Qu et al., 2009) and Ce/Ce* cross-plots for the Cretaceous OAE1a and OAE2 bulk limestone records. The dashed lines are contamination models between sample and PAAS endmembers (Taylor and McLennan, 1985) and solid grey and green lines are contamination models between sample and alluvial sediment and basalt endmembers, respectively (Robinson et al., 1999; Kamber et al., 2005). Red crosses mark percentage levels of contamination with detrital material.

Since Cau and DPM REE-Y concentrations were obtained from bulk rock samples, the potential effect of mixing between the carbonate REE-Y signal and detrital material was investigated with a linear mixing model (Figure 5.14). For this mixing model, sample DPM +380 was mixed with varying fractions of average basalt values , alluvial sediment values and PAAS values (Robinson et al., 1999; Kamber et al., 2005; Taylor and McLennan, 1985) and the same mixing model was applied to Cau 57 for PAAS and alluvial values. If samples are contaminated, one would expect these to fall on or around a mixing line towards the detrital values of Ce/Ce* (Ce/Ce^*_{PAAS} = 1; $Ce/Ce^*_{alluvial}$ = 1.01; Ce/Ce^*_{basalt} = 0.95) and Y/Ho (Y/Ho_{PAAS} = 37.7; $Y/Ho_{alluvial}$ = 36.8; Y/Ho_{basalt} = 34.1). All Y/Ho ratios in samples (and alluvial values) are recast to seawater values following Qu et al. (2009). Both the impacts of mixing with average alluvial sediment and PAAS on the Y/Ho and Ce/Ce* of the carbonate samples show that the bulk rock analyses of DPM do not fall on the detrital mixing line and that the rough trends in the data between Y/Ho and Ce/Ce* from DPM are steeper than the mixing trends. However, the DPM data do fall on the mixing line with basalt. However, substantial contamination of up to 30% is needed to explain the full spread of the data. While these samples may have experienced an influence by basaltic REE-Y values, there is no evidence that contamination was this severe in these samples (section 5.4.1.). These samples are therefore likely not contaminated and reflect environmental signals. The trend in the Cau data is steeper than the mixing lines. The samples from Cau, however, do fall on or near the mixing lines, in particular the mixing line with average alluvial sediments, which implies these may have been impacted by mixing with clays to a certain extent. For example, to produce a Y/Ho value of 41.8 like that of Cau 88, which falls directly on the alluvial sediment mixing line from a starting composition of Cau 57, 7% of the dissolved sample should have consisted of detrital material. A 7% contamination is unlikely given the very low concentrations of elements such as Zr in the samples that fall below contamination cut-offs (Figure 5.10) and because REE concentrations are lower in Cau 88 than in Cau 57 despite having Ce and Y anomalies closer to that of detrital material. A contamination with detrital material of 7% would require a substantial overall increase in REE-Y concentrations as detrital material has REE-Y concentrations that are an order of magnitude higher than in the carbonates from Cau (Figure 5.15).

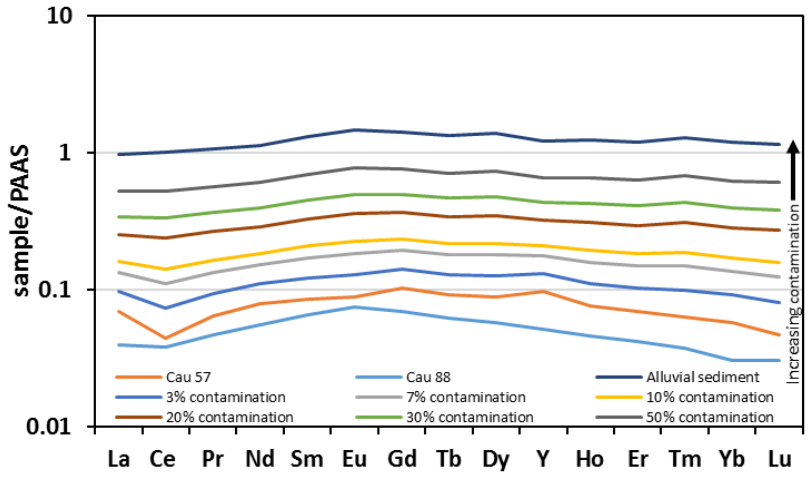

Figure 5.15: Contamination model for Cau samples with 0%, 3%, 7%, 10%, 20 %, 30%, and 50% contamination with alluvial sediment (Kamber et al., 2005).

5.4.4. REE-Y enrichment in carbonates

Holocene and Pleistocene foraminifera have normalised REE-Y ratios between 0.01-0.1 (Figures 5.6, 5.7), whereas Palaeogene foraminifera and Cretaceous bulk carbonates have REE-Y ratios around 0.1 (Figures 5.4, 5.5, 5.8, 5.9). While this may reflect a longer exposure to post-depositional processes, the higher trace metal concentrations could also have been caused by true differences in climatic and geological conditions between the greenhouse worlds of the Palaeogene and Cretaceous and the Pleistocene and Holocene iceworlds. If these concentration differences have an environmental cause it would imply that oceans in past greenhouse worlds had higher REE-Y concentrations (and likely metals in general), possibly through an increased hydrological cycle delivering dissolved metals extensive weathering and run-off or through large-scale sub-marine volcanism (e.g. Jenkyns, 2010).

Recent studies have found that ocean basins have distinct MREE/MREE* and HREE/LREE ratios depending on the age of the water mass and that these are reflected in foraminifera (Osborne et al., 2017). MREE/MREE* ratios are high where inputs (e.g. fluvial or aeolian) of unfractionated REE-Y are high (in the modern North Atlantic Ocean) and HREE/LREE ratios increase while MREE/MREE* decrease with the age of the water mass as REE-Y are increasingly fractionated such as in the modern Pacific Ocean (Osborne et al., 2017). A compilation of carbonate HREE/LREE and MREE/MREE* data from this study show a negative correlation where MREE/MREE* decreases as HREE/LREE increases (R^2 = 0.72; p < 0.00001; Figure 5.16). While this is consistent with the expected REE-Y behaviour in the ocean, the correlation is linear and does not follow the strongly curved arrays found in oxic seawater, oxic pore water and foraminifera in previous studies (Du et al., 2016; Osborne et al., 2017).

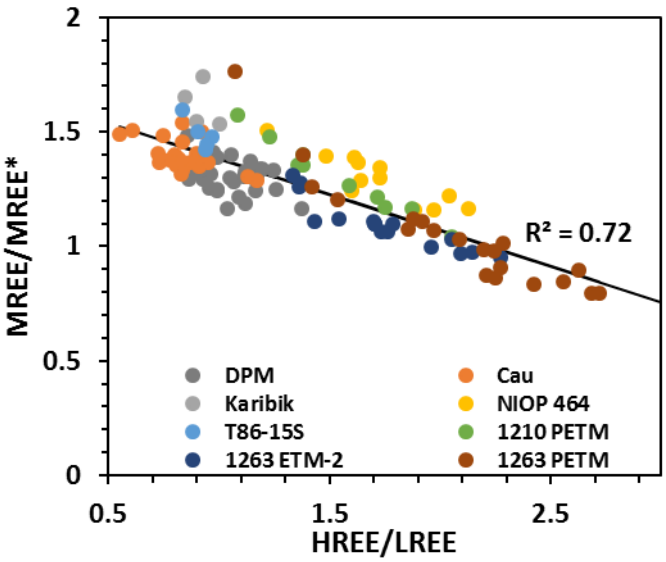

Figure 5.16: MREE/MREE* and HREE/LREE cross-plot for all carbonate samples assessed in this study show a significant negative correlation.

Palaeogene foraminifera from Walvis Ridge in the South Atlantic Ocean have the highest HREE/LREE values of up to ~2.72 and lowest MREE/MREE* values of down to 0.80 (Figure 5.16), while the lowest HREE/LREE values down to 0.55 and highest MREE/MREE* values of up to 1.74 are recorded by Holocene Caribbean and North Atlantic samples as well as Cretaceous carbonates from Cau (Figure 5.16). This suggests that the South Atlantic Ocean was relatively starved from nutrients (trace metals) and represents and older water mass, which confirms potential large scale ocean circulation changes during this time (e.g. Tripati and Elderfield 2005; Lunt et al. 2010; Jennions et al.,, 2015; Chapter 3). On Walvis Ridge MREE/MREE* values peak at 1.76 during the PETM (recorded by ODP Site 1263 14-2 101-103) coinciding with the main episode of deoxygenation determined by Cr isotopes (Chapter 3). A likely implication would be that an increased run-off from the continents due to an intense hydrological cycle could have supplied extra nutrients into the generally oligotrophic area (e.g. Carmichael et al., 2017) producing a microbial and plankton bloom with associated deoxygenation. An elevated input of trace metals and nutrients into the South Atlantic Ocean during the PETM is in clear disagreement with observations of increasing oligotrophy in the open ocean (e.g. Gibbs et al., 2006; Carmichael et al., 2017). High MREE/MREE* values in Holocene Atlantic foraminifera confirm observations with modern Atlantic seawater that water masses are currently relatively young in this area.

5.4.5. Implications of REE-Y for Cr preservation

The preservation of REE-Y patterns similar to the patterns characteristic of seawater with prominent negative Ce anomalies and positive Y/Ho ratios (Figure 5.1; e.g. Zhang and Nozaki, 1998) suggests the carbonate samples assessed in this study have been subject to minimal alteration after deposition. Thus, it is likely that Cr will also not have been overprinted. It must be noted that Fe-Mn coatings and Cr are both thought to be added to carbonates post-depositionally and will therefore be a primary bottom water or pore water signal (Chapter 2).

5.5. Conclusions

In this chapter, I assessed the preservation state of the carbonate samples used for Cr isotopic analyses. Carbonate samples used in this dissertation were checked for detrital contamination by monitoring Zr, Ti, and Th concentrations and by comparing bulk samples to a mixing line between sample and detrital material with PAAS and alluvial sediment values for Ce/Ce* and Y/Ho ratios in the Cretaceous Dover Plenus Marl and Cau bulk carbonate samples. None of the samples used in this dissertation are likely to have been impacted by contamination. All samples show seawater-like REE-Y patterns which suggests a primary seawater signature has been preserved.

In addition, several palaeo-environmental REE-Y indicators were tested for their veracity and potential additional information they could provide about the settings in which the carbonate samples used for Cr isotope analysis were deposited. Er/Yb ratios in carbonates were found not to be good indicators for the depth range at which they were deposited. Y/Ho in carbonates can be used to determine the relative location of the depositional environment to the shore (open marine versus near shore environments). Y/Ho ratios became very low (36.14 – 36.58) during prior to the Plenus Cold Event during OAE2. This may reinforce the hypothesis posed in chapter 4 and by Jenkyns et al. (2017) that authigenic metals in the Plenus Marls experienced extensive weathering down the sediment column or mixing with volcanically derived trace metals during the Plenus Cold Event. A negative correlation between Y/Ho and Ce/Ce* for both shallow marine sites during OAE1a and OAE2 indicates that increased freshwater input strenghtened the halocline leading to a reduction in dissolved oxygen during these events. Palaeogene and Cretaceous carbonates analysed in this study are generally more enriched in REE-Y than younger ones. This suggests that seawater in greenhouse worlds (Palaeogene and Cretaceous) may have had higher dissolved metal concentrations than those in icehouse worlds (Holocene and Pleistocene) either through an intensified hydrological cycle or through increased LIP volcanism. MREE/MREE* values peaked at Walvis Ridge at the same time as the main episode of hypoxia during the PETM as determined by Cr isotopes. A potential explanation is that increased run-off could have supplied more trace metals creating a plankton bloom with associated deoxygenation. This is in clear disagreement with previous studies.

Chapter 6

Conclusions

This dissertation explored the effects of foraminiferal biomineralisation on Cr and whether Cr can be used for palaeoceanographic reconstructions. At the start of this work, the main outstanding questions regarding the use of Cr in carbonates as a redox proxy were focussed on how and where Cr is incorporated in carbonates (specifically the shell remains of foraminifera), what biological control calcifying organisms might have on Cr uptake, and what implications this may have on it the interpretation of Cr isotope data in a palaeoceanographic context. This work has challenged assumptions and previous work, and has deepened the understanding of the incorporation mechanism of Cr into biogenic carbonates through a multipronged investigation of the Cr concentration and distribution, the distribution coefficient and the vital effects associated with Cr uptake in foraminiferal calcite using state-of-the-art analytical techniques. This improved base understanding of Cr in carbonates has allowed for a more thorough assessment of Cr isotopic data as a recorder of the response of oceanic dissolved oxygen to past climatic changes.

This dissertation shows that Cr is incorporated into foraminiferal tests and represents a bottom/pore water signal. LA-MC-ICP-MS measurements show that larger benthic foraminifera *Amphistegina* sp. in culture growth have a distribution coefficient (D_{Cr}) of 250 ± 43 comparable to scleractinian corals (Pereira et al., 2016) and have Cr concentrations between 0.04 to 0.13 ppm under natural seawater Cr concentrations. Chromium is distributed across the whole foraminiferal shell in both the larger benthic foraminifera and planktic foraminifera and is mostly associated with the calcite phase of foraminifera. In planktic foraminifera, Cr concentrations are higher in Mg-rich bands closely linked to the previous location of the primary organic sheet. These bands likely have been a pathway for secondary Cr derived from pore and bottom waters to enter the foraminiferal test. On average, sedimentary foraminifera have an order of magnitude more Cr than foraminifera that were collected before deposition (e.g. by sediment trap, plankton net, culture). Taken all together, the post-depositional addition of Cr by exchange with pore and bottom waters is likely to be the main uptake mechanism of Cr. This suggested post-depositional origin of foraminiferal Cr is corroborated by the presence of two distinct populations in Cr to Fe/Ca and Mn/Ca cross-plots in sedimentary foraminifera based on both laser ablation and nanoSIMS data. The overlap between some core-top and non-sedimentary specimens may provide a tool for assessing the impact of post-depositional incorporation of Cr into foraminiferal tests. Furthermore, there are no interspecies isotope fractionations ("vital effects"). Changes in isotopic composition related to the size of the foraminiferal test are present and may have been caused by surface area/volume ratio

effects on the exchange with Cr in pore and bottom waters. In extension, it is assumed that bulk biogenic carbonate will behave in a similar way to foraminiferal calcite and record bottom/pore water signatures. The conclusion from my work that carbonates record bottom/pore water Cr is in contrast to the previous school of thought which assumed that most Cr is actively incorporated into carbonate structures by living organisms and that Cr in carbonates would therefore record a surface water signature. My findings therefore demand a re-interpretation of the existing carbonate Cr isotope records.

I have therefore applied the knowledge that carbonates, and foraminifera in particular, mostly record post-depositional Cr to past extreme climatic episodes as analogues for present-day anthropogenic warming. As such I explored the implications of large climatic changes are on the development of bottom water hypoxia in the oceans.

During the PETM, foraminiferal Cr isotopes record that bottom water deoxygenation was controlled by local oceanographical factors. This agrees with the observed heterogeneity of Cr in modern oceans and relatively short residence time of Cr in the ocean (e.g. Qin and Wang, 2017; Goring-Harford et al, 2018). Despite the local controls, deoxygenation was a widespread phenomenon in the open oceans during the PETM. Open ocean deoxygenation (and its controlling factors) can mainly be attributed to rising temperatures in intermediate ocean waters caused by a rise in atmospheric CO_2 during the latest Palaeocene. This conclusion is partly based on the strong correlation between the magnitude of the benthic oxygen isotope and the Cr isotope excursions. The warming of intermediate waters, and the increased microbial loop and remineralisation, as well as the decline in oxygen solubility this would have generated would jointly have been able to cause local deoxygenation. If there was any geographical spread of low oxygen waters, it will most likely have originated in the North Atlantic, which is the purported location of a large injection of reduced carbon (Svensen et al., 2004; Gutjahr et al., 2017). Climate model-data comparison results and geochemical records from both this study and previous publications indicate the North Pacific was less impacted by deoxygenation than the Atlantic Ocean. However, Cr isotope work in this study disagrees with previous work on the extent of low-oxygen conditions prior to and after the PETM event itself where other proxies suggest prolonged low oxygen levels throughout the Late Palaeocene and the Early Eocene.

The correlation between chromium isotope excursions and benthic oxygen isotope excursions extends from within the PETM to different climatic events throughout the Cenozoic and confirms intermediate and deep-water temperature is a major control on bottom water deoxygenation. Deoxygenation through solely the direct effects of temperature-driven solubility of dissolved oxygen cannot explain the inferred expansion of hypoxic and anoxic conditions during the PETM, ETM-2 and the Pleistocene. Thus, indirect effects of temperature changes, such as an enhanced microbial metabolic rate and remineralisation are needed to fully drive the severe oxygen losses observed throughout the Cenozoic.

During the Cretaceous, this correlation breaks down, which may have been due to measurements having been obtained from bulk carbonates rather than foraminifera for the Cenozoic Cr measurements. On the other hand, an alternative explanation may be that there is a fundamental difference in climate state and continental configuration between the Cretaceous and the Cenozoic. The Cretaceous hothouse world would have primed the global oceans for wide-spread OAEs. This suggestion implies that climate events in the Mesozoic and in the Cenozoic were potentially fundamentally different due to background climate and tectonic conditions and that initiation mechanisms of climate events during the Mesozoic and Cenozoic therefore cannot be easily compared. This calls into question the hypothesis that the Eocene hyperthermals are smaller ('failed') versions of the OAEs.

Investigating and contrasting potential pathways for ocean deoxygenation during past climatic extremes in the greenhouse and icehouse worlds of the Cretaceous, Palaeogene and Pleistocene has provided an insight into a complex interplay of multiple drivers for the loss of dissolved oxygen depending on the background climate state and regional settings. The extent of modern-day open ocean deoxygenation caused by the anthropogenic greenhouse effect is therefore likely to also be highly controlled by local settings. Thus, closely monitoring local climatic and oceanographical changes is needed to ensure a full understanding of the future spread of low-oxygen environments in the oceans.

Chapter 7

Future research perspectives

Author contributions and declaration: Dr N.J. Planavsky (Yale University), Dr C. Reinhard and Dr Y. Tang (Georgia Institute of Technology) provided advice on the design of the study proposed by S.R.C. Remmelzwaal.

Abstract

In an effort to build on the foundation used to search for remotely detectable atmospheric biosignatures, there has been a surge of work over the past decade aimed to reconstruct the history of Earth's atmosphere. Chromium isotopes are a redox proxy that have played a key role in debate about the history of atmospheric biosignatures on Earth. The traditional view is that Cr isotopic fractionation requires oxidation of Cr(III) to Cr(VI) and subsequent redox cycling to generate significant isotopic fractionation. Building on this idea, the onset of sedimentary Cr isotope variability has been used to pinpoint an oxidizing atmosphere. My proposed work challenges this assumption. Specifically, I will assess whether isotopic fractionation occurs during Cr(III) incorporation into carbonates. Discovery of a significant fractionation during this process would challenge the idea the carbonate record can be used to track atmospheric oxygen levels. I will support this experimental work by exploring the extent of isotopic variability in Archaean carbonates deposited under a reducing ocean-atmosphere system. This work builds directly from preliminary results that show isotopically fractionated Cr(III) can occur in Archean carbonates, and that stromatolites record Cr isotopic variability in the Archaean. Thus, this work has the potential to transform the use of Cr isotopes as a proxy.

7.1 Introduction

7.1.1. Rationale, objectives, and significance

Early in Earth's history, the development of oxygenic photosynthesis sets apart our planet: it made the environment favourable for multicellular life to appear. To our knowledge, our planet is unique in having a biological moderating force on the surface environment. Increasingly, inorganic geochemical methods have been applied to assess the rise of free oxygen (O_2). One of these methods is the chromium (Cr) isotope system. Historically, it has been suggested that redox changes are the only means to significantly fractionate Cr isotopes (Ellis et al., 2004; Schauble et al., 2004 Frei et al., 2009; Planavsky

et al., 2014). Chromium isotopes have been instrumental in increasing our understanding of the evolution of Earth's oxygen cycle—purportedly providing evidence for fluctuations in free atmospheric oxygen (Frei et al., 2009) and for the delay in the appearance of more complex life forms in the mid-Proterozoic (Planavsky et al., 2014). Further, it was also recently argued (based on Cr isotope records) that atmospheric oxygen levels through the vast majority of Earth's history were so low that Earth would have appeared lifeless when viewed from space (using the technology planned for upcoming space telescopes). Stated in other words, it is possible that Earth did not develop a remotely detectable atmospheric biosignature until relatively recently in Earth's history.

All palaeo-redox studies are based on the premise that Cr isotope fractionation occurs only by redox-related processes. However, there have been limited attempts at investigating the effect of Cr isotope fractionation associated with non-redox reactions, and thus the validity of this paradigm is unresolved (Fang et al., 2017; Saad et al., *in press*). A lack of experimental work has seriously impeded attempts at establishing an accurate quantification and timeline of Earth's early oxygenation history. I hypothesise that non-redox related reactions involving Cr(III) and Cr(III)-ligand complexes may lead to the incorporation of isotopically fractionated Cr into carbonates. Cr(III) – ligand complexes have been shown to solubilise otherwise insoluble Cr(III) compounds (Saad et al., 2017) and could therefore be incorporated into a carbonate lattice structure. Carbonates have also been reported to contain Cr(III) (Fang et al., 2017) which can alter the way Cr isotope measurements from carbonates have to be interpreted.

The main goal of the research proposed here is to explore mechanisms of Cr(III) precipitation into carbonates and how this process will shift standard interpretations of Cr isotope data from carbonate records. Quantifying isotopic fractionation caused by bound Cr(III) incorporation into carbonates will create a more solid foundation for the interpretation of Cr isotopes. I propose a suite of novel laboratory experiments combined with the analysis of Archaean carbonates that explore the following research question: **'Can Cr(III) and Cr(III) – ligand complexes be co-precipitated with carbonates and will this process induce large Cr isotope fractionations?'** This question will be approached through the examination of three main objectives through controlled experiments and Cr isotopic measurements:

Objective 1: Co-precipitate solubilised Cr(III) in carbonates and measure the resulting Cr(III) concentrations and Cr isotopic composition;
Objective 2: Co-precipitate solubilised Cr(III) – ligand complexes in carbonates and measure the resulting Cr(III) concentrations and Cr isotopic composition;
Objective 3: Measure the Cr isotopic composition of Archaean carbonates that formed under an anoxic atmosphere.

Searching for remotely detectable biosignatures is one of the most exciting avenues of modern science. We are closer than ever to identifying, exploring, and characterizing habitable exoplanets and biosignatures. My proposal in grounded in the idea that understanding the history of atmospheric biosignatures on Earth and the mechanisms controlling Earth's atmospheric composition will help establish a robust foundation for exoplanetary atmospheric work. Therefore, I want to pursue post-doctoral work in the Alternative Earths Astrobiology Institute, where the central goal is to understand the factors leading to the persistent inhabitation of the early Earth and factors that have controlled atmospheric biosignatures on Earth. My background in Cr isotope research make me ideally suited to tie into this Astrobiology team, and to help establish a more thorough understanding of the extent Cr isotopes can speak to Earth's oxygenation.

7.1.2. Chromium isotope geochemistry

Chromium isotopes have been used extensively in recent years to observe the rise and changes in atmospheric and oceanic oxygen concentrations (e.g. Frei et al., 2009; Planavsky et al., 2014; Wang et al., 2016). Chromium is present as Cr(III) within igneous rocks and is largely insoluble and immobile.

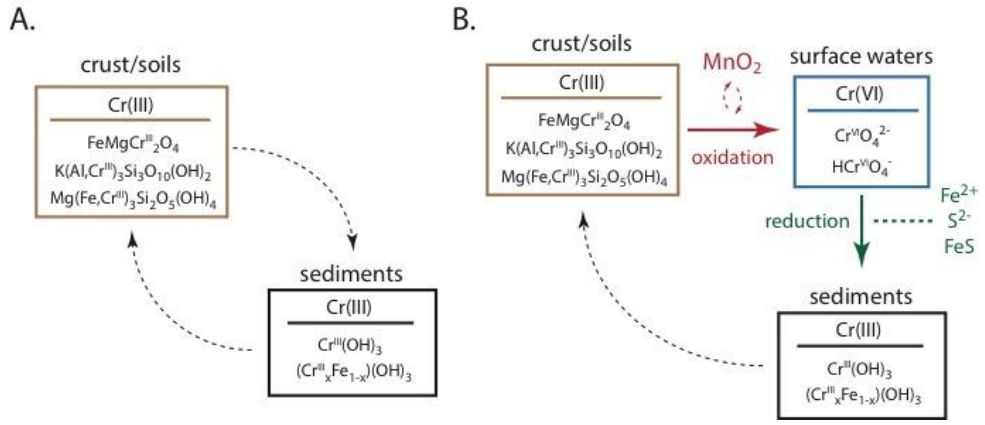

Figure 1: Overview of low temperature Cr cycling after Saad et al. (2017): A. Cr(III) cycling is thought to be characterized by limited isotope fractionations. However, this framework has not been tested. B. At high oxygen levels, dissolved Cr(III) will oxidise to Cr(VI) through a MnO_2 catalisation. This reaction is thought to be necessary for Cr isotopic variability in the geological record.

In the presence of free oxygen and a manganese catalyst, Cr(III) oxidises to the soluble and mobile oxyanion $Cr(VI)O_4^{2-}$. During riverine transport Cr(VI) can experience partial reduction enriching the remaining dissolved chromate in the heavier isotope ^{53}Cr (e.g. Ellis et al., 2002; Kitchen et al., 2012). All the above processes require that at least some Cr(III) has initially been oxidised to Cr(VI) which can only occur in the presence of free oxygen. The implication of this requirement is that prior to oxygenic photosynthesis, Cr cycling on Earth's surface was comprised only of Cr(III) and precludes any significant Cr isotopic fractionation. The starting point of isotopic fractionation of Cr is therefore

traditionally seen as evidence for the advent of free atmospheric oxygen (Frei et al., 2009; Crowe et al., 2013).

7.1.3. Chromium isotopes in carbonates

Carbonates are often used to extract geochemical information for palaeo-environmental reconstructions. The chromium isotopic composition of modern carbonates has consequently received much focus in recent years (Bonnand et al., 2011; Bonnand et al., 2013; Pereira et al., 2016; Wang et al., 2017). The Cr isotope system has also been applied to times of suspected redox changes in the environment including the early rise of free oxygen (e.g. Crowe et al., 2013; Frei et al., 2009; Konhauser et al., 2011; Planavsky et al., 2014). The recent detection of Cr(III) in carbonates (Fang et al., 2017) can have far-reaching implications for interpreting Cr isotope signatures and the timing of Earth's oxygenation. Further, the process of scavenging Cr(III) by carbonates may induce a significant non-redox-independent isotopic fractionation as this process may result in a significant change in coordination state.

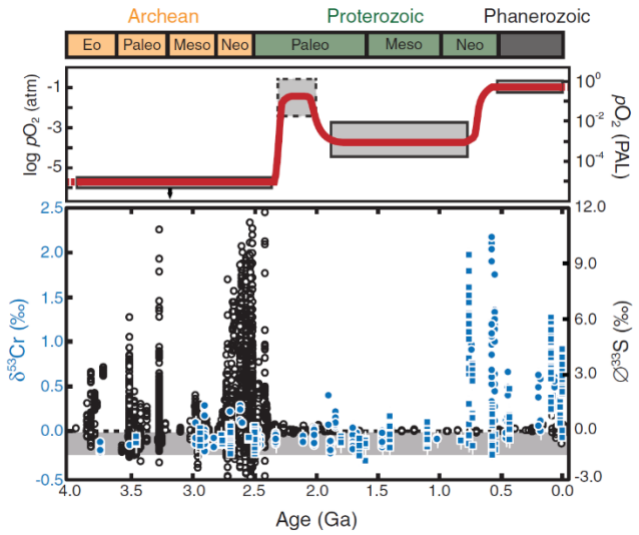

Figure 2: Evolution of free oxygen in Earth's atmosphere (Reinhard et al., 2017) There are three main states of atmospheric evolution: a reducing Archaean atmosphere (~3.8 – 2.5 Ga), the presence of free oxygen at low concentrations during the Proterozoic as indicated by shale-hosted Cr isotopes (Cole et al., 2016) (~2.5 – 0.5 Ga), and the elevated oxygen concentrations throughout the Phanerozoic.

Initial work in co-precipitation experiments has focused on the incorporation of Cr(VI) into the carbonate lattice (Rodler et al., 2015; Tang et al., 2007). Early co-precipitation of chromate with calcite focused on the partitioning behaviour and distribution of Cr onto the surfaces of single calcite crystals. These experiment showed preferential $Cr(VI)O_4^{2-}$ incorporation and confirmed that with a significant lattice distortion, chromate can replace carbonate ions in a calcite lattice (Tang et al., 2007). A more recent co-precipitation experiment determined that the Cr isotope fractionation associated with chromate incorporation into the calcite lattice is negligible at modern marine concentrations but can be significant at higher concentrations and slow precipitation rates (Rodler et al., 2015). To date there has not been a systematic study of Cr(III) incorporation into carbonates.

7.2. Scientific research objectives

7.2.1. Objective 1: Co-precipitation of Cr(III) in carbonates

Conventionally, Cr(III) is considered insoluble under neutral pH conditions and therefore unable to co-precipitate with carbonates. However, Cr speciation work has found that there are significant concentrations of dissolved Cr(III) in seawater (Murray et al., 1983). A recent X-ray absorption study also reported that carbonates can contain Cr(III) (Fang et al. 2017; Holmden, *pers. comm*., 2017). I will co-precipitate Cr(III) with carbonates to understand under what circumstances dissolved Cr(III) can enter the carbonate lattice and whether this process fractionates Cr isotopes. I hypothesise that the uptake of Cr(III) into the carbonate lattice is related to both the concentration of dissolved Cr(III) and its relative proportion to Cr(VI), as well as the Eh conditions in which calcite is precipitated. Eh conditions can vary widely in the environment and there is potential that seawater might be reducing prior to co-precipitation by microbial activity or pore water redox processes (Fang et al. 2017). The notion that the Cr isotopic composition of carbonates is potentially set by post-depositional alteration by pore waters is also suggested by other studies (Holmden et al., 2016; Remmelzwaal et al., *in prep*-a). Investigating the potential of Cr(III) interfering in Cr isotopic measurements is therefore crucial for our ability to quantify redox effects recorded by carbonates.

7.2.2. Objective 2: Co-precipitation of Cr(III) – ligand complexes in carbonates

A pathway for dissolving Cr(III) is through complexing with organic molecules (Bartlett & Kimble, 1976; Gustafsson et al., 2014; Saad et al., *in press*; Walsh & O'Halloran, 1996). Siderophores and organic acids both commonly occur in the environment. Siderophores are secreted by microbial life and have a strong preference for solid-phase Fe(III) and Cr(III) (Neilands 1995; Duckworth et al., 2014). Fe(III) and Cr(III) tend to co-precipitate in Fe(III)-Cr(III) oxyhydroxides (Saad et al., 2017) and can therefore both be solubilised.

Recent progress in our understanding of the solubilisation of Cr(III) under circumneutral conditions by complexing with commonly occurring environmental ligands demonstrates that the dissolution by ligand complexing causes Cr isotopic fractionation in the range of Cr isotope signatures observed in the rock record (-0.27 to +1.23‰) traditionally attributed to redox processes (Saad et al., *in press*). The implications are that in the marine environment isotopically fractionated Cr(III) may be leached from dust or from Cr(III) bound to organic matter on the seafloor (Saad et al., *in press)*, which is in agreement with the observation of ligand-bound Cr(III) in seawater (e.g. Nakayama et al., 1981; Sander & Koschinsky, 2011). To further assess the impact of redox-independent Cr isotope fractionation on palaeo-studies, it is essential to experimentally survey whether these solubilised Cr(III)-ligand complexes are incorporated into the carbonate lattice. **Crucially, early work on batch Cr(III) carbonate precipitation with citrate as a complexing agent yields a preliminary Cr isotope**

fractionation of 0.4‰ within the carbonate (X. Wang, *pers. comm.*, 2017), a fractionation well beyond that seen in standard igneous rocks (Schoenberg et al., 2008).

7.2.3. Objective 3: Chromium isotopic composition of Archaean carbonates

It is well-established that Archean atmospheric oxygen levels where extremely low. Based foremost on rare sulfur isotope work, the consensus view (Lyons et al., 2014) is that pO_2 levels where less than 10^{-5} present atmospheric levels (PAL). Given that standard framework one would not expect to see significant Cr isotope fractionations at such low pO_2 levels, consistent with what is observed in the shale record (Cole et al., 2016). However, if there is a fractionation associated with Cr(III) transport and incorporation into carbonates one would expect to see isotopically fractionated carbonates in the Archean. Therefore, to test if Cr fractionated in an anoxic past and if this might have been caused by the incorporation of Cr(III) I will analyse a suite of Archaean stromatolites. To this end, I have acquired a stratigraphically continuous succession of samples from the Neoarchaean Cheshire Formation from within the Belingwe greenstone belt in Zimbabwe dated to approximately 2.7 Ga (e.g. Martin et al., 1980). Any isotopic fractionation and presence of Cr(III) within these stromatolitic limestones provides a litmus test for testing the paradigm for an absence of Cr isotopic fractionation in anoxic settings. **Very early Cr isotope measurements in Archean carbonates show isotopic variability of up to 0.4‰, which is inconsistent with the reducing environment in which they formed.**

7.3. Technical research approach

7.3.1. Overall research strategy

We will explore the isotopic fractionation associated with the co-precipitation of Cr(III) and Cr(III) – ligand complexes with carbonate. We will use different types of siderophores and organic acids as complexing agents for studying Cr(III) – ligand and carbonate co-precipitation. Our co-precipitation experiments will follow from earlier solubilisation and complexation studies by (Saad et al., 2017; Saad et al., *in press*). Stromatolites from the Neoarchaean will also be analysed for their Cr speciation and isotopic composition. More detailed methodological descriptions will follow in the following subsections.

7.3.2. Task 1: Cr(III) solubilisation experiments

Following Saad et al. (*in press*), amorphous Cr(III)-oxyhydroxide solids will be solubilised with either a single type of siderophore or organic acid or a combination of these. The siderophores will include DFOB, enterobactin and pyoverdine. The organic acids will include acetate, oxalate, succinate and citrate. For each Cr(III)-ligand solubilisation experiment, Cr(III)-oxyhydroxide is suspended in a 0.1 M NaCl electrolyte solution with a 10 mM 4-(2-hydroxyethyl)-1-piperazineethanesulfonic acid buffer at pH 7 and is sonicated to aid suspension. A siderophore was added to the suspensions to reach a

concentration of 0.1 mM. Organic acid was added to the suspension to reach a concentration of 1 mM. For the treatments containing both siderophore and organic acid, the organic acid was added prior to the siderophore. Cr(VI) and Cr(III) concentrations in the filtrates will be monitored using the diphenylcarbazide assay on a UV-vis spectrophotometer.

7.3.3. Task 2: Cr(III)-ligand and carbonate co-precipitation experiments

We use the constant addition experimental methods that were used for Cr(VI) co-precipitation with calcite in Tang et al. (2007). A reaction vessel which contains a $CaCl_2$ and $NaHCO_3$ solution was bubbled continuously with water-saturated air. NaCl is added at the start to set an ionic strength of 0.1 M. Calcite equilibrated with deionized water is added as nucleation seeds. $CaCl_2$ and Na_2CO_3 solutions are introduced into the reaction vessel at a constant rate. Solubilised Cr(III) (see Task 1) is added at the start of the experiment. The pH is adjusted by adding HCl. Total CO_2 content and pH will be monitored to assess when the system reaches steady-state calcite supersaturation. The final calcite powder will be collected by vacuum filtration, washed with deionized water, and dried in an oven at 50 °C. Chromium speciation concentrations in the solid and in aliquots of solution will be measured by a combination of DCP and total Cr measurements.

7.3.4. Task 3: Chromium isotope analyses

A double spike method with ^{50}Cr-^{54}Cr will be used to correct for any fractionation associated with sample preparation and isotope measurements (Bonnand et al., 2011; Ellis et al., 2002; Schoenberg et al.,2008). The double spike with a known ^{50}Cr-^{54}Cr ratio and in the same valences as the sample is added prior to any purification. To secure optimal spike/sample ratios and minimal propagation of errors related to introducing the spike, the Cr concentrations of all samples are determined by ICP-MS prior to preparation for isotope measurements (Bonnand et al., 2011). Chromium is extracted from the matrix by cation exchange chromatographic separation procedures following Bonnand et al. (2011). The extracted Cr is dissolved in 0.7 N HNO_3 and its isotopic composition is measured on a Neptune Plus multi-collector ICP-MS at Yale University. The interferences of Ti, V, and Fe are corrected for. An unprocessed standard NIST SRM979 with concentrations similar to the samples will bracket the sample analyses to monitor instrument drift. Samples are then normalised to the average standard value. The analytical precision of Cr isotope measurements obtained at Yale University is ±0.08‰ (2SD) using concentrations of 50 – 1000 ng Cr.

7.4. Expected Results

The proposed research will be a major contribution towards understanding and quantifying redox-independent fractionation in the Cr isotope system. It could have large ramifications for our traditional

view of the early evolution of Earth's atmosphere and will challenge the existing paradigm that free oxygen in needed for significant isotope fractionation. Preliminary results show that Cr(III) can be incorporated into a carbonate lattice and is isotopically fractionated. Limited Cr isotope measurements in Archaean carbonates also suggest non-redox related Cr isotopic fractionation and call into question previous Cr palaeo-redox studies into the rise of oxygen. Preliminary results stress the need for the proposed work before we can use Cr isotopes to track Earth's oxygenation.

References

Abbott, A. N., Haley, B. A., Tripati, A. K., Frank, M., 2016. Constraints on ocean circulation at the Paleocene-Eocene Thermal Maximum from neodymium isotopes. *Climate of the Past 12*, 837-847.

Abels, H. A., Clyde, W. C., Gingerich, P. D., Hilgen, F. J., Fricke, H. C., Bowen, G. J., Lourens, L. J., 2012. Terrestrial carbon isotope excursions and biotic change during Palaeogene hyperthermals. *Nature Geoscience* 5, 326–329.

Abu-Saba, K. E., Sedlak, D. L., Flegal, A. R., 2000. Indirect reduction of hexavalent chromium by copper in the presence of superoxide. *Marine Chemistry* 69, 33–41.

Achterberg, E. P., Van Den Berg, C. M. G., 1997. Chemical speciation of chromium and nickel in the western Mediterranean. *Deep Sea Research Part II: Topical Studies in Oceanography* 44, 693–720.

Agnini, C., Macri, P., Backman, J., Brinkhuis, H., Fornaciari, E., Giusberti, L., Luciani, V., Rio, D., Sluijs, A., Speranza, F. (2009). An early Eocene carbon cycle perturbation at ~52.5 Ma in the Southern Alps: Chronology and biotic response. *Paleoceanography* 24.

Albarède, F., & Beard, B., 2004. Analytical methods for non-traditional isotopes. In: Geochemistry of Non-Traditional Stable Isotopes. *Reviews in Mineralogy and Geochemistry* 55, 113–152.

Alegret, L., Ortiz, S., Arenillas, I., Molina, E., 2010. What happens when the ocean is overheated? The foraminiferal response across the Paleocene-Eocene Thermal Maximum at the Alamedilla section (Spain). *GSA Bulletin* 122, 1616-1624.

Alexander, K., Meissner, K. J., Bralower, T. J., 2015. Sudden spreading of corrosive bottom water during the Palaeocene-Eocene Thermal Maximum. *Nature Geoscience* 8, 458-461

Algeo, T., Shen, Y., Zhang, T., Lyons, T., Bates, S., Rowe, H., & Nguyen, T. K. T., 2008. Association of ^{34}S-depleted pyrite layers with negative carbonate δ^{13}C excursions at the Permian-Triassic boundary: Evidence for upwelling of sulfidic deep-ocean water masses. *Geochemistry, Geophysics, Geosystems*, 9.

Allen, K.A., Hönisch, B., Eggins, S.M., Haynes, L.L., Rosenthal, Y., Yu, J., 2016. Trace element proxies for surface ocean conditions: A synthesis of culture calibrations with planktic foraminifera. *Geochimica et Cosmochimica Acta* 193, 197–221.

Altieri, A. H., & Gedan, K. B., 2015. Climate change and dead zones. *Global Change Biology*.

Altman, C., King, E. L., 1961. The mechanism of the exchange of chromium(III) and chromium(VI) in acidic solution. *Journal of the American Chemical Society* 83, 2825.

Alvarez, W., 2009. The historical record in the Scaglia limestone at Gubbio: Magnetic reversals and the Cretaceous-Tertiary mass extinction. *Sedimentology* 56, 137–148.

Ando, A., Kaiho, K., Kawahata, H., Kakegawa, T., 2008. Timing and magnitude of early Aptian extreme warming: Unraveling primary δ^{18}O variation in indurated pelagic carbonates at Deep Sea Drilling Project Site 463, central Pacific Ocean. *Palaeogeography, Palaeoclimatology, Palaeoecology,* 260, 463–476.

Ando, A., Kakegawa, T., 2007. Carbon isotope records of terrestrial organic matter and occurrence of planktonic foraminifera from the Albian stage of Hokkaido, Japan: Ocean-atmosphere ^{13}C trends and chronostratigraphic implications. *Palaios*, 22, 417–432.

Ando, A., Kakegawa, T., Takashima, R., Saito, T., 2002. New perspective on Aptian carbon isotope stratigraphy: Data from delta C-13 records of terrestrial organic matter. *Geology* 30, 227–230.

Ando, A., Nakano, T., Kaiho, K., Kobayashi, T., Kokado, E., Khim, B.-K., 2009. Onset of seawater ^{87}Sr/^{86}Sr excursion prior to Cenomanian-Turonian Oceanic Anoxic Event 2? New Late Cretaceous strontium isotope curve from the Central Pacific Ocean. *The Journal of Foraminiferal Research* 39, 322–334.

Arreguín-Rodríguez, G. J., Alegret, L., 2016. Deep-sea benthic foraminiferal turnover across early Eocene hyperthermal events at Northeast Atlantic DSDP Site 550. *Palaeogeography, Palaeoclimatology, Palaeoecology* 451, 62–72.

Arthur, M. A., 1976. Sedimentology of the Gubbio sequence and its bearing on palaeomagnetism. *Memoire Della Societá Geologica Italiana*, 15, 9–20.

Arthur, M. A., Dean, W. E., Pratt, L. M., 1988. Geochemical and climatic effects of increased marine organic carbon burial at the Cenomanian/Turonian boundary. *Nature* 335, 714-717.

Arthur, M. A., Dean, W. E., Schlanger, S. O., 1985. Variations in the global carbon cycle during the Cretaceous related to climate, volcanism, and changes in atmospheric CO_2. In: The Carbon Cycle and Atmospheric CO_2: Natural Variations Archean to Present. *Geophysical Monograph* 32, 504–529.

Arthur, M. A., Jenkyns, H. C., Brumsack, H. J., Schlanger, S. O., 1990. Stratigraphy, geochemistry and paleoceanography of organic-carbon rich Cretaceous sequences. In: Cretaceous Resources Events and Rhythms (eds. Ginsburg, R. N., Beaudoin, B.). Kluwer, Dordrecht/Boston/London.

Barclay, R. S., McElwain, J. C., Sageman, B. B., 2010. Carbon sequestration activated by a volcanic CO_2 pulse during Ocean Anoxic Event 2. *Nature Geoscience* 3, 205–208.

Barker, S., Greaves, M., Elderfield, H., 2003. A study of cleaning procedures used for foraminiferal Mg/Ca paleothermometry. *Geochemistry, Geophysics, Geosystems* 4.

Barlett R., James, B., 1979. Behavior of chromium in soils: III. Oxidation. *Journal of Environmental Quality* 8, 31.

Bartlett, R. J., Kimble, J. M., 1976. Behavior of chromium in soils: I. Trivalen forms. *Journal of Environmental Quality* 5, 379-383.

Baturin, G. N., Dubinchuk, V. T., 2011. Mineralogy and chemistry of ferromanganese crusts. *Geochemistry International* 49, 578–593.

Bau, M., 1991. Rare-earth element mobility during hydrothermal and metamorphic fluid-rock interaction and the significance of the oxidation state of europium. *Chemical Geology* 93, 219–30.

Bau, M., Dulski, P., 1996. Distribution of yttrium and rare-earth elements in the Penge and Kuruman iron-formations, Transvaal Supergroup, South Africa. *Precambrian Research* 79, 37–55.

Bau, M., Koschinsky, A., Dulski, P., Hein, J. R., 1996. Comparison of the partitioning behaviours of yttrium, rare earth elements, and titanium between hydrogenetic marine ferromanganese crusts and seawater. *Geochimica et Cosmochimica Acta* 60, 1709–25.

Bau, M., Möller, P., Dulski, P., 1997. Yttrium and lanthanides in Eastern Mediterranean seawater and their fractionation during redox-cycling. *Marine Chemistry* 56, 123–31.

Bé, A. W. H., 1980. Gametogenic calcification in a spinose planktonic foraminifer, *Globigerinoides sacculifer* (Brady). *Marine Micropaleontology* 5, 283–310.

Beerling, D. J., 2002. On the nature of methane gas-hydrate dissociation during the Toarcian and Aptian Oceanic anoxic events. *American Journal of Science* 302, 28–49.

Behrenfeld, M. J., O'Malley, R. T., Siegel, D. A., McClain, C. R., Sarmiento, J. L., Feldman, G. C., Milligan, A. J., Falkowski, P. G., Letelier, R. M., Boss, E. S., 2006. Climate-driven trends in contemporary ocean productivity. *Nature* 444, 752–755.

Bertram, C. J., Elderfield, H., 1993. The geochemical balance of the rare earth elements and neodymium isotopes in the oceans. *Geochimica et Cosmochimica Acta* 57, 1957–86.

Bice, K. L., Birgel, D., Meyers, P. A., Dahl, K. A., Hinrichs, K. U., Norris, R. D., 2006. A multiple proxy and model study of Cretaceous upper ocean temperatures and atmospheric CO_2 concentrations. *Paleoceanography* 21.

Bice, K. L., Marotzke, J., 2002. Could changing ocean circulation have destabilized methane hydrate at the Paleocene/Eocene boundary? *Paleoceanography* 17, 1018.

Bigeleisen, J., Mayer, M. G., 1947. Calculation of equilibrium constants for isotopic exchange reactions. *The Journal of Chemical Physics* 15, 261–267.

Birch, H., Coxall, H. K., Pearson, P. N., Kroon, D., O'Regan, M., 2013. Planktonic foraminifera stable isotopes and water column structure: Disentangling ecological signals. *Marine Micropaleontology* 101, 127–145.

Blättler, C. L., Jenkyns, H. C., Reynard, L. M., Henderson, G. M., 2011. Significant increases in global weathering during Oceanic Anoxic Events 1a and 2 indicated by calcium isotopes. *Earth and Planetary Science Letters* 309, 77-88.

Bonnand, P., 2011. Potential of Chromium Isotopes as a Tracer of Past Ocean Oxygenation. Ph.D. thesis. The Open University.

Bonnand, P., Parkinson, I. J., James, R. H., Karjalainen, A.-M., & Fehr, M. A., 2011. Accurate and precise determination of stable Cr isotope compositions in carbonates by double spike MC-ICP-MS. *Journal of Analytical Atomic Spectrometry* 26, 528.

Bonnand, P., James, R.H., Parkinson, I.J., Connelly, D.P., and Fairchild, I.J., 2013. The chromium isotopic composition of seawater and marine carbonates. *Earth and Planetary Science Letters* 382, 10–20.

Bornemann, A., Norris, R. D., Lyman, J. A., D'Haenens, S., Groeneveld, J., Rohl, U., Farley, K. A., Speijer, R. P., 2014. Persistent environmental change after the Paleocene-Eocene Thermal Maximum in the eastern North Atlantic. *Earth and Planetary Science Letters* 394, 70-81.

Bottini, C., Cohen, A. S., Erba, E., Jenkyns, H. C., Coe, A. L., 2012. Osmium-isotope evidence for volcanism, weathering, and ocean mixing during the early Aptian OAE 1a. *Geology* 40, 583–586.

Bralower, T. J., Thierstein, H. R., 1984. Low productivity and slow deep-water circulation in mid-Cretaceous oceans. *Geology* 12, 614-618.

Breitburg, D., Levin, L. A., Oschlies, A., Gregoire, M., Chavez, F. P., Conley, D. J., Garcon, V., Gilbert, D., Gutierrez, D., Isensee, K., Jacinto, G. S., Limburg, K. E., Montes, I., Naqvi, S. W. A., Pitcher, G. C., Rabalais, N. N., Roman, M. R., Rose, K. A., Seibel, B. A., Telszewski, M., Yasuhara, M., Zhang, J., 2018. Declining oxygen in the global ocean and coastal waters. Science 359, 46.

Broecker, W. S., Peng, T.-H., 1982. Tracers in the sea. Lamont-Doherty Geological Observatory, New York, USA.

Brookins, D. G., 1988. Eh-pH Diagrams for Geochemistry. Springer, Berlin, Heidelberg, Germany.

Byrne, R. H., Kim, K. H., 1990. Rare earth element scavenging in seawater. Geochimica et Cosmochimica Acta 54: 2645–56. doi:10.1016/0016-7037(90)90002-3.

Campbell, J. A., Yeats, P. A., 1984. Dissolved chromium in the St. Lawrence estuary. *Estuarine, Coastal and Shelf Science* 19, 513–522.

Canfield, D. E., 2001. Isotope fractionation by natural populations of sulfate-reducing bacteria. *Geochimica et Cosmochimica Acta* 65, 1117–1124.

Canfield, D. E., Stewart, F. J., Thamdrup, B., De Brabandere, L., Dalsgaard, T., Delong, E. F., Revsbech, N. P., Ulloa, O., 2010. A cryptic sulfur cycle in oxygen-minimum-zone waters off the Chilean coast. *Science* 330, 1375–1378.

Carmichael, M. J., Inglis, G. N., Badger, M. P. S., Naafs, B. D. A., Behrooz, L., Remmelzwaal, S., Monteiro, F. M., Rohrssen, M., Farnsworth, A., Buss, H. L., Dickson, A. J., Valdes, P. J., Lunt, D. J., Pancost, R. D., 2017. Hydrological and associated biogeochemical consequences of rapid global warming during the Paleocene-Eocene Thermal Maximum. *Global and Planetary Change* 157, 114-138.

Caron, D. A., Roger Anderson, O., Lindsey, J. L., Faber, W. W., Lin Lim, E. E., 1990. Effects of gametogenesis on test structure and dissolution of some spinose planktonic foraminifera and implications for test preservation. *Marine Micropaleontology* 16, 93–116.

Caromel, A.G.M., Schmidt, D.N., Phillips, J.C., Rayfield, E.J., 2014. Hydrodynamic constraints on the evolution and ecology of planktic foraminifera. *Marine Micropaleontology* 106, 69–78.

Chappell, J., Shackleton, N. J., 1986. Oxygen isotopes and sea level. *Nature* 324, 137–140.

Chun, C. O. J., Delaney, M. L., Zachos, J. C., 2010. Paleoredox changes across the Paleocene-Eocene thermal maximum, Walvis Ridge (ODP Sites 1262, 1263, and 1266): Evidence from Mn and U enrichment factors. *Paleoceanography* 25, PA4202.

Clarkson, M. O., Stirling, C. H., Jenkyns, H. C., Dickson, A. J., Porcelli, D., Moy, C. M., Pogge von Strandmann, P. A. E., Cooke, I. R., Lenton, T. M., 2018. Uranium isotope evidence for two episodes of deoxygenation during Oceanic Anoxic Event 2. *Proceedings of the National Academy of Sciences*.

Clementz, M., Bajpai, S., Ravikant, V., Thewissen, J. G. M., Saravanan, N., Singh, I. B., Prasad, V., 2011. Early Eocene warming events and the timing of terrestrial faunal exchange between India and Asia. *Geology* 39, 15–18.

Coccioni, R., Nesci, O., Tramontana, C. F., Wezel, C. F., Moretti, E., 1987. Descrizione di un livello guida "Radiolaritico-Bituminoso-Ittiolitico" alla base delle Marne a Fucoidi nell'Appennino Umbro-Marchigiano. *Bolletino Società Geologica Italiana* 106, 183–192.

Codispoti, L. A., 1991. Primary productivity and carbon and nitrogen cycling in the Arabian Sea. In S. L. Smith, K. Banse, J. K. Cochran, L. A. Codispoti, H. W. Ducklow, M. E. Luther, … K. Wishner (Eds.), U.S. JGOFS: Arabian Sea Process Study. U.S. JGOFS Planning Report No. 13

Codispoti, L. A., Brandes, J. A., Christensen, J. P., Devol, A. H., Naqvi, S. W. A., Paerl, H. W., Yoshinari, T., 2001. The oceanic fixed nitrogen and nitrous oxide budgets: Moving targets as we enter the anthropocene? *Scientia Marina* 65, 85–105.

Cole, D. B., Reinhard, C. T., Wang, X., Gueguen, B., Halverson, G. P., Gibson, T., Hodgskiss, S. W., McKenzie, N. R., Lyons, T. W., Planavsky, N. J., 2016. A shale-hosted Cr isotope record of low atmospheric oxygen during the Proterozoic. *Geology* 44, 555-558.

Colosimo, A. B., Bralower, T. J., Zachos, J. C., 2006. Evidence for lysocline shoaling at the Paleocene/Eocene Thermal Maximum on Shatsky Rise, northwest Pacific. In: Bralower, T. J., Premoli Silva, Malone M. J. (Eds.), 2006. Proceedings of the Ocean Drilling Program, Scientific Results 198: College Station, TX (Ocean Drilling Program).

Comber, S., Gardner, M., 2003. Chromium redox speciation in natural waters. *Journal of Environmental Monitoring* 5, 410–413.

Connelly, D. P., Statham, P. J., Knap, A. H., 2006. Seasonal changes in speciation of dissolved chromium in the surface Sargasso Sea. *Deep-Sea Research Part I: Oceanographic Research Papers* 53, 1975–1988.

Corfield, R. M., Cartlidge, J. E., Premoli-Silva, I., Housley, R. A., 1991. Oxygen and carbon isotope stratigraphy of the Palaeogene and Cretaceous limestones in the Bottaccione Gorge and the Contessa Highway sections, Umbria, Italy. *Terra Nova* 3, 414–422.

Courtillot, V. E., Renne, P. R., 2003. On the ages of flood basalt events. *Comptes Rendus - Geoscience* 335, 113–140.

Cramer, B. S., Wright, J. D., Kent, D. V., Aubry, M.-P., 2003. Orbital climate forcing of $\delta^{13}C$ excursions in the late Paleocene–early Eocene (chrons C24n–C25n). *Paleoceanography* 18, 1097.

Cranston, R. E., Murray, J. W., 1978. The determination of chromium species in natural waters. *Analytica Chimica Acta* 99, 275–82.

Cranston, R. E., Murray, J. W., 1980. Chromium species in the Columbia River and estuary. *Limnology and oceanography* 25, 1104–1112.

Crowe, S. A., Døssing, L. N., Beukes, N. J., Bau, M., Kruger, S. J., Frei, R., Canfield, D. E., 2013. Atmospheric oxygenation three billion years ago. *Nature* 501, 535–538.

Crowe, S. A., Katsev, S., Leslie, K., Sturm, A., Magen, C., Nomosatryo, S., Pack, M. A., Kessler, J. D., Reeburgh, W. S., Roberts, J. A., Gonzalez, L., Douglas Haffner, G., Mucci, A., Sundby, B., Fowle, D. A., 2011. The methane cycle in ferruginous Lake Matano. *Geobiology* 9, 61–78.

Cutter, G. A., 1992. Kinetic controls on metalloid speciation in seawater. *Marine Chemistry* 40, 65-80.

D'Arcy, J., Babechuk, M. G., Døssing, L. N., Gaucher, C., Frei, R., 2016. Processes controlling the chromium isotopic composition of river water: Constrains from basaltic river catchments. *Geochimica et Cosmochimica Acta* 186, 296–315.

Davidson, E. A., Janssens, I. A., 2006. Temperature sensitivity of soil carbon decomposition and feedbacks to climate change. *Nature* 440, 165–173.

De Baar, H. J. W., German, C. R., Elderfield, H., Vangaans, P., 1988. Rare-earth element distributions in anoxic waters of the Cariaco Trench. *Geochimica et Cosmochimica Acta* 52, 1203-1219.

De Baar, H. J. W., Schijf, J., Byrne, R. H., 1991. Solution chemistry of the rare earth elements in seawater. *European Journal of Solid State Inorganic Chemistry* 28, 357–73.

De Carlo, E. H., Green, W. J., 2002. Rare earth elements in the water column of Lake Vanda, McMurdo Dry Valleys, Antarctica. *Geochimica et Cosmochimica Acta* 66, 1323–33.

Deconto, R. M., Galeotti, S., Pagani, M., Tracy, D., Schaefer, K., Zhang, T., Pollard, D., Beerling, D. J., 2012. Past extreme warming events linked to massive carbon release from thawing permafrost. *Nature* 48, 87–91.

Dedert, M., Stoll, H. M., Kroon, D., Shimizu, N., Kanamaru, K., Ziveri, P., 2012. Productivity response of calcareous nannoplankton to Eocene Thermal Maximum 2 (ETM2). *Climate of the Past* 8, 977–993.

Deutsch, C., Emerson, S., Thompson, L., 2005. Fingerprints of climate change in North Pacific oxygen. *Geophysical Research Letters* 32, L16604.

D'Haenens, S., Bornemann, A., Claeys, P., Röhl, U., Steurbaut, E., Speijer, R. P., 2014. A transient deep-sea circulation switch during Eocene Thermal Maximum 2. Paleoceanography 29, 370–388.

D'Haenens, S., Bornemann, A., Stassen, P., Speijer, R. P., 2012. Multiple early Eocene benthic foraminiferal assemblage and $\delta^{13}C$ fluctuations at DSDP Site 401 (Bay of Biscay - NE Atlantic). *Marine Micropaleontology* 88–89, 15–35.

Diaz, R. J., Rosenberg, R., 2008. Spreading dead zones and consequences for marine ecosystems. *Science* 321, 926–929.

Dickson, A. J., Cohen, A. S., Coe, A. L., 2012. Seawater oxygenation during the Paleocene-Eocene Thermal Maximum. *Geology* 40, 639-642.

Dickson, A. J., Cohen, A. S., Coe, A. L., 2014. Continental margin molybdenum isotope signatures from the early Eocene. *Earth and Planetary Science Letters* 404, 389-395.

Dickson, A. J., Cohen, A. S., Coe, A. L., Davies, M., Shcherbinina, E. A., Gavrilov, Y. O., 2015. Evidence for weathering and volcanism during the PETM from Arctic Ocean and Peri-Tethys osmium isotope records. *Palaeogeography, Palaeoclimatology, Palaeoecology* 438, 300-307.

Dickson, A. J., Saker-Clark, M., Jenkyns, H. C., Bottini, C., Erba, E., Russo, F., Gorbanenko, O., Naafs, B. D. A., Pancost, R. D., Robinson, S. A., Van Den Boorn, S. H. J. M., Idiz, E., 2017. A Southern Hemisphere record of global trace-metal drawdown and orbital modulation of organic-matter burial across the Cenomanian–Turonian boundary (Ocean Drilling Program Site 1138, Kerguelen Plateau). *Sedimentology* 64, 186–203.

Doney, S. C., Ruckelshaus, M., Emmett Duffy, J., Barry, J. P., Chan, F., English, C. A., Galindo, H. M., Grebmeier, J. M., Hollowed, A. B., Knowlton, N., Polovina, J., Rabalais, N. N., Sydeman, W. J., Talley, L. D., 2012. Climate Change Impacts on Marine Ecosystems. *Annual Review of Marine Science* 4, 11–37.

D'Onofrio, R., Luciani, V., Giusberti, L., Fornaciari, E., Sprovieri, M., 2014. Tethyan planktic

foraminiferal record of the early Eocene hyperthermal events ETM2, H2 and I1 (Terche section, northeastern Italy). Rendiconti Online Società Geologica Italiana, 31, 66–67.

Døssing, L. N., Dideriksen, K., Stipp, S. L. S., Frei, R., 2011. Reduction of hexavalent chromium by ferrous iron: A process of chromium isotope fractionation and its relevance to natural environments. *Chemical Geology* 285, 157-166.

Douville, E., Bienvenu, P., Charlou, J. L., Donval, J. P., Fouquet, Y., Appriou, P., Gamo, T., 1999. Yttrium and rare earth elements in fluids from various deep-sea hydrothermal systems. *Geochimica et Cosmochimica Acta* 63, 627–43.

Dragun, Z., Roje, V., Mikac, N., Raspor, B., 2009. Preliminary assessment of total dissolved trace metal concentrations in Sava River water. *Environmental Monitoring and Assessment* 159, 99–110.

Du, J., Haley, B. A., Mix, A. C., 2016. Neodymium isotopes in authigenic phases, bottom waters and detrital sediments in the Gulf of Alaska and their implications for paleo-circulation reconstruction. *Geochimica et Cosmochimica Acta* 193, 14–35.

Dubinin, A. V., 2004. Geochemistry of rare earth elements in the ocean. *Lithology and Mineral Resources* 39, 289–307.

Duckworth, O. W., Akafia, M. M., Andrews, M. Y., Bargar, J. R., 2014. Siderophore-promoted dissolution of chromium from hydroxide minerals. Environmental Science Processes & Impacts 16, 1348.

Dunkley-Jones, T., Lunt, D. J., Schmidt, D. N., Ridgwell, A., Sluijs, A., Valdes, P. J., Maslin, M., 2013. Climate model and proxy data constraints on ocean warming across the Paleocene-Eocene Thermal Maximum. *Earth-Science Reviews* 125, 123-145.

Dupré, B., Gaillardet, J., Rousseau, D., Allègre, C. J., 1996. Major and trace elements of river-borne material: the Congo Basin. *Geochimica et Cosmochimica Acta* 60, 1301–21.

Economou-Eliopoulos, M., Frei, R., and Megremi, I., 2016. Potential leaching of Cr(VI) from laterite mines and residues of metallurgical products (red mud and slag): an integrated approach. *Journal of Geochemical Exploration* 162, 40–49.

Eggins, S.M., De Deckker, P., and Marshall, J., 2003. Mg/Ca variation in planktonic foraminifera tests:

implications for reconstructing palaeo-seawater temperature and habitat migration. *Earth and Planetary Science Letters* 212, 291–306.

Elderfield, H., 1970. Chromium speciation in sea water. *Earth and Planetary Science Letters* 9, 10–16.

Elderfield, H., Ferretti, P., Greaves, M., Crowhurst, S., McCave, I. N., Hodell, D., Piotrowski, A. M., 2012. Evolution of ocean temperature and ice volume through the mid-Pleistocene climate transition. *Science* 337, 704–709.

Elderfield, H., Rickaby, R., and Henderiks, J., 2006. How do marine carbonate Mg/Ca and Sr/Ca proxies constrain Cenozoic ocean history? *Geochimica et Cosmochimica Acta* 70, A158.

Elderfield, H., Upstill-Goddard, R., Sholkovitz, E. R., 1990. The rare earth elements in rivers, estuaries, and coastal seas and their significance to the composition of ocean waters. *Geochimica et Cosmochimica Acta* 54, 971–91.

Ellis, A. S., Johnson, T. M., Bullen, T. D., 2002. Chromium isotopes and the fate of hexavalent chromium in the environment. *Science* 295, 2060–2062.

Ellis, A. S., Johnson, T. M., & Bullen, T. D., 2004. Ratios to quantify Cr(VI) reduction: lack of sorption effects. *Environmental Science & Technology* 38, 3604–3607.

Elrick, M., Polyak, V., Algeo, T. J., Romaniello, S., Asmerom, Y., Herrmann, A. D., Anbar, A. D., Zhao, L., Chen, Z. Q., 2017. Global-ocean redox variation during the middle-late Permian through Early Triassic based on uranium isotope and Th/U trends of marine carbonates. *Geology* 45, 163–166.

Eppley, R. W. (1972). Temperature and phytoplankton growth in the sea. *Fishery Bulletin* 70, 1063–1085.

Erba, E. (1994). Nannofossils and superplumes: The Early Aptian “nannoconid crisis.” *Paleoceanography* 9, 483–501.

Erba, E. (2004). Calcareous nannofossils and Mesozoic oceanic anoxic events. Marine *Micropaleontology* 52, 85–106.

Erbacher, J., Friedrich, O., Wilson, P. A., Birch, H., Mutterlose, J., 2005. Stable organic carbon isotope stratigraphy across Oceanic Anoxic Event 2 of Demerara Rise, western tropical Atlantic. *Geochemistry, Geophysics, Geosystems* 6.

Erez, J., 2003. The source of ions for biomineralization in foraminifera and their implications for paleoceanographic proxies. *Reviews in Mineralogy and Geochemistry* 54, 115.

Erwin, D., 1994. The Permo-Triassic extinction. *Nature* 367, 231–236.

Fang, Z., Qin, L., Wei, S., Yao, T., Liu, W., Shen, Y., Zhou, G., 2017. XANES evidence of Cr species in carbonate: Implication for the use of Cr isotope as a proxy for atmospheric oxygenation. Goldschmidt 2017 Abstract.

Farkaš, J., Chrastný, V., Novák, M., Čadkova, E., Pašava, J., Chakrabarti, R., Jacobsen, S. B., Ackerman, L., Bullen, T. D., 2013. Chromium isotope variations ($\delta^{53/52}$Cr) in mantle-derived sources and their weathering products: Implications for environmental studies and the evolution of $\delta^{53/52}$Cr in the Earth's mantle over geologic time. *Geochimica et Cosmochimica Acta* 123, 74–92.

Faure, G., Mensing, T. M., 2009. Isotopes: Principles and Applications (Third Edition). Wiley, New York, USA.

Feng, Q., Algeo, T. J., 2014. Evolution of oceanic redox conditions during the Permo-Triassic transition: Evidence from deepwater radiolarian facies. *Earth-Science Reviews* 137, 34-51.

Föllmi, K. B., 2012. Early Cretaceous life, climate and anoxia. *Cretaceous Research* 35, 230-257.

Forster, A., Schouten, S., Baas, M., Sinninghe Damsté, J. S., 2007. Mid-Cretaceous (Albian-Santonian) sea surface temperature record of the tropical Atlantic Ocean. *Geology* 35, 919–922.

Forster, A., Schouten, S., Moriya, K., Wilson, P. A., Sinninghe Damsté, J. S., 2007. Tropical warming and intermittent cooling during the Cenomanian/Turonian oceanic anoxic event 2: Sea surface temperature records from the equatorial Atlantic. Paleoceanography 22.

Freeman, K. H., Hayes, J. M., 1992. Fractionation of carbon isotopes by phytoplankton and estimates of ancient CO_2 levels. *Global Biogeochemical Cycles* 6, 185–198.

Frei, R., Gaucher, C., Døssing, L. N., Sial, A. N., 2011. Chromium isotopes in carbonates - A tracer for

climate change and for reconstructing the redox state of ancient seawater. *Earth and Planetary Science Letters* 312, 114–125.

Frei, R., Gaucher, C., Poulton, S. W., Canfield, D. E., 2009. Fluctuations in Precambrian atmospheric oxygenation recorded by chromium isotopes. *Nature* 461, 250–253.

Frei, R., Gaucher, C., Stolper, D., Canfield, D. E., 2013. Fluctuations in late Neoproterozoic atmospheric oxidation — Cr isotope chemostratigraphy and iron speciation of the late Ediacaran lower Arroyo del Soldado Group (Uruguay). *Gondwana Research* 23, 797–811.

Frei, R., Poiré, D., Frei, K. M., 2014. Weathering on land and transport of chromium to the ocean in a subtropical region (Misiones, NW Argentina): A chromium stable isotope perspective. *Chemical Geology* 381, 110–124.

Frei, R., Polat, A., 2013. Chromium isotope fractionation during oxidative weathering—Implications from the study of a Paleoproterozoic (ca. 1.9 Ga) paleosol, Schreiber Beach, Ontario, Canada. *Precambrian Research* 224, 434–453.

Frimmel, H. E., 2009. Trace element distribution in Neoproterozoic carbonates as palaeoenvironmental indicator. *Chemical Geology* 258, 338–53.

Gale, A. S., Christensen, W. K., 1996. Occurrence of the belemnite *Actinocamax plenus* in the Cenomanian of SE France and its significance. *Bulletin of the Geological Society of Denmark* 43, 68–77.

Galeotti, S., Krishnan, S., Pagani, M., Lanci, L., Gaudio, A., Zachos, J. C., Monechi, S., Morelli, G., Lourens, L., 2010. Orbital chronology of Early Eocene hyperthermals from the Contessa Road section, central Italy. *Earth and Planetary Science Letters* 290, 192–200.

Gavrilov, Y., Shcherbina, E. A., Oberhänsli, H., 2003. Paleocene-Eocene boundary events in the northeastern Peri-Tethys. In: Wing, S.L., et al., (eds.). Causes and consequences of globally warm climates in the early Paleogene. *Geological Society of America Special Paper* 369, 147-168.

Geiser, P. A., Sansone, S., 1981. Joints, microfractures, and the formation of solution cleavage in limestone. *Geology* 9, 280–285.

German, C. R., Masuzawa, T., Greaves, M. J., Elderfield, H., Edmond, J. M., 1995. Dissolved rare earth elements in the Southern Ocean: cerium oxidation and the influence of hydrography. *Geochimica et Cosmochimica Acta* 59, 1551–58.

German, C. R., Elderfield, H., 1990. Application of the Ce anomaly as a paleoredox indicator: the ground rules. *Paleoceanography* 5, 823–33.

Gibbs, S. J., Bralower, T. J., Bown, P. R., Zachos, J. C., Bybell, L. M., 2006. Shelf and open-ocean calcareous phytoplankton assemblages across the Paleocene-Eocene Thermal Maximum: Implication for global productivity gradients. *Geology* 34, 233-236.

Gilleaudeau, G. J., Frei, R., Kaufman, A. J., Kah, L. C., Azmy, K., Bartley, J. K., Chernyavskiy, P., Knoll, A. H., 2016. Oxygenation of the Mid-Proterozoic atmosphere: Clues from chromium isotopes in carbonates. Geochemical Perspectives Letters 2, 178-187.

Gilly, W. F., Beman, J. M., Litvin, S. Y., Robison, B. H., 2013. Oceanographic and biological effects of shoaling of the oxygen minimum zone. *Annual Review of Marine Science* 5, 393–420.

Giusberti, L., Coccioni, R., Sprovieri, M., Tateo, F., 2009. Perturbation at the sea floor during the Paleocene-Eocene Thermal Maximum: Evidence from benthic foraminifera at Contessa Road, Italy. *Marine Micropaleontology* 70, 102–119.

Goldstein, S. J., Jacobsen, S. B., 1988. Rare earth elements in river waters. *Earth and Planetary Science Letters* 89, 35–47.

Gomes, M. L., Hurtgen, M. T., Sageman, B. B., 2016. Biogeochemical sulfur cycling during Cretaceous oceanic anoxic events: A comparison of OAE1a and OAE2. *Paleoceanography* 3, 233–251.

Gordon, A. L., Huber, B. A., 1990. Southern Ocean winter mixed layer. *Journal of Geophysical Research* 95, 11655.

Goring-Harford, H. J., James, R. H., Pearce, C. R., Connelly, D. P., Klar, J. K., Parkinson, I. J., 2017. On the Cr isotopic composition of seawater. *Goldschmidt Abstracts* 2017.

Goring-Harford, H., Klar, J. K, Pearce, C. R., Connelly, D. P., Achterberg, E. P., James, R. H., 2018. Behaviour of chromium isotopes in the eastern sub-tropical Atlantic Oxygen Minimum Zone. *Geochimica et Cosmochimica Acta*.

Gradstein, F. M., Ogg, J. G., Schmitz, M. D., Ogg, G. M., Gradstein, F. M., All, A., 2012. The Geologic Time Scale 2012. Elsevier, Amsterdam.

Gray, J. S., Wu, R. S., Or, Y. Y., 2002. Effects of hypoxia and organic enrichment on the coastal marine environment. *Marine Ecology Progress Series* 238, 249–279.

Greaves, M. J., Statham, P. J., Elderfield, H., 1994. Rare earth element mobilization from marine atmospheric dust into seawater. *Marine Chemistry* 46, 255–60.

Gruber, N., 2008. The Marine Nitrogen Cycle. In: Capone, D. G., Bronk D. A., Mulholland, M. R., Carpenter, E. J. (eds). Nitrogen in the Marine Environment, 1–50. Elsevier, Amsterdam.

Gruber, N., Sarmiento, J. L., 2002. Large-scale Biogeochemical-Physical Interactions in Elemental Cycles. In: A. R. Robinson, J. J. McCarthy, & B. J. Rothschild (eds.). The Sea, 337–399. Wiley, New York, USA.

Gueguen, B., Reinhard, C. T., Algeo, T. J., Peterson, L. C., Nielsen, S. G., Wang, X., Rowe, H., Planavsky, N. J., 2016. The chromium isotope composition of reducing and oxic marine sediments. *Geochimica et Cosmochimica Acta* 184, 1–19.

Gustafsson, J. P., Persson, I., Oromieh, A. G., Van Schaik, J. W. J., Sjöstedt, C., Kleja, D. B., 2014. Chromium(III) complexation to natural organic matter: mechanisms and modeling. Environmental Science and Technology 48, 1753-1761.

Gutjahr, M., Ridgwell, A., Sexton, P. F., Anagnostou, E., Pearson, P. N., Pälike, H., Norris, R. D., Thomas, E., Foster, G. L., 2017. Very large release of mostly volcanic carbon during the Palaeocene-Eocene Thermal Maximum. *Nature* 548, 573-577.

Haley, B. A., Klinkhammer, G. P., McManus, J., 2004. Rare earth elements in pore waters of marine sediments. *Geochimica et Cosmochimica Acta* 68, 1265-1279.

Haley, B. A., Klinkhammer, G. P., Mix, A. C., 2005. Revisiting the rare earth elements in foraminiferal tests. *Earth and Planetary Science Letters* 239, 79–97.

Hatta, M., Measures, C.I., Wu, J., Roshan, S., Fitzsimmons, J.N., Sedwick, P., Morton, P., 2015. An

overview of dissolved Fe and Mn distributions during the 2010-2011 U.S. GEOTRACES North Atlantic cruises: GEOTRACES GA03. *Deep-Sea Research Part II: Topical Studies in Oceanography* 116, 117–29.

Hay, W. W., 2011. Can humans force a return to a "Cretaceous" climate? *Sedimentary Geology* 235, 5–16.

Helm, K. P., Bindoff, N. L., Church, J. A., 2011. Observed decreases in oxygen content of the global ocean. *Geophysical Research Letters* 38.

Hemleben, C., Spindler, M., Anderson, O. R., 1989. Modern Planktonic Foraminifera. Springer, New York, USA.

Herbel, M. J., Johnson, T. M., Oremland, R. S., Bullen, T. D., 2000. Fractionation of selenium isotopes during bacterial respiratory reduction of selenium oxyanions. *Geochimica et Cosmochimica Acta* 64, 3701-3709.

Herguera, J. C., 2000. Last glacial paleoproductivity patterns in the eastern equatorial Pacific: Benthic foraminifera records. *Marine Micropaleontology* 40, 259–275.

Holland, K., Eggins, S.M., Hönisch, B., Haynes, L.L., Branson, O., 2017. Calcification rate and shell chemistry response of the planktic foraminifer *Orbulina universa* to changes in microenvironment seawater carbonate chemistry. *Earth and Planetary Science Letters* 464, 124-34.

Holmden, C., Jacobson, A.D., Sageman, B.B., Hurtgen, M.T., 2016. Response of the Cr Isotope Proxy to Cretaceous Ocean Anoxic Event 2 in a Pelagic Carbonate Succession from the Western Interior Seaway. *Geochimica et Cosmochimica Acta* 186, 277–95.

Hönisch, B., Gary Hemming, N., 2004. Ground-Truthing the Boron Isotope-Paleo-pH Proxy in Planktonic Foraminifera Shells: Partial Dissolution and Shell Size Effects. *Paleoceanography* 19, 1–13.

Hönisch, B., Ridgwell, A., Schmidt, D. N., 2012. The geological record of ocean acidification. *Science* 335, 1058–63.

Hülse, D., Arndt, S., Wilson, J. D., Munhoven, G., Ridgwell, A., 2017. Understanding the causes and consquences of past marine carbon cycling variability through models. *Earth-Science Reviews* 171, 349-82.

Impert, O., Katafias, A., Kita, P., Wrzeszcz, G., 2008. Kinetics of Chromium (V) formation from some tetraazamacrocyclic chromium (III) complexes in alkaline media. *Polish Journal of Chemistry* 82, 1673–1679.

Izbicki, J. a., Ball, J. W., Bullen, T. D., Sutley, S. J., 2008. Chromium, chromium isotopes and selected trace elements, western Mojave Desert, USA. *Applied Geochemistry* 23, 1325–1352.

Jacob, D. E., Wirth, R., Agbaje, O. B. A., Branson, O., Eggins, S. M., 2017. Planktic foraminifera form their shells via metastable carbonate phases. *Nature Communications* 8.

Jahren, A. H., Arens, N. C., Sarmiento, G., Guerrero, J., Amundson, R., 2001. Terrestrial record of methane hydrate dissociation in the Early Cretaceous. *Geology* 29, 159–162.

James, R. H., Elderfield, H., Palmer, M. R., 1995. The chemistry of hydrothermal fluids from the Broken Spur site, 29°N Mid-Atlantic Ridge. Geochimica et Cosmochimica Acta 59, 651–59.

Jarvis, I., Lignum, J. S., Gröcke, D. R., Jenkyns, H. C., Pearce, M. A., 2011. Black shale deposition, atmospheric CO_2 drawdown, and cooling during the Cenomanian-Turonian Oceanic Anoxic Event. *Paleoceanography* 26, PA3201.

Jarvis, I., Murphy, A., Gale, A., 2001. Geochemistry of pelagic and hemipelagic sediments: criteria for identifying systems tracts and sea-level change. *Journal of the Geological Society* 158, 685–696.

Jeans, C. V., Long, D., Hall, M. A., Bland, D. J., Cornford, C., 1991. The geochemistry of the Plenus Marls at Dover, England: Evidence of fluctuating oceanographic conditions and of glacial control during the development of the Cenomanian–Turonian $\delta^{13}C$ anomaly. *Geological Magazine* 128, 603–632.

Jefferies, R. P. S., 1961. The palaeoecology of the *Actinocamax Plenus* Subzone (Turonian) in the Anglo-Paris Basin. *Palaeontology* 4, 609–647.

Jefferies, R. P. S., 1963. The stratigraphy of the *Actinocamax plenus* Subzone (Turonian) in the Anglo-Paris Basin. *Proceedings of the Geologists' Association* 74, 1-33.

Jenkyns, H. C., 1980. Cretaceous anoxic events: from continents to oceans. *Journal of the Geological Society* 137, 171–188.

Jenkyns, H. C., 2003. Evidence for rapid climate change in the Mesozoic-Palaeogene greenhouse world. *Philosophical Transactions of the Royal Society A: Mathematical, Physical and Engineering Sciences* 361, 1885–1916.

Jenkyns, H. C., 2010. Geochemistry of oceanic anoxic events. *Geochemistry, Geophysics, Geosystems*, 11.

Jenkyns, H. C., Dickson, A. J., Ruhl, M., Van Den Boorn, S. H. J. M., 2017. Basalt-seawater interaction, the Plenus Cold Event, enhanced weathering and geochemical change: deconstructing Oceanic Anoxic Event 2 (Cenomanian-Turonian, Late Cretaceous). *Sedimentology* 64, 16–43.

Jenkyns, H. C., Gale, A. S., Corfield, R. M., 1994. Carbon- and oxygen-isotope stratigraphy of the English Chalk and Italian Scaglia and its palaeoclimatic significance. *Geological Magazine* 131, 1–34.

Jennions, S. M., Thomas, E., Schmidt, D. N., Lunt, D., Ridgwell, A., 2015. Changes in benthic ecosystems and ocean circulation in the Southeast Atlantic across Eocene Thermal Maximum 2. *Paleoceanography* 30, 1059–1077.

John, C. M., Bohaty, S. M., Zachos, J. C., Sluijs, A., Gibbs, S., Brinkhuis, H., Bralower, T. J., 2008. North American continental margin records of the Paleocene-Eocene thermal maximum: Implications for global carbon and hydrological cycling. *Paleoceanography* 23, PA2217.

Johnson, C. M., Beard, B. L., Albarède, F., 2004. Overview and General Concepts. In: Geochemistry of Non-Traditional Stable Isotopes *Reviews in Mineralogy and Geochemistry* 55, 1–24.

Johnson, T. M., Bullen, T. D., 2004. Selenium and Chromium Isotopes in Low-Temperature Environments. In: Geochemistry of Non-Traditional Stable Isotopes. *Reviews in Mineralogy and Geochemistry* 55, 289–317.

Kaiho, K., Takeda, K., Petrizzo, M. R., Zachos, J. C., 2006. Anomalous shifts in tropical Pacific planktonic and benthic foraminiferal test size during the Paleocene-Eocene thermal maximum. *Palaeogeography, Palaeoclimatology, Palaeoecology* 237, 456-464.

Kamber, B. S., Whitehouse, M. J., Bolhar, R., Moorbath, S., 2005. Volcanic resurfacing and the early terrestrial crust: zircon U-Pb and REE constraints from the Isua Greenstone Belt, Southern West Greenland. *Earth and Planetary Science Letters* 240, 276–90.

Karstensen, J., Stramma, L., Visbeck, M., 2008. Oxygen minimum zones in the eastern tropical Atlantic and Pacific oceans. *Progress in Oceanography* 77, 331–350.

Keeling, R. E., Körtzinger, A., Gruber, N., 2010. Ocean deoxygenation in a warming world. *Annual Review of Marine Science* 2, 199–229.

Keeling, R. F., Garcia, H. E., 2002. The change in oceanic O_2 inventory associated with recent global warming. *Proceedings of the National Academy of Sciences* 99, 7848–7853.

Keeling, R. F., Manning, A. C., 2014. Studies of Recent Changes in Atmospheric O_2 Content. In: Treatise on Geochemistry (Second Edition) 5, 385–404.

Kelly, D. C., Nielsen, T. M. J., McCarren, H. K., Zachos, J. C., Röhl, U., 2010. Spatiotemporal patterns of carbonate sedimentation in the South Atlantic: Implications for carbon cycling during the Paleocene-Eocene thermal maximum. *Palaeogeography, Palaeoclimatology, Palaeoecology* 293, 30-40.

Kitchen, J. W., Johnson, T. M., Bullen, T. D., Zhu, J., Raddatz, A., 2012. Chromium isotope fractionation factors for reduction of Cr(VI) by aqueous Fe(II) and organic molecules. *Geochimica et Cosmochimica Acta* 89, 190-201.

Kolonic, S., Wagner, T., Forster, A., Sinninghe Damsté, J. S., Walsworth-Bell, B., Erba, E., Turgeon, S., Brumsack, H.-J., Chellai, E. H., Tsikos, H., Kuhnt, W., Kuypers, M. M. M., 2005. Black shale deposition on the northwest African Shelf during the Cenomanian/Turonian oceanic anoxic event: Climate coupling and global organic carbon burial. *Paleoceanography* 20, 1–18.

Konhauser, K. O., Lalonde, S. V., Planavsky, N. J., Pecoits, E., Lyons, T. W., Mojzsis, S. J., Rouxel, O. J., Barley, M. E., Rosiere, C., Fralick, P. W., Kump, L. R., Bekker, A., 2011. Aerobic bacterial pyrite oxidation and acid rock drainage during the Great Oxidation Event. *Nature* 478, 369–73.

Kortenkamp, A., Casadevall, M., Faux, S. P., Jenner, A., Shayer, R. O., Woodbridge, N., & O'Brien,

P., 1996. A role for molecular oxygen in the formation of DNA damage during the reduction of the carcinogen chromium (VI) by glutathione. *Archives of Biochemistry and Biophysics* 329, 199–207.

Kritzberg, E. S., Duarte, C. M., Wassmann, P., 2010. Changes in Arctic marine bacterial carbon metabolism in response to increasing temperature. *Polar Biology* 33, 1673–1682.

Kuroda, J., Ogawa, N. O., Tanimizu, M., Coffin, M. F., Tokuyama, H., Kitazato, H., Ohkouchi, N., 2007. Contemporaneous massive subaerial volcanism and late cretaceous Oceanic Anoxic Event 2. *Earth and Planetary Science Letters* 256, 211–223.

Kuypers, M. M. M., Pancost, R. D., Sinninghe Damsté, J. S., 1999. A large and abrupt fall in atmospheric CO_2 concentration during Cretaceous times. *Nature* 399, 342–345.

Langer, G., Sadekov, A., Thoms, S., Keul, N., Nehrke, G., Mewes, A., Greaves, M., Misra, S., Reichart, G. J., De Nooijer, L. J., Bijma, J., and Elderfield, H., 2016. Sr Partitioning in the Benthic Foraminifera Ammonia Aomoriensis and Amphistegina Lessonii. *Chemical Geology* 440, 306–12.

Laskar, J., Fienga, A., Gastineau, M., Manche, H., 2011. La2010: A new orbital solution for the long-term motion of the Earth. *Astronomy and Astrophysics* 532, A89.

Lau, K. V., Maher, K., Altiner, D., Kelley, B. M., Kump, L. R., Lehrmann, D. J., Silva-Tamayo, J. C., Weaver, K. L., Yu, M., Payne, J. L., 2016. Marine anoxia and delayed Earth system recovery after the end-Permian extinction. *Proceedings of the National Academy of Sciences* 113, 2360–2365.

Lauretano, V., Littler, K., Polling, M., Zachos, J. C., Lourens, L. J., 2015. Frequency, magnitude and character of hyperthermal events at the onset of the Early Eocene Climatic Optimum. *Climate of the Past* 11, 1313–1324.

Lawrence, M. G., Greig, A., Collerson, K. D., Kamber, B. S., 2006. Rare earth element and yttrium variability in South East Queensland waterways. *Aquatic Geochemistry* 12, 39–72.

Lechler, M., Pogge von Strandmann, P. A. E., Jenkyns, H. C., Prosser, G., Parente, M., 2015. Lithium-isotope evidence for enhanced silicate weathering during OAE1a (Early Aptian Selli event). *Earth and Planetary Science Letters* 432, 210-22.

Li, H., Xin, H.L., Kunitake, M.E., Keene, E.C., Muller, D.A., and Estroff, L.A., 2011. Calcite prisms from mollusk shells (*Atrina Rigida*): swiss-cheese-like organic-inorganic single-crystal composites. *Advanced Functional Materials* 21, 2028–34.

Littler, K., Röhl, U., Westerhold, T., Zachos, J. C., 2014. A high-resolution benthic stable-isotope record for the South Atlantic: Implications for orbital-scale changes in Late Paleocene-Early Eocene climate and carbon cycling. *Earth and Planetary Science Letters* 401, 18–30.

Lowenstam, H. A., Weiner, S, 1989. On Biomineralization. Oxford University Press.

Lourens, L. J., Sluijs, A., Kroon, D., Zachos, J. C., Thomas, E., Röhl, U., Bowles, J., Raffi, I., 2005. Astronomical pacing of late Palaeocene to early Eocene global warming events. *Nature* 435, 1083–1087.

Luciani, V., Cobianchi, M., Jenkyns, H. C., 2004. Albian high-resolution biostratigraphy and isotope stratigraphy: The Coppa della Nuvola pelagic succession of the Gargano Promontory (Southern Italy). *Eclogae Geologicae Helvetiae* 97, 77–92.

Luciani, V., D'Onofrio, R., Dickens, G. R., Wade, B. S., 2017. Planktic foraminiferal response to early Eocene carbon cycle perturbations in the southeast Atlantic Ocean (ODP Site 1263). *Global and Planetary Change* 158, 119–133.

Lunt, D. J., Valdes, P. J., Dunkley Jones, T., Ridgwell, A., Haywood, A. M., Schmidt, D. N., Marsh, R., Maslin, M., 2010. CO_2-driven ocean circulation changes as an amplifier of Paleocene-Eocene thermal maximum hydrate destabilization. *Geology* 38, 875-878.

Lyons, T. W., Reinhard, C. T., Planavsky, N. J., 2014. The rise of oxygen in Earth's early ocean and atmosphere. *Nature* 506, 307-315.

Ma, Z., Gray, E., Thomas, E., Murphy, B., Zachos, J., Paytan, A., 2014. Carbon sequestration during the Palaeocene-Eocene Thermal Maximum by an efficient biological pump. *Nature Geoscience* 7, 382-388.

Martin, A., Nisbet, E. G., Bickle, M. J., 1980. Archaean stromatolites of the Belingwe Greenstone Belt, Zimbabwe (Rhodesia). *Precambrian Research* 13, 337-362.

McArthur, J. M., Thirlwall, M. F., Gale, A. S., Kennedy, W. J., Burnett, J. A., Mattey, D., Lord, A. R., 1993. Strontium isotope stratigraphy for the Late Cretaceous: a new curve, based on the English Chalk. Geological Society of London Special Publications 70, 195-209.

McCarren, H., Thomas, E., Hasegawa, T., Röhl, U., Zachos, J. C., 2008. Depth dependency of the Paleocene-Eocene carbon isotope excursion: Paired benthic and terrestrial biomarker records (ocean drilling program leg 208, Walvis Ridge). *Geochemistry, Geophysics, Geosystems* 9, Q10008.

McConnaughey, T., 1988. ^{13}C and $^{18}0$ isotopic disequilibrium in biological carbonates: I. Patterns. *Geochimica et Cosmochimica Acta* 53, 151–162.

McCrea, J. M., 1950. On the isotopic chemistry of carbonates and a paleotemperature scale. *Journal of Chemical Physics* 18, 849–857.

McDonough, W. F., Sun, S.-S.,1995. The composition of the Earth. *Chemical Geology* 120, 223–253.

Mclennan, S. M., 2001. Relationships between the trace element composition of sedimentary rocks and upper continental crust. *Geochemistry Geophysics Geosystems* 2.

Méhay, S., Keller, C. E., Bermasconi, S. M., Weissert, H., Erba, E., Bottini, C., Hochuli, P. A., 2009. A volcanic CO_2 pulse triggered the Cretaceous Oceanic Anoxic Event 1a and a biocalcification crisis. *Geology* 37, 819–822.

Menegatti, A. P., Weissert, H., Brown, R. S., Tyson, R. V., Farrimond, P., Strasser, A., Caron, M., 1998. High-resolution ^{13}C stratigraphy through the early Aptian "Livello Selli" of the Alpine Tethys Alessio. *Paleoceanography* 13, 530–545.

Meyer, K. M., Kump, L. R., 2008. Oceanic Euxinia in Earth History: Causes and Consequences. *Annual Review of Earth and Planetary Sciences* 36, 251–288.

Mitchell, K., Mason, P. R. D., Van Cappellen, P., Johnson, T. M., Gill, B. C., Owens, J. D., Diaz, J., Ingall, E. D., Reichart, G.-J., Lyons, T. W., 2012. Selenium as paleo-oceanographic proxy: A first assessment. Geochimica et Cosmochimica Acta 89, 302-17.

Monteiro, F. M., Pancost, R. D., Ridgwell, A., Donnadieu, Y., 2012. Nutrients as the dominant control on the spread of anoxia and euxinia across the Cenomanian-Turonian oceanic anoxic event (OAE2): Model-data comparison. *Paleoceanography* 27, PA4209.

Mora, A., Alfonso, J. A., Luzmila, S., Calzadilla, M., Silva, S., Labrecque, J. J., Az, A., 2009. Temporal variability of selected dissolved elements in the lower Orinoco River, Venezuela. *Hydrological Processes* 485, 476–485.

Mugo, R. K., Orians, K. J., 1993. Seagoing method for the determination of chromium(III) and total chromium in sea water by electron-capture detection gas chromatography. *Analytica Chimica Acta* 271, 1–9.

Murray, J. W., Spell, B., Paul, B., 1983. The contrasting geochemistry of manganese and chromium in the eastern Pacific Ocean. In: Trace metals in sea water. NATO Conference Series 4, Marine Science 13. Plenum, New York, USA, 643-669.

Mutterlose, J., Bottini, C., Schouten, S., Sinninghe Damsté, J. S., 2014. High sea-surface temperatures during the early Aptian Oceanic Anoxic event 1a in the Boreal Realm. *Geology* 42, 439–442.

Myers, C. R., Carstens, B. P., Antholine, W. E., Myers, J. M., 2000. Chromium(VI) reductase activity is associated with the cytoplasmic membrane of anaerobically grown *Shewanella putrefaciens* MR-1. *Journal of Applied Microbiology* 88, 98–106.

Naafs, B. D. A., Castro, J. M., De Gea, G. A., Quijano, M. L., Schmidt, D. N., Pancost, R. D., 2016. Gradual and sustained carbon dioxide release during Aptian Oceanic Anoxic Event 1a. *Nature Geoscience* 9, 135–139.

Nakayama, E., Tokoro, H., Kuwamoto, T., Fujinaga, T., 1981. Dissolved state of chromium in seawater. *Nature* 290, 768-770.

Neilands, J.B., 1995. Siderophores: Structure and function of microbial iron transport compounds. *Journal of Biological Chemistry* 270, 26723–26726.

Ni, Y., Foster, G.L., Bailey, T., Elliott, T., Schmidt, D.N., Pearson, P., Haley, B., and Coath, C., 2007. A core top assessment of proxies for the ocean carbonate system in surface-dwelling foraminifers. *Paleoceanography* 22, PA3212.

Nicolo, M. J., Dickens, G. R., Hollis, C. J., 2010. South Pacific intermediate water oxygen depletion at the onset of the Paleocene-Eocene thermal maximum as depicted in New Zealand margin sections. *Paleoceanography* 25, PA4210.

Nicolo, M. J., Dickens, G. R., Hollis, C. J., Zachos, J. C., 2007. Multiple early Eocene hyperthermals: Their sedimentary expression on the New Zealand continental margin and in the deep sea. *Geology* 35, 699–702.

Nightingale, P. D., Liss, P. S., 2003. Gases in Seawater. In: Treatise on Geochemistry 6–9, 49–81.

Norris, R. D., Bice, K. L., Magno, E. A., Wilson, P. A., 2002. Jiggling the tropical thermostat in the Cretaceous hothouse. *Geology* 30, 299–302.

Nothdurft, L. D., Webb, G. E., Kamber, B. S., 2004. Rare earth element geochemistry of Late Devonian reefal carbonates, Canning Basin, Western Australia: confirmation of a seawater REE proxy in ancient limestones. *Geochimica et Cosmochimica Acta* 68, 263–83.

Novak, M., Chrastny, V., Cadkova, E., Farkas, J., Bullen, T. D., Tylcer, J., Szurmanova, Z., Cron, M., Prechova, E., Curik, J., Sepanova, M., Pasava, J., Erbanova, L., Houskova, M., Pucochar, K., Hellerich, L. A., 2014. Common occurrence of a positive $\delta^{53}Cr$ shift in central european waters contaminated by geogenic/industrial chromium relative to source values. *Environmental Science and Technology* 48, 6089–6096.

Nunes, F., Norris, R. D., 2006. Abrupt reversal in ocean overturning during the Palaeocene/Eocene warm period. *Nature* 439, 60-63.

Ogg, J. G., Hinnov, L. A., Huang, C., 2012. Cretaceous. In: The Geologic Time Scale, 793–853.

Olson, D. B., Hitchcock, G. L., Fine, R. A., Warren, B. A., 1993. Maintenance of the low-oxygen layer in the central Arabian Sea. *Deep-Sea Research Part II* 40, 673–685.

Orth, C. J., Attrep, M., Quintana, L. R., Elder, W. P., Kauffman, E. G., Diner, R., Villamil, T., 1993. Elemental abundance anomalies in the late Cenomanian extinction interval: a search for the source(s). *Earth and Planetary Science Letters* 117, 189–204.

Osborne, A. H., Hathorne, E. C., Schijf, J., Plancherel, Y., Böning, P., Frank, M., 2017. The potential of sedimentary foraminiferal rare earth element patterns to trace water masses in the past. *Geochemistry, Geophysics, Geosystems* 18: 1550–68.

Pälike, C., Delaney, M. L., Zachos, J. C., 2014. Deep-sea redox across the Paleocene-Eocene thermal maximum. *Geochemistry, Geophysics, Geosystems* 15, 1038-1053.

Palmer, M. R., 1985. Rare earth elements in foraminifera tests. *Earth and Planetary Science Letters* 73, 285-298.

Palmer, M. R, Elderfield, H., 1986. Rare earth elements and neodymium isotopes in ferromanganese oxide coatings of Cenozoic foraminifera from the Atlantic Ocean. *Geochimica et Cosmochimica Acta* 50, 409–17.

Pancost, R. D., Crawford, N., Magness, S., Turner, A., Jenkyns, H. C., Maxwell, J. R., 2004. Further evidence for the development of photic-zone euxinic conditions during Mesozoic oceanic anoxic events. *Journal of the Geological Society* 161, 353–364.

Paulukat, C., Døssing, L.N., Mondal, S.K., Voegelin, A.R., Frei, R., 2015. Oxidative release of chromium from Archean ultramafic rocks, its transport and environmental impact - a Cr isotope perspective on the Sukinda Valley Ore District (Orissa, India). *Applied Geochemistry* 59, 125–38.

Paulukat, C., Gilleaudeau, G.J., Chernyavskiy, P., Frei, R., 2016. The Cr-isotope signature of surface seawater — a global perspective. *Chemical Geology* 444, 101–9.

Pearce, M. A., Jarvis, I., Tocher, B. A., 2009. The Cenomanian-Turonian boundary event, OAE2 and palaeoenvironmental change in epicontinental seas: New insights from the dinocyst and geochemical records. *Palaeogeography, Palaeoclimatology, Palaeoecology* 280, 207–234.

Pearson, P. N., 2012. Oxygen Isotopes in Foraminifera: Overview and Historical Review. *The Paleontological Society Papers* 18, 1–38.

Pedersen, T. F., Calvert, S. E., 1990. Anoxia vs. productivity: what controls the formation of organic-carbon-rich sediments and sedimentary rocks? *American Association of Petroleum Geologists Bulletin* 75, 500-501

Penman, D. E., Hönisch, B., Zeebe, R. E., Thomas, E., Zachos, J. C., 2014. Rapid and sustained surface ocean acidification during the Paleocene-Eocene Thermal Maximum. *Paleoceanography* 29, 357–369.

Pereira, N.S., Voegelin, A.R., Paulukat, C., Sial, A.N., Ferreira, V.P., Frei, R., 2016. Chromium-isotope signatures in scleractinian corals from the Rocas Atoll, Tropical South Atlantic. *Geobiology* 14, 54–67.

Pettine, M., Campanella, L., Millero, F. J., 2002. Reduction of hexavalent chromium by H_2O_2 in acidic solutions. *Environmental Science and Technology* 36, 901–907.

Pettine, M., Camusso, M., Martinotti, W., 1992. Dissolved and particulate transport of arsenic and chromium in the Po River (Italy). *Science of the Total Environment* 119, 253–280.

Pettine, M., D'Ottone, L., Campanella, L., Millero, F. J., Passino, R., 1998. The reduction of chromium (VI) by iron (II) in aqueous solutions. *Geochimica et Cosmochimica Acta* 62, 1509–1519.

Planavsky, N. J., Reinhard, C. T., Wang, X., Thomson, D., McGoldrick, P., Rainbird, R. H., Johnson, T., Fischer, W. W., Lyons, T. W., 2014. Earth history. Low mid-Proterozoic atmospheric oxygen levels and the delayed rise of animals. *Science* 346, 635–638.

Pogge Von Strandmann, P. A. E., Jenkyns, H. C., Woodfine, R. G., 2013. Lithium isotope evidence for enhanced weathering during Oceanic Anoxic Event 2. *Nature Geoscience* 6, 668–672.

Polerecky, L., Adam, B., Milucka, J., Musat, N., Vagner, T., Kuypers, M.M., 2012. Look@NanoSIMS – a tool for the analysis of nanoSIMS data in environmental microbiology. *Environmental Microbiology* 14, 1009-1023.

Pörtner, H. O., Karl, D., Boyd, P. W., Cheung, W., Lluch-Cota, S. E., Nojiri, Y., Schmidt, D. N., Zavialov, P., 2014. Ocean systems, in: Field, C. B., Barros, V. R., Dokken, D. J., Mach, K. J., Mastrandrea, M. D., Bilir, T. E., Chatterjee, M., Ebi, K. L., Estrada, Y. O., Genova, R. C., Girma, B., Kissel, E. S., Levy, A. N., MacCracken, S., Mastrandrea, P. R., White, L. L. (Eds.), Climate Change 2014: Impacts, Adaptation, and Vulnerability. Part A: Global and Sectoral Aspects. Contribution of Working Group II to the Fifth Assessment Report of the Intergovernmental Panel on Climate Change. Cambridge University Press, Cambridge, United Kingdom and New York, USA, 411-484.

Post, J. E., Thomas, E., Heaney, P. J., 2016. Jianshuiite in oceanic manganese nodules at the Paleocene-Eocene boundary. *American Mineralogist* 101, 407-414.

Pourmand, A., Dauphas, N., Ireland, T. J., 2012. A novel extraction chromatography and MC-ICP-MS technique for tapid analysis of REE, Sc and Y: revising CI-chondrite and Post-Archean Australian Shale (PAAS) abundances. *Chemical Geology* 291, 38–54.

Premoli Silva, I., Sliter, W. V., 1999. Cretaceous paleoceanography: Evidence from planktonic foraminiferal evolution. *Special Paper of the Geological Society of America* 332, 301–328.

Qasim, S. Z., 1982. Oceanography of the northern Arabian Sea. *Deep Sea Research Part A,*

Oceanographic Research Papers 29, 1041–1068.

Qin, L., Wang, X., 2017. Chromium Isotope Geochemistry. In: Reviews in Mineralogy & Geochemistry 82, 379-414

Qu, C., Liu, G., Zhao, Y., 2009. Experimental study on the fractionation of yttrium from holmium during the coprecipitation with calcium carbonates in seawater solutions. *Geochemical Journal* 43, 403–14.

Rachold, V., Alabyan, A., Hubberten, H. W., Korotaev, V. N., Zaitsev, A. A., 1996. Sediment transport to the Laptev Sea - hydrology and geochemistry of the Lena River. *Polar Research* 15, 183–96.

Ravizza, G., Norris, R. N., Blusztajn, J., Aubry, M.-P., 2001. An osmium isotope excursion associated with the late Paleocene thermal maximum: evidence of intensified chemical weathering. *Paleoceanography* 16, 155-163.

Reichart, G. J., den Dulk, M., Visser, H. J., van der Weijden, C. H., Zachariasse, W. J., 1997. A 225 kyr record of dust supply, paleoproductivity and the oxygen minimum zone from the Murray Ridge (northern Arabian Sea). *Palaeogeography, Palaeoclimatology, Palaeoecology* 134, 149–169.

Reichart, G. J., Nortier, J., Versteegh, G., Zachariasse, W. J., 2002. Periodical breakdown of the Arabian Sea oxygen minimum zone caused by deep convective mixing. *Geological Society, London, Special Publications* 195, 407–419.

Reichart, G., Lourens, L., Zachariasse, W., 1998. Temporal variability in the northern Arabian Sea oxygen minimum zone (OMZ) during the last 225,000 years. *Paleoceanography* 13, 607–621.

Reinhard, C. T., Olson, Sl. L., Schwieterman, E. W., Lyons, T. W., 2017. False negatives for remote life detection on ocean-bearing planets: Lessons from the early Earth. *Astrobiology* 17, 287-297.

Reinhard, C. T., Planavsky, N. J., Wang, X., Fischer, W. W., Johnson, T. M., Lyons, T. W., 2014. The isotopic composition of authigenic chromium in anoxic marine sediments: A case study from the Cariaco Basin. Earth and Planetary Science Letters 407, 9-18.

Remmelzwaal., S. R. C., Sadekov, A. Y., Parkinson, I. J., Schmidt, D. N., Titelboim, D., Abramovich,

S., Roepert, A., Kienhuis, M., Polerecky, L., Goring-Harford, H., Kimoto, K., Allen, K. A., Holland, K., Middelburg, J. J., in review. Assessing the utility of foraminifera as seawater chromium recorders. *Earth and Planetary Science Letters*.

Ridgwell, A., Hargreaves, J. C., Edwards, N. R., Annan, J. D., Lenton, T. M., Marsh, R., Yool, A., Watson, A., 2007. Marine geochemical data assimilation in an efficient Earth System Model of global biogeochemical cycling. *Biogeosciences* 4, 87-104.

Ridgwell, A., Schmidt, D. N., 2010. Past constraints on the vulnerability of marine calcifiers to massive carbon dioxide release. *Nature Geoscience* 3, 196–200.

Roberts, N. L., Piotrowski, A. M., Elderfield, H., Eglinton, T. I., Lomas, M. W., 2012. Rare earth element association with foraminifera. *Geochimica et Cosmochimica Acta* 94, 57–71.

Roberts, N. L., Piotrowski, A. M., McManus, J. F., Keigwin, L. D., 2010. Synchronous deglacial overturning and water mass source changes. *Science* 327, 75–78.

Rodler, A., Sánchez-Pastor, N., Fernández-Díaz, L., Frei, R., 2015. Fractionation behavior of chromium isotopes during coprecipitation with calcium carbonate: implications for their use as paleoclimatic proxy. *Geochimica et Cosmochimica Acta* 164, 221–35.

Röhl, U., Westerhold, T., Bralower, T. J., Zachos, J. C., 2007. On the duration of the Paleocene-Eocene thermal maximum (PETM). *Geochemistry Geophysics Geosystems* 8, Q12002.

Romaniello, S. J., Herrmann, A. D., Anbar, A. D., 2013. Uranium concentrations and $^{238}U/^{235}U$ isotope ratios in modern carbonates from the Bahamas: Assessing a novel paleoredox proxy. *Chemical Geology* 362, 305–316.

Ruiz-Ortiz, P. A., Castro, J. M., de Gea, G. A., Jarvis, I., Molina, J. M., Nieto, L. M., Pancost, R. D., Quijano, M. L., Reolid, M., Skelton, P. W., Weissert, H. J., 2016. New drilling of the early Aptian OAE1a: The Cau core (Prebetic Zone, south-eastern Spain). *Scientific Drilling* 21, 41–46.

Russell, A.D., Hönisch, B., Spero, H.J., Lea, D.W., 2004. Effects of seawater carbonate ion concentration and temperature on shell U, Mg, and Sr in cultured planktonic foraminifera. *Geochimica et Cosmochimica Acta* 68, 4347–61.

Saad, E. M., Sun, J., Chen, S., Borkiewicz, O. J., Zhu, M., Duckworth, O. W., Tang, Y., 2017a.

Siderophore and Organic Acid Promoted Dissolution and Transformation of Cr(III)-Fe(III)-(oxy)hydroxides. *Environmental Science and Technology* 51, 3223–3232.

Saad, E. M., Wang, X., Planavsky, N. J., Reinhard, C. T., Tang, Y., 2017b. Redox-independent chromium isotope fractionation induced by ligand-promoted dissolution. *Nature Communications* 8.

Sadekov, A. Y., Eggins, S. M., De Deckker, P., 2005. Characterization of Mg/Ca distributions in planktonic foraminifera species by electron microprobe mapping. *Geochemistry, Geophysics, Geosystems* 6.

Sadekov, A., Eggins, S.M., De Deckker, P., and Kroon, D., 2008. Uncertainties in seawater thermometry deriving from intratest and intertest Mg/Ca variability in *Globigerinoides ruber*. *Paleoceanography* 23, PA1215.

Sageman, B. B., Meyers, S. R., Arthur, M. A., 2006. Orbital time scale and new C-isotope record for Cenomanian-Turonian boundary stratotype. *Geology* 34, 125–128.

Sander, S. G., Koschinsky, A., Halbach, P., 2003. Redox speciation of chromium in the oceanic water column of the Lesser Antilles and offshore Otago Peninsula, New Zealand. *Marine and Freshwater Research* 54, 745–754.

Sander, S. G., Koschinsky, A., 2011. Metal flux from hydrothermal vents increased by organic complexation. *Nature Geoscience* 4, 145–150.

Schauble, E. A., 2004. Fractionation Theory to New Systems. In: Reviews in Mineralogy & Geochemistry 55, 65–111.

Schauble, E., Rossman, G. R., Taylor, H. P., 2004. Theoretical estimates of equilibrium chromium-isotope fractionations. *Chemical Geology* 205, 99–114.

Scheiderich, K., Amini, M., Holmden, C., and Francois, R., 2015. Global Variability of Chromium Isotopes in Seawater Demonstrated by Pacific, Atlantic, and Arctic Ocean Samples. *Earth and Planetary Science Letters* 423, 87–97.

Schijf, J., Christenson, E. A., Byrne, R. H., 2015. YREE Scavenging in seawater: a new look at an old model. *Marine Chemistry* 177, 460–71.

Schlanger, S. O., Arthur, M. A., Jenkyns, H. C., Scholle, P. A., 1987. The Cenomanian-Turonian

oceanic event, I. Stratigraphy and distribution of organic carbon-rich beds and the marine d^{13}C excursion. *Marine Petroleum Source Rocks* 26, 371–400.

Schlanger, S. O., Jenkyns, H. C., 1976. Cretaceous Oceanic Anoxic Events: Causes and Consequences. *Geologie En Mijnbouw* 55, 179–184.

Schmidt, D. N., Elliott, T., Kasemann, S. A., 2008. The influences of growth rates on planktic foraminifers as proxies for palaeostudies - a review. *Geological Society, London, Special Publications.*

Schmidt, D. N., Lazarus, D., Young, J. R., and Kucera, M., 2006. Biogeography and evolution of body size in marine pankton. *Earth-Science Reviews* 78, 239–66.

Schmidtko, S., Stramma, L., Visbeck, M., 2017. Decline in global oceanic oxygen content during the past five decades. *Nature* 542, 335–339.

Schoenberg, R., Zink, S., Staubwasser, M., Von Blanckenburg, F., 2008. The stable Cr isotope inventory of solid Earth reservoirs determined by double spike MC-ICP-MS. *Chemical Geology* 249, 294–306.

Schroeder, D. C., Lee, G. F., 1975. Potential transformations of chromium in natural waters. *Water, Air, and Soil Pollution* 4, 355-365.

Seibel, B. A., 2011. Critical oxygen levels and metabolic suppression in oceanic oxygen minimum zones. *The Journal of Experimental Biology* 214, 326–336.

Sholkovitz, E. R., 1993. The geochemistry of rare earth elements in the Amazon river estuary. *Geochimica et Cosmochimica Acta* 57, 2181–90.

Sholkovitz, E. R., 1995. The aquatic chemistry of rare earth elements in rivers and estuaries. *Aquatic Geochemistry* 1, 1–34.

Sikora, E. R., Johnson, T. M., Bullen, T. D., 2008. Microbial mass-dependent fractionation of chromium isotopes. *Geochimica et Cosmochimica Acta* 72, 3631–3641.

Sinninghe Damsté, J. S., Köster, J., 1998. A euxinic southern North Atlantic Ocean during the Cenomanian/Turonian oceanic anoxic event. *Earth and Planetary Science Letters* 158, 165–173.

Sinninghe Damsté, J. S., Rijpstra, W. I. C., Hopmans, E. C., Prahl, F. G., Wakeham, S. G., Schouten,

S., 2002. Distribution of membrane lipids of planktonic Crenarchaeota in the Arabian Sea. *Applied and Environmental Microbiology* 68, 2997–3002.

Sinninghe Damsté, J. S., Van Bentum, E. C., Reichart, G.-J., Pross, J., Schouten, S., 2010. A CO_2 driven cooling and increased latitudinal temperature gradient during the mid-Cretaceous Oceanic Anoxic Event 2. *Earth and Planetary Science Letters* 293, 97–103.

Sirinawin, W., Turner, D. R., Westerlund, S., 2000. Chromium(VI) distributions in the Arctic and the Atlantic Oceans and a reassessment of the oceanic Cr cycle. *Marine Chemistry* 71, 265–282.

Slotnick, B. S., Dickens, G. R., Nicolo, M. J., Hollis, C. J., Crampton, J. S., Zachos, J. C., Sluijs, A., 2012. Large-amplitude variations in carbon cycling and terrestrial weathering during the Latest Paleocene and Earliest Eocene: The record at Mead Stream, New Zealand. *The Journal of Geology* 120, 487–505.

Sluijs, A., Schouten, S., Donders, T. H., Schoon, P. L., Röhl, U., Reichart, G.-J., Sangiorgi, F., Kim, J.-H., Sinninghe Damsté, J. S., Brinkhuis, H., 2009. Warm and wet conditions in the Arctic region during Eocene Thermal Maximum 2. *Nature Geoscience* 2, 777–780.

Sluijs, A., Van Roij, L., Harrington, G. J., Schouten, S., Sessa, J. A., Levay, L. J., Reichart, G.-J., Slomp, C. P., 2014. Warming, euxinia and sea level rise during the paleocene-eocene thermal maximum on the gulf coastal plain: Implications for ocean oxygenation and nutrient cycling. *Climate of the Past* 10, 1421–1439.

Snow, L. J., Duncan, R. A., Bralower, T. J., 2005. Trace element abundances in the Rock Canyon Anticline, Pueblo, Colorado, marine sedimentary section and their relationship to Caribbean plateau construction and ocean anoxic event 2. *Paleoceanography* 20, 1–14.

Soldati, A.L., Jacob, D.E., Glatzel, P., Swarbrick, J.C., Geck, J., 2016. Element substitution by living organisms: The case of manganese in mollusc shell aragonite. *Scientific Reports* 6, 22514.

Soyol-Erdene, T. O., Huh, Y., 2013. Rare earth element cycling in the pore waters of the Bering Sea slope (IODP Exp. 323). *Chemical Geology* 358, 75–89.

Stap, L., Lourens, L. J., Thomas, E., Sluijs, A., Bohaty, S., Zachos, J. C., 2010. High-resolution deep-sea carbon and oxygen isotope records of Eocene Thermal Maximum 2 and H2. *Geology* 38, 607–610.

Stap, L., Sluijs, A., Thomas, E., Lourens, L., 2009. Patterns and magnitude of deep sea carbonate dissolution during Eocene Thermal Maximum 2 and H2, Walvis Ridge, southeastern Atlantic Ocean. *Paleoceanography 2*4.

Staubwasser, M., Sirocko, F., 2002. On the formation of laminated sediments on the continental margin off Pakistan. *Marine Geology* 192, 431–433.

Stein, R., Boucsein, B., Meyer, H., 2006. Anoxia and high primary production in the Paleogene central Arctic Ocean: First detailed records from Lomonosov Ridge. *Geophysical Research Letters* 33.

Stocker, T. F., Qin, D., Plattner, G.-K., Tignor, M., Allen, S. K., Boschung, J., … Midgley, P. M. (Eds.), 2013. IPCC, 2013: Climate Change 2013: The Physical Science Basis. Contribution of Working Group I to the Fifth Assessment Report of the Intergovernmental Panel on Climate Change. IPCC AR5. Cambridge, UK and New York, USA: Cambridge University Press.

Stramma, L., Johnson, G. C., Sprintall, J., Mohrholz, V., 2008. Expanding oxygen-minimum zones in the tropical oceans. *Science* 320, 655–658.

Svensen, H., Planke, S., Malthe-Sørenssen, A., Jamtveit, B., Myklebust, R., Eidem, T. R., Rey, S. S., 2004. Release of methane from a volcanic basin as a mechanism for initial Eocene global warming. *Nature* 429, 542-545.

Takashima, R., Nishi, H., Yamanaka, T., Tomosugi, T., Fernando, A. G., Tanabe, K., Moriya, K., Kawabe, F., Hayashi, K., 2011. Prevailing oxic environments in the Pacific Ocean during the mid-Cretaceous Oceanic Anoxic Event 2. *Nature Communications* 2.

Tang, Y., Elzinga, E.J., Lee, Y.J., Reeder, R.J., 2007. Coprecipitation of chromate with calcite: Batch experiments and X-ray absorption spectroscopy. *Geochimica et Cosmochimica Acta* 71, 1480–93.

Tang, Y., Marc Michel, F., Zhang, L., Harrington, R., Parise, J.B., Reeder, R.J., 2010. Structural properties of the Cr(III)-Fe(III) (oxy)hydroxide compositional series: Insights for a nanomaterial 'solid solution'. *Chemistry of Materials* 22, 3589–98.

Tang, Y., Martin, S. T., 2011. Siderite dissolution in the presence of chromate. *Geochimica et Cosmochimica Acta* 75, 4951–4962.

Tang, Y., Webb, S. M., Estes, E. R., Hansel, C. M., 2014. Chromium(III) oxidation by biogenic

manganese oxides with varying structural ripening. Environmental Science: Processes & Impacts 16, 2127-2136.

Taylor, H. E., Antweiler, R. C., Roth, D. A., Alpers, C. N., Dileanis, P., 2012. Selected trace elements in the Sacramento River, California: Occurrence and distribution. *Archives of Environmental Contamination and Toxicology* 62, 557–569.

Taylor, S. R., McLennan, S. M., 1985. The continental crust: its composition and evolution. An examination of the geochemical record preserved in sedimentary rocks. The Continental Crust: Its Composition and Evolution. An Examination of the Geochemical Record Preserved in Sedimentary Rocks. Blackwell Scientific.

Tejada, M. L. G., Suzuki, K., Kuroda, J., Coccioni, R., Mahoney, J. J., Ohkouchi, N., Sakamoto, T., Tatsumi, Y., 2009. Ontong Java Plateau eruption as a trigger for the early Aptian oceanic anoxic event. *Geology* 37, 855–858.

Ter Kuile, B., Erez, J., Padan, E., 1989. Mechanisms for the uptake of inorganic carbon by two species of symbiont-bearing foraminifera. *Marine Biology* 103, 241–251.

Thamdrup, B., Dalsgaard, T., Revsbech, N. P., 2012. Widespread functional anoxia in the oxygen minimum zone of the Eastern South Pacific. *Deep Sea Research Part I: Oceanographic Research Papers* 65, 36–45.

Titelboim, D., Sadekov, A., Almogi-Labin, A., Herut, B., Kucera, M., Schmidt, C., Hyams-Kaphzan, O., and Abramovich, S., 2017. Geochemical Signatures of Benthic Foraminiferal Shells from a Heat-Polluted Shallow Marine Environment Provide Field Evidence for Growth and Calcification under Extreme Warmth. Global Change Biology 23, 4346–53.

Tostevin, R., Shields, G. A., Tarbuck, G. M., He, T., Clarkson, M. O., Wood, R. A., 2016. Effective use of cerium anomalies as a redox proxy in carbonate-dominated marine settings. *Chemical Geology* 438, 146-162.

Tremolada, F., Bralower, T. J., 2004. Nannofossil assemblage fluctuations during the Paleocene–Eocene Thermal Maximum at Sites 213 (Indian Ocean) and 401 (North Atlantic Ocean): palaeoceanographic implications. *Marine Micropaleontology* 52, 107-116.

Tripati, A., Elderfield, H., 2005. Deep-sea temperature and circulation changes at the Paleocene-Eocene Thermal Maximum. *Science* 308, 1894-1898.

Trinquier, A., Birck, J.-L., Allègre, C. J., 2008. High-precision analysis of chromium isotopes in terrestrial and meteorite samples by thermal ionization mass spectrometry. *Journal of Analytical Atomic Spectrometry* 23, 1565.

Troelstra, S. R., Ganssen, G. M., Sennema, E. J., Klaver, G. Th., Anderliesten, C., Van Den Borg, K., and De Jong, A. M. F., 1987. Late Quaternary Stratigraphy and Sedimentology of the Central North Atlantic: A Progress Report. *Nuclear Instruments and Methods in Physics Research Section B* 29, 317–321.

Tsikos, H., Jenkyns, H. C., Walsworth-Bell, B., Petrizzo, M. R., Forster, A., Kolonic, S., Erba, E., Premoli Silva, I., Baas, M., Wagner, T., Sinninghe Damsté, J. S., 2004. Carbon-isotope stratigraphy recorded by the Cenomanian-Turonian Oceanic Anoxic Event: correlation and implications based on three key localities. *Journal of the Geological Society* 161, 711–719.

Turgeon, S. C., Creaser, R. A., 2008. Cretaceous oceanic anoxic event 2 triggered by a massive magmatic episode. *Nature* 454, 323–326.

Tyson, R. V., 2001. Sedimentation rate, dilution, preservation and total organic carbon: Some results of a modelling study. *Organic Geochemistry* 32, 333–339.

Ulloa, O., Canfield, D. E., DeLong, E. F., Letelier, R. M., Stewart, F. J., 2012. Microbial oceanography of anoxic oxygen minimum zones. *Proceedings of the National Academy of Sciences of the United States of America* 109, 15996–16003.

Urey, H. C., Lowenstam, H. A., Epstein, S., Mckinney, C. R., 1951. Measurement of paleotemperatures and temperatures of the upper cretaceous of England, Denmark, and the southeastern United States. *Bulletin of the Geological Society of America* 62, 399–416.

Van Bennekom, A. J., Hiehle, M. A., 1994. CTD operations and calibrations during legs D1, D2 and D3 of the Netherlands Indian Ocean Programme. In: Van Der Linden, W. J. M., Van der Weijden, C. H. (Eds.), Geological Study of the Arabian Sea, 37–66. Netherlands Geoscience Foundation, The Hague, Netherlands.

Van Helmond, N. A. G. M., Ruvalcaba Baroni, I., Sluijs, A., Sinninghe Damsté, J. S., Slomp, C. P., 2014. Spatial extent and degree of oxygen depletion in the deep proto-North Atlantic basin during Oceanic Anoxic Event 2. *Geochemistry, Geophysics, Geosystems* 15, 4254–4266.

Van Helmond, N. A. G. M., Sluijs, A., Reichart, G. J., Damsté, J. S. S., Slomp, C. P., Brinkhuis, H., 2014. A perturbed hydrological cycle during Oceanic Anoxic Event 2. Geology 42, 123–126.

Van Helmond, N. A. G. M., Sluijs, A., Sinninghe Damsté, J. S., Reichart, G. J., Voigt, S., Erbacher, J., Pross, J., Brinkhuis, H., 2015. Freshwater discharge controlled deposition of Cenomanian-Turonian black shales on the NW European epicontinental shelf (Wunstorf, northern Germany). *Climate of the Past* 11, 495–508.

Voigt, S., Erbacher, J., Mutterlose, J., Weiss, W., Westerhold, T., Wiese, F., Wilmsen, M., Wonik, T., 2008. The Cenomanian – Turonian of the Wunstorf section – (North Germany): global stratigraphic reference section and new orbital time scale for Oceanic Anoxic Event 2. *Newsletters on Stratigraphy* 43, 65–89.

Vaquer-Sunyer, R., Duarte, C. M., 2008. Thresholds of hypoxia for marine biodiversity. *Proceedings of the National Academy of Sciences of the United States of Americ*a 105, 15452–15457.

Walsh, A. R., O'Halloran, J., 1996. Chromium speciation in tannery effluent – I. An assessment of techniques and the role of organic Cr(III) complexes. *Water Research* 30, 2393-2400.

Wang, X., Planavsky, N. J., Hull, P. M., Tripati, A. E., Zou, H. J., Elder, L., Henehan, M., 2017. Chromium isotopic composition of core-top planktonic foraminifera. *Geobiology* 15, 51-64.

Wang, X., Reinhard, C. T., Planavsky, N. J., Owens, J. D., Lyons, T. W., Johnson, T. M., 2016. Sedimentary chromium isotopic compositions across the Cretaceous OAE2 at Demerara Rise Site 1258. *Chemical Geology* 429, 85-92.

Webb, G. E., Kamber, B. S., 2000. Rare earth elements in Holocene reefal microbialites: a new shallow seawater proxy. *Geochimica et Cosmochimica Acta* 64, 1557–65.

Weiner, S., Israel, R., Dove, P. M., 2004. An Overview of Biomineralization Processes and the Problem of the Vital Effect. *Reviews in Mineralogy & Geochemistry* 55.

Weissert, H., 1981. The environment of deposition of black shales in the Early Cretaceous: an ongoing controversy. In: *The Deep Sea Drilling Project: A Decade of Progress* 32, 547–560.

Weissert, H., Erba, E., 2004. Volcanism, CO_2 and palaeoclimate: A Late Jurassic-Early Cretaceous carbon and oxygen isotope record. *Journal of the Geological Society* 161, 695–702.

Westerhold, T., Röhl, U., Raffi, I., Fornaciari, E., Monechi, S., Reale, V., Bowles, J., Evans, H. F., 2008. Astronomical calibration of the Paleocene time. *Palaeogeography, Palaeoclimatology, Palaeoecology* 257, 377-403.

Westerhold, T., Röhl, U., McCarren, H. K., Zachos, J. C., 2009. Latest on the absolute age of the Paleocene - Eocene Thermal Maximum (PETM): New insights from exact stratigraphic position of key ash layers +19 and -17. *Earth and Planetary Science Letters* 287, 412-419.

Westerhold, T., Röhl, U., Frederichs, T., Agnini, C., Raffi, I., Zachos, J. C., Wilkens, R. H., 2017. Astronomical calibration of the Ypresian timescale: implications for seafloor spreading rates and the chaotic behavior of the solar system? *Climate of the Past* 13, 1129-1152.

Whitfield, M., Turner, D. R., 1987. The role of particles in regulating the composition of seawater. In: Aquatic Surface Chemistry: Chemical Processes at the Particle-Water Interface. John Wiley and Sons, New York., 457–493.

Winguth, C., Winguth, A. M. E., 2012. Simulating Permian-Triassic oceanic anoxia distribution: Implications for species extinction and recovery. *Geology* 40, 127–130.

Wu, W., Wang, X., Reinhard, C. T., Planavsky, N. J., 2017. Chromium isotope systematics in the Connecticut River. *Chemical Geology* 456, 98–111.

Yamaguchi, T., Norris, R. D., 2012. Deep-sea ostracode turnovers through the Paleocene-Eocene thermal maximum in DSDP Site 401, Bay of Biscay, North Atlantic. *Marine Micropaleontology* 86-87, 32-44.

Zachos, J. C., Wara, M. W., Bohaty, S., Delaney, M. L., Petrizzo, M. R., Brill, A., Bralower, T. J., Premoli-Silva, I., 2003. A transient rise in tropical sea surface temperature during the Paleocene-Eocene thermal maximum. *Science* 302, 1551-1554.

Zachos, J. C., Röhl, U., Schellenberg, S. A., Sluijs, A., Hodell, D. A., Kelly, D. C., Thomas, E., Nicolo, M., Raffi, I., Lourens, L. J., McCarren, H., Kroon, D., 2005. Rapid acidification of the ocean during the Paleocene-Eocene thermal maximum. *Science* 308, 1611-1615.

Zeebe, R. E., 2013. What caused the long duration of the Paleocene-Eocene Thermal Maximum. *Paleoceanography* 28, 440–452.

Zeebe, R. E., Zachos, J. C., Dickens, G. R., 2009. Carbon dioxide forcing alone insufficient to explain Palaeocene-Eocene Thermal Maximum warming. *Nature Geoscience* 2, 576-580.

Zeebe, R. E., Ridgwell, A., Zachos, J. C., 2016. Anthrophogenic carbon release rate unprecedented during the past 66 million years. *Nature Geoscience* 9, 325-329.

Zhang, F., Algeo, T. J., Romaniello, S. J., Cui, Y., Zhao, L., Chen, Z.-Q., Anbar, A. D., 2018. Congruent Permian-Triassic $\delta^{238}U$ records at Panthalassic and Tethyan sites: Confirmation of global-oceanic anoxia and validation of the U-isotope paleoredox proxy. *Geology* 46, 327-330.

Zhang, J., Nozaki, Y., 1996. Rare earth elements and yttrium in seawater: ICP-MS determinations in the East Caroline, Coral Sea, and South Fiji Basins of the Western South Pacific Ocean. *Geochimica et Cosmochimica Acta* 60, 4631–44.

Zhang, J., Nozaki, Y., 1998. Behavior of rare earth elements in seawater at the ocean margin: a study along the slopes of the Sagami and Nankai Troughs near Japan. *Geochimica et Cosmochimica Acta* 62, 1307–17.

Zhou, X., Thomas, E., Winguth, A. M. E., Ridgwell, A., Scher, H., Hoogakker, B. A. A., Rickaby, R. E. M., Lu, Z., 2016. Expanded oxygen minimum zones during the late Paleocene early Eocene: Hints from multiproxy comparison and ocean modeling. *Paleoceanography* 31, 1532-1546.

Zink, S., Schoenberg, R., Staubwasser, M., 2010. Isotopic fractionation and reaction kinetics between Cr(III) and Cr(VI) in aqueous media. *Geochimica et Cosmochimica Acta* 74, 5729–5745.

Zweere, T. C., Dickson, A. J., Jenkyns, H. C., Porcelli, Do., Elrick, M., Van den Boom, S. H. J. M., Henderson, G. M., 2018. Isotopic evidence for changes in the zinc cycle during Oceanic Anoxic Event 2 (Late Cretaceous). Geology 46, 463-66.

Supplementary Material A

Geochemical data

Table A1: PETM at DSDP 48-401 (Bay of Biscay)

DSDP 48-401	$\delta^{53}Cr$ (‰)	2SE (‰)	[Cr] (ppm)	Ce/Ce*
14R-2 8-10	0.11	0.04	0.29	1.01
14R-2 21-23	0.06	0.04	0.37	1.15
14R-2 40-42	-0.03	0.04	0.31	0.98
14R-2 63-65			0.28	1.27
14R-2 83-85	0.06	0.04	0.26	1.31
14R-2 140-142	0.05	0.06	0.32	1.13
14R-3 11-13			0.18	1.23
14R-3 31-33	0.15	0.06	0.37	1.24
14R-3 37-39	0.16	0.06	0.36	1.12
14R-3 47-49	0.41	0.02	0.38	1.02
14R-3 47-49	0.43	0.02	0.38	1.00
14R-3 52-54	0.56	0.02	0.27	1.11
14R-3 63-65	0.46	0.02	0.29	1.07
14R-3 74-76	0.58	0.02	0.34	1.10
14R-3 103-106	2.12	0.02	1.56	1.18
14R-3 108-110	1.54	0.02	1.20	0.96
14R-3 112-114	0.78	0.02	1.29	1.01
14R-3 122-123			1.86	0.94
14R-3 133-134	0.94	0.02	1.96	0.89

Table A2: REE-Y during the PETM at DSDP 48-401 (Bay of Biscay)

DSDP 48-401	La (ppm)	Ce (ppm)	Pr (ppm)	Nd (ppm)	Sm (ppm)	Eu (ppm)	Gd (ppm)	Tb (ppm)	Dy (ppm)	Y (ppm)	Ho (ppm)	Er (ppm)	Tm (ppm)	Yb (ppm)	Lu (ppm)
14R-2 8-10	3.72	4.32	0.64	2.40	0.49	0.12	0.52	0.08	0.48	2.84	0.11	0.34	0.05	0.36	0.05
14R-2 21-23	4.64	5.92	0.92	3.78	0.81	0.21	0.93	0.13	0.74	4.54	0.17	0.51	0.06	0.46	0.07
14R-2 40-42	3.88	4.24	0.67	2.53	0.51	0.13	0.57	0.09	0.52	3.21	0.12	0.38	0.05	0.39	0.06
14R-2 63-65	4.14	6.08	0.80	3.10	0.67	0.17	0.71	0.11	0.63	3.48	0.14	0.42	0.06	0.41	0.06
14R-2 83-85	4.75	7.44	1.02	4.16	0.92	0.23	1.00	0.14	0.81	4.46	0.18	0.52	0.06	0.45	0.06
14R-2 140-142	3.91	5.04	0.73	2.82	0.60	0.16	0.68	0.09	0.59	3.54	0.13	0.41	0.04	0.39	0.05
14R-3 11-13	4.83	6.96	0.93	3.52	0.77	0.19	0.83	0.12	0.72	4.08	0.16	0.47	0.05	0.46	0.06
14R-3 31-33	7.60	11.3	1.66	7.04	1.51	0.37	1.70	0.22	1.28	7.53	0.28	0.81	0.09	0.66	0.09
14R-3 37-39	5.97	7.60	1.11	4.38	0.91	0.22	1.01	0.14	0.87	5.16	0.19	0.59	0.07	0.55	0.07
14R-3 47-49	2.28	2.56	0.37	1.38	0.28	0.07	0.30	0.05	0.28	1.76	0.07	0.21	0.03	0.22	0.03
14R-3 47-49	5.05	5.68	0.85	3.07	0.63	0.16	0.67	0.10	0.63	3.97	0.15	0.47	0.06	0.50	0.06
14R-3 52-54	5.02	5.92	0.87	3.46	0.71	0.17	0.79	0.11	0.70	4.32	0.16	0.49	0.06	0.48	0.06
14R-3 63-65	4.83	5.52	0.79	3.01	0.60	0.14	0.67	0.09	0.62	3.86	0.14	0.45	0.06	0.46	0.06
14R-3 74-76	4.86	5.68	0.78	2.98	0.59	0.14	0.65	0.09	0.62	3.81	0.13	0.45	0.05	0.47	0.06
14R-3 103-106	8.17	10.2	1.47	6.05	1.24	0.30	1.39	0.18	1.12	6.67	0.24	0.73	0.09	0.69	0.09
14R-3 108-110	6.50	6.72	0.95	3.39	0.65	0.15	0.67	0.10	0.65	3.94	0.14	0.50	0.07	0.58	0.08
14R-3 112-114	6.19	6.40	0.93	3.46	0.68	0.16	0.73	0.10	0.68	4.19	0.15	0.51	0.07	0.59	0.08
14R-3 122-123	6.27	6.48	1.01	3.68	0.75	0.19	0.79	0.12	0.74	4.54	0.17	0.54	0.07	0.61	0.09
14R-3 133-134	5.59	5.76	0.91	3.23	0.64	0.16	0.68	0.10	0.63	3.92	0.14	0.47	0.06	0.53	0.07

Table A3: PETM at ODP 198-1210 (Shatsky Rise)

ODP 198-1210A	δ^{53}Cr (‰)	2SE (‰)	[Cr] (ppm)	Ce/Ce*
20H-6W 7-8	-0.11	0.14	0.38	0.19
20H-6W 10-11	0.10	0.03	0.66	0.19
20H-6W 13-14	-0.08	0.14	0.29	0.18
20H-6W 16-17	-0.23	0.24	0.88	0.17
20H-6W 19-20			0.14	0.28
20H-6W 25-26			0.09	0.19
20H-6W 31-32	-0.04	0.006	1.57	0.19
20H-6W 33-34			0.06	0.18
20H-6W 35-36			0.03	0.18
20H-6W 36-37			0.03	0.19
20H-6W 37-39			0.01	0.19
20H-6W 38-40			0.01	0.18
20H-6W 39-41			0.02	0.18
20H-6W 40-42			0.02	0.18
20H-6W 41-43	0.00	0.13	0.01	0.18
20H-6W 42-44			0.02	0.17
20H-6W 43-45	0.06	0.13	0.02	0.17
20H-6W 44-46			0.02	0.19
20H-6W 45-47			0.00	0.18
20H-6W 46-48	0.71	0.19	0.00	0.19
20H-6W 47-49	0.2	0.12	0.02	0.16
20H-6W 48-50	0.17	0.15	0.03	0.19
20H-6W 50-51	-0.03	0.14	0.00	0.17
20H-6W 51-52			0.02	0.11
20H-6W 52-54			0.02	0.10
20H-6W 53-55	-0.17	0.17	0.02	0.13
20H-6W 55-56			0.02	0.15
20H-6W 62-63			0.02	0.17
20H-6W 64-65			0.30	0.18
20H-6W 67-68	0.00	0.01	0.34	0.16
20H-6W 70-71	-0.02	0.13	0.48	0.18
20H-6W 73-74	0.20	0.26	0.33	0.19
20H-6W 76-77	0.04	0.10	0.08	0.18
20H-6W 80-81	-0.23	0.18	0.05	0.18

Table A4: REE-Y during the PETM at ODP 198-1210 (Shatsky Rise)

ODP 198-1210A	La (ppm)	Ce (ppm)	Pr (ppm)	Nd (ppm)	Sm (ppm)	Eu (ppm)	Gd (ppm)	Tb (ppm)	Dy (ppm)	Y (ppm)	Ho (ppm)	Er (ppm)	Tm (ppm)	Yb (ppm)	Lu (ppm)
20H-6W 7-8	6.10	0.65	4.56	5.49	6.11	8.14	8.52	7.77	8.97	10.1	8.55	9.07	9.35	11.3	9.64
20H-6W 10-11	6.47	0.72	5.11	6.20	6.97	9.83	10.1	9.14	10.7	12.3	10.1	10.8	11.5	11.6	10.7
20H-6W 13-14	6.20	0.67	4.88	5.95	6.56	8.57	9.56	8.59	9.61	11.0	9.31	9.78	10.1	10.4	10.3
20H-6W 16-17	6.07	0.61	4.75	5.71	6.31	8.45	9.32	8.31	9.56	10.9	9.01	9.43	10.2	9.80	9.8
20H-6W 19-20	13.1	4.54	2.46	10.9	2.12	0.54	2.46	0.37	2.24	16.2	0.51	1.52	0.22	1.49	0.23
20H-6W 25-26	9.01	2.06	1.68	7.27	1.47	0.38	1.72	0.26	1.52	11.5	0.36	1.04	0.15	1.05	0.16
20H-6W 31-32	11.6	2.75	2.09	8.86	1.73	0.45	2.06	0.31	1.83	13.8	0.44	1.33	0.19	1.35	0.21
20H-6W 33-34	7.34	1.64	1.40	6.10	1.23	0.31	1.39	0.21	1.21	9.16	0.28	0.84	0.12	0.83	0.13
20H-6W 35-36	17.3	4.06	3.69	16.5	3.31	0.85	3.86	0.56	3.02	23.1	0.73	2.05	0.29	1.86	0.28
20H-6W 36-37	15.6	3.68	3.05	13.5	2.70	0.68	3.08	0.46	2.51	18.7	0.60	1.72	0.26	1.67	0.26
20H-6W 37-39	10.8	2.56	2.08	9.04	1.78	0.46	2.00	0.30	1.64	12.2	0.40	1.16	0.17	1.11	0.17
20H-6W 38-40	7.9	1.68	1.39	5.86	1.16	0.30	1.30	0.19	1.09	8.34	0.27	0.80	0.12	0.85	0.13
20H-6W 39-41	10.7	2.81	2.50	11.6	2.26	0.57	2.60	0.38	2.33	14.1	0.47	1.28	0.17	1.15	0.17
20H-6W 40-42	8.5	1.96	1.62	6.91	1.38	0.34	1.60	0.24	1.49	9.36	0.31	0.93	0.13	0.91	0.14
20H-6W 41-43	10.9	2.68	2.35	10.4	2.15	0.54	2.49	0.35	2.17	13.8	0.45	1.28	0.18	1.21	0.17
20H-6W 42-44	22.0	5.50	5.47	25.1	5.23	1.33	6.15	0.85	5.12	32.1	1.04	2.87	0.36	2.33	0.34
20H-6W 43-45	15.3	3.92	3.85	17.5	3.65	0.91	4.18	0.60	3.54	22.7	0.72	1.95	0.26	1.60	0.23
20H-6W 44-46	7.85	1.91	1.44	6.05	1.15	0.31	1.39	0.21	1.34	8.89	0.29	0.87	0.13	0.91	0.14
20H-6W 45-47	10.4	2.66	2.29	10.0	1.97	0.52	2.38	0.35	2.16	13.9	0.46	1.27	0.18	1.17	0.18
20H-6W 46-48	8.32	2.03	1.53	6.51	1.35	0.32	1.47	0.23	1.43	9.47	0.32	0.95	0.15	1.03	0.16
20H-6W 47-49	16.7	3.94	3.94	17.6	3.56	0.92	4.19	0.60	3.69	23.4	0.75	2.11	0.28	1.88	0.27
20H-6W 48-50	8.19	1.98	1.44	5.99	1.19	0.30	1.35	0.21	1.29	8.85	0.30	0.91	0.14	1.02	0.16
20H-6W 50-51	9.86	2.25	1.74	7.27	1.46	0.37	1.67	0.26	1.55	10.7	0.36	1.10	0.17	1.23	0.19
20H-6W 51-52	98.8	18.2	26.7	124	25.2	6.61	30.5	4.26	25.1	171	4.98	13.2	1.60	9.29	1.27
20H-6W 52-54	157	29.2	46.5	200	40.4	10.6	48.9	6.85	40.5	275	8.02	21.1	2.56	14.9	2.05
20H-6W 53-55	50.0	10.8	14.1	65.4	13.2	3.45	15.8	2.20	13.1	84.6	2.62	7.00	0.86	5.12	0.71
20H-6W 55-56	12.9	2.78	2.90	13.1	2.60	0.69	3.19	0.47	2.83	19.4	0.59	1.66	0.23	1.49	0.22
20H-6W 62-63	5.64	1.21	0.92	3.87	0.67	0.18	0.84	0.12	0.84	5.80	0.19	0.58	0.09	0.66	0.10
20H-6W 64-65	5.99	0.59	4.67	5.96	6.71	9.49	10.0	8.35	9.52	10.9	9.31	9.16	9.77	9.47	9.53
20H-6W 67-68	8.83	0.91	8.10	10.1	11.8	15.4	16.6	14.6	15.7	17.3	14.4	14.2	14.6	13.7	12.9
20H-6W 70-71	6.17	0.62	5.12	6.63	7.53	9.85	11.3	9.31	10.1	12.1	9.82	9.97	10.2	9.15	9.69
20H-6W 73-74	5.39	0.55	4.38	5.91	6.68	8.30	10.6	8.32	9.05	11.0	8.85	8.74	8.33	8.14	8.16
20H-6W 76-77	3.96	0.38	3.28	4.53	5.04	6.76	8.20	6.04	6.67	8.40	6.52	6.33	5.70	4.91	5.35
20H-6W 80-81	4.99	0.47	4.02	5.60	6.32	8.38	10.2	7.73	8.32	10.4	8.23	8.08	7.29	6.90	7.07

Table A5: PETM at ODP 208-1263 (Walvis Ridge)

ODP 208-1263	$\delta^{53}Cr$ (‰)	2SE (‰)	[Cr] (ppm)	Ce/Ce*	Coarse Fraction (%)
C 14H-1A 19-21	0.24	0.02	0.26	0.72	1.74
C 14H-1A 100-102	0.26	0.02	0.26	0.82	1.67
C 14H-1A 125-126	0.13	0.04	0.13	0.79	1.31
C 14H-2A 1-3	0.25	0.02	0.55	0.87	1.40
C 14H-2A 20-22	0.39	0.03	0.32	0.83	0.93
C 14H-2A 40-42	0.19	0.04	0.35	0.82	1.97
C 14H-2A 59-61	0.13	0.04	0.29	0.81	3.25
C 14H-2A 75-77	0.32	0.05	0.81	0.87	1.08
C 14H-2A 80-82			0.06	0.94	0.73
C 14H-2A 88-90	3.55	0.17	0.08	1.00	0.35
C 14H-2A 92-94			0.00	1.05	0.32
C 14H-2A 96-98			0.00	1.01	0.25
C 14H-2A 101-103	2.99	0.14	0.05	1.14	0.17
C 14H-2A 105-107					0.10
C 14H-2A 111-113					0.03
C 14H-2A 116-118					0.05
C 14H-2A 120-122					0
C 14H-2A 122-124					0
C 14H-2A 125-128					0.02
C 14H-2A 128-130					0
C 14H-2A 132-134					0
D 4H-1A 55-56					0
C 14H-2A 138-140					0.14
C 14H-2A 140-142					0.09
C 14H-2W 145-146					0.06
C 14H-2A 145-146					0.06
D 4H-1A 65-67					0
C 14H-CC W 1-3	0.33	0.04	0.15	0.95	2.01
C 14H-CC W 4-6	0.11	0.04	0.57	0.93	2.97
C 14H-CC A 6-8	0.06	0.01	0.71	0.92	3.88
C 14H-CC A 8-10	0.26	0.04	0.18	0.91	4.35
C 14H-CCW 10-12	0.00	0.04	0.42	0.92	4.78
C 14H-CC W12-14				0.92	4.43
C 14H-CC A 14-16	0.25	0.04	0.10	0.85	4.46

Table A6: REE-Y during the PETM at ODP 208-1263 (Walvis Ridge)

ODP 208-1263	La (ppm)	Ce (ppm)	Pr (ppm)	Nd (ppm)	Sm (ppm)	Eu (ppm)	Gd (ppm)	Tb (ppm)	Dy (ppm)	Y (ppm)	Ho (ppm)	Er (ppm)	Tm (ppm)	Yb (ppm)	Lu (ppm)
C 14H-1A 19-21	3.40	1.36	2.32	2.77	2.83	4.10	4.14	3.70	4.32	5.39	4.06	4.27	4.08	3.94	3.90
C 14H-1A 100-102	3.02	1.21	2.02	2.64	2.77	4.22	4.22	3.31	3.88	5.25	3.78	3.94	3.86	4.07	3.95
C 14H-1A 125-126	3.53	1.52	2.31	2.66	2.77	3.72	4.08	3.53	4.38	5.78	4.23	4.75	4.87	5.24	4.98
C 14H-2A 1-3	3.70	1.67	2.36	2.75	2.90	4.14	4.25	3.57	4.49	5.96	4.45	4.93	5.04	6.16	5.59
C 14H-2A 20-22	3.68	1.69	2.38	2.71	2.77	3.99	4.14	3.68	4.40	5.97	4.57	5.02	5.31	5.96	5.63
C 14H-2A 40-42	4.10	1.81	2.45	2.70	2.73	3.81	4.06	3.92	4.71	6.27	4.89	5.57	6.40	7.08	6.92
C 14H-2A 59-61	5.16	2.16	3.34	3.94	4.20	5.56	6.06	5.37	6.51	8.14	6.60	7.12	7.43	8.23	8.35
C 14H-2A 75-77	5.29	2.52	3.61	4.17	4.51	6.09	6.71	5.95	7.16	8.66	7.08	7.69	8.54	9.54	8.88
C 14H-2A 80-82	3.09	1.42	2.09	2.69	2.91	3.91	4.29	3.52	4.00	4.82	4.06	4.17	4.43	5.01	4.69
C 14H-2A 88-90	3.24	1.66	2.20	2.64	2.91	4.10	4.15	3.56	4.35	5.04	4.27	4.51	5.02	4.96	4.83
C 14H-2A 92-94	3.11	1.57	2.07	2.55	2.88	3.48	4.28	3.43	4.01	4.67	3.96	4.18	4.37	4.90	4.51
C 14H-2A 96-98	2.73	1.64	2.35	2.99	3.39	4.93	5.24	4.22	4.72	5.30	4.48	4.29	3.83	4.13	3.54
C 14H-2A 101-103	5.29	3.74	5.23	6.73	8.38	11.28	13.11	10.63	11.49	13.30	10.52	9.69	8.28	7.21	6.03
C 14H-2A 105-107	7.78	3.75	4.36	4.61	4.81	5.77	6.11	5.55	6.83	8.20	6.80	7.66	9.06	10.37	10.41
C 14H-2A 111-113	7.49	3.66	4.15	4.44	4.36	5.66	5.95	5.40	6.49	8.07	6.79	7.61	9.05	9.81	10.38
C 14H-2A 116-118	7.84	3.90	4.57	4.96	4.93	6.50	6.69	5.95	7.49	9.18	7.64	8.25	9.89	12.01	10.63
C 14H-2A 120-122	7.42	3.61	4.16	4.52	4.35	5.68	6.28	5.78	7.13	8.73	6.97	8.10	9.57	10.26	11.01
C 14H-2A 122-124	6.83	3.25	3.73	4.06	3.97	5.66	5.46	5.29	6.43	8.03	6.55	7.45	8.84	10.90	9.95
C 14H-2A 125-128	6.67	3.14	3.71	3.98	4.02	5.26	5.78	5.13	6.23	8.04	6.56	7.43	8.84	10.19	9.97
C 14H-2A 128-130	6.79	3.13	3.75	4.04	3.83	5.55	5.53	5.13	6.45	8.22	6.33	7.45	8.96	10.97	10.43
C 14H-2A 132-134	3.40	1.36	2.32	2.77	2.83	4.10	4.14	3.70	4.32	5.39	4.06	4.27	4.08	3.94	3.90
D 4H-1A 55-56	3.02	1.21	2.02	2.64	2.77	4.22	4.22	3.31	3.88	5.25	3.78	3.94	3.86	4.07	3.95
C 14H-2A 138-140	3.53	1.52	2.31	2.66	2.77	3.72	4.08	3.53	4.38	5.78	4.23	4.75	4.87	5.24	4.98
C 14H-2A 140-142	3.70	1.67	2.36	2.75	2.90	4.14	4.25	3.57	4.49	5.96	4.45	4.93	5.04	6.16	5.59
C 14H-2W 145-146	3.68	1.69	2.38	2.71	2.77	3.99	4.14	3.68	4.40	5.97	4.57	5.02	5.31	5.96	5.63
C 14H-2A 145-146	4.10	1.81	2.45	2.70	2.73	3.81	4.06	3.92	4.71	6.27	4.89	5.57	6.40	7.08	6.92
D 4H-1A 65-67	5.16	2.16	3.34	3.94	4.20	5.56	6.06	5.37	6.51	8.14	6.60	7.12	7.43	8.23	8.35
C 14H-CC W 1-3	5.29	2.52	3.61	4.17	4.51	6.09	6.71	5.95	7.16	8.66	7.08	7.69	8.54	9.54	8.88
C 14H-CC W 4-6	3.09	1.42	2.09	2.69	2.91	3.91	4.29	3.52	4.00	4.82	4.06	4.17	4.43	5.01	4.69
C 14H-CC A 6-8	3.24	1.66	2.20	2.64	2.91	4.10	4.15	3.56	4.35	5.04	4.27	4.51	5.02	4.96	4.83
C 14H-CC A 8-10	3.11	1.57	2.07	2.55	2.88	3.48	4.28	3.43	4.01	4.67	3.96	4.18	4.37	4.90	4.51
C 14H-CCW 10-12	2.73	1.64	2.35	2.99	3.39	4.93	5.24	4.22	4.72	5.30	4.48	4.29	3.83	4.13	3.54
C 14H-CC W12-14	5.29	3.74	5.23	6.73	8.38	11.28	13.11	10.63	11.49	13.30	10.52	9.69	8.28	7.21	6.03
C 14H-CC A 14-16	7.78	3.75	4.36	4.61	4.81	5.77	6.11	5.55	6.83	8.20	6.80	7.66	9.06	10.37	10.41

Table A7: ETM-2 at ODP 208-1263 (Walvis Ridge)

ODP 208-1263C	$\delta^{53}Cr$ (‰)	2SE (‰)	[Cr] (ppm)	Ce/Ce*
10H-7A 1-2			0.35	0.39
10H-7A 3-4			0.09	0.39
10H-7A 5-6			0.16	0.37
10H-7A 6-7			0.12	0.36
10H-7A 7-8			0.05	0.36
10H-7A 8-9			0.18	0.43
10H-7A 10-11			0.04	0.39
10H-7A 11-12	0.57	0.11	0.15	0.39
10H-7A 12-13			0.14	0.36
10H-7A 13-14			0.12	0.37
10H-7A 15-16	1.94	0.30	0.65	0.37
10H-7A 21-22			0.06	0.36
10H-7A 27-28	-0.23	0.27	0.59	0.31
20H-6W 35-36			0.23	0.29
20H-6W 45-46			0.33	0.43
20H-6W 98-99	-0.05	0.17	0.13	0.44

Table A8: REE-Y during the ETM-2 at ODP 208-12163 (Walvis Ridge)

ODP 208-1263C	La (ppm)	Ce (ppm)	Pr (ppm)	Nd (ppm)	Sm (ppm)	Eu (ppm)	Gd (ppm)	Tb (ppm)	Dy (ppm)	Y (ppm)	Ho (ppm)	Er (ppm)	Tm (ppm)	Yb (ppm)	Lu (ppm)
10H-7A 1-2	2.78	1.87	0.41	1.60	0.28	0.08	0.34	0.06	0.38	2.60	0.09	0.27	0.04	0.29	0.04
10H-7A 3-4	2.61	1.62	0.37	1.44	0.26	0.06	0.30	0.05	0.34	2.32	0.07	0.25	0.04	0.29	0.04
10H-7A 5-6	2.26	1.37	0.33	1.26	0.22	0.06	0.26	0.04	0.29	1.92	0.06	0.21	0.03	0.24	0.04
10H-7A 6-7	4.24	2.64	0.63	2.43	0.46	0.11	0.49	0.08	0.54	3.73	0.13	0.40	0.06	0.45	0.06
10H-7A 7-8	5.07	4.21	1.01	4.13	0.83	0.21	0.92	0.13	0.86	5.67	0.18	0.51	0.07	0.49	0.07
10H-7A 8-9	2.81	1.96	0.46	1.88	0.34	0.09	0.38	0.06	0.41	2.71	0.09	0.28	0.04	0.28	0.04
10H-7A 10-11	4.17	3.05	0.76	3.19	0.61	0.16	0.71	0.11	0.68	4.85	0.15	0.43	0.06	0.37	0.06
10H-7A 11-12	4.18	2.63	0.64	2.50	0.45	0.11	0.51	0.08	0.53	3.54	0.11	0.36	0.05	0.39	0.06
10H-7A 12-13	5.39	3.40	0.79	3.05	0.54	0.14	0.61	0.10	0.67	4.59	0.15	0.48	0.08	0.52	0.08
10H-7A 13-14	5.79	3.73	0.90	3.56	0.68	0.16	0.75	0.12	0.76	5.29	0.17	0.51	0.08	0.53	0.08
10H-7A 15-16	5.44	3.36	0.82	3.25	0.58	0.15	0.64	0.10	0.70	4.86	0.15	0.51	0.07	0.49	0.08
10H-7A 21-22	7.04	3.87	1.12	4.42	0.80	0.20	0.88	0.14	0.90	6.07	0.20	0.60	0.09	0.60	0.09
10H-7A 27-28	6.90	3.52	1.10	4.31	0.79	0.19	0.82	0.13	0.83	5.54	0.18	0.56	0.08	0.54	0.08
20H-6W 35-36	4.12	3.33	0.74	3.04	0.59	0.15	0.66	0.10	0.62	4.63	0.13	0.42	0.06	0.36	0.05
20H-6W 45-46	3.45	2.64	0.54	2.15	0.40	0.10	0.44	0.07	0.47	3.37	0.10	0.32	0.05	0.32	0.05
20H-6W 98-99	5.61	3.91	0.89	3.65	0.68	0.18	0.76	0.12	0.82	5.89	0.18	0.57	0.08	0.57	0.09

Table A9: Pleistocene at NIOP 464 (Murray Ridge)

NIOP 464	Depth (m)	δ^{53}Cr (‰)	2SE (‰)	[Cr] (ppm)	Ce/Ce*
78	995	0.52	0.01	2.35	0.78
78 *O. universa*	995	0.22	0.02	2.26	0.84
76	984.5	0.46	0.01	2.89	0.71
76 *O. universa*	984.5	0.44	0.02	3.42	0.82
101	814	-0.04	0.01	1.72	0.68
99	802	-0.01	0.01	1.51	0.66
112	682	-0.03	0.02	1.79	0.87
110	671	0.16	0.02	1.16	0.79
126	570	0.08	0.02	0.85	0.84
152	562	0.09	0.03	0.77	0.87

Table A10: REE-Y during the Pleistocene at NIOP 464 (Murray Ridge)

NIOP 464	La (ppm)	Ce (ppm)	Pr (ppm)	Nd (ppm)	Sm (ppm)	Eu (ppm)	Gd (ppm)	Tb (ppm)	Dy (ppm)	Y (ppm)	Ho (ppm)	Er (ppm)	Tm (ppm)	Yb (ppm)	Lu (ppm)
78	0.91	0.67	0.82	0.94	1.12	1.49	1.52	1.37	1.69	2.03	1.58	1.64	1.81	1.55	1.83
78 *O. universa*	0.65	0.53	0.63	0.73	0.88	1.05	1.18	1.01	1.19	1.42	1.14	1.23	1.28	1.17	1.36
76	1.39	0.93	1.21	1.52	1.87	2.42	2.71	2.52	2.93	4.08	2.91	3.27	3.45	3.10	3.89
76 *O. universa*	0.92	0.76	0.93	1.08	1.43	1.82	1.68	1.78	1.93	2.22	1.85	1.93	2.16	2.04	2.12
101	0.94	0.60	0.83	1.02	1.50	1.80	1.87	1.74	1.74	2.31	1.72	1.75	1.81	1.76	2.06
99	0.83	0.49	0.64	0.78	1.01	1.11	1.31	1.24	1.37	1.97	1.39	1.54	1.75	1.54	1.58
112	0.74	0.62	0.67	0.83	1.15	1.57	1.38	1.34	1.41	1.62	1.15	1.24	1.14	1.01	1.07
110	0.99	0.75	0.91	1.14	1.57	2.11	1.91	1.95	2.18	2.45	1.79	1.89	2.06	1.86	2.03
126	1.44	1.14	1.29	1.63	2.13	2.90	2.93	2.73	2.98	4.13	2.79	3.10	2.78	2.63	2.93
152	0.75	0.63	0.68	0.85	1.07	1.45	1.50	1.33	1.44	1.87	1.37	1.42	1.51	1.26	1.44

Table A11: OAE1a at Cau (SE Spain)

Cau	$\delta^{53}Cr$ (‰)	2SE (‰)	[Cr] (ppm)
88	0.47	0.06	0.54
85	0.53	0.02	1.16
81	0.33	0.05	1.11
77	0.75	0.03	2.10
71	0.54	0.02	2.53
63	0.86	0.02	2.26
57	0.80	0.02	2.44
49	0.61	0.02	3.43
43	0.85	0.01	3.69
37			2.72
36	0.90	0.01	2.71
35	0.11	0.01	1.83
33			0.73
28			2.24
25	0.43	0.01	1.63
21	0.36	0.01	1.66
11	0.41	0.01	1.35
3	0.46	0.02	1.03

Table A12: REE-Y during OAE1a at Cau (SE Spain)

Cau	La (ppm)	Ce (ppm)	Pr (ppm)	Nd (ppm)	Sm (ppm)	Eu (ppm)	Gd (ppm)	Tb (ppm)	Dy (ppm)	Y (ppm)	Ho (ppm)	Er (ppm)	Tm (ppm)	Yb (ppm)	Lu (ppm)
88	1.50	3.03	0.42	1.77	0.36	0.08	0.33	0.05	0.25	1.38	0.05	0.12	0.01	0.09	0.01
85	2.59	4.17	0.63	2.72	0.53	0.11	0.51	0.07	0.40	2.48	0.08	0.20	0.03	0.17	0.02
81	2.88	4.75	0.68	2.91	0.56	0.11	0.56	0.08	0.45	2.84	0.09	0.23	0.03	0.21	0.02
77	2.35	3.25	0.51	2.18	0.42	0.09	0.45	0.06	0.35	2.49	0.07	0.20	0.02	0.17	0.02
71	2.66	3.96	0.62	2.63	0.50	0.10	0.51	0.07	0.39	2.43	0.08	0.19	0.02	0.19	0.02
63	3.33	4.73	0.74	3.14	0.63	0.12	0.62	0.09	0.49	3.46	0.09	0.27	0.03	0.23	0.03
62	3.31	4.94	0.76	3.24	0.63	0.14	0.66	0.10	0.53	3.46	0.10	0.27	0.03	0.25	0.03
57	2.65	3.53	0.57	2.51	0.47	0.10	0.48	0.07	0.39	2.62	0.08	0.20	0.03	0.16	0.02
49	3.30	4.82	0.76	3.25	0.64	0.14	0.69	0.10	0.55	3.63	0.11	0.28	0.04	0.27	0.03
43	2.69	3.89	0.61	2.59	0.51	0.12	0.56	0.07	0.43	2.92	0.08	0.21	0.03	0.19	0.02
37	3.31	4.46	0.73	3.14	0.59	0.14	0.62	0.09	0.50	3.23	0.10	0.24	0.03	0.23	0.03
36	3.46	4.58	0.76	3.26	0.63	0.15	0.66	0.09	0.49	3.33	0.10	0.25	0.03	0.23	0.03
35	2.97	4.82	0.74	3.16	0.62	0.16	0.67	0.09	0.50	2.90	0.09	0.24	0.03	0.21	0.03
33	2.04	3.38	0.54	2.32	0.47	0.11	0.47	0.06	0.34	1.89	0.06	0.16	0.02	0.12	0.02
28	3.68	3.73	0.74	3.22	0.60	0.16	0.67	0.09	0.49	3.51	0.10	0.24	0.03	0.23	0.03
25	2.29	3.95	0.58	2.50	0.50	0.13	0.49	0.07	0.38	2.23	0.08	0.19	0.02	0.18	0.02
21	3.59	5.88	0.86	3.64	0.72	0.18	0.73	0.10	0.57	3.26	0.11	0.28	0.03	0.26	0.03
13b	3.83	3.96	0.80	3.48	0.66	0.17	0.71	0.09	0.50	3.42	0.10	0.25	0.03	0.24	0.02
11	2.55	4.33	0.63	2.72	0.56	0.14	0.59	0.08	0.45	2.62	0.09	0.21	0.03	0.21	0.03
3	1.46	2.29	0.34	1.48	0.29	0.07	0.33	0.05	0.26	1.72	0.05	0.14	0.02	0.15	0.02

Table A13: OAE2/Plenus Cold Event at the Dover Plenus Marls (SE England)

Dover Plenus Marls	$\delta^{53}Cr$ (‰)	2SE (‰)	[Cr] (ppm)
-30	0.70	0.04	1.97
-20	1.24	0.07	1.88
-10	0.66	0.05	0.93
0	0.83	0.05	0.92
10	0.44	0.04	1.06
20	0.97	0.13	1.46
30	0.68	0.12	0.76
40	-0.24	0.22	0.84
50	-0.25	0.14	1.93
60	0.46	0.05	0.80
70	0.18	0.05	0.77
80	0.09	0.06	0.98
90	-0.75	0.08	0.91
110			0.73
120			0.80
130			0.56
140			0.51
150			0.84
160			0.32
170			0.68
180			0.43
190			1.23
200			0.68
210			0.58
220			1.50
230			0.91
240	-0.70	0.03	2.38
250	-0.28	0.02	4.77
260	-1.07	0.03	4.33
270	-1.19	0.03	4.54
280	-1.11	0.05	2.67
290	-0.53	0.02	5.06
300	-1.06	0.03	5.48
330			1.30
360			0.32

Table A14: REE-Y during OAE2/Plenus Cold Event at the Dover Plenus Marls (SE England)

DPM	La (ppm)	Ce (ppm)	Pr (ppm)	Nd (ppm)	Sm (ppm)	Eu (ppm)	Gd (ppm)	Tb (ppm)	Dy (ppm)	Y (ppm)	Ho (ppm)	Er (ppm)	Tm (ppm)	Yb (ppm)	Lu (ppm)
-30	4.00	3.64	0.67	2.77	0.49	0.12	0.59	0.08	0.52	3.46	0.12	0.35	0.05	0.31	0.05
-20	4.92	5.16	0.91	3.82	0.72	0.17	0.79	0.11	0.65	4.00	0.15	0.40	0.05	0.36	0.05
-10	3.19	3.86	0.63	2.51	0.49	0.11	0.52	0.07	0.40	2.33	0.09	0.23	0.03	0.21	0.03
0	4.90	5.03	0.89	3.47	0.63	0.14	0.69	0.10	0.56	3.46	0.12	0.35	0.05	0.34	0.05
10	5.51	6.98	1.10	4.61	0.85	0.20	0.91	0.12	0.72	3.98	0.15	0.41	0.05	0.35	0.05
20	5.71	7.64	1.21	4.91	0.92	0.20	0.96	0.13	0.73	4.15	0.16	0.42	0.06	0.37	0.05
30	4.87	5.54	0.91	3.77	0.66	0.15	0.69	0.10	0.58	3.34	0.13	0.34	0.05	0.34	0.05
40	5.27	5.80	0.96	4.02	0.75	0.17	0.76	0.10	0.67	3.70	0.14	0.37	0.05	0.35	0.05
50	5.89	6.47	1.11	4.73	0.89	0.21	0.94	0.13	0.74	4.48	0.16	0.42	0.06	0.38	0.05
60	5.02	5.62	0.98	3.83	0.74	0.16	0.75	0.10	0.60	3.78	0.13	0.36	0.05	0.33	0.05
70	5.07	5.51	0.94	3.88	0.72	0.16	0.76	0.11	0.60	3.75	0.13	0.37	0.05	0.33	0.05
80	5.62	5.77	0.99	3.97	0.74	0.17	0.78	0.11	0.65	3.79	0.14	0.39	0.05	0.38	0.05
90	6.68	7.31	1.28	5.19	0.96	0.22	1.05	0.14	0.80	5.07	0.18	0.47	0.06	0.42	0.06
110	6.05	6.75	1.18	4.97	0.91	0.21	0.98	0.13	0.79	4.75	0.16	0.46	0.06	0.39	0.05
120	6.18	7.07	1.17	4.81	0.90	0.21	1.01	0.14	0.80	5.04	0.17	0.46	0.06	0.39	0.06
130	5.99	6.01	1.06	4.26	0.79	0.18	0.86	0.12	0.78	5.31	0.17	0.47	0.07	0.43	0.06
140	5.28	4.81	0.93	3.77	0.76	0.17	0.82	0.12	0.72	4.98	0.15	0.44	0.06	0.35	0.05
150	5.78	5.31	1.02	4.15	0.80	0.18	0.89	0.12	0.75	5.17	0.17	0.47	0.06	0.50	0.06
160	3.56	3.13	0.61	2.52	0.48	0.11	0.54	0.08	0.48	3.45	0.11	0.29	0.04	0.26	0.04
170	5.59	4.86	0.93	3.77	0.73	0.16	0.82	0.12	0.74	5.25	0.16	0.45	0.06	0.39	0.06
180	6.10	5.15	1.04	4.25	0.77	0.18	0.93	0.13	0.80	5.98	0.18	0.50	0.07	0.43	0.06
190	6.39	5.10	1.05	4.15	0.81	0.18	0.89	0.14	0.87	6.32	0.18	0.53	0.07	0.45	0.07
200	6.89	5.45	1.13	4.54	0.88	0.20	1.00	0.15	0.91	6.61	0.20	0.57	0.07	0.48	0.07
210	5.06	3.95	0.83	3.44	0.65	0.15	0.70	0.11	0.68	4.81	0.14	0.41	0.05	0.34	0.05
220	7.43	5.80	1.20	5.03	0.92	0.21	1.07	0.14	0.92	6.08	0.21	0.54	0.08	0.49	0.07
230	8.65	7.13	1.52	6.16	1.15	0.26	1.29	0.18	1.05	7.39	0.23	0.63	0.08	0.57	0.08
240	10.4	8.75	1.84	7.63	1.46	0.34	1.63	0.22	1.34	9.14	0.27	0.77	0.10	0.64	0.09
250	8.76	7.95	1.67	6.76	1.32	0.32	1.47	0.21	1.22	8.09	0.24	0.71	0.09	0.58	0.08
260	9.54	7.77	1.63	6.56	1.29	0.30	1.42	0.20	1.31	8.81	0.27	0.78	0.11	0.68	0.10
270	6.49	5.28	1.15	4.83	0.93	0.22	1.04	0.15	0.89	6.01	0.19	0.54	0.08	0.47	0.07
280	4.54	3.65	0.93	4.08	0.81	0.18	0.92	0.12	0.69	4.34	0.14	0.38	0.05	0.31	0.04
290	6.24	5.31	1.19	5.10	0.98	0.23	1.10	0.15	0.91	6.11	0.19	0.53	0.07	0.44	0.06
300	8.76	6.60	1.53	6.25	1.25	0.30	1.36	0.20	1.26	8.28	0.26	0.75	0.10	0.63	0.09
330	11.6	7.45	1.80	7.29	1.36	0.33	1.47	0.23	1.44	10.7	0.31	0.90	0.12	0.74	0.11
360	5.60	3.61	0.88	3.49	0.63	0.16	0.72	0.10	0.65	4.89	0.13	0.41	0.05	0.34	0.05

Table A15: The average Cr concentrations of the core-top, sediment trap, plankton net, and culture samples measured by LA-MC-ICP-MS. Chromium concentrations are mostly higher by up to two orders of magnitude in core-top samples than in foraminifera that have not reached the seafloor.

Sample	Type	Species	Average [Cr] (ppm)	(2SD)
SO456 0-1 cm	Core-top	*T. sacculifer*	1.25	0.10
SO456 0-1 cm	Core-top	*O. universa*	0.78	0.08
SO488 0-1 cm	Core-top	*T. sacculifer*	0.77	0.05
GeoB3915	Core-top	*T. sacculifer*	0.38	0.03
CB14	Sediment trap	*T. sacculifer*	0.04	0.00
CB14	Sediment trap	*G. truncatulinoides*	0.02	0.00
KT02-15 B-2 10 m	Plankton net	*T. sacculifer*	0.16	0.00
KT02-15 B-2 50 m	Plankton net	*T. sacculifer*	0.14	0.00
KT02-15 B-2 75 m	Plankton net	*T. sacculifer*	0.08	0.01
KT02-15 B-2 100 m	Plankton net	*T. sacculifer*	0.14	0.01
KT02-15 B-5	Plankton net	*T. sacculifer*	0.08	0.01
***G. ruber* culture**	Culture	*G. ruber*	0.05	0.00
***O. universa* culture**	Culture	*O. universa*	0.05	0.00
1 x Cr (Mediterranean)	Culture	*A. lessonii*	0.04	0.01
50 x Cr (Mediterranean)	Culture	*A. lessonii*	0.06	0.01
100 x Cr (Mediterranean)	Culture	*A. lessonii*	0.07	0.01
150 x Cr (Mediterranean)	Culture	*A. lessonii*	0.13	0.01
1 x Cr (Red Sea)	Culture	*Amphistegina sp.*	0.04	0.01
50 x Cr (Red Sea)	Culture	*Amphistegina sp.*	0.06	0.01
100 x Cr (Red Sea)	Culture	*Amphistegina sp.*	0.10	0.01
150 x Cr (Red Sea)	Culture	*Amphistegina sp.*	0.11	0.01

Table A16: Oxygen concentrations in the (Cr spiked and natural) culture medium (Mediterranean seawater) for the larger benthic foraminifera *Amphistegina sp.* from the Red and Mediterranean Seas throughout the duration of the culture.

Sample	Day 1 $[O_2]_{sw}$ (µM)	Day 7 $[O_2]_{sw}$ (µM)	Day 13 $[O_2]_{sw}$ (µM)	Day 25 $[O_2]_{sw}$ (µM)
Mediterranean *A. lessonii*				
1x $[Cr]_{seawater}$	172	73	182	146
50x $[Cr]_{seawater}$	162	74	186	135
100x $[Cr]_{seawater}$	177	163	195	163
150x $[Cr]_{seawater}$	154	155	156	155
Red Sea *Amphistegina sp.*				
1x $[Cr]_{seawater}$	155	61	150	88
50x $[Cr]_{seawater}$	179	73	182	146
100x $[Cr]_{seawater}$	170	140	147	140
150x $[Cr]_{seawater}$	147	154	203	154

Table A17: Expected Cr concentrations in the (Cr spiked and natural) culture medium (Mediterranean seawater) based on the Cr concentration of natural Mediterranean seawater are higher than the Cr concentrations measured. The distribution coefficient (D_{Cr}) show foraminifera are enriched in Cr relative to concentrations in its environment.

Sample	Expected $[Cr]_{sw}$ (nM)	Measured $[Cr]_{sw}$ (nM)	$[Cr]_{calcite}$ (ppm)	D_{Cr}
Mediterranean *A. lessonii*				
1x $[Cr]_{seawater}$	2.8	2.75	0.04	272
50x $[Cr]_{seawater}$	140	5.66	0.06	187
100x $[Cr]_{seawater}$	280	6.73	0.07	200
150x $[Cr]_{seawater}$	420	8.39	0.13	303
Red Sea *Amphistegina sp.*				
1x $[Cr]_{seawater}$	2.8	2.75	0.04	291
50x $[Cr]_{seawater}$	140	5.66	0.06	191
100x $[Cr]_{seawater}$	280	6.73	0.10	296
150x $[Cr]_{seawater}$	420	8.39	0.11	245

Table A18: The $\delta^{53}Cr$ composition and Cr content of core-top foraminifera of different size fractions from the Caribbean and the North Atlantic (T86-15S). These show no isotopic offsets between species within a size fraction, but offsets between different size fractions.

Sample	Size Fraction	[Cr] (ppm)	$\delta^{53}Cr$ (‰)	2SD
Karibik (Caribbean)				
Mixed planktic foraminifera	>500 µm	0.27	0.38	0.13
O. universa	>500 µm	0.15	0.30	0.13
G. menardii	>500 µm	0.28	0.26	0.08
G. menardii	250 – 500 µm	0.3	-0.04	0.24
G. ruber	250 – 500 µm	0.38	-0.16	0.12
T86-15S				
G. truncatulinoides	>500 µm	0.08	0.81	0.15
G. truncatulinoides	250 – 500 µm	0.06	0.33	0.15

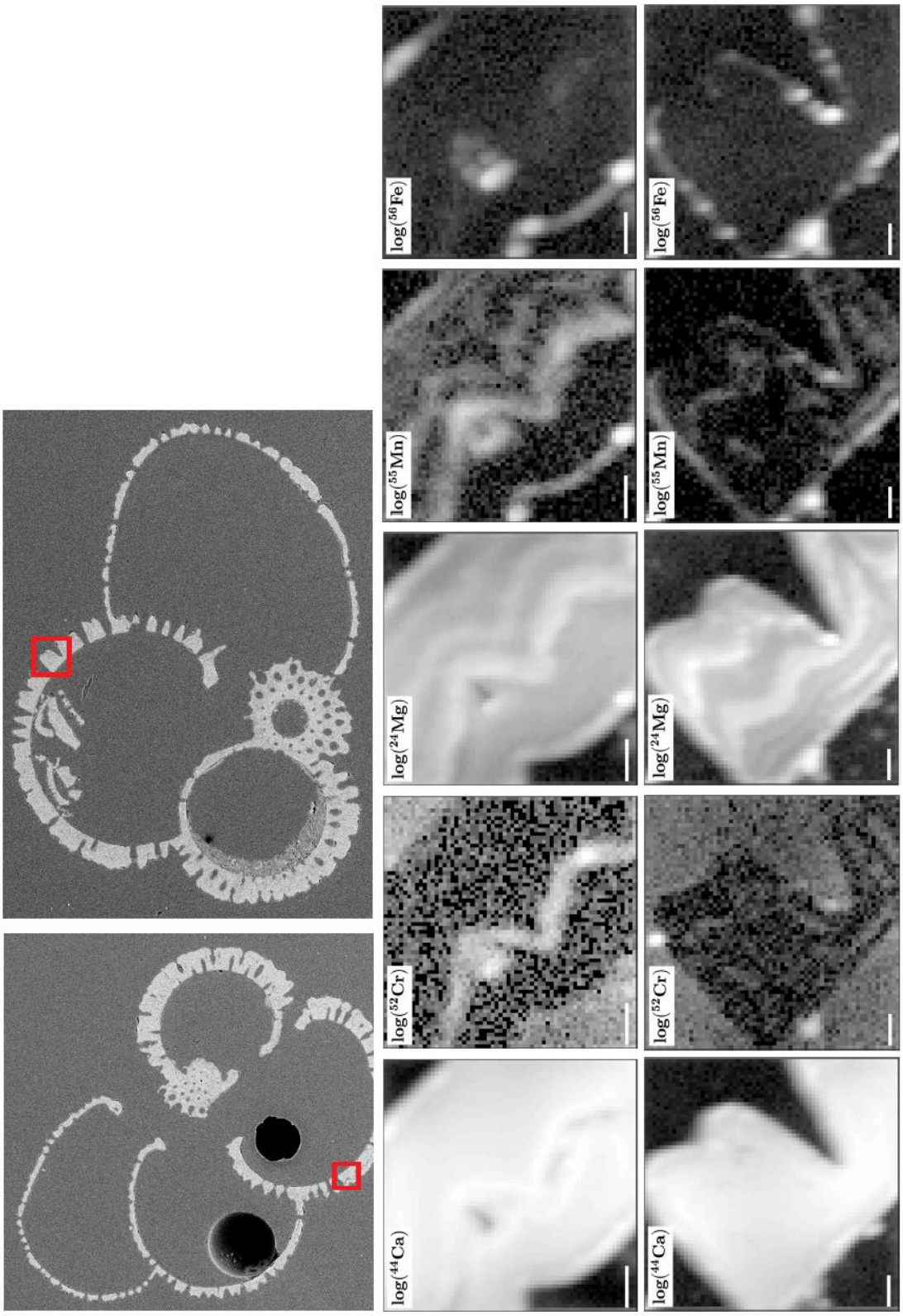

Figure A1: Images of core-top *T. sacculifer* tests by SEM and NanoSIMS. NanoSIMS images show log-transformed counts of secondary ions ^{44}Ca, ^{52}Cr, ^{24}Mg, ^{55}Mn and ^{56}Fe measured in areas indicated by red squares in the SEM images. Scale bar = 5 µm.

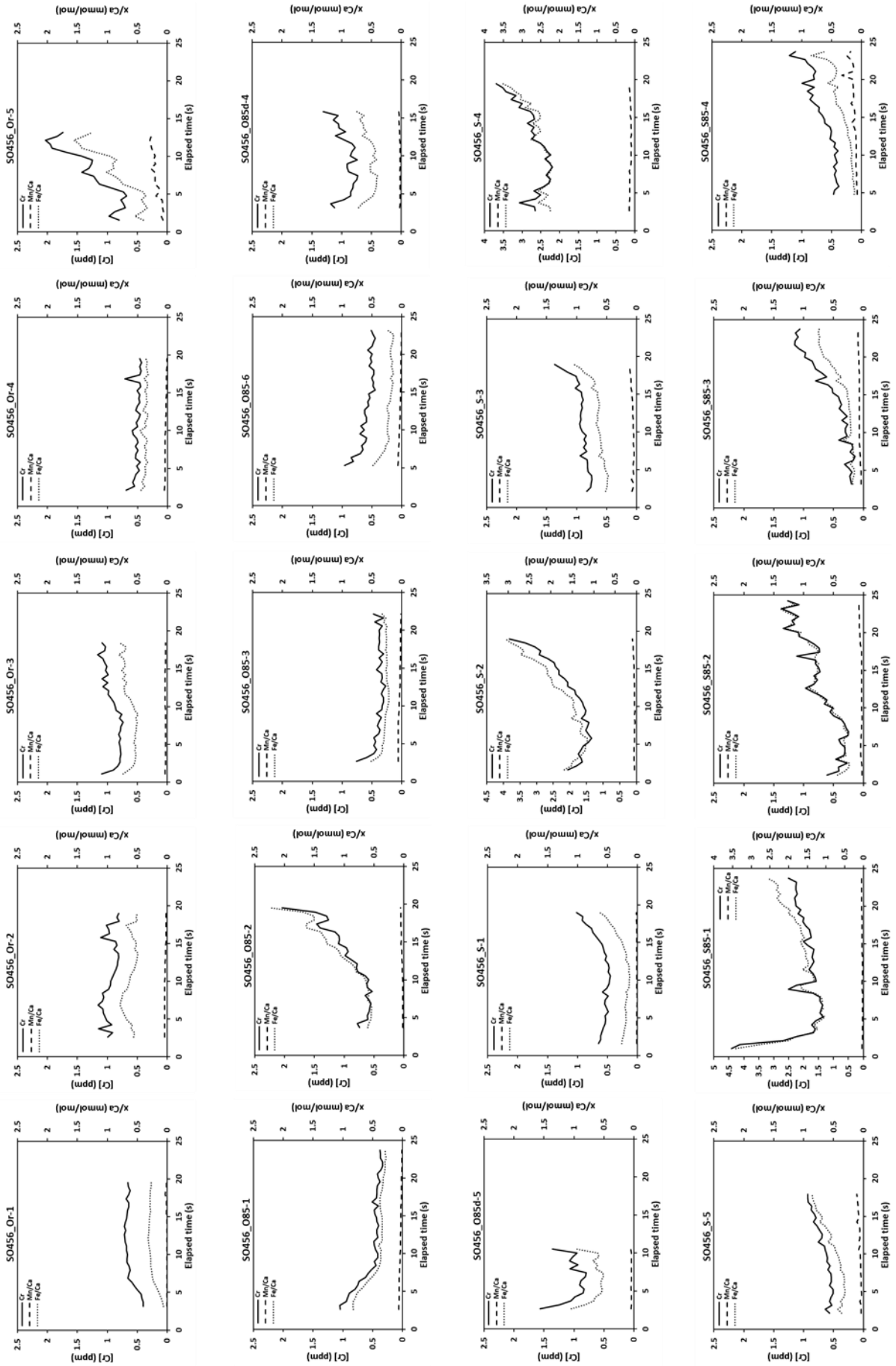
SO456_Or-1
SO456_Or-2
SO456_Or-3
SO456_Or-4
SO456_Or-5
SO456_O85-1
SO456_O85-2
SO456_O85-3
SO456_O85-6
SO456_O85d-4
SO456_O85d-5
SO456_S-1
SO456_S-2
SO456_S-3
SO456_S-4
SO456_S85-1
SO456_S85-2
SO456_S85-3
SO456_S85-4
SO456_S-5
Cr
Mn/Ca
Fe/Ca
[Cr] (ppm)
x/Ca (mmol/mol)
Elapsed time (s)

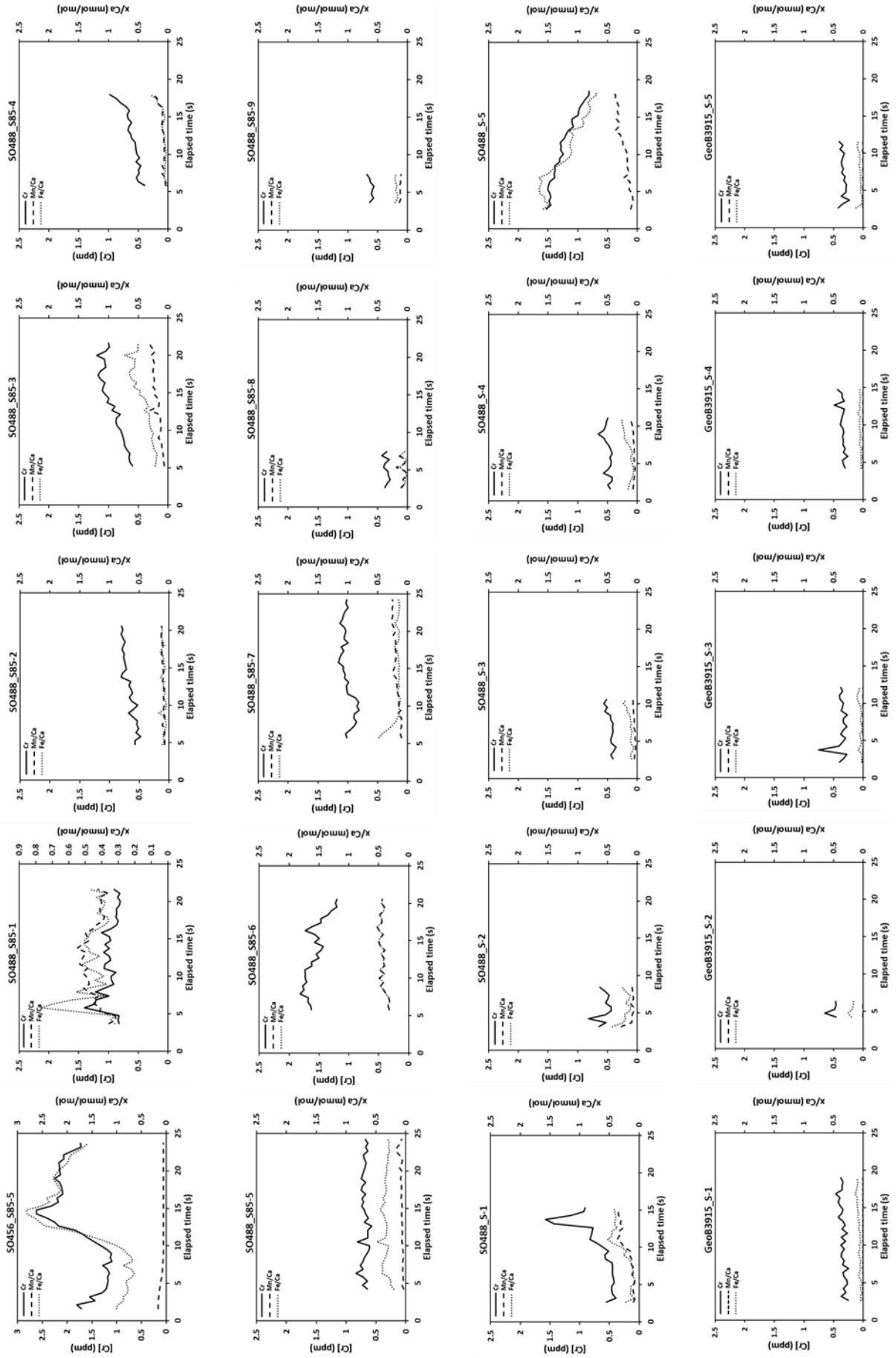
SO456_S85-5
SO488_S85-1
SO488_S85-2
SO488_S85-3
SO488_S85-4
SO488_S85-5
SO488_S85-6
SO488_S85-7
SO488_S85-8
SO488_S85-9
SO488_S-1
SO488_S-2
SO488_S-3
SO488_S-4
SO488_S-5
GeoB3915_S-1
GeoB3915_S-2
GeoB3915_S-3
GeoB3915_S-4
GeoB3915_S-5
Cr
Mn/Ca
Fe/Ca
[Cr] (ppm)
x/Ca (mmol/mol)
Elapsed time (s)

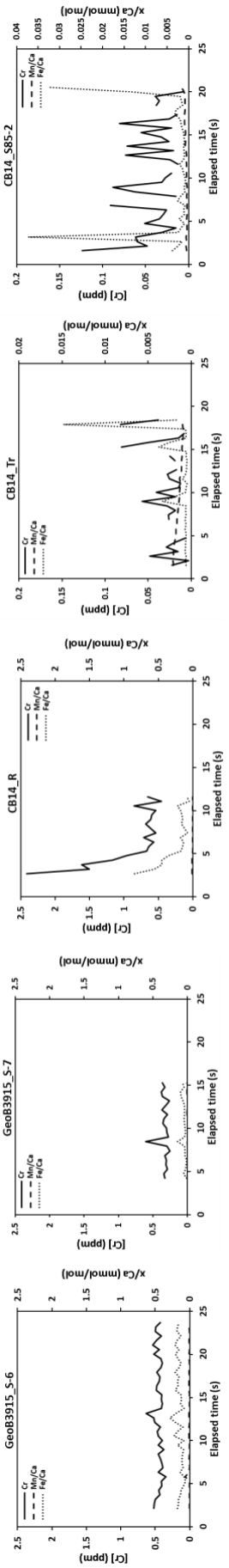

Figure A2: Laser profiles of Cr concentrations through core-top and sediment trap foraminifera. Foraminifera are analysed from the inner wall of the test outwards which means that the more time has elapsed the further towards the outer wall of the foraminifer the measurement has been taken.

Supplementary Material B

cGENIE model-data fit scores and dataset

Carbon dioxide and PO_4 levels correspond to the model settings, where 1x CO_2 equals pre-industrial atmospheric CO_2 levels and 1x PO_4 equals modern phosphate loading into the ocean.

Table B1: Confidence in model fit with pre-PETM anoxia and hypoxia data

	1 x CO_2	**2 x CO_2**	**4 x CO_2**	**6 x CO2**
0.5 x PO_4	0.3	0.3	0.3	0.3
1 x PO_4	0.5	0.5	0.4	0.4
2 x PO_4	0.3	0.3	0.3	0.3
3 x PO_4	0.3	0.3	0.3	0.3

Table B2: Confidence in model fit with PETM anoxia and hypoxia data

	1 x CO_2	**2 x CO_2**	**4 x CO_2**	**6 x CO2**
0.5 x PO_4	0	0	0	0
1 x PO_4	0.4	0.4	0.5	0.6
2 x PO_4	0.5	0.4	0.4	0.4
3 x PO_4	0.4	0.4	0.4	0.4

Table B3: Confidence in model fit with PETM euxinia data

	1 x CO_2	**2 x CO_2**	**4 x CO_2**	**6 x CO2**
0.5 x PO_4	0.9	0.9	0.9	0.9
1 x PO_4	0.9	0.9	0.9	0.9
2 x PO_4	0.9	0.9	0.9	0.9
3 x PO_4	0.8	0.8	0.8	0.8

Table B4: Confidence in model fit with combined PETM anoxia, hypoxia, and euxinia data

	1 x CO_2	**2 x CO_2**	**4 x CO_2**	**6 x CO2**
0.5 x PO_4	0.5	0.5	0.5	0.5
1 x PO_4	0.7	0.7	0.7	0.8
2 x PO_4	0.7	0.7	0.7	0.7
3 x PO_4	0.6	0.6	0.6	0.6

Table B5: Palaeo-coordinates and oxygen status assigned to locations used in the pre-PETM model-data comparison. References can be found in Carmichael et al. (2017) or Supplementary Material C.

Location	**Palaeolongitude**	**Palaeolatitude**	**Oxic**	**Hypoxic**	**Anoxic**	**Conclusive evidence**
ODP Site 1209	-171	24	x			yes
ODP Site 1221	-116	3	x			yes
ODP Site 1258	-43	7		x		yes
ODP Site 1262	-11	-34	x			yes
ODP Site 689	-5	-65		x		yes
ODP Site 738	78	-64		x		yes
Harrell Core	-73	35			x	yes
Ancora, NJ	-57	36	x			yes
DSDP Site 401	-12	43		x		yes
Aktumsuk	51	41			x	yes
Kurpai	63	36			x	yes
Sidi Nasseur	6	27			x	yes

Table B6: Palaeo-coordinates and oxygen status assigned to locations used in the PETM model-data comparison. References can be found in Carmichael et al. (2017) or Supplementary Material C.

Location	Palaeolongitude	Palaeolatitude	Oxic	Hypoxic	Anoxic	Euxinic	Conclusive evidence
ODP Site 1209	-171	24		x			no
ODP Site 1221	-116	3		x			no
ODP Site 1258	-43	7		x			no
ODP Site 1263	-10	-35		x			yes
ODP Site 689	-5	-65		x			no
ODP Site 738	78	-64		x			yes
ODP Site 999	-77	12		x			yes
ODP Site 1001	-73	15		x			yes
ODP Site 865	-151	8		x			no
Harrell Core	-73	35			x	x	yes
Wilson Lake, NJ	-57	36			x		yes
DSDP Site 401	-12	43		x			yes
Aktumsuk	51	41			x	x	yes
Kurpai	63	36			x	x	yes
Sidi Nasseur	6	27			x		yes

Supplementary Material C

Hydrological and associated biogeochemical consequences of rapid global warming during the Palaeocene-Eocene Thermal Maximum

---

This material has been published as a section of an invited review in *Global and Planetary Change* and is citeable as:

Carmichael, M.J., Inglis, G.N., Badger, M.P.S., Naafs, B.D.A., Behrooz, L., **Remmelzwaal, S.**, Monteiro, F.M., Rohrssen, M., Farnsworth, A., Buss, H.L., Dickson, A.J., Valdes, P.J., Lunt, D.J., Pancost, R.D., 2017. Hydrological and associated biogeochemical consequences of rapid global warming during the Palaeocene Eocene Thermal Maximum. Global and Planetary Change 157 114-138

Contributions and declaration: S.R.C. Remmelzwaal and L. Behrooz contributed the review section on ocean deoxygenation during the PETM. Other authors contributed various other sections of the review. The final manuscript was written and edited by Dr M.J. Carmichael and Professor R.D. Pancost.

Abstract

The Paleocene-Eocene Thermal Maximum (PETM) hyperthermal, ~ 56 million years ago (Ma), is the most dramatic example of abrupt Cenozoic global warming. During the PETM surface temperatures increased between 5 and 9 °C and the onset likely took < 20 kyr. The PETM provides a case study of the impacts of rapid global warming on the Earth system, including both hydrological and associated biogeochemical feedbacks, and proxy data from the PETM can provide constraints on changes in warm climate hydrology simulated by general circulation models (GCMs). In this paper, we provide a critical review of biological and geochemical signatures interpreted as direct or indirect indicators of hydrological change at the PETM, explore the importance of adopting multi-proxy approaches, and present a preliminary model-data comparison. Hydrological records complement those of temperature and indicate that the climatic response at the PETM was complex, with significant regional and temporal

variability. This is further illustrated by the biogeochemical consequences of inferred changes in hydrology and, in fact, changes in precipitation and the biogeochemical consequences are often conflated in geochemical signatures. There is also strong evidence in many regions for changes in the episodic and/or intra-annual distribution of precipitation that has not widely been considered when comparing proxy data to GCM output. Crucially, GCM simulations indicate that the response of the hydrological cycle to the PETM was heterogeneous – some regions are associated with increased precipitation – evaporation (P – E), whilst others are characterised by a decrease. Interestingly, the majority of proxy data come from the regions where GCMs predict an increase in PETM precipitation. We propose that comparison of hydrological proxies to GCM output can be an important test of model skill, but this will be enhanced by further data from regions of model-simulated aridity and simulation of extreme precipitation events.

1. Impacts on the marine realm – increased nutrients, algal productivity and anoxia

The apparent increase in marine algal productivity, alongside evidence for warming and increased chemical weathering, has been used to invoke comparisons to Mesozoic OAEs. Crucially, the expansion of anoxia during OAEs is now linked to hydrological changes that impacted the marine realm via weathering-nutrient-productivity feedbacks (Jenkyns, 2010). However, the overall response of marine oxygen concentrations to collective PETM biogeochemical changes remains unclear (Speijer and Wagner, 2002; Sluijs et al., 2006; Sluijs et al., 2014; Chun et al., 2010; Dickson et al., 2012), although it was almost certainly less geographically widespread than the Mesozoic OAEs.

Several proxies indicate de-oxygenation in the deep Atlantic. At three Walvis Ridge Sites, representing different paleo-depths (ODP sites 1262, 1266, and 1263; South Atlantic), both manganese (Mn) and uranium (U) enrichment factors suggest that all sites experienced suboxic conditions during the PETM, with a possible vertical expansion of the oxygen minimum zone (OMZ) from shallow towards the deeper sites (Chun et al., 2010). Pälike et al. (2014) found similar results for Demerara Rise (ODP site 1258). The iodine calcium (I/Ca) ratios of the bulk coarse carbonate fraction at ODP Sites 1262 and 1266 (Zhou et al., 2014) support the previous findings of OMZ expansion, suggesting sea surface deoxygenation. Bralower et al. (1997) also observe lamination and absence of bioturbation in the Palaeocene-Eocene sediments of the West Atlantic (ODP sites 999 and 1001). None of these sites, however, are associated with the dramatic increase in organic matter accumulation rates observed during Mesozoic OAEs, and in fact, many remain organic-lean despite inferred increases in productivity.

The deep Pacific shows even more ambiguous evidence for a decrease in oxygenation. Pälike et al. (2014) and Zhou et al. (2014) find no evidence for deoxygenation in the Pacific at ODP sites 1209 and 1221 (Equatorial Pacific) from Mn and U enrichment factors and I/Ca ratios, respectively. However,

other proxies point to at least some degree of deoxygenation in the Pacific. For example, a peak in pyrite abundance occurs just prior to the onset of the CIE at ODP sites 1209-1212 (West Pacific; Colosimo et al., 2005), whilst a significant reduction in the maximum diameter of benthic foraminifera test sizes at the peak of the PETM occurs at ODP site 1209 and 1210 (Kaiho et al., 2006). Late Paleocene benthic foraminiferal extinctions have been reported in the Central Pacific (ODP site 865; Thomas and Shackleton, 1996) and West Pacific (ODP site 1209-1212 and 1220; Takeda and Kaiho, 2007), although these could have been due to a range of factors. ODP site 1220 also has weak laminations, which is paradoxical considering its sister site (1221) was shown to have experienced oxic conditions across the PETM (Pälike et al., 2014). I/Ca ratios in ODP site 865 indicate relative oxygen depletion (Zhou et al., 2014), which is in agreement with micropalaeontological evidence. As with the Atlantic sites, there is not strong evidence for an increase in organic matter contents.

Whilst deep-sea environments experienced only minimal deoxygenation during the PETM, there is growing evidence for deoxygenation in shelf and marginal marine settings (Sluijs et al., 2014). For example, in the eastern Gulf of Mexico, the presence of sulfur-bound isorenieratane in the PETM interval (Harrell Core) indicates development of intermittent photic zone euxinia during the PETM. Benthic foraminiferal turnover occurs across the New Jersey coastal plain (i.e. Wilson Lake, Ancora and Bass River; Stassen et al., 2012b) and there is an increase of magnetofossils within the same region (Kopp et al., 2009; Lippert and Zachos, 2007). Combined, these observations indicate suboxic conditions were present both within the sediment and in the bottom water in the eastern Gulf of Mexico. Similarly, the Eurasian shelves apparently experienced significant expansions of oxygen minimum zones, as suggested by a decrease in benthic foraminiferal diversity (Boltovskoy et al., 1992; Pak and Miller, 1992; Pardo et al., 1997; Gradstein et al., 1994); similarly, in the Bay of Biscay (DSDP Site 401) a short-term increase in the abundance of low-oxygen tolerant chiloguembelinids and low Mn and U enrichment ratios indicate expansion of the oxygen minimum zone (Pardo et al., 1997; Pälike et al., 2014). The Western Tethyan margins also experienced benthic turnover, notably in the Spanish sections of Zumaia and Caravaca, and in Possagno, Italy (Canudo et al., 1995; Braga et al., 1975). The presence of laminated sediments in Caravaca (Canudo et al., 1995) and the absence of bioturbation in Zumaia (Rodriguez-Tovar et al., 2011) coeval to the faunal turnover implicate deoxygenation as part of the cause of the benthic crisis. A benthic foraminiferal extinction has also been reported for Poland (Bak, 2005). TOC enrichments in Austria (Egger et al., 2003, 2005) suggest increased sea-surface productivity facilitating oxygen depletion in the bottom waters. The presence of isorenieratane in PETM sections from Denmark also indicate the development of photic zone euxinia on the epicontinental North Sea Basin (Schoon et al., 2013; Schoon et al., 2015). As with deep waters, evidence for deoxygenation in Pacific Ocean marginal settings is weaker than for the Atlantic Ocean. Nonetheless, the development of oxygen depletion in intermediate waters of the Southwest Pacific has been inferred

from laminations and a decrease in ichnofossil abundance across the CIE in New Zealand (Nicolo et al., 2010), as well as a benthic foraminiferal turnover (Kaiho et al., 1996).

Evidence for extensive marine anoxia is most pronounced in the epicontinenal shelves of the Eastern Tethys and the Arctic Ocean. The former experienced anoxic bottom water conditions as evidenced by trace metal enrichments (Gavrilov et al., 1997; Gavrilov et al., 2003), the presence of pyrite (Gavrilov et al., 1997, 2003; Bolle et al., 2000), laminations (Gavrilov et al., 2003), and pronounced TOC enrichments (Frieling et al., 2014), documented from sites in the Caucasus and Central Asia. Isorenieratane is present in the West Siberian Sea indicating at least intermittent photic zone euxinia (Frieling et al., 2014), and diaryl isoprenoids (potentially derived from isorenieratane) were found in Kurpai, Tadjikistan (Kodina et al., 1995). Lycopane, a C_{40} isoprenoid of unclear origin but associated with water column anoxia (Sinninghe Damsté et al., 2003) occurs in rocks from Aktumsuk, Uzbekistan (Bolle et al., 2000). Dickson et al. (2014a, 2014b) provided perhaps the most comprehensive evidence for strong and persistent anoxia along the northern margin of the Tethys during the PETM, based on a combination of TOC contents, trace metal enrichments, metal isotopes, characterisation of reactive iron species and biomarkers (lycopane) to show that anoxia occurred in both bottom waters and the water column during the PETM (CIE) but that the entire water column was well-oxygenated in pre and post-PETM intervals. The evidence for anoxia is also compelling for the southern Tethys, albeit less strong than for the northern margin sites. Benthic foraminiferal and nannofossil turnover occurred in sections in Egypt, Tunisia and Israel (Stassen et al., 2012a; Speijer and Wagner, 2002; Ernst et al., 2006; Khozyem et al., 2013). Supporting evidence for suboxic to euxinic environments coeval to the CIE comes from trace metal enrichments, laminated sediments and the presence of pyrite (Dupuis et al., 2003; Khozyem et al., 2013, 2015; Knox et al., 2003; Schulte et al., 2011; Soliman et al., 2011; Speijer and Schmitz, 1998).

The PETM section at Lomonosov Ridge (IODP Leg 302 Site 4) in the Central Arctic Ocean is characterised by a significant increase in the relative abundance of pyrite (Stein et al., 2006), a drastic decrease in C/S values and an increase in sulfur abundance (Sluijs et al., 2008b; Stein et al., 2006), elevated redox-sensitive trace metal concentrations (März et al., 2010; Sluijs et al., 2008a, 2008b; Dickson et al., 2012) and Mo-isotope compositions (Dickson et al., 2012), fine laminations and the occurrence of isorenieratane (Stein et al., 2006; Sluijs et al., 2006). In addition, the enrichment of Mn points to recycling of Mn(II) under restricted conditions in the Lomonosov Ridge PETM section (Sluijs et al., 2008b). Sediment lamination and pyrite abundances in the PETM interval in the Spitsbergen Central Basin, Longyearbyen section, represents a stratified water column during the PETM CIE (Harding et al., 2011). Cui et al. (2011) also infer reducing bottom water conditions at the margins of the Arctic Ocean indicated by well-developed parallel lamination in pyrite-rich shales (the Svalbard archipelago, BH9-05); this interpretation is reinforced by evidence of U and Re enrichment (Dypvik et

al., 2011; Wieczorek et al., 2013), a benthic turnover, changes in benthic (agglutinated) foraminiferal relative morphogroup dominance and test size reduction (Nagy et al., 2013).

Collectively, these data suggest that during the PETM, deep-sea settings experienced a minor reduction in seafloor oxygen (Chun et al., 2010; Pälike et al., 2014) with a greater level of oxygen depletion occurring on some continental slopes (Nicolo et al., 2010) and shelves (Speijer and Wagner, 2002; Sluijs et al., 2008b; Sluijs et al., 2014). Water column anoxia and euxinia was restricted only to some marginal settings or partially restricted basins, i.e. the Arctic Ocean and Tethys. Locations at which deoxygenation has been inferred for the PETM are shown on Fig. 6, alongside those sites for which evidence exists for photic zone euxinia.

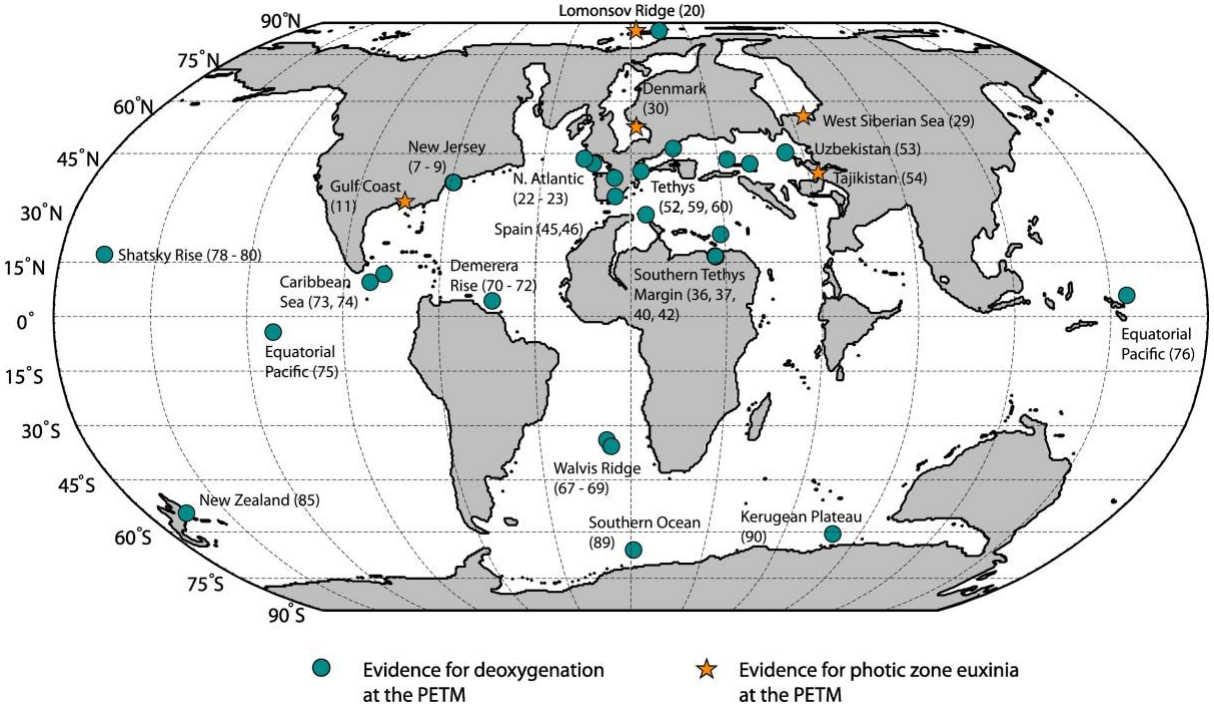

Figure C1: Paleogeographic reconstruction for 56 Ma showing locations where evidence exists for deoxygenation in marine and marginal PETM sites. Also shown are locations where evidence for photic zone euxinia exists (stars). Numbers provided after each location correspond to PETM sites and references provided in Table C1.

Moreover, many of these studies suggest that even where anoxia has been documented for the PETM Ocean, it was intermittent. It is noteworthy that even in the northern Tethys (Kheu River section, Dickson et al., 2014a), there appear to be cyclic variations in trace metal enrichments and lycopane concentrations. This cyclicity could be due to the sensitivity of shallow sites to oscillating depositional conditions, related to an enhanced hydrological cycle and fluctuations in nutrient input to marginal basins, which favours episodic oxygen depletion. By extension, the Arctic Ocean and Tethys could be considered nutrient traps, whereby increased nutrient inputs bring about increased productivity and anoxia only in restricted basins.

Table C1: Summary of sites for which proxy interpretations exist for paleohydrological or biogeochemical change at the PETM. Site numbers correspond to those shown on each of the maps in the manuscript. For each site, principal sections of the manuscript are indicated, along with key references.

Site Ref.	Site Name	Location	Decimal Latitude	Decimal Longitude	Paleo-latitude	Paleo-longitude	Terrestrial/ Ocean	Principal sections of Review	Key References
United States									
1	Cabin Fork, Bighorn Basin	Wyoming	43.96	-107.65	45.5	-89.95	Terrestrial	Deuterium; Plants; Oxygen Isotopes	Wing et al. (2005); Smith et al. (2007); Wing et al. (2013); Secord et al. (2012); Kraus et al. (2007)
2	Clark Fork/McCullough Peaks	Bighorn Basin, Wyoming	44.76	-108.89	46.3	-91.19	Terrestrial	Oxygen Isotopes	Fricke et al. (1993); Fricke et al. (2003); Koch et al. (2003)
3	Highway 16, Willwood Fm, Bighorn Basin	Wyoming	44.02	-107.73	45.56	-90.03	Terrestrial	Paleosol and Weathering; Geomorphology	Foreman et al. (2014); Kraus et al. (2013)
4	Sand Creek Divide, Bighorn Basin	Wyoming	44.16	-107.85	45.7	-90.15	Terrestrial	Paleosols and Weathering	Kraus et al. (2007)
5	Polecat Bench, Bighorn Basin	Wyoming	44.76	-108.89	46.3	-91.19	Terrestrial	Paleosols and Weathering	Kraus et al. (2015); Bowen et al. (2000); Maxbauer et al. (2016)
6	South Dover Bridge	Maryland	38.73	-76	36.05	-60.74	Terrestrial	Calc Nanos	Self-Trail et al. (2012)
7	Bass River	New Jersey	39.6	-74.43	36.89	-58.7	Terrestrial	Anoxia; Clays	Stassen et al. (2012); John et al. (2012); Gibson et al. (2000)
8	Ancora	New Jersey	39.64	-74.84	36.93	-59.11	Terrestrial	Anoxia; Iron Oxides	Stassen et al. (2012); Schumann et al. (2008); Kopp et al. (2009)
9	Wilson Lake	New Jersey	39.65	-75.05	36.94	-59.32	Terrestrial	Anoxia; Dinoflagellates; Oxygen Isotopes; Calcareous Nanos	Stassen et al. (2012); Sluijs et al. (2007); Zachos et al. (2006); Gibbs et al. (2006)
10	Bear Creek, Alabama	Gulf Coast	31.95	-87.64	30.73	-72.91	Terrestrial	Dinoflagellates; Clays	Harrington and Kemp (2001)
11	Harrell Core	Gulf Coast, US	32.36	-88.68	31.62	-73.86	Terrestrial	Anoxia; Dinoflagellate	Sluijs et al. (2014)
12	Farmers Butte	North Dakota	46.92	-102.11	47.43	-83.71	Terrestrial	Clays	Clechenko et al. (2007)
13	Big Bend National Park	Western Texas	29.44	-103.17	30.69	-88.66	Terrestrial	Paleosol and Weathering	White and Schiebout et al. (2008)
14	Axehandle Basin	Utah	39.41	-111.7	41.51	-95.28	Terrestrial	Paleosol and Weathering	Retallack (2005); Van de Velde (2013)
15	Piceance Creek	Colarado	40.08	-108.24	41.69	-91.77	Terrestrial	Geomorphology	Foreman et al. (2012)
16	Tumley Gulch	California	36.53	-120.63	37.96	-105.06	Terrestrial	Sedimentation	John et al. (2008)
17	Lodo Gulch	California	36.58	-120.63	38.01	-105.06	Terrestrial	Sedimentation	John et al. (2008)
High northern latitudes, Europe and Asia									
18	Longyearbyen	Spitsbergen	78.22	15.63	73.94	-1.92	Ocean	Anoxia; Apectodinium; Plants; Clays	Harding et al. (2011); Dypvik et al. (2011)

19	Core BH 9/05	Spitsbergen	77.83	16.5	73.55	-1.05	Ocean	Osmium; Anoxia	Wieczorek et al. (2013); Dypvik et al. (2011)
20	IDOP M004	Lomonsov Ridge, Arctic	87.87	136.18	84.87	15.42	Ocean	Anoxia; Deuterium; Apectodinium; Osmium Isotopes; Oxygen Isotopes; Sedimentation Rates	Sluijs et al. (2006); Pagani et al. (2006); Stein et al. (2006); Dickson et al. (2012; 2015); Waddell and Moore (2008); Slujs et al. (2008); Denis et al. (2017).
21	Beigou, Nanyang	China	32.73	111.46	38.24	107.53	Terrestrial	Paleosol and Weathering	Chen et al. (2016)
22	DSDP 401	Bay of Biscay	47.4	-8.81	42.15	-12.74	Ocean	Anoxia; Clays	Pälike et al. (2014); Tremolada and Bralower (2004); Bornemann et al. (2014)
23	DSDP 548	North Atlantic	48.92	-12.17	43.49	-15.99	Ocean	Anoxia	Boltovskoy et al. (1992); Sluijs et al. (2014)
24	DSDP 549	Atlantic Ocean	49.09	-13.1	43.66	-16.92	Ocean	Osmium Isotopes	Ravizza et al. (2001)
25	Offshore W Greenland Well	Atlantic	66.93	-56.58	60.26	-35.62	Ocean	Apectodinium	Nøhr-Hansen et al. (2003)
26	Cobham Lignite	UK	51.4	0.41	46.55	-4.85	Terrestrial	Methane; Plants	Pancost et al. (2007); Collinson et al. (2009)
27	Well 221/20a-4	North Sea	57.73	1.83	52.85	-4.23	Ocean	Plants; Dinoflagellates	Kender et al. (2012)
28	Well 22/11-N1	North Sea	57.65	1.13	52.77	-4.93	Ocean	Apectodinium	Eldrett et al. (2014)
29	Well 10	West Siberian Sea	53.5	73.53	55.58	64.9	Ocean	Anoxia	Cited in Sluijs et al. (2014)
30	Fur Island	Denmark	56.83	9.01	52.43	2.07	Terrestrial	Anoxia	Schoon et al. (2013; 2015)
31	Kallo Borehole	North Sea/Netherlands	51.25	4.27	46.63	-1.36	Ocean	Apectodinium	Steurbaut et al. (2003)
32	Outer Voring	North Sea	67.23	2.93	62.49	-6.15	Ocean	Apectodinium	Boulter and Manum (1989)
33	Vasterival Section, Normandy	France	49.91	0.96	45.07	-3.95	Terrestrial	Deuterium; Paleosols; Weathering	Garel et al. (2013); Storme et al. (2012)
Paleo-Tethys, northern Africa and southern Europe									
35	Sokolovsky Quarry	Kazakhstan	52.97	63.46	53.89	54.6	Terrestrial	Apectodinium	Iakovleva et al. (2001)
36	Gebel Duwi	Egypt	25.25	32.75	16.47	26.92	Terrestrial	Anoxia; Sedimentation Rate	Speijer and Wagner (2002); Bolle et al. (2000); Bolle and Adatte (2001)
37	Dababiya	Egypt	25.5	32.52	16.72	26.69	Terrestrial	Anoxia	Schulte et al. (2011); Soliman et al. (2013)
38	Abu Zenima	Egypt	29.07	33.16	20.11	27.08	Terrestrial	Sed Rates; Clays	Bolle et al. (2000); Khozyem et al. (2013)
39	Gebel Matulla	Egypt	29.05	33.17	20.09	27.09	Terrestrial	Sed Rates	Bolle et al. (2000)
40	Ben Gurion	Israel	31.43	34.48	22.65	28.75	Terrestrial	Anoxia	Speijer and Wagner (2002); Bolle and Adatte (2001)
41	Zomet Telalim	Israel	31.46	34.43	22.68	28.7	Terrestrial	Sed Rates	Bolle et al. (2000)
42	Sidi Nasseur	Tunisia	35.74	8.45	28.05	4.98	Terrestrial	Anoxia; Sedimentation Rate	Stassen et al. (2012)
43	Elles Section	Tunisia	35.86	9.45	27.92	5.68	Terrestrial	Apectodinium	Crouch et al. (2003); Bolle and Adatte (2001);
44	Forum Selja	Southern Tunisia	34.32	6.32	26.63	2.85	Terrestrial	Clays	Bolle and Adatte (2001)
45	Caravaca	Spain	38.1	-1.86	33.05	-5.08	Terrestrial	Anoxia	Canudo et al. (1995)

46	Zumaia	Spain	43.3	-2.25	38.16	-5.4	Terrestrial	Anoxia; Clays; Osmium Isotopes	Bolle and Adatte (2001); Rodríguez-Tovar et al. (2011); Schmitz et al. (2001)
47	Alamedilla	Spain	37.5	3.2	33.19	-0.72	Terrestrial	Clays; Sedimentation Rates	Lu et al. (1998)
48	Esplugafreda, Tremp Basin	Spain	42.25	0.8	37.19	-2.62	Terrestrial	Clays; Sedimentation Rates	Schmitz and Pujalte (2003)
49	Trabaku Pass	Spain	43.3	-2.48	38.16	-5.63	Terrestrial	Sedimentation Rates	Schmitz et al. (2001); Bolle et al. (1998)
50	Ermua	Spain	43.19	2.5	38.24	-1.19	Terrestrial	Sedimentation Rates	Schmitz et al. (2001); Bolle et al. (1998)
51	Kurpai/Tadjik Depression	Kurpai	38	69	39.48	63.44	Terrestrial	Anoxia	Garilov et al. (1997); Garilov et al. (2003)
52	Kheu River	Caucasus	43.63	39.5	42.32	33.28	Terrestrial	Anoxia; Osmium Isotopes	Garilov et al. (2003); Dickson et al. (2015)
53	Aktumsuk	Uzbekistan	44.62	58.33	45.24	51.31	Terrestrial	Anoxia; Dinoflagellates; Sedimentation Rates	Garilov et al. (2003); Crouch et al. (2003); Bolle et al. (2000)
54	Guru-Fatima	Tajikistan	38	69	39.48	63.44	Terrestrial	Osmium Isotopes	Dickson et al. (2014); Dickson et al. (2015)
55	Dzhengutay,	Dagestan	42.69	47.24	42.15	40.84	Terrestrial	Osmium Isotopes	Dickson et al. (2014); Dickson et al. (2015)
56	Kaurtakapy	Kazakhstan	44.25	52.32	44.08	45.36	Terrestrial	Sedimentation Rates	Bolle and Adatte (2001)
57	Forada Section	Italy	46.04	12.07	38.21	12.24	Terrestrial	Deuterium; Sedimentation Rates; Calcareous Nanos	Tipple et al. (2011); Giusberti et al. (2007); Agnini et al. (2007)
58	Belluno Basin	Italy	46.06	12.24	38.23	12.41	Terrestrial	Deuterium; Iron Oxides	Krishnan et al. (2014); Dallanave et al. (2010)
59	Possagno	Italy	45.83	11.5	38	11.67	Terrestrial	Anoxia	Agnini et al. (2006); Dallanave et al. (2010)
60	Anthering	Austria	47.88	13.02	41	7.43	Terrestrial	Anoxa; Apectodinium	Egger et al. (2005); Egger et al. (2003)
61	Untersberg	Austria	47.72	12.92	40.84	7.33	Terrestrial	Clays	Egger et al. (2005); Egger et al. (2009)
Tropics, Subtropics and Africa									
62	Tanzania Drilling Program	Tanzania	-9.27	39.5	-18.05	33.57	Terrestrial	Calc Nanos; Deuteriums	Bown and Pearson (2009); Handley et al. (2012); Aze et al. (2014)
63	DSDP 530	Angola Basin	-19.18	9.38	-26.98	1.51	Terrestrial	Clays	Robert and Chamley (1991)
64	Mar2X	Venezuela	11.06	-72.17	4.68	-61.76	Terrestrial	Deuterium; Plants	Jaramillo et al. (2010)
65	Bogota Basin	Colombia	4.52	-74.15	-1.22	-63.54	Terrestrial	Iron Oxides; Paleosols	Morón et al. (2013)
66	Riecito Mache	Venezuela	10.74	-72.37	4.36	-61.96	Terrestrial	Plants	Jaramillo et al. (2010)
67	ODP 1266	Walvis Ridge	-28.54	2.34	-35.69	-6.82	Ocean	Anoxia	Chun et al. (2010) Zhou et al. (2014)
68	ODP 1263	Walvis Ridge	-28.53	2.78	-35.68	-6.38	Ocean	Anoxia; Nannoplankton	Chun et al. (2010); Zhou et al. (2014); Raffi et al. (2009)
69	ODP 1262	Walvis Ridge	-27.19	1.58	-33.98	-7.84	Ocean	Anoxia	Chun et al. (2010); Zhou et al. (2014); Raffi et al. (2009)
70	ODP 128	Demerara Rise	9.43	-54.73	4.3	-43.28	Ocean	Anoxia	Pälike et al. (2014)
71	ODP 1260	Demerara Rise	9.27	-54.54	4.14	-43.09	Ocean	Nannoplankton	Mutterlose et al. (2007)

72	ODP 1259	Demerara Rise	9.3	-54.2	4.3	-42.79	Ocean	Nannoplankton	Jiang and Wise (2006)
73	ODP 999	Colombia Basin	12.75	-78.73	9.48	-81.72	Ocean	Anoxia	Bralower et al. (1997)
74	ODP 1001	Nicaragua Rise	15.75	-74.92	11.68	-77.52	Ocean	Anoxia	Bralower et al. (1997)
75	ODP 1220	Equatorial Pacific	10.18	-142.75	-4.28	-111.8	Ocean	Anoxia	Chun et al. (2010)
76	ODP 1221	Equatorial Pacific	12.03	143.7	5.88	155.24	Ocean	Anoxia	Zhou et al. (2014)
77	ODP 865	Allison Guyot	18.43	-179.55	1.62	-147.89	Ocean	Anoxia	Thomas (1988)
78	ODP 1211	Shatsky Rise	32.22	158.5	17.09	-166.57	Ocean	Anoxia	Colosimo et al. (2005)
79	ODP 1210	Shatsky Rise	32.5	158.5	17.37	-166.57	Ocean	Anoxia	Kaiho et al. (2006)
80	ODP 1209	Shatsky Rise	32.65	158.51	17.52	-166.56	Ocean	Anoxia	Kaiho et al. (2006); Zhou et al. (2014)
81	Khasi Hills	India	25.28	91.71	-0.17	79.96	Terrestrial	Apectodinium	Prasad et al. (2006)
82	Vastan and Valia Regions	Western India	21.44	73.12	-0.56	62.81	Terrestrial	Carbon Isotopes; Clays and Sedimentation Rates	Samanta et al. (2013); also see Gibson et al. (2000) for Pakistan
83	DSDP 213	Indian Ocean	-10.21	93.9	-27.96	79.75	Ocean	Calcareous Nannos and Osmium Isotopes	Tremolada and Bralower (2004); Ravizza et al. (2001)
High southern latitudes									
84	Mead Stream	New Zealand	-41.96	173.79	-54.51	-165.55		Anoxia; Iron Oxides; Sedimentation Rates	Nicolo et al. (2010); Hollis et al. (2005); Villasante-Marcos et al. (2009)
85	Tawanui	New Zealand	-40.38	176.38	-54.62	-166	Terrestrial	Anoxia; Clays; Sedimentation Rates; Apectodinium	Kaiho et al. (1996); Crouch et al. (2001); Crouch et al. (2003)
86	Kumara	New Zealand	-42.58	171.2	-55.13	-168.14	Terrestrial	Deuterium	Handley et al. (2011)
87	Kakahu	New Zealand, South Island	-51	171.06	-63.39	-171.25	Terrestrial	Vegetation	Pole (2010)
88	Site 1172	East Tasman Plateau	-43.97	149.93	-64.09	155.97	Ocean	Vegetation	Contreras et al. (2013); Sluijs et al. (2011)
89	ODP 690, Maud Rise and Site 1135	Southern Ocean	-65.16	1.2	-65.55	1.21	Ocean	Anoxia; Calc Nannos; Clays	Pälike et al. (2014); Zhou et al. (2014); Bralower (2002); Robert and Chamley (1991); Robert and Kennett (1994)
90	ODP 738	Kerguelen Plateau	-62.71	82.79	-60.61	79.42	Ocean	Anoxia; Iron Oxides	Pälike et al. (2014); Zhou et al. (2014); Lu and Keller (1993); Chang et al. (2012); Larrasoaña et al. (2012)

2. References

Aze, T., Pearson, P.N., Dickson, A.J., Badger, M.P.S., Bown, P.R., Pancost, R.D., Gibbs, S.J., Huber, B.T., Leng, M.J., Coe, A.L., Cohen, A.S., Foster, G.L., 2014. Extreme warming of tropical waters during the Paleocene-Eocene thermal maximum. Geology 42, 739–742.

Bak, K., 2005. Deep-water agglutinated foraminiferal changes across the Cretaceous/ Tertiary and Paleocene/Eocene transitions in the deep flysch environment: eastern outer Carpathians (Boiesczady Mts, Poland). In: Proceedings of the 6th International Workshop on Agglutinated Foraminifera, Grzybowski Foundation Special Publication. Volume 8. pp. 1–56.

Bolle, M.P., Adatte, T., 2001. Palaeocene early Eocene climatic evolution in the Tethyan realm: clay mineral evidence. Clay Miner. 36, 249–261.

Bolle, M.P., Pardo, A., Adatte, T., Tantawy, A.A., Hinrichs, K.U., Von Salis, K., Burns, S., 2000. Climatic evolution on the southern and northern margins of the Tethys from the Paleocene to the early Eocene. GFF 122, 31–32.

Boltovskoy, E., Watanabe, S., Totah, V.I., Vera Ocampo, J., 1992. Cenozoic benthic bathyal foraminifers of DSDP Site 548 (North Atlantic). Micropaleontology 38, 183–207.

Bornemann, A., Norris, R.D., Lyman, J.A., D'Haenens, S., Groeneveld, J., Röhl, U., Farley, K.A., Speijer, R.P., 2014. Persistent environmental change after the Paleocene-Eocene Thermal Maximum in the eastern North Atlantic. Earth Planet. Sci. Lett. 394, 70–81.

Bowen, G.J., Bowen, B.B., 2008. Mechanisms of PETM global change constrained by a new record from central Utah. Geology 36, 379–382.

Bowen, G.J., Beerling, D.J., Koch, P.L., Zachos, J.C., Quattlebaum, T., 2004. A humid climate state during the Palaeocene/Eocene thermal maximum. Nature 432, 495–499.

Braga, G., De, B.R., Grunig, A., Proto Decima, F., 1975. Foraminiferi bentonici del Paleocene ed Eocene della Sezione di Possagno. Schweiz Palaontol Abh 97, 85–111.

Canudo, J., Keller, G., Molina, E., Ortiz, N., 1995. Planktic foraminiferal turnover and $\delta^{13}C$ isotopes across the Paleocene-Eocene transition at Caravaca and Zumaya, Spain. Palaeogeogr. Palaeoclimatol. Palaeoecol. 114, 75–100.

Chun, C.O.J., Delaney, M.L., Zachos, J.C., 2010. Paleoredox changes across the Paleocene-Eocene thermal maximum, Walvis Ridge (ODP Sites 1262, 1263, and 1266): evidence from Mn and U enrichment factors. Paleoceanography 25.

Cohen, A.S., Coe, A.L., Harding, S.M., Schwark, L., 2004. Osmium isotope evidence for the regulation of atmospheric CO_2 by continental weathering. Geology 32, 157–160.

Collinson, M.E., Steart, D.C., Harrington, G.J., Hooker, J.J., Scott, A.C., Allen, L.O., Glasspool, I.J., Gibbons, S.J., 2009. Palynological evidence of vegetation dynamics in response to palaeoenvironmental change across the onset of the Paleocene-Eocene Thermal Maximum at Cobham, Southern England. Grana 48, 38–66.

Colosimo, A.B., Bralower, T.J., Zachos, J.C., 2005. Evidence for lysocline shoaling at the Paleocene/Eocene Thermal Maximum on Shatsky Rise, northwest Pacific. In: Bralower, T.J., Silva, I.P., Malone, M.J. (Eds.), Proceedings of the Ocean Drilling Program, Scientific Results. Ocean Drilling Program Vol. 198. College Station, TX, 1–36.

Conant, R.T., Ryan, M.G., Ågren, G.I., Birge, H.E., Davidson, E.A., Eliasson, P.E., Evans, S.E., Frey, S.D., Giardina, C.P., Hopkins, F.M., Hyvönen, R., Kirschbaum, M.U.F., Lavallee, J.M., Leifeld, J., Parton, W.J., Megan Steinweg, J., Wallenstein, M.D., Martin Wetterstedt, J.Å., Bradford, M.A., 2011. Temperature and soil organic matter decomposition rates - synthesis of current knowledge and a way forward. Glob. Chang. Biol.

Contreras, L., Pross, J., Bijl, P.K., Koutsodendris, A., Raine, J.I., van de Schootbrugge, B., Brinkhuis, H., 2013. Early to Middle Eocene vegetation dynamics at the Wilkes Land Margin (Antarctica). Rev. Palaeobot. Palynol. 197, 119–142.

Cotton, J.M., Sheldon, N.D., Hren, M.T., Gallagher, T.M., 2015. Positive feedback drives carbon release from soils to atmosphere during Paleocene/Eocene warming. Am. J. Sci. 315, 337–361.

Cramer, B.S., 2003. Orbital climate forcing of $d^{13}C$ excursions in the late Paleocene–early Eocene (chrons C24n–C25n). Paleoceanography 18, 1–25.

Creech, J.B., Baker, J.A., Hollis, C.J., Morgans, H.E.G., Smith, E.G.C., 2010. Eocene sea temperatures for the mid-latitude southwest Pacific from Mg/Ca ratios in planktonic and benthic foraminifera. Earth Planet. Sci. Lett. 299, 483–495.

Crouch, E.M., Heilmann-Clausen, C., Brinkhuis, H., Morgans, H.E.G., Rogers, K.M., Egger, H., Schmitz, B., 2001. Global dinoflagellate event associated with the late Paleocene Thermal Maximum. Geology 29, 315–318.

Crouch, E.M., Dickens, G.R., Brinkhuis, H., Aubry, M.P., Hollis, C.J., Rogers, K.M., Visscher, H., 2003. The Apectodinium acme and terrestrial discharge during the Paleocene-Eocene thermal maximum: new palynological, geochemical and calcareous nannoplankton observations at Tawanui, New Zealand. Palaeogeogr. Palaeoclimatol. Palaeoecol. 194, 387–403

Cui, Y., Kump, L.R., Ridgwell, A.J., Charles, A.J., Junium, C.K., Diefendorf, A.F., Freeman, K.H., Urban, N.M., Harding, I.C., 2011. Slow release of fossil carbon during the Palaeocene–Eocene Thermal Maximum. Nat. Geosci. 4, 481–485.

Curry, R., Dickson, B., Yashayaev, I., 2003. A change in the freshwater balance of the Atlantic Ocean over the past four decades. Nature 426, 826–829.

Dai, A., 2006. Precipitation characteristics in eighteen coupled climate models. J. Clim. 19, 4605–4630.

Dallanave, E., Agnini, C., Muttoni, G., Rio, D., 2009. Magneto-biostratigraphy of the Cicogna section (Italy): implications for the late Paleocene-early Eocene time scale. Earth Planet. Sci. Lett. 285, 39–51. Dansgaard, W., 1964. Stable isotopes in precipitation. Tellus 16, 436–468.

DeConto, R.M., Galeotti, S., Pagani, M., Tracy, D., Schaefer, K., Zhang, T., Pollard, D., Beerling, D.J., 2012. Corrigendum: past extreme warming events linked to massive carbon release from thawing permafrost. Nature 490 292–292.

Denis, E.H., Pedentchouk, N., Schouten, S., Pagani, M., Freeman, K.H., 2017. Fire and ecosystem change in the Arctic across the Paleocene-Eocene Thermal Maximum. Earth Planet. Sci. Lett. 467, 149–156.

Denman, K.L., Brasseur, G., Chidthaisong, A., Ciais, P., Cox, P.M., Dickinson, R.E., Hauglustaine, D., Heinze, C., Holland, E., Jacob, D., Lohmann, U., Ramachandran, S., Leite da Silva Dias, P., Wofsy,

S.C., Zhang, X., Steffen, W., 2007. Couplings between changes in the climate system and biogeochemistry. In: Climate Change 2007: The Physical Science Basis. 21. pp. 499–587.

Dickens, G.R., O'Neil, J.R., Rea, D.K., Owen, R.M., 1995. Dissociation of oceanic methane hydrate as a cause of the carbon isotope excursion at the end of the Paleocene. Paleoceanography 10, 965–971.

Dickson, A.J., Cohen, A.S., Coe, A.L., 2012. Seawater oxygenation during the Paleocene Eocene Thermal Maximum. Geology 40, 639–642.

Dickson, A.J., Cohen, A.S., Coe, A.L., 2014a. Continental margin molybdenum isotope signatures from the Early Eocene. Earth Planet. Sci. Lett. 404, 389–395.

Dickson, A.J., Rees-Owen, R.L., Marz, C., Coe, A.L., Cohen, A.S., Pancost, R.D., Taylor, K., Shcherbinina, E., 2014b. The spread of marine anoxia on the northern Tethys margin during the Paleocene-Eocene thermal maximum. Paleoceanography 29, 471–488.

Dickson, A.J., Cohen, A.S., Coe, A.L., Davies, M., Shcherbinina, E.A., Gavrilov, Y.O., 2015. Evidence for weathering and volcanism during the PETM from Arctic Ocean and Peri-Tethys osmium isotope records. Palaeogeogr. Palaeoclimatol. Palaeoecol. 438, 300–307.

Domingo, L., López-Martínez, N., Leng, M.J., Grimes, S.T., 2009. The Paleocene-Eocene Thermal Maximum record in the organic matter of the Claret and Tendruy continental sections (South-central Pyrenees, Lleida, Spain). Earth Planet. Sci. Lett. 281, 226–237.

Van Dongen, B.E., Talbot, H.M., Schouten, S., Pearson, P.N., Pancost, R.D., 2006. Well preserved Palaeogene and Cretaceous biomarkers from the Kilwa area, Tanzania. Org. Geochem. 37, 539–557.

Doria, G., Royer, D.L., Wolfe, A.P., Fox, A., Westgate, J.A., Beerling, D.J., 2011. Declining atmospheric CO2 during the late Middle Eocene climate transition. Am. J. Sci. 311, 63–75.

Dunkley Jones, T., Ridgwell, A., Lunt, D.J., Maslin, M.A., Schmidt, D.N., Valdes, P.J., 2010. A Palaeogene perspective on climate sensitivity and methane hydrate instability. Philos. Trans. R. Soc. A - Math. Phys. Eng. Sci. 368, 2395–2415.

Dunkley Jones, T., Lunt, D.J., Schmidt, D.N., Ridgwell, A., Sluijs, A., Valdes, P.J., Maslin, M., 2013. Climate model and proxy data constraints on ocean warming across the Paleocene-Eocene Thermal Maximum. Earth-Sci. Rev. 125, 123–145.

Dupuis, C., Aubry, M.P., Steurbat, E., Berggren, W.A., Ouda, K., Magioncalda, R., Cramer, B.S., Kent, D.V., Speijer, R.P., Heilmann-Clausen, C., 2003. The Dababiya Quarry section: lithostratigraphy, clay mineralogy, geochemistry and paleontology. Micropaleontology 49, 41–59.

Dypvik, H., Riber, L., Burca, F., Ruther, D., Jargvoll, D., Nagy, J.J., Jochmann, M., Rüther, D., 2011. The Paleocene-Eocene Thermal Maximum (PETM) in Svalbard - clay mineral and geochemical signals. Palaeogeogr. Palaeoclimatol. Palaeoecol. 302, 156–169.

Eberle, J.J., Greenwood, D.R., 2012. Life at the top of the greenhouse Eocene world – a review of the Eocene flora and vertebrate fauna from Canada's high Arctic. Geol. Soc. Am. Bull. 124, 3–23.

Egger, H., Homayoun, M., Schnabel, W., 2002. Tectonic and climatic control of Paleogene sedimentation in the Rhenodanubian Flysch basin (eastern Alps, Austria). Sediment. Geol. 152, 247–262.

Egger, H., Fenner, J., Heilmann-Clausen, C., Rögl, F., Sachsenhofer, R.F., Schmitz, B., 2003. Paleoproductivity of the northwestern Tethyan margin (Anthering section, Austria) across the Paleocene-Eocene transition. Geol. Soc. Am. Spec. Pap. 369, 133–146.

Egger, H., Homayoun, M., Huber, H., Rögl, F., Schmitz, B., 2005. Early Eocene climatic, volcanic, and biotic events in the northwestern Tethyan Untersberg section, Austria. Palaeogeogr. Palaeoclimatol. Palaeoecol. 217, 243–264.

Eglinton, T.I., Eglinton, G., 2008. Molecular proxies for paleoclimatology. Earth Planet. Sci. Lett. 275, 1–16.

Eglinton, G., Hamilton, R.J., 1967. Leaf epicuticular waxes. Science 80, 1322–1335.

Ernst, S.R., Guasti, E., Dupuis, C., Speijer, R.P., 2006. Environmental perturbation in the southern Tethys across the Paleocene/Eocene boundary (Dababiya, Egypt): foraminiferal and clay mineral records. Mar. Micropaleontol. 60, 89–111.

Fabricius, K.E., 2005. Effects of terrestrial runoff on the ecology of corals and coral reefs: review and synthesis. Mar. Pollut. Bull. 50, 125–146.

Farquhar, G.D., Hubick, K.T., Condon, A.G., Richards, R.A., 1989. Carbon isotope fractionation and plant water-use efficiency. In: Stable Isotopes in Ecological Research, 21–40.

Feakins, S.J., Sessions, A.L., 2010. Controls on the D/H ratios of plant leaf waxes in an arid ecosystem. Geochim. Cosmochim. Acta 74, 2128–2141.

Fletcher, B.J., Brentnall, S.J., Anderson, C.W., Berner, R.A., Beerling, D.J., 2008. Atmospheric carbon dioxide linked with Mesozoic and early Cenozoic climate change. Nat. Geosci. 1, 43–48.

Foreman, B.Z., 2014. Climate-driven generation of a fluvial sheet sand body at the Paleocene-Eocene boundary in north-west Wyoming (USA). Basin Res. 26, 225–241.

Foreman, B.Z., Heller, P.L., Clementz, M.T., 2012. Fluvial response to abrupt global warming at the Palaeocene/Eocene boundary. Nature 490, 92–95.

Fricke, H.C., 2003. Investigation of early Eocene water-vapor transport and paleoelevation using oxygen isotope data from geographically widespread mammal remains. Geol. Soc. Am. Bull. 115, 1088–1096.

Fricke, H.C., Clyde, W.C., O'Neil, J.R., Gingerich, P.D., 1998. Evidence for rapid climate change in North America during the latest Paleocene thermal maximum: oxygen isotope compositions of biogenic phosphate from the Bighorn Basin (Wyoming). Earth Planet. Sci. Lett. 160, 193–208.

Frieling, J., Iakovleva, A.I., Reichart, G.J., Aleksandrova, G.N., Gnibidenko, Z.N., Schouten, S., Sluijs, A., 2014. Paleocene-Eocene warming and biotic response in the epicontinental West Siberian Sea. Geology 42, 767–770.

Garel, S., Schnyder, J., Jacob, J., Dupuis, C., Boussafir, M., Le Milbeau, C., Storme, J.Y., Iakovleva, A.I., Yans, J., Baudin, F., Flehoc, C., Quesnel, F., Fléhoc, C., Quesnel, F., Flehoc, C., Quesnel, F., Fléhoc, C., Quesnel, F., 2013. Paleohydrological and paleoenvironmental changes recorded in terrestrial sediments of the Paleocene-Eocene boundary (Normandy, France). Palaeogeogr. Palaeoclimatol. Palaeoecol. 376, 184–199.

Gat, J.R., 1996. Oxygen and hydrogen isotopes in the hydrologic cycle. Annu. Rev. Earth Planet. Sci. 24, 225–262.

Gavrilov, Y.O., Kodina, L.A., Lubchenko, I.Y., Muzylöv, N.G., 1997. The Late Paleocene anoxic event in epicontinental seas of Peri-Tethys and formation of the sapropelite unit: sedimentology and geochemistry. Lithol. Miner. Resour. 32, 427–450.

Gavrilov, Y.O., Shcherbinina, E.A., Oberhänsli, H., 2003. Paleocene-Eocene boundary events in the northeastern Peri-Tethys. Geol. Soc. Am. Spec. Pap. 369, 147–168.

Gibbs, S.J., Bralower, T.J., Bown, P.R., Zachos, J.C., Bybell, L.M., 2006. Shelf and open ocean calcareous phytoplankton assemblages across the Paleocene-Eocene thermal maximum: implications for global productivity gradients. Geology 34, 233–236.

Gibson, T.G., Bybell, L.M., Mason, D.B., 2000. Stratigraphic and climatic implications of clay mineral changes around the Paleocene/Eocene boundary of the northeastern US margin. Sediment. Geol. 134, 65–92.

Gislason, S.R., Oelkers, E.H., Eiriksdottir, E.S., Kardjilov, M.I., Gisladottir, G., Sigfusson, B., Snorrason, A., Elefsen, S., Hardardottir, J., Torssander, P., Oskarsson, N., 2009. Direct evidence of the feedback between climate and weathering. Earth Planet. Sci. Lett. 277, 213–222.

Giusberti, L., Rio, D., Agnini, C., Backman, J., Fornaciari, E., Tateo, F., Oddone, M., 2007. Mode and tempo of the Paleocene-Eocene thermal maximum in an expanded section from the Venetian pre-Alps. Bull. Geol. Soc. Am. 119, 391–412.

Giusberti, L., Boscolo Galazzo, F., Thomas, E., 2016. Variability in climate and productivity during the Paleocene-Eocene Thermal Maximum in the western Tethys (Forada section). Clim. Past 12, 213–240.

Goodbred, S.L., Kuehl, S.A., Steckler, M.S., Sarker, M.H., 2003. Controls on facies distribution and stratigraphic preservation in the Ganges-Brahmaputra delta sequence. Sediment. Geol. 155, 301–316.

Gradstein, F.M., Kaminski, M.A., Berggren, W.A., Kristiansen, I.L., D'lorio, M.A., 1994. Cenozoic biostratigraphy of the North Sea and Labrador Shelf. Micropaleontology 40 (i-ii + 1–152).

Gran, K., Paola, C., 2001. Riparian vegetation controls on braided stream dynamics. Water Resour. Res. 37, 3275–3283.

Greenwood, D.R., Moss, P.T., Rowett, A.I., Vadala, A.J., Keefe, R.L., 2003. Plant communities

and climate change in southeastern Australia during the early Paleogene. In: Causes and Consequences of Globally Warm Climates in the Early Paleogene, 365–380.

Greve, P., Orlowsky, B., Mueller, B., Sheffield, J., Reichstein, M., Seneviratne, S.I., 2014. Global assessment of trends in wetting and drying over land. Nat. Geosci. 7, 716–721.

Handley, L., Pearson, P.N., McMillan, I.K., Pancost, R.D., 2008. Large terrestrial and marine carbon and hydrogen isotope excursions in a new Paleocene/Eocene boundary section from Tanzania. Earth Planet. Sci. Lett. 275, 17–25.

Handley, L., Crouch, E.M., Pancost, R.D., 2011. A New Zealand record of sea level rise and environmental change during the Paleocene-Eocene Thermal Maximum. Palaeogeogr. Palaeoclimatol. Palaeoecol. 305, 185–200.

Handley, L., O'Halloran, A., Pearson, P.N., Hawkins, E., Nicholas, C.J., Schouten, S., McMillan, I.K., Pancost, R.D., 2012. Changes in the hydrological cycle in tropical East Africa during the Paleocene-Eocene Thermal Maximum. Palaeogeogr. Palaeoclimatol. Palaeoecol. 329, 10–21.

Harding, I.C., Charles, A.J., Marshall, J.E.A., Pälike, H., Roberts, A.P., Wilson, P.A., Jarvis, E., Thorne, R., Morris, E., Moremon, R., Pearce, R.B., Akbari, S., 2011. Sea-level and salinity fluctuations during the Paleocene-Eocene thermal maximum in Arctic Spitsbergen. Earth Planet. Sci. Lett. 303, 97–107.

Harrington, G., Kemp, S., Koch, P., 2004. Palaeocene-Eocene paratropical floral change in North America: responses to climate change and plant immigration. J. Geol. Soc. Lond. 161, 173–184.
Harrington, G.J., Clechenko, E.R., Kelly, D.C., 2005. Palynology and organic-carbon isotope ratios across a terrestrial Palaeocene/Eocene boundary section in the Williston Basin, North Dakota, USA. Palaeogeogr. Palaeoclimatol. Palaeoecol. 226, 214–232.

Haywood, A.M., Ridgwell, A., Lunt, D.J., Hill, D.J., Pound, M.J., Dowsett, H.J., Dolan, A.M., Francis, J.E., Williams, M., 2011. Are there pre-Quaternary geological analogues for a future greenhouse warming? Philos. Trans. R. Soc. A Math. Phys. Eng. Sci. 369, 933–956.

Held, I.M., Soden, B.J., 2006. Robust responses of the hydrological cycle to global warming. J. Clim. 19, 5686–5699.

Hollis, C.J., Taylor, K.W.R., Handley, L., Pancost, R.D., Huber, M., Creech, J.B., Hines, B.R., Crouch, E.M., Morgans, H.E.G., Crampton, J.S., Gibbs, S., Pearson, P.N., Zachos, J.C., 2012. Early Paleogene

temperature history of the Southwest Pacific Ocean: reconciling proxies and models. Earth Planet. Sci. Lett. 349–350, 53–66.

Huber, M., Caballero, R., 2011. The early Eocene equable climate problem revisited. Clim. Past 7, 603–633.

Huber, M., 2012. Progress in greenhouse climate modeling. Reconstr. Earth Deep. Clim. State Art 18, 213–262.

Hyland, E.G., Sheldon, N.D., Van der Voo, R., Badgley, C., Abrajevitch, A., 2015. A new paleoprecipitation proxy based on soil magnetic properties: implications for expanding paleoclimate reconstructions. Bull. Geol. Soc. Am. 127, 975–981.

Inglis, G.N., Collinson, M.E., Riegel, W., Wilde, V., Robson, B.E., Lenz, O.K., Pancost, R.D., 2015a. Ecological and biogeochemical change in an early Paleogene peat-forming environment: linking biomarkers and palynology. Palaeogeogr. Palaeoclimatol. Palaeoecol. 438, 245–255.

Inglis, G.N., Farnsworth, A., Lunt, D., Foster, G.L., Hollis, C.J., Pagani, M., Jardine, P.E., Pearson, P.N., Markwick, P., Galsworthy, A.M.J., Raynham, L., Taylor, K.W.R., Pancost, R.D., 2015b. Descent toward the Icehouse: Eocene sea surface cooling inferred from GDGT distributions. Paleoceanography 30, 1000–1020.

Inglis, G.N., Collinson, M.E., Riegel, W., Wilde, V., Farnsworth, A., Lunt, D.J., Valdes, P., Robson, B.E., Scott, A.C., Lenz, O.K., Naafs, B.D.A., Pancost, R.D., 2017. Mid-latitude continental temperatures through the early Eocene in western Europe. Earth Planet. Sci. Lett. 460, 86–96.

IPCC, 2013. Climate Change 2013: The Physical Science Basis. Contribution of Working Group I to the Fifth Assessment Report of the Intergovernmental Panel on Climate Change. Cambridge University Press, Cambridge, UK and New York, NY, USA. Jagniecki, E.A., Lowenstein, T.K.T.K., Jenkins, D.M., Demicco, R.V., 2015. Eocene atmospheric CO_2 from the nahcolite proxy. Geology 43, 1075–1078.

Jaramillo, C., Ochoa, D., Contreras, L., Pagani, M., Carvajal-Ortiz, H., Pratt, L.M., Krishnan, S., Cardona, A., Romero, M., Quiroz, L., Rodriguez, G., Rueda, M.J., de la Parra, F., Morón, S., Green, W., Bayona, G., Montes, C., Quintero, O., Ramirez, R., Mora, G., Schouten, S., Bermudez, H., Navarrete, R., Parra, F., Alvarán, M., Osorno, J., Crowley, J.L., Valencia, V., Vervoort, J., 2010. Effects

of rapid global warming at the Paleocene-Eocene boundary on neotropical vegetation. Science 330, 957–961.

Jenkyns, H.C., 2010. Geochemistry of oceanic anoxic events. Geochem. Geophys. Geosyst. 11.

Jiang, S., Wise Jr., S.W., 2006. Surface-water chemistry and fertility variations in the tropical Atlantic across the Paleocene/Eocene Thermal Maximum as evidenced by calcareous nannoplankton from ODP Leg 207, Hole 1259B. Rev. Micropaleontol. 49, 227–244.

Jiang, Y., Zhuang, Q., Schaphoff, S., Sitch, S., Sokolov, A., Kicklighter, D., Melillo, J., 2012. Uncertainty analysis of vegetation distribution in the northern high latitudes during the 21st century with a dynamic vegetation model. Ecol. Evol. 2, 593–614.

Jiménez Cisneros, B.E., Oki, T., Arnell, N.W., Benito, G., Cogley, J.G., Döll, P., Jiang, T., Mwakalila, S.S., 2014. Freshwater resources. In: Field, C.B., Barros, V.R., Dokken, D.J., Mach, K.J., Mastrandrea, M.D., Bilir, T.E., Chatterjee, M., Ebi, K.L., Estrada, Y.O., Genova, R.C., Girma, B., Kissel, E.S., Levy, A.N., MacCracken, S., Mastrandrea, P.R., White, L.L. (Eds.), Climate Change 2014: Impacts, Adaptation, and Vulnerability. Part A: Global and Sectoral Aspects. Contribution of Working Group II to the Fifth Assessment Report of the Intergovernmental Panel of Climate Change. Cambridge University Press, Cambridge, United Kingdom and New York, NY, USA, 229–269.

Jobbagy, E.G., Jackson, R., 2000. The vertical distribution of soil organic carbon and its relation to climate and vegetation. Ecol. Appl. 10 (2), 423–436.

John, C.M., Bohaty, S.M., Zachos, J.C., Sluijs, A., Gibbs, S., Brinkhuis, H., Bralower, T.J., 2008. North American continental margin records of the Paleocene-Eocene thermal maximum: implications for global carbon and hydrological cycling. Paleoceanography 23.

John, C.M., Banerjee, N.R., Longstaffe, F.J., Sica, C., Law, K.R., Zachos, J.C., 2012. Clay assemblage and oxygen isotopic constraints on the weathering response to the Paleocene-Eocene thermal maximum, east coast of North America. Geology 40, 591–594.

Kaiho, K., Arinobu, T., Ishiwatari, R., Morgans, H.E.G., Okada, H., Takeda, N., Tazaki, K., Zhou, G., Kajiwara, Y., Matsumoto, R., Hirai, A., Niitsuma, N., Wada, H., 1996. Latest Paleocene benthic foraminiferal extinction and environmental changes at Tawanui, New Zealand. Paleoceanography 11, 447–465.

Kaiho, K., Takeda, K., Petrizzo, M.R., Zachos, J.C., 2006. Anomalous shifts in tropical Pacific planktonic and benthic foraminiferal test size during the Paleocene-Eocene thermal maximum. Palaeogeogr. Palaeoclimatol. Palaeoecol. 237, 456–464.

Kelly, D.C., Zachos, J.C., Bralower, T.J., Schellenberg, S.A., 2005. Enhanced terrestrial weathering/runoff and surface ocean carbonate production during the recovery stages of the Paleocene-Eocene thermal maximum. Paleoceanography 20

Kender, S., Stephenson, M.H., Riding, J.B., Leng, M.J., Knox, R.W.O.B., Peck, V.L., Kendrick, C.P., Ellis, M.A., Vane, C.H., Jamieson, R., 2012. Marine and terrestrial environmental changes in NW Europe preceding carbon release at the Paleocene-Eocene transition. Earth Planet. Sci. Lett. 353–354, 108–120.

Khozyem, H., Adatte, T., Spangenberg, J.E., Tantawy, A.A., Keller, G., 2013. Palaeoenvironmental and climatic changes during the Palaeocene–Eocene Thermal Maximum (PETM) at the Wadi Nukhul Section, Sinai, Egypt. J. Geol. Soc. Lond. 170, 341–352.

Khozyem, H., Adatte, T., Spangenberg, J.E., Keller, G., Tantawy, A.A., Ulianov, A., 2015. New geochemical constraints on the Paleocene-Eocene thermal maximum: Dababiya GSSP, Egypt. Palaeogeogr. Palaeoclimatol. Palaeoecol. 429, 117–135.

Kiehl, J.T., Shields, C.A., 2013. Sensitivity of the Palaeocene-Eocene Thermal Maximum climate to cloud properties. Philos. Trans. R. Soc. A-Mathematical Phys. Eng. Sci. 371.

Kirschke, S., Bousquet, P., Ciais, P., Saunois, M., Canadell, J.G., Dlugokencky, E.J., Bergamaschi, P., Bergmann, D., Blake, D.R., Bruhwiler, L., Cameron-Smith, P., Castaldi, S., Chevallier, F., Feng, L., Fraser, A., Heimann, M., Hodson, E.L., Houweling, S., Josse, B., Fraser, P.J., Krummel, P.B., Lamarque, J.-F., Langenfelds, R.L., Le Quéré, C., Naik, V., O'Doherty, S., Palmer, P.I., Pison, I., Plummer, D., Poulter, B., Prinn, R.G., Rigby, M., Ringeval, B., Santini, M., Schmidt, M., Shindell, D.T., Simpson, I.J., Spahni, R., Steele, L.P., Strode, S.A., Sudo, K., Szopa, S., van der Werf, G.R., Voulgarakis, A., van Weele, M., Weiss, R.F., Williams, J.E., Zeng, G., 2013. Three decades of global methane sources and sinks. Nat. Geosci. 6, 813–823.

Knox, R.W.O., Aubry, M.P., Berggren, W.A., Dupuis, C., Ouda, K., Magioncalda, R., Soliman, M., 2003. The Qreiya section at Gebel Abu Had: lithostratigraphy, clay mineralogy, geochemistry and biostratigraphy. Micropaleontology 49, 93–104.

Knutti, R., Sedláček, J., 2013. Robustness and uncertainties in the new CMIP5 climate model projections. Nat. Clim. Chang. 3, 369–373.

Kodina, L.A., Huang, Y., Gavrilov, Y.O., Jones, M., Eglinton, G., 1995. Environment of upper Paleocene black shale deposition in Southern Russia and adjacent regions as revealed by isotope and biomarker study. In: Grimalt, J.O., Dorrosoro, C. (Eds.), Organic Geochemistry: Developments and Applications to Energy, Climate, Environment and Human History: Selected Papers from the 17th International Meeting on Organic Geochemistry, Special Papers. Volume 369. Geological Society of America, 192–194.

Kohn, M.J., 2016. Carbon isotope discrimination in C3 land plants is independent of natural variations in pCO_2. Geochem. Perspect. Lett. 2, 35–43

Kopp, R.E.., Schumann, D., Raub, T.D., Powars, D.S., Godfrey, L.V., Swanson-Hysell, N.L., Maloof, A.C., Vali, H., 2009. An Appalachian Amazon? Magnetofossil evidence for the development of a tropical river-like system in the midAtlantic United States during the Paleocene-Eocene thermal maximum. Paleoceanography 24, 1–17.

Kraus, M.J., McInerney, F.A., Wing, S.L., Secord, R., Baczynski, A.A., Bloch, J.I., 2013. Paleohydrologic response to continental warming during the Paleocene-Eocene Thermal Maximum, Bighorn Basin, Wyoming. Palaeogeogr. Palaeoclimatol. Palaeoecol. 370, 196–208.

Kraus, M.J., Woody, D.T., Smith, J.J., Dukic, V., 2015. Alluvial response to the Paleocene-Eocene Thermal Maximum climatic event, Polecat Bench, Wyoming (U.S.A.). Palaeogeogr. Palaeoclimatol. Palaeoecol. 435, 177–192.

Kraus, M., Riggins, S., 2007. Transient drying during the Paleocene–Eocene Thermal Maximum (PETM): analysis of paleosols in the bighorn basin, Wyoming. Palaeogeogr. Palaeoclimatol. Palaeoecol. 245, 444–461.

Krishnan, S., Pagani, M., Agnini, C., 2015. Leaf waxes as recorders of paleoclimatic changes during the Paleocene-Eocene Thermal Maximum: regional expressions from the Belluno Basin. Org. Geochem. 80, 8–17.

Larrasoaña, J.C., Roberts, A.P., Chang, L., Schellenberg, S.A., Fitz Gerald, J.D., Norris, R.D., Zachos, J.C., 2012. Magnetotactic bacterial response to Antarctic dust supply during the Palaeocene-Eocene thermal maximum. Earth Planet. Sci. Lett. 333–334, 122–133.

Lebedeva, M.I., Fletcher, R.C., Brantley, S.L., 2010. A mathematical model for steadystate regolith production at constant erosion rate. Earth Surf. Process. Landf. 35, 508–524.

Leier, A.L., DeCelles, P.G., Pelletier, J.D., 2005. Mountains, monsoons, and megafans. Geology 33, 289–292.

Lippert, P.C., Zachos, J.C., 2007. A biogenic origin for anomalous fine-grained magnetic material at the Paleocone-Eocene boundary at Wilson Lake, New Jersey. Paleoceanography 22.

Littler, K., Röhl, U., Westerhold, T., Zachos, J.C., 2014. A high-resolution benthic stableisotope record for the South Atlantic: implications for orbital-scale changes in Late Paleocene-Early Eocene climate and carbon cycling. Earth Planet. Sci. Lett. 401, 18–30.

Loptson, C.A., Lunt, D.J., Francis, J.E., 2014. Investigating vegetation-climate feedbacks during the early Eocene. Clim. Past 10, 419–436.

Lourens, L., Sluijs, A., Kroon, D., Zachos, J.C., Thomas, E., Röhl, U., Bowles, J., Raffi, I., 2005. Astronomical pacing of late Palaeocene to early Eocene global warming events. Nature 435, 1083–1087.

Lunt, D.J., Valdes, P.J., Jones, T.D., Ridgwell, A., Haywood, A.M., Schmidt, D.N., Marsh, R., Maslin, M., 2010. CO2-driven ocean circulation changes as an amplifier of Paleocene-Eocene thermal maximum hydrate destabilization. Geology 38, 875–878.

Lunt, D.J., Dunkley Jones, T., Heinemann, M., Huber, M., LeGrande, A., Winguth, A., Loptson, C., Marotzke, J., Roberts, C.D., Tindall, J., Valdes, P., Winguth, C., Jones, T.D., Heinemann, M., Huber, M., LeGrande, A., Winguth, A., Loptson, C., Marotzke, J., Roberts, C.D., Tindall, J., Valdes, P., Winguth, C., 2012. A model-data comparison for a multi-model ensemble of early Eocene atmosphere-ocean simulations: EoMIP. Clim. Past 8, 1717–1736.

Lunt, D.J., Elderfield, H., Pancost, R., Ridgwell, A., Foster, G.L., Haywood, A., Kiehl, J., Sagoo, N., Shields, C., Stone, E.J., Valdes, P., 2013. Warm climates of the past—a lesson for the future? Philos. Trans. A. Math. Phys. Eng. Sci. 371, 20130146.

Macklin, M.G., Lewin, J., Woodward, J.C., 2012. The fluvial record of climate change. Philos. Trans. R. Soc. A Math. Phys. Eng. Sci. 370, 2143–2172.

Manners, H.R., Grimes, S.T., Sutton, P.A., Domingo, L., Leng, M.J., Twitchett, R.J., Hart, M.B., Dunkley Jones, T., Pancost, R.D., Duller, R., Lopez-Martinez, N., 2013. Magnitude and profile of organic carbon isotope records from the Paleocene-Eocene Thermal Maximum: evidence from northern Spain. Earth Planet. Sci. Lett. 376, 220–230.

März, C., Schnetger, B., Brumsack, H.-J., 2010. Paleoenvironmental implications of Cenozoic sediments from the Central Arctic Ocean (IODP expedition 302) using inorganic geochemistry. Paleoceanography 25, PA3206.

Maxbauer, D.P., Feinberg, J.M., Fox, D.L., 2016a. Magnetic mineral assemblages in soils and paleosols as the basis for paleoprecipitation proxies: a review of magnetic methods and challenges. Earth-Sci. Rev. 155, 28–48.

Maxbauer, D.P., Feinberg, J.M., Fox, D.L., Clyde, W.C., 2016b. Magnetic minerals as recorders of weathering, diagenesis, and paleoclimate: a core-outcrop comparison of Paleocene-Eocene paleosols in the Bighorn Basin, WY, USA. Earth Planet. Sci. Lett. 452, 15–26.

McInerney, F.a., Wing, S.L., 2011. The Paleocene-Eocene thermal maximum: a perturbation of carbon cycle, climate, and biosphere with implications for the future. Annu. Rev. Earth Planet. Sci. 39, 489–516.

Meire, L., Soetaert, K.E.R., Meysman, F.J.R., 2013. Impact of global change on coastal oxygen dynamics and risk of hypoxia. Biogeosciences 10, 2633–2653

Murphy, B.H., Farley, K.A., Zachos, J.C., 2010. An extraterrestrial ^{3}He-based timescale for the Paleocene-Eocene thermal maximum (PETM) from Walvis Ridge, IODP Site 1266. Geochim. Cosmochim. Acta 74, 5098–5108.

Nagy, J., Jargvoll, D., Dypvik, H., Jochmann, M., Riber, L., 2013. Environmental changes during the paleocene-eocene thermal maximum in spitsbergen as reflected by benthic foraminifera. Polar Res. 32.

Nearing, M.A., Pruski, F.F., O'Neal, M.R., 2004. Expected climate change impacts on soil erosion rates: a review. J. Soil Water Conserv. 59, 43–50.

Nicholas, C.J., Pearson, P.N., Bown, P.R., Jones, T.D., Huber, B.T., Karega, A., Lees, J.A., McMillan, I.K., O'Halloran, A., Singano, J.M., Wade, B.S., 2006. Stratigraphy and sedimentology of the Upper Cretaceous to Paleogene Kilwa Group, southern coastal Tanzania. J. Afr. Earth Sci. 45, 431–466.

Nicolo, M.J., Dickens, G.R., Hollis, C.J., 2010. South Pacific intermediate water oxygen depletion at the onset of the Paleocene-Eocene Thermal Maximum as depicted in New Zealand margin sections. Paleoceanography 25, PA4210.

Pagani, M., Pedentchouk, N., Huber, M., Sluijs, A., Schouten, S., Brinkhuis, H., Damsté, J.S.S., Dickens, G.R., 2006. Arctic hydrology during global warming at the Palaeocene/Eocene thermal maximum. Nature 442, 671–675.

Pagani, M., Huber, M., Sageman, B., 2013. Greenhouse climates. In: Treatise on Geochemistry, Second Edition. 281–304.

Pak, D.K., Miller, K.G., 1992. Paleocene to Eocene benthic foraminiferal isotopes and assemblages: implications for deepwater circulation. Paleoceanography 7, 405–422.

Pälike, C., Delaney, M.L., Zachos, J.C., 2014. Deep-sea redox across the Paleocene-Eocene thermal maximum. Geochem. Geophys. Geosyst. 15, 1038–1053.

Pancost, R.D., Steart, D.S., Handley, L., Collinson, M.E., Hooker, J.J., Scott, A.C., Grassineau, N.V., Glasspool, I.J., 2007. Increased terrestrial methane cycling at the Palaeocene-Eocene thermal maximum. Nature 449, 332–335.

Pardo, A., Keller, G., Molina, E., Canudo, J.I., 1997. Planktic foraminiferal turnover across the Paleocene-Eocene transition at DSDP Site 401, Bay of Biscay, North Atlantic. Mar. Micropaleontol. 29, 129–158.

Pearson, P.N., Ditchfield, P.W., Singano, J., Harcourt-Brown, K.G., Nicholas, C.J., Olsson, R.K., Shackleton, N.J., Hall, M., 2001. Warm tropical sea surface temperatures in the Late Cretaceous and Eocene epochs. Nature 413, 481–487.

Percival, L.M.E., Cohen, A.S., Davies, M.K., Dickson, A.J., Hesselbo, S.P., Jenkyns, H.C., Leng, M.J., Mather, T.A., Storm, M.S., Xu, W., 2016. Osmium isotope evidence for two pulses of increased continental weathering linked to Early Jurassic volcanism and climate change. Geology 44, 759–762.

Pole, M., 2010. Ecology of Paleocene-Eocene vegetation at Kakahu, South Canterbury, New Zealand. Palaeontol. Electron. 13, 14A–29.

Rabalais, N.N., Turner, R.E., Díaz, R.J., Justić, D., 2009. Global change and eutrophication of coastal waters. ICES J. Mar. Sci. 66, 1528–1537.

Raffi, I., Backman, J., Zachos, J.C., Sluijs, A., 2009. The response of calcareous nannofossil assemblages to the Paleocene Eocene Thermal Maximum at the Walvis Ridge in the South Atlantic. Mar. Micropaleontol. 70, 201–212.

Ravizza, G., Norris, R.N., Blusztajn, J., Aubry, M.-P., 2001. An osmium isotope excursion associated with the Late Paleocene thermal maximum: evidence of intensified chemical weathering. Paleoceanography 16, 155–163.

Retallack, G.J., 2005. Pedogenic carbonate proxies for amount and seasonality of precipitation in paleosols. Geology 33, 333–336.

Robert, C., Chamley, H., 1991. Development of early Eocene warm climates, as inferred from clay mineral variations in oceanic sediments. Glob. Planet. Chang. 3, 315–331.

Robert, C., Kennett, J.P., 1994. Antarctic subtropical humid episode at the Paleocene-Eocene boundary - clay-mineral evidence. Geology 22, 211–214.

Rodriguez-Tovar, F.J., Uchman, A., Alegret, L., Molina, E., 2011. Impact of the Paleocen-eEocene Thermal Maximum on the macrobenthic community: ichnological record from the Zumaia section, northern Spain. Mar. Geol. 282, 178–187.

Samanta, A., Bera, M.K., Ghosh, R., Bera, S., Filley, T., Pande, K., Rathore, S.S., Rai, J., Sarkar, A., 2013. Do the large carbon isotopic excursions in terrestrial organic matter across Paleocene-Eocene boundary in India indicate intensification of tropical precipitation? Palaeogeogr. Palaeoclimatol. Palaeoecol. 387, 91–103.

Schmitz, B., Pujalte, V., 2003. Sea-level, humidity, and land-erosion records across the initial Eocene thermal maximum from a continental-marine transect in northern Spain. Geology 31, 689–692.

Schmitz, B., Pujalte, V., 2007. Abrupt increase in seasonal extreme precipitation at the Paleocene-Eocene boundary. Geology 35, 215–218.

Schmitz, B., Pujalte, V., Nunez-Betelu, K., Núñez-Betelu, K., 2001. Climate and sea-level perturbations during the initial eocene thermal maximum: evidence from siliciclastic units in the Basque Basin

(Ermua, Zumaia and Trabakua Pass), northern Spain. Palaeogeogr. Palaeoclimatol. Palaeoecol. 165, 299–320.

Schoon, P.L., Heilmann-Clausen, C., Pagh Schultz, B., Sluijs, A., Sinninghe Damsté, J.S., Schouten, S., 2013. Recognition of Early Eocene global carbon isotope excursions using lipids of marine Thaumarchaeota. Earth Planet. Sci. Lett. 373, 160–168.

Schoon, P.L., Heilmann-Clausen, C., Pagh Schultz, B., Sinninghe Damste, J.S., Schouten, S., 2015. Warming and environmental changes in the eastern North Sea Basin during the Palaeocene-Eocene Thermal Maximum as revealed by biomarker lipids. Org. Geochem. 78, 79–88.

Schulte, P., Scheibner, C., Speijer, R.P., 2011. Fluvial discharge and sea-level changes controlling black shale deposition during the Paleocene-Eocene Thermal Maximum in the Dababiya Quarry section, Egypt. Chem. Geol. 285, 167–183.

Schumann, D., Raub, T.D., Kopp, R.E., Guerquin-Kern, J.-L., Wu, T.-D., Rouiller, I., Smirnov, A. V, Sears, S.K., Lücken, U., Tikoo, S.M., Hesse, R., Kirschvink, J.L., Vali, H., 2008. Gigantism in unique biogenic magnetite at the Paleocene–Eocene Thermal Maximum. Proc. Natl. Acad. Sci. 105, 17648–17653.

Secord, R., Bloch, J.I., Chester, S.G.B., Boyer, D.M., Wood, A.R., Wing, S.L., Kraus, M.J., McInerney, F.A., Krigbaum, J., 2012. Evolution of the earliest horses driven by climate change in the Paleocene-Eocene Thermal Maximum. Science 335, 959–962.

Self-Trail, J.M., Powars, D.S., Watkins, D.K., Wandless, G.A., 2012. Calcareous nannofossil assemblage changes across the Paleocene-Eocene Thermal Maximum: evidence from a shelf setting. Mar. Micropaleontol. 92–93, 61–80.

Sinninghe Damsté, J.S., Kuypers, M.M.M., Schouten, S., Schulte, S., Rullkötter, J., 2003. The lycopane/C31 n-alkane ratio as a proxy to assess palaeoxicity during sediment deposition. Earth Planet. Sci. Lett. 209, 215–226.

Sluijs, A., Brinkhuis, H., 2009. A dynamic climate and ecosystem state during the Paleocene-Eocene Thermal Maximum: inferences from dinoflagellate cyst assemblages on the New Jersey Shelf. Biogeosciences 6, 1755–1781.

Sluijs, A., Pross, J., Brinkhuis, H., 2005. From greenhouse to icehouse; organic-walled dinoflagellate cysts as paleoenvironmental indicators in the Paleogene. Earth-Sci. Rev. 68, 281–315.

Sluijs, A., Schouten, S., Pagani, M., Woltering, M., Brinkhuis, H., Damste, J.S.S., Dickens, G.R., Huber, M., Reichart, G.J., Stein, R., Matthiessen, J., Lourens, L.J., Pedentchouk, N., Backman, J., Moran, K., Scientists, E., 2006. Subtropical arctic ocean temperatures during the Palaeocene/Eocene thermal maximum. Nature 441, 610–613.

Sluijs, A., Bowen, G.J., Brinkhuis, H., Lourens, L.J., Thomas, E., 2007. The Palaeocene-Eocene Thermal Maximum super greenhouse: biotic and geochemical signatures, age models and mechanisms of global change. In: Geological Society Special Publication, 323–349.

Sluijs, A., Brinkhuis, H., Crouch, E.M., John, C.M., Handley, L., Munsterman, D., Bohaty, S.M., Zachos, J.C., Reichart, G.J., Schouten, S., Pancost, R.D., Damste, J.S.S., Welters, N.L.D., Lotter, A.F., Dickens, G.R., 2008a. Eustatic variations during the Paleocene-Eocene greenhouse world. Paleoceanography 23, PA4216.

Sluijs, A., Röhl, U., Schouten, S., Brumsack, H.J., Sangiorgi, F., Sinninghe Damsté, J.S., Brinkhuis, H., 2008b. Article late Paleocene - Early Eocene paleoenvironments with special emphasis on the Paleocene-Eocene thermal maximum (Lomonosov Ridge, Integrated Ocean Drilling Program Expedition 302). Paleoceanography 23.

Sluijs, A., Bijl, P.K., Schouten, S., Röhl, U., Reichart, G.J., Brinkhuis, H., Röhl, U., 2011. Southern ocean warming, sea level and hydrological change during the Paleocene-Eocene thermal maximum. Clim. Past 7, 47–61.

Sluijs, A., Van Roij, L., Harrington, G.J., Schouten, S., Sessa, J.A., Levay, L.J., Reichart, G.J., Slomp, C.P., 2014. Warming, euxinia and sea level rise during the PaleoceneEocene thermal maximum on the gulf coastal plain: implications for ocean oxygenation and nutrient cycling. Clim. Past 10, 1421–1439.

Soliman, M.F., Aubry, M.P., Schmitz, B., Sherrell, R.M., 2011. Enhanced coastal paleoproductivity and nutrient supply in Upper Egypt during the Paleocene/Eocene Thermal Maximum (PETM): mineralogical and geochemical evidence. Palaeogeogr. Palaeoclimatol. Palaeoecol. 310, 365–377.

Speijer, R.P., Morsi, M.M., 2002. Ostracode turnover and sea-level changes associated with the Paleocene-Eocene thermal maximum. Geology 30, 23–26.

Speijer, R.P., Schmitz, B., 1998. A benthic foraminiferal record of Paleocene sea level and trophic/redox conditions at Gebel Aweina, Egypt. Palaeogeogr. Palaeoclimatol. Palaeoecol. 137, 79–101.

Speijer, R.P., Wagner, T., 2002. Sea-level changes and black shales associated with the late Paleocene thermal maximum: organic-geochemical and micropaleontologic evidence from the southern Tethyan margin (Egypt-Israel). Geol. Soc. Am. Spec. Pap. 356, 533–549.

Stassen, P., Dupuis, C., Steurbaut, E., Yans, J., Speijer, R.P., 2012a. Perturbation of a Tethyan coastal environment during the Paleocene-Eocene thermal maximum in Tunisia (Sidi Nasseur and Wadi Mezaz). Palaeogeogr. Palaeoclimatol. Palaeoecol. 317–318, 66–92.

Stassen, P., Thomas, E., Speijer, R.P., 2012b. Integrated stratigraphy of the Paleocene-Eocene thermal maximum in the New Jersey Coastal Plain: Toward understanding the effects of global warming in a shelf environment. Paleoceanography 27.

Stein, R., Boucsein, B., Meyer, H., 2006. Anoxia and high primary production in the Paleogene central Arctic Ocean: first detailed records from Lomonosov ridge. Geophys. Res. Lett. 33.

Steurbaut, E., Magioncalda, R., Dupuis, C., van Simaeys, S., Roche, E., Roche, M., 2003. Palynology, paleoenvironments, and organic carbon isotope evolution in lagoonal Paleocene-Eocene boundary settings in North Belgium. Spec. Pap. Geol. Soc. Am. 369, 291–317.

Takeda, K., Kaiho, K., 2007. Faunal turnovers in central Pacific benthic foraminifera during the Paleocene-Eocene thermal maximum. Palaeogeogr. Palaeoclimatol. Palaeoecol. 251, 175–197.

Thomas, E., Shackleton, N.J., 1996. The Paleocene-Eocene benthic foraminiferal extinction and stable isotope anomalies. Geol. Soc. Lond. Spec. Publ. 101, 401–441.

Winguth, A., Shellito, C., Shields, C., Winguth, C., 2010. Climate response at the Paleocene-Eocene Thermal Maximum to greenhouse gas forcing-a model study with CCSM3. J. Clim. 23, 2562–2584.

Zhou, X., Thomas, E., Rickaby, R.E.M., Winguth, A.M.E., Lu, Z., 2014. I/Ca evidence for upper ocean deoxygenation during the PETM. Paleoceanography 29, 964–975.